A Combined Experimental and Theoretical Study of NMR Spin-Lattice Relaxation Times in HD-Ar and D_2–Ar mixtures

by

Hasan Sabzyan

A thesis
presented to the University of Waterloo
in fulfilment of the
thesis requirement for the degree of
Doctor of Philosophy
in
Chemistry

Waterloo, Ontario, Canada, 1997

The University of Waterloo requires the signatures of all persons using or photocopying this thesis. Please sign below, and give address and date.

Abstract

The hydrogen-argon system is the preeminent prototype system for the study of atom-diatom interaction potential energy surfaces. The temperature dependence of the NMR spin-lattice relaxation time in the gas phase provides one of the most sensitive tests to the anisotropic part of these potential energy surfaces.

The present work consists of a combined experimental and theoretical study of the NMR spin-lattice relaxation times in HD–Ar and D_2–Ar mixtures. A gas-handling system and a sample cell have been designed and successfully employed in the experimental part of this study. The spin-lattice relaxation times for the proton and deuteron of HD in HD–Ar mixtures, and for the deuteron of D_2 in D_2–Ar mixtures have been measured over a wide range of temperatures at several mole fractions and densities. The quality of the results is tested by the analysis of the one-dimensional spectra. The values of the nuclear Overhauser effect (NOE) enhancements for the proton and deuteron of HD in HD–Ar mixtures have been measured; these NOE measurements represent the first such experiments for the gas phase.

Theoretical values of the spin-lattice relaxation times and the NOE enhancements have been calculated for the same mixtures using the XC(fit) potential energy surface derived by Bissonnette *et al.* [*J. Chem. Phys.* **105**, 2639-2653, (1996)] for hydrogen-argon systems. A complete analysis of the temperature, field and density dependences of the relaxation times has been carried out for both systems. Two reliable methods have been proposed to compare the theoretical and experimental NMR spin-lattice relaxation times obtained for high temperature equilibrium mixtures of the two parity isomers of the D_2–Ar system under the conditions in which

separate measurement of their deuteron relaxation times is not possible.

The experimental and theoretical results for the HD–Ar system show excellent agreement, but the agreement for the D_2–Ar system is relatively good only for higher temperatures. It has been argued that the major source of the difference between the level of agreement for the two systems is due to uncertainties in the anisotropic part of the homonuclear potential energy surface. The accuracy of the anisotropy for the heteronuclear potential energy surface is determined, through transformation, by the accuracy of the isotropic part of the homonuclear potential, which is usually higher than that of the anisotropic parts. The effects of orbiting resonances and the sensitivity of the NMR cross sections to subtle changes in the potential have been studied. Effects of the non-rigidity of the diatom on the coupling constants, and hence on the NMR relaxation times, have also been studied.

Finally, some suggestions for further studies of hydrogen-argon systems have been proposed.

Acknowledgment

I would like to express my thanks and gratitude to my supervisors, professors F.R.W. McCourt and W.P. Power for suggesting the topic of this thesis and for their invaluable support and encouragement throughout this work.

I am thankful to the members of my defense committee, professors R.J. LeRoy, G. Penner and W.-K. Liu for their valuable comments. I should specifically thank professor R.J. LeRoy for all of his support and the fruitful discussions we had throughout this work. I also owe Dr. C. Bissonnette for all his valuable help in the form of discussion and computer programming. I would like to thank E. Hanson and G. B. Clark for their computer technical support. I should also thank our NMR technician Mrs. J. Venne and the NMR facility manager Dr. S. Mooibroek for their assistance in the experimental part of the work. I also appreciate the help of my laboratory fellows C. W. Kirby and M. J. Ditty.

I am also thankful to professors K. R. Jeffrey, J. Jeener, A. Bain and V. Spirko for their valuable help and advice in different stages of the experimental and theoretical parts of this work.

The financial support of the University of Waterloo in the form of TA and scholarship funding, and of NSERC of Canada via RA funding are highly appreciated.

I am also pleased to gratefully acknowledge the financial support of my sponsors, Isfahan University and the Ministry of Culture and Higher Education of the Islamic Republic of Iran, without which this work would not have been possible.

Finally, I should greatly appreciate the help and understanding of my wife, who took care of me and our family in the past couple of years while I was busy with this work. The hardship she endured during this work cannot be described easily. I would like to thank her, and ask Almighty God for keeping us together forever.

Dedications

To my wife and my children (Mahdi and Maryam)

&

To my parents

(for their encouragement and genuine interest in my education)

Contents

List of Tables

List of Figures

Acronyms and Notations

BF	Body-Fixed
SF	Space-Fixed
CC	Close-coupled
CPMG	Carr-Purcel-Meiboom-Gill
D	Dipolar
DCCV	Detachable Compact Coaxial Valve
DQ	Dipolar-Quadrupolar
FID	Free Induction Decay
GHS	Gas Handling System
HF	Hartree-Fock
NMR	Nuclear Magnetic Resonance
NOE	Nuclear Overhauser Effect
PES	Potential Energy Surface
Q	Quadrupolar
SBE	Senftleben-Beenakker Effect
SR	Spin-Rotation

T_1	**Spin-Lattice Relaxation Time**
T_1^*	**Effective Spin-Lattice Relaxation Time**
T_2	**Spin-Spin Relaxation Time**
T_2^*	**Effective Spin-Spin Relaxation Time**
XC	**Exchange-Coulomb**
WS	**Waldmann-Snider**

Chapter 1

Introduction

1.1 General Introduction

Nuclear Magnetic resonance spectroscopy has proven to be one of the most powerful spectroscopic techniques for the detailed study of molecules in all phases of matter. The information obtained from NMR spectra and relaxation time measurements forms a complete data set from which the energetic and dynamical properties of systems can be deduced. NMR chemical shift measurements, which probe only the time-independent interactions between the nuclear spin and its surroundings, can be used for structure and chemical bond characterizations, while NMR relaxation time and lineshape measurements, which probe the time-dependent part of the interactions, can provide information about almost all physical and chemical properties of both the molecule and its surroundings, including dynamical behavior and intermolecular interactions.[1]

In the gas phase, NMR relaxation is due ultimately to collisional reorientation of the molecular rotational angular momentum, which is weakly coupled to the spin system via intramolecular interactions. NMR relaxation time measurements in the

gas phase can thus provide a great deal of useful information about intermolecular interactions governing the collisional reorientation of the rotational angular momentum. NMR relaxation times and the anisotropic part of the intermolecular potential energy surface (PES) for an atom-diatom gas phase system are linked through (collision) cross sections by kinetic theory.[2,3] The kinetic theory approach has been successful in describing NMR relaxation phenomena and predicting relaxation times which are in good agreement with available experimental data.

Previous studies on gas phase systems[4–6] have shown that NMR relaxation times are perhaps the bulk physical properties most sensitive to the anisotropic part of PES's. Thus, gas phase NMR relaxation time measurements can be used to evaluate the anisotropic part of the PES recommended for a given system. This has been a particular goal of molecular and chemical physicists investigating the fundamental nature of interactions in matter. Since the NMR T_1 data are not used in the derivation or improvement of the PES, a comparison between experimental and theoretical NMR T_1 data can therefore be regarded as providing an independent quality test for any proposed PES for a given atom-diatom system.

In a series of studies that has been carried out on hydrogen-helium systems[4–6] it has been found that the best available PES[7] resulted in relaxation times for the homonuclear systems H_2–He and D_2–He in good agreement with the experimental data, while the same potential for the heteronuclear HD–He system, transformed to allow displacement of the center-of-mass of the HD molecule from its center-of-force, resulted in good agreement for the proton relaxation time but poor agreement for the deuteron relaxation time of HD. In order to throw additional light on the source of this exceptional discrepancy in the level of agreement between theory and experiment for the proton and the deuteron relaxation times, a similar study has been undertaken on isotopic hydrogen-argon systems. As H_2–Ar data were already

available, it was decided to study first the HD–Ar system and then to extend the study to include the D_2–Ar system. In the theoretical part of this study the PES derived by Bissonnette *et al.*[8] for the hydrogen-argon system will be employed. The results of such a study will thus be used, in the first place, to evaluate the anisotropy of this PES.

1.2 Nuclear spin relaxation

Nuclear magnetic resonance (NMR) deals with the interactions between nuclear magnetic moments and internal and external magnetic fields. A nucleus possessing (nuclear) spin $\hat{\boldsymbol{I}}$ has a magnetic moment $\hat{\boldsymbol{\mu}} = g_I \mu_N \hat{\boldsymbol{I}}$, in which g_I is the nuclear g-factor and μ_N is the nuclear magneton. If this nucleus is placed in a static homogeneous magnetic field $\boldsymbol{B}_0$ whose direction is commonly used to define the z-axis, the interaction between the magnetic moment and the field creates a splitting in the (otherwise degenerate) $2I + 1$ nuclear spin levels, with a spacing $\Delta E = |\hbar\omega_I|$, where $\omega_I = -g_I \mu_N B_0/\hbar = -\gamma_I B_0$ is the nuclear precession frequency of $\hat{\boldsymbol{\mu}}$ about $\boldsymbol{B}_0$, also known as the Larmor frequency.[9] The interaction between a magnetic moment and a magnetic field is called the Zeeman interaction. At equilibrium, the nuclei are distributed among the available energy levels according to the Boltzmann distribution. Following any process that disturbs the equilibrium distribution, such as a small time-dependent field $\boldsymbol{B}_1(t)$ applied in a direction perpendicular to $\boldsymbol{B}_0$, thereby causing a non-equilibrium macroscopic magnetization, the nuclear spin system will return to its equilibrium state by exchanging energy with its surroundings, historically called the *lattice*, via a first-order relaxation process called *spin-lattice* relaxation, characterized by a time constant T_1, known as the spin-lattice, or longitudinal, relaxation time. For a static homogeneous magnetic field $\boldsymbol{B}_0$ applied

along the z-axis, relaxation of the total magnetization M, defined as the ensemble average of the nuclear magnetic moments (*i.e.*, $M = <\mu>_0$) and known as the Curie magnetization, is expressed in terms of set of equations,

$$\frac{dM_z}{dt} = -\frac{1}{T_1}(M_z - M_{eq}), \tag{1.1}$$

for the longitudinal (*i.e.*, parallel to the direction of the static field) component and

$$\frac{dM_x}{dt} = -\omega_I M_y - \frac{1}{T_2}M_x, \tag{1.2}$$

$$\frac{dM_y}{dt} = +\omega_I M_x - \frac{1}{T_2}M_y, \tag{1.3}$$

for the corresponding transverse (*i.e.*, perpendicular to the direction of the static magnetic field) components. These equations are known as the Bloch equations.[10] The decay constant T_2 used in Eqs. (1.2) and (1.3) is called the spin-spin, or transverse, relaxation time. For a given nucleus, the relaxation times T_1 and T_2 are characteristics of the physicochemical properties of the surroundings, such as size and electric charge distribution in the molecule, magnetic properties of neighboring nuclei, intermolecular interactions, temperature and density.

Determination of T_1 and T_2

The best method for determination of the spin-lattice relaxation time T_1 is the *inversion-recovery* method.[9,11] In this method an rf pulse sequence consisting of a pair of π and $\frac{\pi}{2}$ pulses is used to probe the evolution of the z-component of the total magnetization with time. Application of the first pulse, or preparation pulse, inverts the direction of magnetization (*i.e.*, rotates the magnetization by 180°). After a time τ a second pulse, the observation pulse, rotates the recovered magnetization at

this time into the xy-plane so that it can be observed. The measured magnetization at time τ, M_τ, is related to τ by

$$\frac{M_\tau}{M_\infty} = 1 - 2\exp(-\frac{\tau}{T_1}), \tag{1.4}$$

in which $M_\infty = M_{eq}$ is the equilibrium magnetization. This equation is the integral form of Eq. (1.1). The relaxation time T_1 is obtained from a plot of $\ln(\frac{2M_\infty}{M_\infty - M_\tau})$ versus τ, which has a slope of T_1^{-1}. The accuracy of T_1 measurement depends upon the number of τ values used in the experiment; the larger the number of τ values the smaller the standard deviation of the measured value of T_1. Other important experimental conditions determining the final accuracy of T_1 measurement are discussed in Chs. 3 and 5.

The method of determination of the transverse relaxation time T_2 is known as the CPMG method. The pulse sequence used in this method consists of a preparation $\frac{\pi}{2}$-pulse, which puts the magnetization in the xy-plane, followed by a series of n $(\pi, -\pi)$ pairs of observation pulses, which are phase-shifted by 90° with respect to the preparation $\frac{\pi}{2}$-pulse. The spacing between the two pulses of each pair, and the spacing between the pairs are the same, and is $2\tau_0$. The magnetization is observed a time τ_0 after either the π or the $-\pi$ pulses. The relaxation time T_2 is obtained from the slope T_2^{-1} of a plot of $\ln(\frac{M_0}{M_\tau})$ versus $\tau = 2i\tau_0$ with $i = 1, 2, \ldots, n$. This relationship can be derived by adding, and then integrating Eq. (1.2) and (1.3) in the frame rotating at the frequency of ω_1. The role of each π or $-\pi$ pulse is to refocus the dephased M_{xy} magnetization due to processes such as chemical shifts and heteronuclear J-coupling, in order to cancel their contributions to the decay of the M_{xy} magnetization. Alternation of the direction of the π pulses takes care of the effects of possible inaccuracies in the pulse-length calibrations.

The spin-spin relaxation time T_2 can also be determined from linewidth measurement on simple one-dimensional spectra. Since interfering processes such as those mentioned above are unavoidable, the measured relaxation time in this method is not the actual spin-spin relaxation time. The relaxation time measured from the linewidth is thus an effective transverse relaxation time. This effective transverse relaxation time is denoted by T_2^*, and is related to the linewidth $\Delta\nu_{1/2}$ via Fourier transformation as

$$T_2^* = (\pi\Delta\nu_{1/2})^{-1}. \tag{1.5}$$

Under all conditions, T_2^* is shorter than T_2, because all interfering processes and experimental problems result in a faster decay of the nuclear magnetization. Short acquisition times and inaccuracies in pulse-length calibrations are examples of experimental problems contributing to the T_2^* values. Other experimental problems such as poor shimming, *i.e.*, magnetic field inhomogeneity, temperature gradients and diffusion of molecules into and out of the effective volume of the rf coil, also contribute to the measured values of all relaxation times. In the absence of diffusion into and out of the effective volume of the rf coil, the effects of magnetic field inhomogeneities on the measured T_1 appears only as an increase in the standard deviation when the signal is weak.[11,12]

Mechanisms of NMR spin-lattice relaxation

Relaxation of the nuclear magnetization towards the equilibrium state is induced by oscillating (*i.e.*, time-dependent) local magnetic fields. In the solid phase, the thermal vibration of the crystalline lattice, paramagnetic centers or impurities and conduction electrons (in semiconductors and metals) are possible sources of an

oscillating local magnetic field inducing NMR relaxation.[13,14]

In the liquid phase the time-dependent local magnetic field observed at the site of a nucleus is produced by modulation of various interactions by random tumbling and translational motions of the molecules.[13] These interactions include: the dipole-dipole interaction with another nuclear moment (D) or with unpaired electrons (UE), the interaction with the shielding anisotropy (SA), the J-coupling (J) to another spin, which may arise in two different ways, one from the time-dependent coupling constant (*e.g.*, in exchange systems), and the other from the very short relaxation time of the coupled nucleus, and the direct interaction with the rotational angular momentum of the molecule, which is called the spin-rotation (SR) interaction. For quadrupolar nuclei with spin $I > \frac{1}{2}$, the interaction with the projection of the electric field gradient along the direction of the magnetic field at the site of a nucleus, which is called the quadrupolar interaction (Q), should be added to the above list.

For monatomic gases, relaxation of the nuclear magnetization is induced directly by collisions. This is because all mechanisms through which the spin system may be coupled to the lattice (*i.e.*, its surroundings) directly involve the intermolecular interactions. Since such interactions are naturally weak, such as the nuclear spin-spin interaction between two atoms, or operational only during the very short life-time of the collision complex, relaxation times for monatomic gases are normally very long.[15–19]

In polyatomic gases NMR relaxation proceeds, not only via such very weak intermolecular processes, but also via collisional modulation of the intramolecular interactions between the nuclear spin system and the rotational angular momentum of the molecule.[3,20] It will be shown later in this chapter that such a modulation can only occur if the intermolecular PES of the system has anisotropic components (*i.e.*,

it is angle-dependent), which is the case for almost all systems with at least one polyatomic component. The anisotropy of the intermolecular PES determines the effectiveness of the inelastic collisions in reorienting and/or changing the magnitude of the rotational angular momentum; this in turn determines the NMR relaxation times. An isotropic PES leads to purely elastic collisions, and consequently does not contribute to NMR relaxation through the intramolecular mechanisms. Since the collision frequency in the gas phase depends on the number density and temperature,[21] it can thus be expected that the NMR relaxation times should depend upon these two variables. These dependences are discussed in detail in Chs. 4 and 5.

Basically, there are two approaches to link the relaxation of the macroscopic magnetization to microscopic properties of atoms and molecules; these are the *correlation function*[22] and *kinetic theory*[23] approaches. In the correlation function approach the fluctuation of the local magnetic field is described by a correlation function $G(\tau)$. The Fourier transform of this correlation function in the frequency domain, $J(\omega_i)$, is called the spectral density, and is used to derive equations for the relaxation times. The spectral density is a measure of the strength of the interaction, and is given by

$$J(\omega_i) = \frac{2\tau_i}{1+\omega_i^2\tau_i^2} , \tag{1.6}$$

in which the time constant τ_i, called the correlation time, is related to the collisional reorientation of the rotational angular momentum of the diatomic molecule. For a given molecule, the correlation time τ_i is a function of the interaction i and the physical properties of the phase, and is determined either from NMR relaxation time data, or from other techniques.[13] The contribution of various interactions

to the total relaxation time of a nucleus can then be expressed in terms of the corresponding correlation times. Before giving the expressions for the relaxation times from the correlation function approach, it is useful to review briefly the interactions between the spin system and the rotational motion of the molecules.

For the X nucleus of a diatomic molecule XY the part of the spin Hamiltonian describing the time-dependent interactions between the nuclear spin system and the rotational angular momentum of the molecule, which is of interest in this thesis can be written as

$$\hat{\mathcal{H}}_t = \hat{\mathcal{H}}_{SR} + \hat{\mathcal{H}}_D + \hat{\mathcal{H}}_Q, \tag{1.7}$$

with $\hat{\mathcal{H}}_{SR}$, $\hat{\mathcal{H}}_D$ and $\hat{\mathcal{H}}_Q$ representing the contributions of the spin-rotation, dipolar and quadrupolar interactions, respectively. The explicit forms for these intramolecular interactions are[13]

$$\hat{\mathcal{H}}_{SR} = \hbar\gamma_X B_R(\hat{j}\cdot\hat{I}_X), \tag{1.8}$$

$$\hat{\mathcal{H}}_D = \left(\frac{\gamma_X\gamma_Y\hbar^2}{r_{XY}^3}\right)\left[\hat{I}_X\cdot\hat{I}_Y - 3(\hat{I}_X\cdot u)(\hat{I}_Y\cdot u)\right], \tag{1.9}$$

$$\hat{\mathcal{H}}_Q = \frac{(e^2qQ_X/\hbar)}{2I(2I-1)(2j-1)(2j+3)}\left[3(\hat{j}\cdot\hat{I}_X)^2 + \frac{3}{2}(\hat{j}\cdot\hat{I}_X) - \hat{j}^2\cdot\hat{I}_X^2\right], \tag{1.10}$$

in which I_i is the nuclear spin quantum number of nucleus i, B_R is the magnitude of the local magnetic field created by the rotational angular momentum $\hat{j}$ of the molecule with rotational quantum number j, r_{XY} is the internuclear distance, u is a unit vector along the bond axis of the molecule, Q_X is the quadrupolar moment of the nucleus X (for $I_X > \frac{1}{2}$), and q is the electric field gradient at the site of

nucleus X. It is obvious that the eigenvalues of these Hamiltonians depend upon the rotational quantum number j. The time-dependences of these Hamiltonians arise from the collisional changes in both the orientation and the magnitude of the rotational angular momentum of the molecule. These changes can be ascribed to redistributions of the total angular momentum and the total energy between different degrees of freedom of the collision complex, including the rotational motions of the diatomic molecule and the collision complex.

In the correlation function formalism, the contributions of the SR, D and Q interactions, described respectively in Eqs. (1.8), (1.9) and (1.10), to the total relaxation time for nucleus X of the diatomic molecule XY in rotational level j, are given by[24]

$$T_{1\mathrm{SR}}^{-1}(j) = \frac{2}{3}(\omega_{\mathrm{SR}}^{\mathrm{X}})^2\,[j(j+1)]\left[\frac{\tau_1(j)}{1+(\omega_B^{\mathrm{XY}}-\omega_I^{\mathrm{X}})^2\tau_1^2(j)}\right], \tag{1.11}$$

$$T_{1\mathrm{D}}^{-1}(j) = \frac{2}{45}(\omega_{\mathrm{D}}^{\mathrm{XY}})^2 I_{\mathrm{Y}}(I_{\mathrm{Y}}+1)\left[\frac{j(j+1)}{6(2j-1)(2j+3)}\right] \times\left[\frac{\tau_2(j)}{1+(\omega_B^{\mathrm{XY}}-\omega_I^{\mathrm{X}})^2\tau_2^2(j)}+\frac{4\tau_2(j)}{1+4(\omega_B^{\mathrm{XY}}-\omega_I^{\mathrm{X}})^2\tau_2^2(j)}\right], \tag{1.12}$$

$$T_{1\mathrm{Q}}^{-1}(j) = \frac{1}{5}(\omega_{\mathrm{Q}}^{\mathrm{XY}})^2\left[\frac{j(j+1)}{6(2j-1)(2j+3)}\right] \times\left[\frac{\tau_2(j)}{1+(\omega_B^{\mathrm{XY}}-\omega_I^{\mathrm{X}})^2\tau_2^2(j)}+\frac{4\tau_2(j)}{1+4(\omega_B^{\mathrm{XY}}-\omega_I^{\mathrm{X}})^2\tau_2^2(j)}\right], \tag{1.13}$$

in which $\omega_{\mathrm{SR}}^{\mathrm{X}}$, $\omega_{\mathrm{D}}^{\mathrm{XY}}$ and $\omega_{\mathrm{Q}}^{\mathrm{XY}}$ are spin-rotation dipolar and quadrupolar coupling constants, respectively, and ω_I^{X} and ω_B^{XY} are, respectively, the Larmor frequencies associated with the nuclear spin X and the rotational angular momentum of the diatomic molecule XY. The correlation times τ_1 and τ_2 are characteristic time con-

stants of the interactions involving, respectively, first and second rank irreducible tensors in $\boldsymbol{J}$.

When more than one independent mechanism is involved in the relaxation process, the overall relaxation time is given by*

$$\frac{1}{T_{1t}} = \sum_i \frac{1}{T_{1i}}, \tag{1.14}$$

in which i is a label designating an individual mechanism involved in the relaxation process (*e.g.*, i = SR, D, Q).

The kinetic theory approach to the relaxation of the macroscopic nuclear magnetization is based on the Waldmann-Snider (WS) equation[27] for the time evolution of the perturbation of the single-particle distribution function $\Phi(t, \boldsymbol{\jmath}, \boldsymbol{I})$ applied to a system initially at equilibrium. In the presence of an external magnetic field, the internal Hamiltonian for a diatomic molecule is made up of three parts: that governing the rotational motion, $\hat{\mathcal{H}}_{\rm rot} = \hbar^2 \hat{\jmath}^2 / 2I_0$ with I_0 the moment of inertia of the diatom, the Zeeman interaction, $\hat{\mathcal{H}}_{\rm Z} = \hbar\omega_{\rm I}\, \boldsymbol{b}\cdot\boldsymbol{I} + \hbar\omega_{\rm B}\, \boldsymbol{b}\cdot\boldsymbol{\jmath}$ with $\boldsymbol{b}$ the unit vector along the direction of the static magnetic field, and the intramolecular interactions, $\hat{\mathcal{H}}_{\rm intra}$, given by Eq. (1.7). The return of the perturbed system to its equilibrium state is described via the linearized WS equation,

$$\frac{\mathrm{d}\Phi}{\mathrm{d}t} + \frac{1}{\hbar}\left[\hat{\mathcal{H}}_{\rm Z}, \Phi\right]_- + \frac{1}{\hbar}\left[\hat{\mathcal{H}}_{\rm intra}, \Phi\right]_- + \mathcal{R}\Phi = 0\ , \tag{1.15}$$

in which the square brackets denote the commutators, and $\mathcal{R}$ is the linearized collision operator.[2] The equation of motion for the nonequilibrium macroscopic nuclear magnetization is obtained from Eq. (1.15). The results of the kinetic theory

*Assuming that there is no interrelation between different interactions.[25,26]

approach for the relaxation of the nuclear magnetization can be summarized as[2]

$$T_1^{-1} = \boldsymbol{bb}: \int_0^\infty \mathrm{d}\tau \boldsymbol{K}(\tau) \cdot \exp\left(\omega_I \tau \boldsymbol{b} \cdot \boldsymbol{\epsilon}\right) , \tag{1.16}$$

$$T_2^{-1} = \frac{1}{2}(\boldsymbol{\delta} - \boldsymbol{bb}): \int_0^\infty \mathrm{d}\tau \boldsymbol{K}(\tau) \cdot \exp\left(\omega_I \tau \boldsymbol{b} \cdot \boldsymbol{\epsilon}\right) , \tag{1.17}$$

$$\omega_I \delta_{coll} = \frac{1}{2}(\boldsymbol{b} \cdot \boldsymbol{\epsilon}) : \int_0^\infty \mathrm{d}\tau \boldsymbol{K}(\tau) \cdot \exp\left(\omega_I \tau \boldsymbol{b} \cdot \boldsymbol{\epsilon}\right) , \tag{1.18}$$

in which $\boldsymbol{\delta}$ and $\boldsymbol{\epsilon}$ are second rank unit tensor and third rank unit antisymmetric tensor, respectively, and the kernel $\boldsymbol{K}(\tau)$ is defined by

$$\boldsymbol{K}(\tau) = \frac{3}{< \boldsymbol{I}^2 >} < \mathcal{R}_{\mathrm{intra}} \boldsymbol{I} | \exp\left(-\tau \mathcal{R}\right) | \mathcal{R}_{\mathrm{intra}} \boldsymbol{I} >, \tag{1.19}$$

with $\mathcal{R}_{\mathrm{intra}}$ the commutator (super) operator derived from $\hat{\mathcal{H}}_{\mathrm{intra}}$. These equations lead to a set of expressions for the components of the total relaxation time for the nucleus X of the diatom XY diluted in a monatomic gas, which are similar to those obtained from the correlation function approach, given in Eqs. (1.11)-(1.13), with the exception that the correlation times τ_1 and τ_2 are given, respectively, in terms of the state-to-state effective collision cross sections by $\tau_1 = [n\sigma_{\mathrm{V}}(j,j')\bar{c}_{\mathrm{r}}]^{-1}$ and $\tau_2 = [n\sigma_{\mathrm{T}}(j,j')\bar{c}_{\mathrm{r}}]^{-1}$ with n the number density of the gas mixture, and $\bar{c}_{\mathrm{r}}$ the relative velocity of the colliding atom-diatom pair.

The effective cross sections $\sigma_{\mathrm{V}}(j,j')$ and $\sigma_{\mathrm{T}}(j,j')$ appearing in the relaxation time expressions derived from the kinetic theory approach are well-defined quantities, related to the probabilities of transition between a given pair of states of the collision complex involving first and second rank irreducible tensors, respectively. These cross sections are determined by the anisotropic part of the intermolecular

PES via scattering theory. A brief review of the atom-diatom scattering theory from which the expressions for the NMR cross sections may be obtained, is presented in the next section. The final expressions for the components of the relaxation times for the nuclei of a diatomic molecule diluted in a monatomic gas, will be deferred until Ch. 4, where the temperature, density and field effects on the relaxation times are discussed. A detailed derivation of the explicit expressions for the relaxation times can be found elsewhere.[2,3]

1.3 Atom-diatom scattering and NMR relaxation cross sections

The time-independent Schrödinger equation which describes the internal motion of the collision complex formed between a ^1S atom Z and a $^1\Sigma$ diatomic rigid-rotor XY has the form

$$\left[-\frac{\hbar^2}{2\mu R}\left(\frac{\partial^2}{\partial R^2}R\right)+\frac{\widehat{\ell^2}}{2\mu R^2}+\frac{\widehat{j^2}}{2\mu' r^2}+\mathbf{V}(R,r,\theta)-E\right]\Psi^E_{j,m_j}(R,\omega_R,\omega_r)=0. \quad (1.20)$$

The quantities appearing in this equation are: the eigenvalue E of the total Hamiltonian, the reduced masses of the collision complex and diatom μ and μ' given, respectively, by $\mu = (m_{\mathrm{XY}}^{-1} + m_{\mathrm{Z}}^{-1})^{-1}$ and $\mu' = (m_{\mathrm{X}}^{-1} + m_{\mathrm{Y}}^{-1})^{-1}$, with m_i being the atomic (or molecular) mass of species i, the fixed diatom bond-length r, the distance R between centers of mass of the colliding particles, the orientation angle θ between $\boldsymbol{r}$ and $\boldsymbol{R}$ (see Fig 4.1), and finally the spherical polar coordinate sets $\omega_R \equiv (\theta_{\mathrm{R}}, \phi_{\mathrm{R}})$ and $\omega_r \equiv (\theta_{\mathrm{r}}, \phi_{\mathrm{r}})$ which define the orientations of the vectors $\boldsymbol{R}$ and $\boldsymbol{r}$, respectively, in a spaced-fixed frame. The first term in Eq. (1.20) represents the radial part of the kinetic energy operator for the relative motion of the atom-

diatom pair, while the second term represents its angular part. The second term can also be considered to represent the centrifugal potential associated with the orbital angular momentum of the collision complex. The third term can either be considered to represent the internal (rotational) energy of the diatomic component, or as a centrifugal potential associated with the rotational angular momentum of the diatom. Finally, the interaction between the colliding pair is governed by the PES $V(R,r,\theta)$. The coordinates of the interaction PES (*i.e.*, r, R and θ) form a complete coordinate set in the body-fixed frame. Note that the orientation angle θ is determined by the coordinate sets ω_R and ω_r, and thus is not an independent variable of the Schrödinger equation.

For an isolated non-reactive collision complex, the total angular momentum is conserved during the course of collision. This means that in addition to the total energy E, the eigenvalues $J(J+1)\hbar^2$ and $m_J\hbar$ of the operators $\widehat{J^2}$ and $\hat{J}_z$ associated with the total angular momentum $\hat{\boldsymbol{J}}$ and its projection onto the z-axis $\hat{J}_z$, defined respectively by

$$\hat{\boldsymbol{J}} = \hat{\boldsymbol{j}} + \hat{\boldsymbol{\ell}}\,, \qquad \hat{J}_z = \hat{j}_z + \hat{\ell}_z, \tag{1.21}$$

are constants of the motion. The good quantum numbers of the collision complex are now J and m_J. These conserved quantum numbers are given in terms of the quantum numbers j, l, m_j and m_l, associated with non-conservative angular momenta $\hat{\boldsymbol{j}}$ and $\hat{\boldsymbol{\ell}}$ and their z-axis projections, $\hat{j}_z$ and $\hat{\ell}_z$, respectively, via

$$|j-l| \le J \le j+l \quad \text{and} \quad m_J = m_j + m_l. \tag{1.22}$$

The conservation of the total angular momentum implies also that the operators $\widehat{J^2}$ and $\hat{J}_z$ should commute with the total Hamiltonian. This commutation simpli-

fies the solution of the Schrödinger equation considerably. Arthurs and Dalgarno[28] have shown that in this *total-J* representation it is convenient to factorize the total wavefunction $\Psi^E_{j,m_j}(R,\omega_R,\omega_r)$ into the products of radial and angular wavefunctions as

$$\Psi^E_{j,m_j}(R,\omega_R,\omega_r) = \frac{1}{R}\sum_{Jm_J}\sum_{j'l'l} C^{Jm_J}_{jm_jl}\psi^{JE}(j'l',jl|R)\mathcal{Y}^{Jm_J}_{j'l'}(\omega_R,\omega_r), \qquad (1.23)$$

where the $C^{Jm_J}_{jm_jl}$ are constants to be determined from orthonormality and boundary conditions, and $\psi^{JE}(j'l',jl|R)$ and $\mathcal{Y}^{Jm_J}_{j'l'}(\omega_R,\omega_r)$ are (pure) radial and angular parts of the total wavefunction, respectively. The angular part of the total wavefunction can be written as a linear combination of two sets of spherical harmonics, one describing the orbital angular momentum of the collision complex, $Y_{l'm_{l'}}(\omega_R)$, and the other describing the rotational angular momentum of the diatom, $Y_{j'm_{j'}}(\omega_r)$, given by

$$\begin{aligned}\mathcal{Y}^{Jm_J}_{j'l'}(\omega_R,\omega_r) &= \sum_{m_{j'},m_{l'}}(-1)^{(j'-l'+m_J)}\sqrt{2J+1} \\ &\quad\times\begin{pmatrix} j' & l' & J \\ m_{j'} & m_{l'} & -m_J\end{pmatrix} Y_{j'm_{j'}}(\omega_r)Y_{l'm_{l'}}(\omega_R), \qquad (1.24)\end{aligned}$$

in which the coefficient $(\cdots)$ is a Wigner 3-j symbol.[29] These functions form a complete orthonormal set, and are simultaneously eigenfunctions of the operators $\widehat{j^2}$, $\widehat{\ell^2}$, $\widehat{J^2}$ and $\hat{J}_z$ with eigenvalues $j'(j'+1)\hbar^2$, $l'(l'+1)\hbar^2$, $J(J+1)\hbar^2$ and $m_J\hbar$, respectively. This choice for the angular part of the wavefunction in the space-fixed frame leads to a differential equation for the radial part of the wavefunction

$\psi^{JE}(j'l', jl|R)$, namely[28]

$$\frac{\hbar^2}{2\mu}\left[\frac{\mathrm{d}^2}{\mathrm{d}R^2} - \frac{l(l+1)}{R^2} + k_{j'}^2\right]\psi^{JE}(j'l', jl|R) = \sum_{j''l''} V^J(j''l'', j'l'|R)\psi^{JE}(j'l', j''l''|R), \quad (1.25)$$

in which the unprimed and primed variables denote the pre- and post-collisional quantities, and $k_{j'}$, the so-called *channel wavenumber*, is defined as

$$k_{j'} = [\frac{2\mu}{\hbar^2}(E - E_{j'})]^{\frac{1}{2}}, \quad (1.26)$$

with $E_{j'}$ the rotational energy of the diatom (in level j'). Each pair (j, l) is called a channel. The number of possible channels (*i.e.*, the number of combinations of the possible pre-collisional values of j and l) that a pair of colliding particles can access depends upon the total energy of the system, and the highest rotational level of the diatom at or below that specific energy. A (j, l) combination with an energetically accessible diatom rotational level j is called an open channel, while a (j, l) combination for which the rotational state j is not accessible is called a closed channel. For an open channel $E > E_j$, so that the channel wavenumber is real, while for a closed channel $E < E_j$, so that the channel wavenumber is imaginary. Equation (1.25) shows that the radial wavefunction of a collision complex may have contributions from closed channels, in spite of the fact that they are not energetically accessible. The superscript J in Eq. (1.25) specifies the quantum number of the conserved total angular momentum. Equation (1.25) represents a set of ordinary differential equations in R which are coupled by the coupling coefficients $V^J(j''l'', j'l'|R)$. These coupling coefficients are related to the interaction PES via

$$V^J(j''l'', j'l'|R)\delta_{JJ'}\delta_{m_J m'_J} = \iint \mathcal{Y}_{j''l''}^{Jm_J *}(\omega_R, \omega_r) V(r, R, \theta) \mathcal{Y}_{j'l'}^{J'm'_J}(\omega_R, \omega_r) \mathrm{d}\omega_R \mathrm{d}\omega_r. \quad (1.27)$$

If the interaction potential can be expanded in terms of Legendre polynomials as $V(r,R,\theta) = \sum_\lambda V_\lambda(r,R)P_\lambda(\cos\theta)$, the above equation can be simplified to

$$V^J(j''l'',j'l'|R) = \sum_\lambda f_\lambda^J(j''l'',j'l')V_\lambda(r,R), \tag{1.28}$$

in which the $f_\lambda^J(j''l'',j'l')$ are Percival-Seaton coefficients, given explicitly by[30]

$$\begin{aligned} f_\lambda^J(j''l'',j'l') &= (-1)^{(J+\lambda)}\left[(2j+1)(2j'+1)(2l''+1)(2l'+1)\right]^{\frac{1}{2}} \\ &\times \begin{pmatrix} j'' & j' & \lambda \\ 0 & 0 & 0 \end{pmatrix} \begin{pmatrix} l'' & l' & \lambda \\ 0 & 0 & 0 \end{pmatrix} \begin{Bmatrix} l' & l'' & \lambda \\ j'' & j' & J \end{Bmatrix}, \end{aligned} \tag{1.29}$$

with $\{\cdots\}$ a Wigner 6-j symbol. Using Eq. (1.28) in Eq. (1.25) yields

$$\begin{aligned} \frac{\hbar^2}{2\mu}\left[\frac{\mathrm{d}^2}{\mathrm{d}R^2} - \frac{l(l+1)}{R^2} + k_j^2\right]\psi^{JE}(j'l',jl|R) &= \sum_{j''l''\lambda} f_\lambda^J(j''l'',j'l') \\ &\times V_\lambda(r,R)\psi^{JE}(j'l',j''l''|R). \end{aligned} \tag{1.30}$$

Equation (1.30) shows that the interaction PES couples (mixes) all radial wavefunctions (states) of the collision complex. The extent of this coupling is determined by the magnitudes of the coefficients $V_\lambda(r,R)$ of the Legendre expansion with $\lambda \neq 0$, *i.e.*, the anisotropy, of the PES. The properties of the Percival-Seaton coefficients dictate a certain pattern for the coupling between different states, based upon the specifications of the PES. This pattern can be summarized as:

a) The even-λ terms of the interaction PES couple only those states in which both the rotational states of the diatom and the rotational states of the collision complex have the same parities, that is, the quantum numbers j'' and j' are

either both even or both odd (the same condition applies to the quantum numbers l'' and l'). The terms with λ odd couple any two states of opposite parity with, of course, the same J. One immediate outcome of this coupling pattern is that for a homonuclear diatom with $D_{\infty h}$ symmetry, for which the Legendre expansion of the PES has only terms with λ even, an atom-diatom collision does not couple the rotational states with j even to those with j odd. This means that the two parity isomers of a homonuclear diatom do not undergo parity changes in a collision.

b) For an atom-diatom collision complex with an isotropic (*i.e.*, angle-independent) PES so that all of the terms, apart from V_0, of its Legendre expansion vanish, the collision does not introduce any coupling between states, and the quantum numbers l and j are both conserved. Thus, collisions under an isotropic PES are elastic. In other words, inelastic collisions are induced *only* by the anisotropic part of the interaction PES.

A detailed solution of the Schrödinger equation for an atom-diatom collision, first presented by Arthurs and Dalgarno,[28] is not intended here. However, for the purposes of this thesis the final results of their solution will be discussed.

In the space-fixed frame, which has been used throughout this section[†] a reasonable choice for the boundary conditions applied on the radial wavefunction of the collision complex is given as[32]

$$\psi^{JE}(j'l', jl|R) \xrightarrow[R\to 0]{} 0, \tag{1.31}$$

$$\psi^{JE}(j'l', jl|R) \xrightarrow[R\to\infty]{} \frac{1}{k_j^{\frac{1}{2}}}\left[\delta_{jj'}\delta_{ll'}e^{-i(k_jR-l\pi/2)} - S^J_{SF}(j'l', jl)e^{i(k_{j'}R-l'\pi/2)}\right], \tag{1.32}$$

[†] For the treatment of the atom-diatom collision in other frames see Refs. 31, 32.

in which channel wavenumbers k_j and $k_{j'}$ are given by Eq. (1.26). The first condition, given by Eq. (1.31), is based on the fact that the atom and diatom cannot physically coexist at the same point in space. The second condition specifies the asymptotic functional form of the wavefunction. The first term in Eq. (1.32) represents an incoming spherical wave from the entrance channel (j, l), which accounts for the initial approach of the colliding particles. The Kronecker deltas ensure that the pre-collisional radial wavefunctions (or the entrance channels) are not coupled. The second term in Eq. (1.32) represents an outgoing spherical wave from the exit channel (j', l') weighted by a factor $S^J_{SF}(j'l', jl)$, an element of the scattering, or S-matrix. The S-matrix elements are of central importance in scattering calculations. As can be seen from Eq. (1.32), the $S^J_{SF}(j'l', jl)$ element of the S-matrix determines the contribution of the exit channel (j', l') in the post-collisional asymptotic wavefunction. It can thus be concluded that the probability of the (inelastic) transition from the (j, l) state (the entrance channel) to the (j', l') state (the exit channel) is determined by the S-matrix element $S^J_{SF}(j'l', jl)$, which couples the two states.[32]

Using Eq. (1.23) and the boundary conditions for the radial wavefunctions, given in Eqs. (1.31) and (1.32), the boundary conditions for the total wavefunction can be derived as[32]

$$\Psi^E(R, \omega_R, \omega_r) \xrightarrow[R\to 0]{} 0, \tag{1.33}$$

$$\Psi^E(R, \omega_R, \omega_r) \xrightarrow[R\to\infty]{} e^{-ikR_z} Y_{jm_j}(\omega_r) + \sum_{j'm_{j'}} f^E(j'm_{j'} \leftarrow jm_j|\omega_R) \frac{e^{ik_{j'}R}}{R} Y_{j'm_{j'}}(\omega_r), \tag{1.34}$$

in which R_z is the projection of R onto the z-axis of the SF frame, and the factor $f^E(j'm_{j'} \leftarrow jm_j|\omega_R)$, called the scattering amplitude, is related to the S-matrix

element $S^J_{SF}(j'l', jl)$ via

$$f^B(j'm_{j'} \leftarrow jm_j|\omega_R) = \sum_{Jm_J}\sum_{ll'm_{l'}} i^{(l-l'+1)}\sqrt{\frac{\pi}{k_j k_{j'}}}(2J+1)\sqrt{2l+1}$$
$$\times \begin{pmatrix} j & l & J \\ m_j & 0 & -m_J \end{pmatrix}\begin{pmatrix} j' & l' & J \\ m_{j'} & m_{l'} & -m_J \end{pmatrix}$$
$$\times \left[\delta_{jj'}\delta_{ll'} - S^J_{SF}(j'l', jl)\right] Y_{lm_l}(\omega_R). \qquad (1.35)$$

The two terms of the asymptotic total wavefunction have the same meaning as those of the radial wavefunctions discussed previously. The boundary conditions, given in Eqs. (1.33) and (1.34), and the orthonormality of the total wavefunction can be used to calculate the coefficients appearing in the expansion of the total wavefunction, Eq. (1.23), as

$$C^{Jm_J}_{jm_jl} = \left[\frac{(2J+1)(2l+1)\pi}{k_j}\right]^{\frac{1}{2}}(-1)^{(j-l+m_j)}i^{(l+1)}\begin{pmatrix} j & l & J \\ m_j & 0 & -m_J \end{pmatrix}. \qquad (1.36)$$

The remaining step towards a complete solution of the Schrödinger equation for the collision complex is to solve the inhomogeneous differential equation for the radial wavefunction, given in Eq. (1.30). As mentioned earlier, the detailed procedure of such a solution can be found elsewhere,[32,33] and is not relevant to this introduction. Once the radial wavefunctions have been found, Eq. (1.23) can be used to obtain the total wavefunction.

Mathematically, the sums appearing in the calculation of the total wavefunction, Eq. (1.23), are unlimited. The existence of such unlimited sums does not allow a complete derivation of the total wavefunction, and hence limits the physical appli-

cation of the quantum mechanical method presented in this section. Inspection of the asymptotic behavior of the total wavefunction, given in Eq. (1.34), shows that the contribution of the closed channels (*i.e.*, the energetically unaccessible levels) to the wavefunction are exponentially decreasing functions of R; the farther the closed channel is above the total energy, the faster is the rate of decrease.[‡] This means that as R increases, *i.e.*, as the colliding particles recede from one another and from the collision center, the already insignificant contributions of the upper closed channels to the wavefunction decrease much faster than do those of the lower closed channel. This suggests that the sum over j', the rotational quantum number of the exit channel (j', l'), can be truncated at j' values very close to the highest open channel, *i.e.*, the highest energetically accessible rotational level of the diatom. It can be shown, similarly, that the other sums over J, l and l' in the equation for the total wavefunction can also be truncated at finite values determined by the total energy and total angular momentum of the collision complex.

The role of the factor $f^E(j'm_{j'} \leftarrow jm_j|\omega_R)$ in the total wavefunction is similar to that of the S-matrix elements in the radial wavefunctions. In addition to the information contained in the S-matrix elements, the scattering amplitudes contain angular information about the scattered (outgoing) particles. This could also be seen from the arguments chosen to identify the two quantities. Thus, it should be possible to calculate the transition probabilities between a given pair of rotational states of the diatomic molecule scattering at a given solid angle ω_R if the scattering amplitude can be calculated. Equation (1.35) shows that the calculation of the

---

[‡]For a closed channel (j', l'), the channel wavenumber $k_{j'}$ is imaginary, and can be written as $k_{j'} = ia_{j'}$ where $a_{j'}$ is a real number given by $a_{j'} = [\frac{2\mu}{\hbar^2}(E_{j'} - E)]^{\frac{1}{2}}$. Substituting $k_{j'}ia_{j'}$ in the exponential factor in the second term of the Eq. (1.34) results in the exponential factor $e^{-a_{j'}R}$ which is a rapidly decreasing function of R. This factor is an oscillatory function of R for open channels.

scattering amplitudes is possible if the S-matrix elements are known.

Once the probabilities of the collisional transitions between different states are known, all physical properties of the system, whether of the collision complex or of the colliding particles infinitely after the collision, can be calculated using standard quantum and statistical methods. The transition probabilities can be expressed in terms of transition cross sections through the definition of the collision operator.[2] The translation of the probabilities to cross sections has been necessary in order to facilitate the analogy with classical collision theory.[34] It can be shown that the differential cross section describing the transition from the initial state (j, m_j) to the final state $(j', m_{j'})$ observed at the scattering solid angle ω_R is related to the scattering amplitude via[32]

$$\frac{\mathrm{d}\sigma(j', m_{j'} \leftarrow j, m_j|\omega_R)}{\mathrm{d}\omega_R} = \frac{k_{j'}}{k_j} \left| f^E(j' m_{j'} \leftarrow j m_j|\omega_R) \right|^2 . \tag{1.37}$$

In the present study it is not possible to obtain any information about individual collisions, as the NMR relaxation times are macroscopic properties of the bulk system. Proper quantum and statistical methods are thus required to link the properties of the bulk system to individual collisions. Fitz *et al.*[35] have shown that the generalized (transition) cross section for atom-diatom (rigid-rotor) scattering, which describes the collisional properties of the bulk system is given by

$$\sigma^{K_i' K_j' ; K_i K_j}_{j' j' ; j j | E}(K) = \frac{\pi}{k_j^2} \sum_{J_t} \mathcal{P}^{K_i' K_j' ; K_i K_j}_{j' j' ; j j | E}(J_t, K), \tag{1.38}$$

in which E is the total energy of the system, k_j is the channel wavenumber given by Eq. (1.26), and $\mathcal{P}^{K_i' K_j' ; K_i K_j}_{j' j' ; j j | E}(J_t, K)$, is a generalized opacity of rank K for a collision complex with total angular momentum quantum number J_t. The generalized

opacities are given in terms of binary products of S-matrix elements by

$$\begin{aligned}\mathcal{P}^{K_i'K_j';K_iK_j}_{j'j';jj|E}(J_f,K) &= (2J_f+1)\sum_{J_i}\sum_{l_i,l_f}\sum_{l_i',l_f'}(-1)^{(l_f+l_f')}\,i^{(l_f-l_i-l_f'+l_i')}(2J_i+1)(2J_f+1)\\ &\times[(2l_i+1)(2l_f+1)(2l_i'+1)(2l_f'+1)]^{\frac{1}{2}}\begin{pmatrix} l_f' & K_l' & l_i' \\ 0 & 0 & 0\end{pmatrix}\\ &\times\begin{pmatrix} l_f & K_l & l_i \\ 0 & 0 & 0\end{pmatrix}\begin{Bmatrix} j' & l_f' & J_f \\ j' & l_i' & J_i \\ K_j' & K_l' & K'\end{Bmatrix}\begin{Bmatrix} j & l_f & J_f \\ j & l_i & J_i \\ K_j & K_l & K\end{Bmatrix}\\ &\times\left[\delta_{j'j}\delta_{l_f'l_f}\delta_{l_i'l_i}-S^{J_f}_{SF}(j'l_f',jl_f)S^{J_i}_{SF}(j'l_i',jl_i)^*\right], \qquad (1.39)\end{aligned}$$

in which, as earlier, unprimed and primed quantities represent the corresponding pre- and post-collisional values, respectively. When spectroscopic line-shifting or line-broadening cross sections are involved, the subscripts "i" (for initial) and "f" (for final) represent, respectively, the corresponding pre- and post-transition values in the spectroscopic transition. For other types of cross sections, such as those being considered in this thesis, they are simply convenient labels to distinguish between two values of the tensor ranks of the same type of angular momentum tensors coupled to give a total rank K. The equalities $j_i = j_f = j$, $j_i' = j_f' = j'$, $l_i = l_f = l$ and $l_i' = l_f' = l'$ apply for the specific cross sections relevant to the NMR relaxation processes. In the absence of spectroscopic transitions the subscripts "i" and "f" on the total angular momentum quantum number J also lose their physical identification and become a set of convenient labels used to distinguish the corresponding values appearing in the terms of the two independent J-sums. In Eq. (1.39), the coefficients $\{\cdots\}$ are Wigner 9-j symbols[29] and the values of of the K indices are defined according to the coupling scheme given by the vector

equations $K_l = \ell_f - \ell_i$, $K_j = j_f - j_i$, $K'_l = \ell'_f - \ell'_i$, $K'_j = j'_f - j'_i$ and $K = K_l + K_j = K'_l + K'_j = K'$. A derivation of this generalized cross section and a more detailed definition of the quantities upon which it depends can be found in Refs. 32 and 35–37.

As pointed out previously, and can be seen from Eq. (1.39), the calculation of the S-matrix elements is the heart of the quantum mechanical study of the atom-diatom collision. Efficient quantum numerical methods, such as the *Close-Coupled* (CC), centrifugal sudden (CS) and infinite-order sudden (IOS) methods, are available for the calculation of the S-matrix elements. The latter two methods apply best to higher energy collisions of heavier atoms and molecules. The IOS method, especially should not be applied for the calculation of S-matrix elements when hydrogenic molecules are involved.[31] Among these methods the CC method is the only one which is essentially exact. The quantum mechanical method briefly described in this section for the study of atom-diatom collisions, forms the basis for the CC calculation of S-matrix elements.

The cross section matrices involved in the interactions between the nuclear spin and rotational angular momenta containing first rank tensors (as in the spin-rotation interaction) and second rank tensors (as in the dipolar and quadrupolar interactions), which determine the gas phase NMR relaxation processes, are denoted by $\boldsymbol{\sigma}_{\mathrm{V}}^{E}$, with elements $\left[\sigma_{\mathrm{V}}^{E}(j', j)\right]$, and $\boldsymbol{\sigma}_{\mathrm{T}}^{E}$, with elements $\left[\sigma_{\mathrm{T}}^{E}(j', j)\right]$, respectively. As earlier, E denotes the total energy of the colliding pair. For the $\boldsymbol{\sigma}_{\mathrm{T}}$ cross section matrix $K_l = K'_l = 0$, $K_j = K'_j = 2$, and thus $K = K' = 2$. Substitution of these values into the formula for the generalized opacity, Eq. (1.39), and use of Eq. (1.38)

for the $\sigma_{\mathrm{T}}^{E}(j',j) = 5\sigma_{j'j';jj|E}^{02;02}(2)$ yields the expression[38]

$$\sigma_{\mathrm{T}}^{E}(j',j) = \frac{\pi}{k_j^2}\sum_{J_t}\mathcal{P}_{\mathrm{T}}^{E}(J_t;j',j) = \sum_{J_t,J_i}\sum_{l,l'}\frac{\pi}{k_j^2}(-1)^{(j+j'+l+l')}(2J_t+1)(2J_i+1)$$
$$\times\begin{Bmatrix} j' & J_i & l' \\ J_t & j' & 2 \end{Bmatrix}\begin{Bmatrix} j & J_i & l \\ J_t & j & 2 \end{Bmatrix}\left[\delta_{jj'}\delta_{ll'} - S^{J_t}(j'l',jl)S^{J_i}(j'l',jl)^*\right] \quad (1.40)$$

for the σ_{T}^{E} cross section matrix elements. In this expression $\mathcal{P}_{\mathrm{T}}^{E}(J_t;j',j)$ is a shorthand version of $\mathcal{P}_{j'j';jj|E}^{02;02}(J_t,2)$. For the σ_{V} cross section matrix $K_l = K_l' = 0$, $K_j = K_j' = 1$, and $K = K' = 1$. Thus, the formula for the $\sigma_{\mathrm{V}}^{E}(j',j) = 3\sigma_{j'j';jj|E}^{01;01}(1)$ cross section is similar to that for the σ_{T} cross section with the exception that the values "2" in the 6-j symbols are replaced by "1", while the corresponding opacity for the σ_{V} cross section is denoted by $\mathcal{P}_{\mathrm{V}}^{E}(J_t;j',j)$.

The NMR cross section, given in Eq. (1.40), or generally, the generalized cross section, given in Eq. (1.38), describes the relevant collisional transitions for a collision complex with a fixed value of the total energy E. Since in a macroscopic sample the total energy of a collision complex can have virtually all values from zero to infinity, it is not possible experimentally to isolate or to probe those collision complexes that have the same total energy. In a typical measurement on a macroscopic system, such as a NMR relaxation time measurement on a gas sample, what is measured is the ensemble average of the observable. This means that in order to calculate a macroscopic property which arises from collisional transitions, an ensemble average of the cross sections over all values of the total energy should be used. This ensemble average relates the microscopic cross sections to their macroscopic equivalents via the Boltzmann distribution function as

$$\overline{\sigma}_{j'j';jj}^{K_l'K_j';K_lK_j}(K) = \int_0^\infty \sigma_{j'j';jj|E}^{K_l'K_j';K_lK_j}(K) f(x,x') x e^{-x} dx \quad (1.41)$$

in which x is the reduced kinetic energy of the collision complex in the entrance channel, given by $x = E_K/kT = E - E_j/kT$ with k being the Boltzmann's constant, and $f(x, x')$ is a function of x and x'. For both NMR cross sections $f(x, x') = 1$.

1.4 A brief outline of this thesis

A review of the aspects of the experimental setup for gas phase NMR experiments is presented in Ch. 2, where the design and the specifications of the gas handling system and sample cell used in the experiments on the HD–Ar and D_2–Ar mixtures are detailed. In the beginning of Ch. 3 an overview of the experimental considerations related to the physical properties of the systems under study is presented. The presentation and a brief analysis of the experimental spin-lattice relaxation times measured for HD–Ar and D_2–Ar mixtures follows a careful study of their respective one-dimensional spectra, in Secs. 3.2 and 3.3, respectively. The detailed equations for the spin-lattice relaxation times are first introduced in Ch. 4, and the role of the physical parameters in determining the values of the relaxation times are discussed briefly. Results and details of the theoretical calculations of the relaxation times for the HD–Ar and D_2–Ar systems are discussed separately in Secs. 4.4 and 4.5, respectively. The theoretical and experimental results obtained in Ch. 3 and 4 are then compared in Ch. 5. Evaluation of the XC(fit) potential based on these comparisons is given in Sec. 5.4. Discussions on the experiments and calculations can be found in Secs. 5.6 and 5.5, respectively. Chapter 5 concludes with a few general remarks and a summary of the results obtained in the present study. Some plans for future studies in a direction similar to that of the current research are presented in Ch. 6. More detailed summaries of the contents of individual chapters are given at beginning of each chapter.

Chapter 2

Design of a Gas-Handling System for Gas Phase NMR Experiments

This chapter is concerned with the design of a gas-handling system (GHS). In section 2.1 the difficulties with existing methods for carrying out gas phase NMR experiments are reviewed, and it is concluded that new designs for the sample cell and the GHS are needed for this work. Detailed descriptions of the GHS and the sample cell are presented in sections 2.2 and 2.3, respectively. Section 2.4 discusses some experiments carried out to test the GHS and the sample cell.

2.1 Introduction

In gas phase NMR it is not possible to acquire a strong signal from a dilute or low pressure sample in a short period of time. This is due to the small number of nuclei in the effective volume of the transmitter-receiver coil. Obviously, the situation is even worse for insensitive nuclei. A trivial solution to this problem would be to increase the size of the sample. However, NMR differs from some other spectro-

scopic techniques in that the sample size and shape are extremely limited, and are strongly restricted by the designs of the magnet and the probe. These limitations arise from the small volume over which the required high homogeneity of the static and rf magnetic fields can be attained. Such a high degree of homogeneity ($\simeq$1 part in 10^8) is crucial for the accuracy of all energetic, dynamic and relaxation studies. Therefore, the size and shape of the sample cannot be expanded arbitrarily in order to increase the number of nuclei in the effective volume of the transmitter-receiver coil so that a stronger NMR signal can be obtained. Thus, it is not possible simply to use a larger sample with commercial NMR instruments.

In most gas phase experiments[39-42] a flame-sealed glass tube, as shown in Fig. 2.1-(a), is used as the sample cell. In this method, a jointed glass tube connected to a gas-handling setup is first evacuated, and is then placed in a cryogenic liquid, commonly liquid nitrogen. When the sample is introduced into the glass tube via the gas-handling setup the cryogenic liquid causes the sample, which is not necessarily a gas at room temperature, to condense at the bottom of the glass tube. Next, a flame is used to seal off the tube at the point below the joint to the gas-handling setup. After this, the glass tube is removed from the cryogenic liquid, and is placed in the standard solution probe, and the sample is studied. The glass tube necessarily has the same outer dimensions as a standard NMR tube. It has, however, a totally different inner size and shape. To minimize diffusion of the sample in and out of the effective volume of the coil, the glass tube is constricted by a piece of capillary beyond the effective length of the coil. In other cases,[43-46] the length of the glass tube is set to be not more than the effective length of the coil, and hence no capillary is used. The pressure of the sample is set by choosing the initial amount of the sample and the internal dimensions of the tube. When it is not possible to fix the amount at the time of sample preparation, a differential

weighing method is used to measure the amount of the sample.[46] Usually a thick-walled tube is used to carry out the experiment with the highest degree of safety; the higher the pressure, the thicker the glass wall should be.

In addition to the dangers inherent to the sample preparation step, this method has many disadvantages, a few of which deserve mention here. The cryogenic liquid should have a much lower boiling point than the sample itself. This means that samples containing helium cannot be prepared in this way, since there is no liquid with a lower boiling point than helium. Further, for hydrogen the only choice for the cryogenic liquid is helium. Although some other cooling techniques can be used to condense these samples in the NMR tube, they are expensive and demanding. Yet another disadvantage of this method is that for each total density of the gas mixture, a new sample should be prepared. This means that the experimentalist should prepare as many samples as the number of densities s/he wishes to study. This increases the risks associated with the sample preparation step. Another disadvantage of this method is that the response of the flame-sealed glass to heating and cooling procedures, *i.e.*, thermal expansion and contraction, is unpredictable. This problem, which is caused mostly by the way in which the tube is sealed off by a flame, can be removed, although not perfectly, by the use of isotropic zone melting methods.[47] Such methods are, however, difficult to carry out and are expensive. These heating and cooling procedures are needed in the study of the temperature dependence of the NMR characteristics of the sample.

A modified version of the commercial valved NMR tube,[48,49] as shown in Fig. 2.1-(b), is another option for gas phase experiments. But this option also has many disadvantages. The temperature and pressure ranges over which this tube can be used are extremely narrow. For example, the higher limit of the pressure range doesn't exceed 1 atm at room temperature. This limit becomes significantly lower

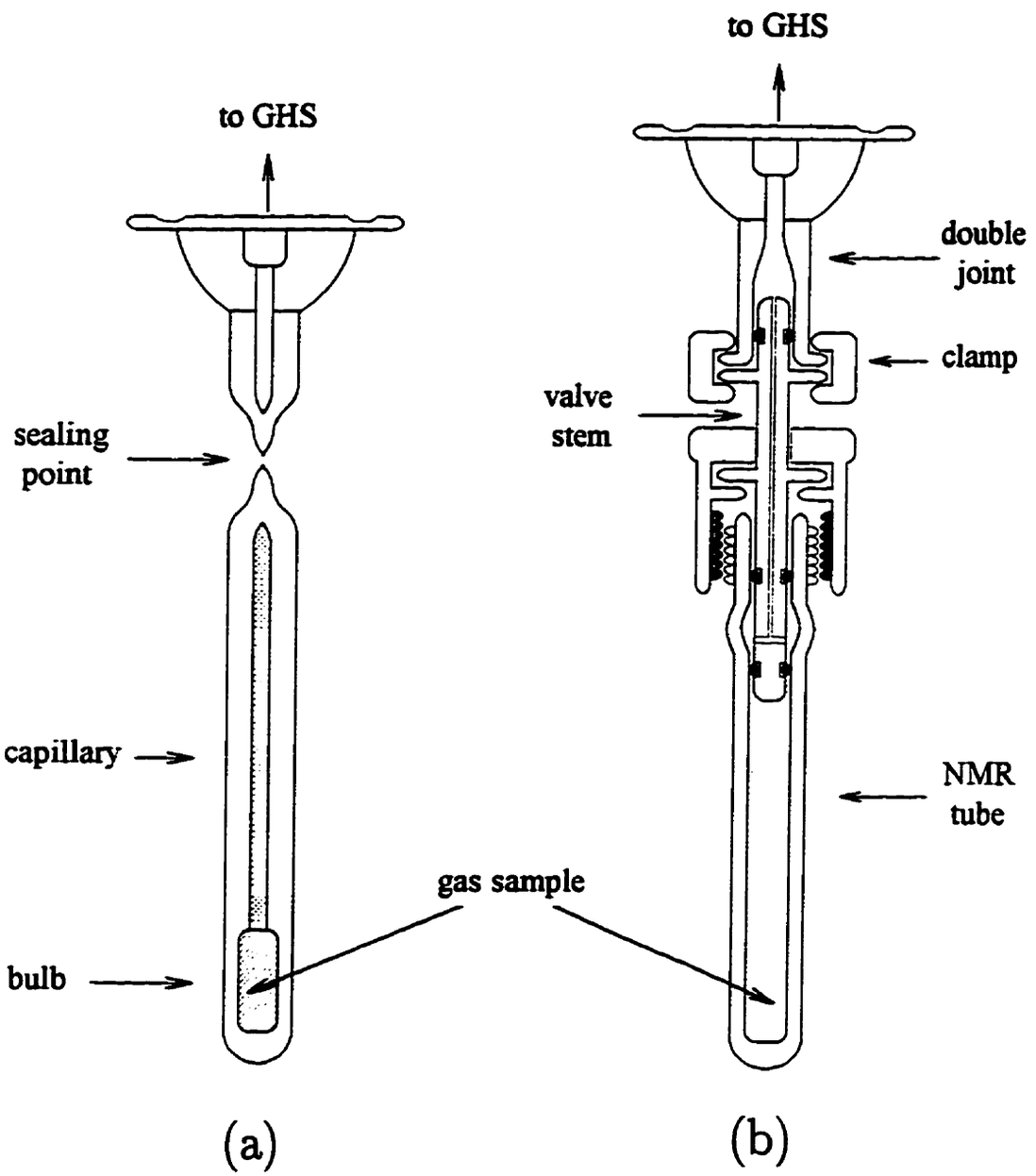

Figure 2.1: (a) A flame-sealed glass tube used as a gas phase NMR sample cell. (b) A commercial valved NMR tube modified for gas phase studies.

if high-temperature experiments are necessary. Also, its design precludes any great variation in temperature due to different thermal expansions or contractions of the materials and the concomitant risk of leakage or breakage. This valved tube was originally designed for experiments on degassed solution samples for which relaxation time or chemical shift measurements cannot be carried out in the presence of a dissolved gas, usually oxygen. Another disadvantage of this tube is that no constriction is designed to prevent the diffusion of the sample to and from the effective volume of the coil. Moreover, leaking of small molecules and atoms of the gaseous samples through the seals and into the Teflon stem of the valve of the tube, even at room temperature, is another real concern. As in the previous method, the experimentalist should prepare as many samples as the number of densities s/he wishes to study. The sample preparation step in this method is exactly the same as that of the previously-described method, except that the tube is disconnected easily by closing its valve and removing the double joint connecting the tube to the gas-handling setup. For this procedure, the risks in the sample preparation step are much lower than those of the previous method. Such a reduced risk is a great advantage.

The other advantage of this tube over the thick-walled tube mentioned above is in its maximal concentricity or isotropy. This causes a small increase in the signal by increasing the value of T_2^* and hence the sensitivity. This feature also improves the precision of the chemical shift measurement. Unfortunately, these advantages are not sufficient enough to overcome several disadvantages of this method. In brief, the commercial valved NMR tubes are not useful for gas phase experiments, especially at high pressures and temperatures, and for samples involving small molecules.

One systematic solution to the problems of gas phase experiments in NMR is the use of specialized gas phase probes.[4,6,50-52] Using special gas phase probes to

study gaseous samples has been the best and most reliable method so far. However, there are also some difficulties with this approach. The major difficulty is that a home-built probe can rarely provide a homogeneous field over the required volume of the sample. This is due mostly to the perturbation of the magnetic field caused by the shielding effects of the probe components. It should be mentioned here that this problem exists for commercial probes too. However, these probes provide a uniform susceptibility so that shimming, *i.e.*, adjusting the homogeneity, of the magnetic field is very easy. By contrast, the non-uniform susceptibility of home-built probes and variations in the susceptibility induced by the introduction of the sample make shimming of the magnetic field very difficult, or even impossible. Design of a home-built probe with uniform susceptibility, although feasible, is extremely time-consuming and laborious, and is beyond the scope of the present study. Inhomogeneity of the field reduces sensitivity and resolution of the spectrum dramatically, and requires a larger number of scans in order to obtain acceptable resolution and accuracy.

Another difficulty that arises for strong fields, such as that employed in these studies, is the sensitivity of the LC circuit of the probe to small changes in the input power and temperature.* An accurate and proper selection of the materials and electronic components of this circuit is needed in order to have stable pulses of minimum duration. This is more crucial when two or more nuclei with a large difference in their magnetogyric ratios are to be studied.

The direct metal-glass joints that are used in such probes are reported to limit the temperature range over which the experiment can be done free of problems.[55] To decrease the risk of explosion of the sample cell in high pressure experiments,

*The part of the electronics of the probe that produces radio-frequency fields, consisting of an inductor (L) and a capacitor (C), is called an LC circuit.[53,54]

the pressure of the probe is kept close to the pressure in the sample cell. This precaution needs a special sealing setup for the entire probe.

It should be noted here that the conduction of experiments with an instrument which is not dedicated to gas phase studies, but is shared with other research groups, requires a fast and convenient setup, as well as a safe method of switching between gas phase and other standard experiments. This means that a home-built gas phase probe that needs several preparation and checkup steps in its setup is not suitable.

In spite of numerous advantages, the use of a superconducting magnet in an NMR instrument introduces some extra limitations for gas phase experiments. The most important limitation is that no substance with magnetic impurities can be used in the components of the GHS or in its fittings to the sample cell. Although magnetic substances may affect the fields of permanent and electromagnets, they do not harm the magnet itself. But, bringing or moving a magnetic object in the vicinity of a superconducting magnet may result in a *quenching* of the magnet. To avoid such a costly incident one should be extremely careful in selecting the materials and in the design of the GHS. Another limitation that is introduced by using a superconducting magnet is that no electrical vacuum pump can be used within a specified distance from the magnet. An electric pump is much more detrimental to the magnet than a magnetic substance, due to vibrations produced by its operation. It can easily cause *quenching* of the magnet if it is not properly handled and situated in the NMR room.

In the experimental part of the current work, NMR spin-lattice relaxation times of the nuclei in different mixtures of argon with hydrogen isotopomers are to be studied over a wide range of temperatures and pressures in an NMR instrument with an 11.75 Tesla superconducting magnet. From what has been discussed in this

section, it can be concluded that none of the existing methods for dealing with gas phase experiments in NMR is suitable for these studies. Therefore, it was necessary to design and build a new GHS and sample cell. The rest of this chapter is devoted to the details of the design of a GHS and its compatible sample cell.

2.2 Design of a gas-handling system (GHS)

The first step towards any gas phase experiment is to prepare the gas mixture at the desired pressures from its pure components, usually stored in cylinders at high pressures. There have been great advances in pressure measurement methods in the past few decades. However, there have not been any important changes in methods for mixing two non-reactive gases, such as those studied in this work. Two containers with known volumes are filled with pure gases at predetermined pressures. The mixture is prepared simply by connecting the two containers to one another. Mole fractions of components of the mixture are calculated from the measured pressures and volumes of the GHS components. At this stage the mixture is ready to be sampled and studied.

There are two ways of introducing the sample into the NMR probe, namely on-line and off-line sampling. Flame-sealed glass and commercial valved tube methods are categorized as off-line sampling, whereas a gas phase probe is considered an on-line sampling technique. Advantages and disadvantages of these methods have been discussed in detail in the previous section. The GHS designed for this work is shown schematically in Fig. 2.2. In the design of this GHS, described below, the advantages of an on-line sampling method were deemed most desirable. In this design, difficulties with the gas phase probe discussed in Sec. 2.1 are also avoided.

The GHS shown in Fig. 2.2 consists of two containers with approximately a

1:10 volume ratio. After the mixture has been prepared at the desired pressure and mole fraction, these containers are isolated from the rest of the GHS, and are used as storage tanks to store the prepared mixture for the next set of experiments. These containers and all other components of the GHS are made of copper, brass or non-magnetic SS316 type stainless steel. This is a necessary precaution when working near superconducting magnets. The connecting copper tubes of the GHS are all thick-walled with a volume of 0.185 cm^3 per inch (3.05 mm inner-diameter). This type of tube was chosen because of its minimal volume per unit length and maximal pressure and diffusion resistance. Volumes of different components of the GHS are calculated using their nominal sizes. These calculated volumes are verified by expansion experiments on pure argon and the use of the virial equation of state.[21,56] Except for the pressure gauge and sample cell, brass nuts are used in all fittings for better sealing. All valves of the GHS are of a sealed type. This type of valve has the most reliable sealing feature. Essentially perfect sealing is required when the gas mixture contains components with small molecules, such as hydrogen gas. The o-rings used in this GHS are Viton (different fluorocarbons) with a durameter (hardness) of 75, see Ref.57, provided by Apple Rubber Products.

The sample is introduced into the probe via a thick-walled copper tube. This copper tube is long enough to place the whole GHS well beyond the 5 Gauss line[†], see Fig. 2.2. A Cajon VCO fitting is used to connect this copper tube to the o-ring joint of the sample cell. A description of the sample cell is given in the next section. After connection to the sample cell by proper fittings, the copper tube is placed in the probe, and then is connected to one of the ports of the GHS that is controlled by a valve. The GHS, the tube and the sample cell are evacuated

[†]The line beyond which the stray field of the superconducting magnet is effectively decreased, and its effects on magnetic material can be safely neglected, is known as 5 Gauss line (1 Gauss = 1×10^{-4} Tesla).

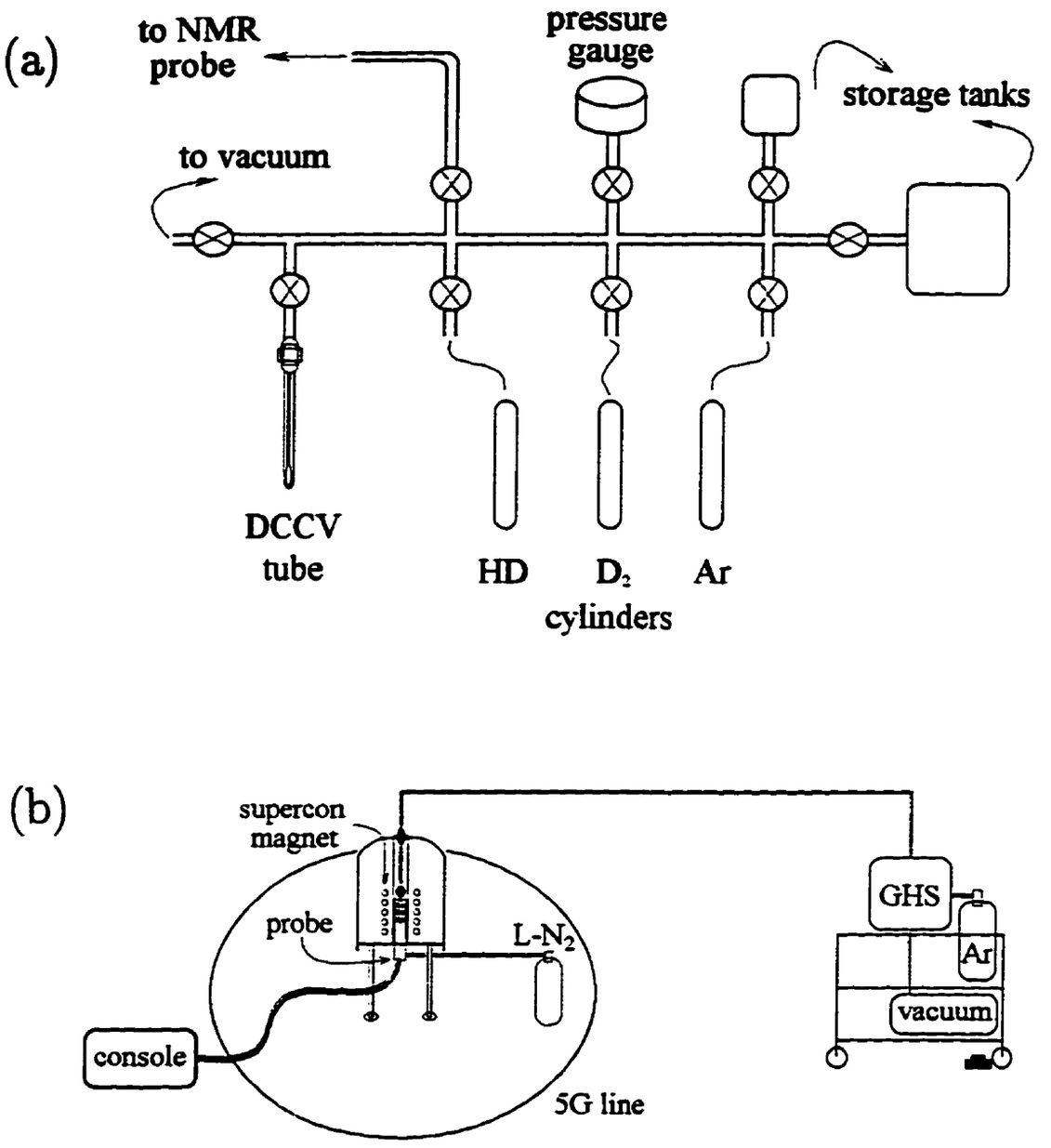

Figure 2.2: (a) Schematic diagram of the gas-handling system used in the study of NMR spin-lattice relaxation times in HD-Ar and D_2–Ar mixtures, and (b) its location in the NMR room. The DCCV tube is a miniature gas-handling system and will be described in Ch. 6.

after being purged with nitrogen for an hour and then with pure argon for several minutes before sample preparation. The mixture is first prepared at the highest pressure of interest. To carry out experiments at lower pressures, the pressure is dropped in several steps by evacuation of a fraction of the mixture that is trapped in the tubes between the valves of the GHS. This volume is filled with the mixture and is isolated from the rest of the GHS before evacuation.

A type 122B Baratron capacitive absolute pressure transducer, made by MKS Instruments, is used as pressure gauge. This gauge is able to measure pressures up to 35 atm with an accuracy of 0.5%. The temperature coefficient of the gauge is 0.04% of the reading pressure per centigrade degree. The gauge is connected to the GHS by a Cajon VCO fitting through a half-inch stainless steel tube. The total volume of the gauge, including its tube, is 8.50 cm^3. The gauge has excellent stability and is operated by a 15 V DC power supply at 35 mA. Pressure measurements of both components before preparation of the mixture is performed by this single gauge, which is also used to monitor the pressure of the mixture during the experiment. A zero adjustment is done before each set of experiments. A stable zero pressure could be achieved within 2-3 minutes of evacuation. Because of changes in room temperature, a small change in zero pressure is observed from one experiment to another. This change was in agreement with the stated temperature coefficient.

The whole GHS, including HD and D_2 cylinders, is mounted on an aluminum board box with 50 × 50 × 20 cm dimensions. This box can be carried easily by hand. However, a cart is used for safer displacement. The argon cylinder and the vacuum pump are also mounted on this cart. This setup makes it a totally portable and attractive GHS. Problems with this GHS will be discussed in Sec. 5.6.

A novel miniature GHS which is designed, built, and tested for gas phase NMR experiments, will be introduced in Ch. 6.

2.3 Gas phase sample cell

The sample cell is the most important part of the gas phase experimental setup. The sample cell used in these studies is shown in Fig. 2.3. This cell consists of three parts. The top part of the cell is an o-ring joint through which the cell is connected to the GHS tube by a brass fitting. The outer-diameter of the joint at its top is 18 mm. Maximum outer-diameter of the fitting is 24 mm. All these sizes are designed based on the diameter of the upper magnet bore, which is approximately 26 mm in this case. The glass joint sits on a Teflon band inside the fitting. This Teflon band allows a stronger tightening of the fitting without breaking the glass joint. A #110 Viton o-ring is used to seal the junction between the glass joint of the cell and the metal joint of the tubing of the GHS. Proper selection of size and material of the o-ring and accurate design and precise machining of its groove[57] are critical parameters in the performance of this type of seal. In all experiments, spanning temperatures between 180 and 420 K, no leaks were observed. For two reasons this type of glass-metal connection is superior to the direct joint used in previous studies.[4-6,55,58] Firstly, the rigid connection is replaced by a flexible junction, thus allowing larger temperature variations. Secondly, the solution to the problem of incidental breaking of the seal, already largely removed because of the flexibility of the connection, is reduced to simple replacement of either the o-ring or the glass cell. These replacements are much easier and cheaper than is the replacement of the direct glass-metal joint. In order to avoid possible contamination, no lubricant is used to preserve the flexibility and sealing properties of the o-ring. Because thermal expansion and contraction affects the elastic properties of the o-ring, as a precaution the o-ring is replaced after each set of experiments on a given mixture.

The second and middle part of the sample cell is a 160 mm long capillary with

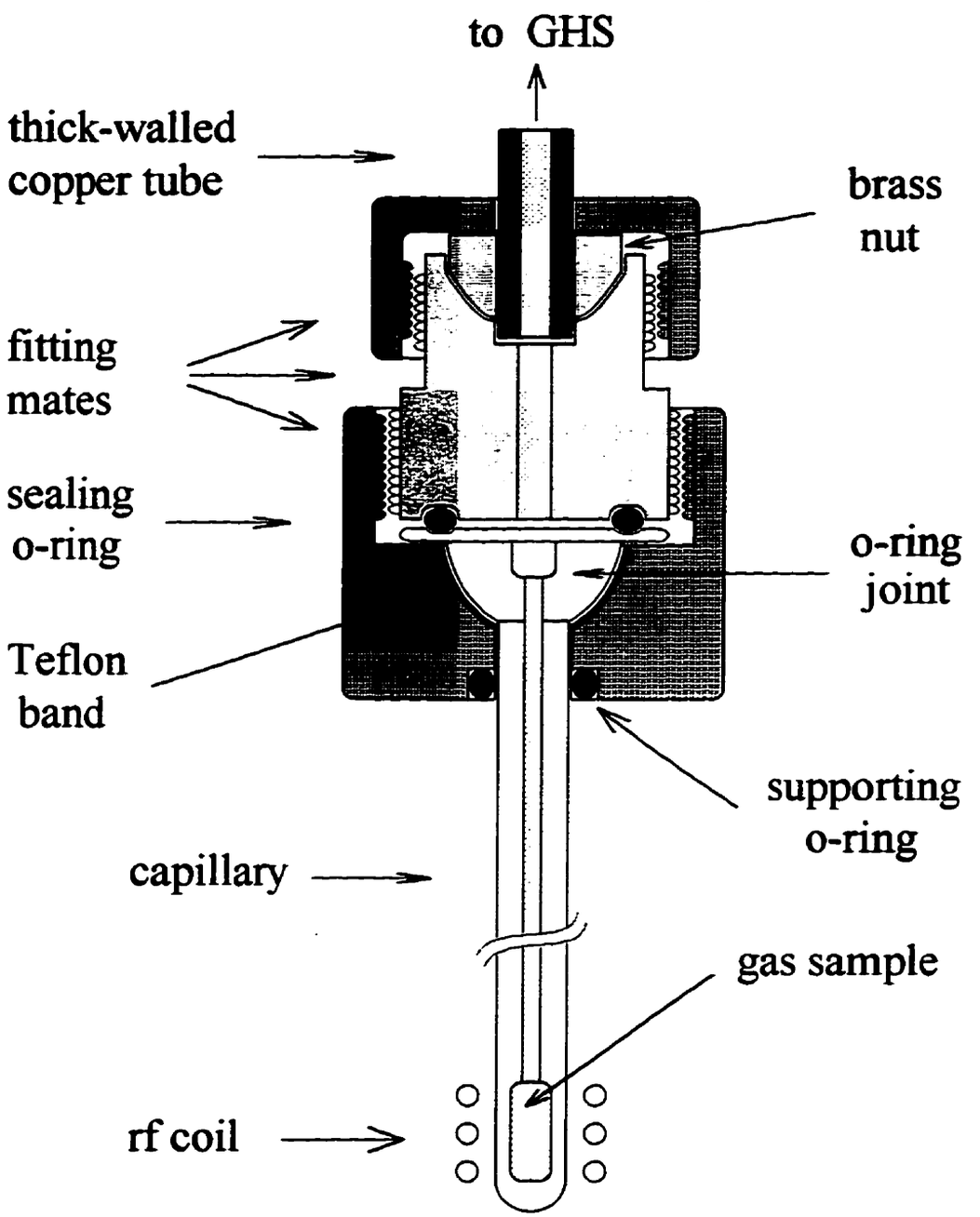

Figure 2.3: Gas phase sample cell used with the gas-handling system described in Sec. 2.2 in the study of HD-Ar and D_2–Ar mixtures.

maximum inner-diameter of 0.5 mm. The role of this capillary is to confine the gas mixture in the effective volume of the transmitter-receiver coil as much as possible.

The third and bottom part of the cell is a bulb with the same outer-diameter as that of the capillary. The thickness of the bulb wall depends on the outer-diameter and the maximum pressure at which experiments are to be carried out. Under conditions of these studies, *i.e.*, a 5 mm outer-diameter cell and pressures less than 35 atm, a 1 mm thick wall meets all safety precautions. To have a more symmetric bulb, the thickness of the bottom of the bulb is designed to be approximately 3 mm. The bulb length is approximately 20 mm, and is slightly shorter than the effective length of the rf coil. Although the short length of the bulb reduces the available volume of the cell, it improves the homogeneity of the magnetic field over the sample.

The only possible choices for the material making up the cell are glass and quartz. Due to its crystalline structure, quartz has much higher pressure stability than does glass. The thermal stability of quartz is less than that of glass for the same reason. However, preparation of the entire cell from quartz requires higher temperatures and more precise instruments than are commonly available in glass-blowing shops. Glass blowing of the cell can be done either by human or by machine. The human-made cells usually are non-symmetric and often contain air bubbles saturated with water vapor. If the bulb wall contains such bubbles, it will cause problems in proton experiments, especially for dilute samples.

2.4 Test of the gas-handling system and the sample cell

To test the seals of the GHS and sample cell, they are connected to one another and filled with helium gas at 70 atm. This pressure is twice that of the GHS specifications, and approximately five times the highest pressure used in these studies. Non-reactive helium gas has the smallest molecules, and hence provides a perfect test gas for checking seals and diffusion through the materials. After 24 hours, no drop in pressure was observed in this test. All components of the GHS were included in the test.

The sample cell is cleaned with common solvents and is dried in an oven for several hours. It is then connected to the copper tube while maintaining a flow of nitrogen gas through both. After the sample cell is placed in the probe, the copper tube is connected to the GHS. A Teflon or ceramic fitting is used to keep the cell aligned with the common axis of the probe and the coil. In order to have a stable temperature throughout the sample the probe is capped while the experiments are performed. The effects of temperature gradients in the probe are discussed in Sec. 5.6. No modification or change is necessary for a standard probe to fit this GHS and sample cell.

Prior to each experiment on gas samples, the magnetic field is shimmed on a standard lineshape sample. The 90° pulse lengths of the proton and deuteron channels are optimized on a 1:1 H_2O/D_2O liquid mixture. To check for any contamination, proton and deuteron spectra were collected using an empty cell. Except for some weak and unusual peaks with very different 90° pulse lengths, in most of the cases no background peak was observed with the empty cell. Experiments performed using an empty probe showed that adsorbed species on the rf coils and their

glass supports are responsible for these (negligible) background peaks. This suggested that cleaning the coils and their glass supports was necessary for gas phase experiments. These components of the probe were cleaned frequently with different solvents and were then dried with nitrogen gas.

Pure hydrogen gas at approximately 3 atm pressure was used as the first sample to test the GHS and to run a test NMR experiment. Because of the strong signal, shimming could be improved on this gas sample. All valves, fittings and connections were checked. No pressure drop was observed during two days of testing. A mixture of 10% H_2 in argon at 6 atm pressure was used as the second test sample. A relatively strong signal could be observed after only 32 scans. However, it was not strong enough to shim the magnetic field on this sample. The change in the shimming is due to replacement of a highly symmetric NMR tube used for shimming on the lineshape sample with an unsymmetrical gas phase glass cell. To test the temperature response of the seals, a few high and low temperatures were examined. The probe could be tuned up to the same level as that for standard solution samples at all temperatures. The pulse lengths were not very different from those in solution samples, and increased with increasing temperature. This was due to temperature effects on the coil. No pressure drop was observed during these test experiments.

When unfiltered air was used for the cooling and heating flows, a strong peak (relative to the gas phase signals) was observed in the proton spectrum. This signal was attributed to water vapor in the air flow which passes through the probe and fills all free spaces, including the clearance between the coil and the glass sample cell. This peak decreased with decreasing temperature and was replaced by an extremely broad peak for temperatures lower than 273 K. No such problem was observed with nitrogen gas. To avoid this problem, only nitrogen gas was used throughout this work for heating and cooling flows.

Chapter 3

Experimental Measurement of Spin-Lattice Relaxation Times in HD–Ar and D_2–Ar Gas Mixtures

In this chapter experimental measurements of NMR spin-lattice relaxation times of the nuclei of various HD–Ar and D_2–Ar mixtures over a wide range of temperatures and at different total densities are presented. In Sec. 3.1, some points about sample preparation and other steps of the experiments are discussed. Spin-lattice relaxation times of nuclei in HD–Ar and D_2–Ar mixtures are measured using the gas handling system described in Chapter 2, and the results are presented and discussed briefly in sections 3.2 and 3.3, respectively. In an attempt to measure the dipolar contribution to the spin-lattice relaxation times of the proton and deuteron in HD–Ar mixtures, a number of Nuclear Overhauser Effect (NOE) experiments have also been carried out. The NOE results, which represent the first NOE measurements performed for a gas phase system, are presented in Sec. 3.2.3.

3.1 Introduction

In the experimental part of this work, the potential energy surface (PES) for the isotopic hydrogen–argon system is studied through NMR spin-lattice relaxation time measurements. To be certain that the NMR relaxation results are only those driven by this PES for the unlike interaction, the experiments must be carried out in such a way that the effects of collisions between hydrogen molecules and argon atoms on the NMR relaxation are isolated. The only direct method of accomplishing this is to carry out experiments on supersonic jets of interacting molecular beams.[59] Because of the extremely low concentration of nuclei in supersonic jets, a very long period of time would be required in order to obtain the desired results with an acceptable accuracy. Further, no commercial NMR instrument is equipped with the required setup to carry out such experiments, the most important of which is a homogeneous magnetic field over a large volume. Thus, accessible but indirect methods should be used for the NMR study of PES's.

One indirect method for accessing the isolated contribution of this PES is to carry out spin-lattice relaxation experiments on mixtures with different (low) mole fractions of hydrogen in argon. Extrapolation of the results for these mixtures to the infinite dilution limit will ideally give the isolated contributions from the hydrogen–argon PES. From preliminary NMR experiments with the GHS described in Chapter 2, it was found that mixtures with as low as 1% hydrogen in argon can be studied in a reasonable period of time. Even at low total densities, the concentrations of nuclei in such mixtures are many orders of magnitude larger than those in molecular beams. Because a linear relationship between contribution of hydrogen–argon collisions in the spin-lattice relaxation time and the mole fraction of hydrogen is utilized, the range of the mole fractions used for extrapolation becomes

very important for the ultimate accuracy of the linearly extrapolated results;[5,60,61] the lower the mole fractions employed, the more reliable the final extrapolated results. The use of a limited range of low mole fractions of hydrogen justifies such an assumption.

Basically, this method could also be used for the component of the mixture at the other extreme of the mole fraction scale. The only necessary condition is that each component of the mixture should contain at least one NMR active nucleus. Hydrogen–nitrogen, hydrogen–^{13}CO, hydrogen–xenon and hydrogen–^{3}He mixtures give a few examples on which such an *inverse method* can be employed. When one of the components is monatomic, however, this will not be practical, as relaxation of nuclear spins in single atoms necessarily occurs via intermolecular mechanisms. An important example of such a mechanism is the interaction between the nuclear spin angular momentum of the single atom and the orbital angular momentum of the transient collision complex (the so-called spin-rotation relaxation mechanism[17,18]). Under the same conditions, the rates associated with NMR intermolecular relaxation mechanisms are orders of magnitude slower than those of the intramolecular mechanisms that dominate nuclear relaxation in polyatomic molecules.[2,62] Experimental uncertainties associated with wall contributions and diffusion, as discussed in Sec. 5.1, become significant in the study of systems with slower relaxation rates. Thus the slow relaxation rates, *i.e.*, long relaxation times, of the monatomic component can be problematic. A more important point regarding NMR relaxation of the monatomic component in such binary mixtures is that there is no direct relationship between the spin-lattice relaxation times and the usual PES.[19] Thus, the inverse method cannot be used in the evaluation of such a PES for systems containing monatomic components. Even if the appropriate relationship were formulated, this inverse method could not be employed for the hydrogen–argon system, because all

three naturally abundant isotopes of argon (consisting of 99.59% ^{40}Ar, 0.07% ^{38}Ar and 0.34% ^{36}Ar) have zero nuclear spins, and thus cannot be observed or studied by NMR. In contrast to the hydrogen–argon system, hydrogen–helium and hydrogen–xenon systems could be studied using this inverse method, as ^{3}He and ^{129}Xe are excellent NMR active stable nuclei.[15–19,46]

At first glance it appears that each experimental datum can be compared with the results of theoretical calculations independently, so that there is no limitation on the range of temperatures and densities or on the number of data points needed for these studies. However, a closer look at the systems and their specifications (see Secs. 5.1) shows that this is not the case, and experiments should be carried out over a relatively wide range of temperatures and at two or more densities. Apart from the limitations imposed by the GHS and the NMR instrumentation, extremely high or low temperatures and densities should be avoided. The lowest accessible temperature is essentially limited by the boiling point of argon, 87.5 K. Formation of clusters of argon atoms, and argon density gradients in the cell become major problems even at temperatures above the boiling point of argon. If experiments are necessary at temperatures close to the boiling point of one of the components, they should be carried out either at very low densities or by the inverse method mentioned above, where appropriate.

The allowed density range is bound by two limits. The lower limit of the density range is set such that the contribution from collisions with the wall of the cell to the relaxation times is negligible relative to that of inter-particle collisions. The higher limit of the density range is set such that the contributions from three-body collisions are negligible. Three-body contributions cause a non-linear relationship between T_1/ρ and the mixture density, ρ, above the extreme-narrowing regime (see Sec. 4.1).

Sample preparation consists of two steps. In the first step individual components are prepared in the two storage tanks of the GHS at known pressures. Since the mixtures should have low mole fractions of the hydrogen isotopes, the smaller tank is assigned to them. In the second step the two components are mixed and saved in the tanks. Non-ideal behavior of the components has been taken into account in the calculation of the mole fractions. Because of the low mole fraction of hydrogen, it could likely be assumed that the mixture has the same non-ideal behavior as does argon. Nonetheless, the contribution of the minor component was taken into account using available data on the interaction virial coefficients of argon–hydrogen mixtures.[56,63,64]

The pressure of the mixture in the sample cell is monitored during the experiments as a check for any possible leak from the seals or any change in the volume of the copper tubing and the fitting inside the magnet bore. Since the sample cell is not isolated from the GHS, its pressure is the same as that of the GHS. The temperature of the sample cell and that part of the copper tubing located in the upper magnet bore is the same as that of the probe, and is monitored by the built-in thermocouple of the probe. However, as this thermocouple does not actually register the true temperature of the probe, it must be calibrated.

Hydrogen has six isotopomers, namely, H_2, D_2, T_2, HD, HT and DT. A basic question is which of them will make the best choice for the experimental part of the present studies. Three of them are homonuclear diatomics, while the other three are heteronuclear. Quantum statistics[65,66] requires the existence of two different nuclear spin modifications for homonuclear isotopomers. No direct photonic or thermal transitions can occur between these two spin modifications. Indeed, only separation and recombination of the atoms or a direct magnetic interaction can change one spin modification into the other. For this reason and because of the origin of the

differences between the two modifications, they are sometimes referred to as parity isomers. At room temperature the rate of *ortho*-H_2 to *para*-H_2 conversion is less than 2% of *ortho*-H_2 per week (or less than 0.67% of *para*-H_2 per week). The rate of *para*-D_2 to *ortho*-D_2 conversion is so slow that only negligible conversion* has been observed after one year.[67]

Any physical property of one homonuclear isotopomer will be an ensemble average of that property over all its modifications. Therefore, each measurement of one physical property on these isotopomers represents an average value of that property. This fact makes the study of these systems more difficult to carry out, because two different systems must be dealt with simultaneously. This problem doesn't arise when one of the parity isomers does not contribute to the property being measured. NMR measurements on H_2 provide a nice example of this exception, since the nuclear spin of *para*-H_2 is zero, so that it does not contribute to the NMR signal. Also, the *ortho-para* conversion rate for H_2 is much slower than the time scale of the NMR experiment. Thus, the conversion also does not affect NMR measurements.

Three of the six isotopomers of hydrogen containing radioactive tritium are not readily available, and hence are the last candidates for NMR spin-lattice relaxation time studies. Moreover, the NMR probes employed in the present studies cannot access the frequency of tritium, which is 6.7% higher than that of the proton.

Among the remaining isotopomers, heteronuclear HD is the best candidate. The most important advantage of this isotopomer is that measurement of NMR spin-lattice relaxation times can be carried out on two different nuclei for each sample. This can be regarded as two independent measurements on each mixture.

---

*In the solid phase these rates are 1.90% and 0.06% per hour for *ortho*-H_2 to *para*-H_2 and *para*-D_2 to *ortho*-D_2 conversions, respectively.[67]

The other advantage of studying the HD–Ar system is that any abnormal results for one nucleus, which can be caused by either experimental problems or unknown processes in the system, can be probed by studying the other nucleus. Further, previous studies have shown that a proposed potential for the hydrogen–helium system that had given good agreement with the experimental results for H_2–He[5] and D_2–He[6] systems could also give good results for proton of the HD–He system. However, the same *transformed* potential failed to give as good agreement with the deuteron relaxation in the HD–He system.[4] The source of this disagreement has not yet been determined. This suggests that the HD isotopomer would also be a good choice to see if a similar disagreement occurs more generally in the study of HD–rare gas systems. To accomplish this, D_2–Ar and H_2–Ar systems should also be studied.

As the H_2–Ar system had been studied already,[68] it was not chosen for these studies, even though the experimental conditions are totally different. The only remaining isotopomer of hydrogen, D_2, is therefore an appropriate second choice. The rest of this chapter is devoted to the experimental results of the studies on the HD–Ar and D_2–Ar systems.

All of the experiments were performed by a Bruker AMX-500 NMR instrument with an 11.75 Tesla superconductor magnet. A broadband inverse probe was used for the study of both nuclei (proton and deuteron). The probe was tuned at each temperature before performing the experiments on each sample. The pulse lengths of the proton and deuteron channels were calibrated first on a 1:1 mixture of D_2O/H_2O. During the course of carrying out the experiments at several temperatures, pulse length calibrations have been necessary, because of the effects of temperature on the performance of the rf coils. Generally speaking, the pulse length increased with increasing temperature.

3.2 Gas phase NMR study of HD–Ar mixtures

The HD gas was obtained from Cambridge Isotope Laboratories with stated purity of 97.0%. The major impurities, H_2 and D_2, contribute only a negligible amount to the measured signals and, to a much smaller extent, to the relaxation processes (see Section 5.6). The HD gas was provided in a 460 cc carbon steel #12 lecture bottle (cylinder) with a CGA 110/170 brass angle valve under $\simeq$ 11 atm pressure. A CGA 110 to 1/4 inch NPT stainless steel adaptor was used to connect the HD cylinder to the GHS via a 1/4 inch copper tube. Ultra-high purity grade argon gas was obtained from Praxair with stated purity of 99.998%. The major impurity, N_2, does not contribute to the signal measurement, and its effect on the relaxation time measurement is negligible due to its very low concentration. Also, the hydrogen–N_2 interaction is weaker than the hydrogen–argon interaction.[60] This further decreases the contribution of this minor impurity to the relaxation time measurements. The argon cylinder was also connected to the GHS via 1/4 inch copper tubing, and the outlet flow of argon gas was controlled by a regulator. The connecting tubes and the regulator were purged with argon gas before preparing the mixtures.

To optimize NMR parameters for the study of the nuclei of HD in the HD–Ar mixtures, a set of test experiments was performed on pure HD gas. Proton and deuteron spectra were obtained at temperatures of 295, 323 and 350 K and at densities of 0.85, 2.0 and 2.5 amagat. These experiments showed that mixtures with HD partial densities of more than 0.1 amagat could be studied in a reasonable time. This partial density limit would be even lower, by a factor of ten, if only the proton was to be studied. T_1 measurements were also carried out on these samples. The measured T_1 values for the proton and the deuteron were of the order of 500 μsec and 2 msec, respectively. Because T_2^* was very short, no *J-coupling* multiplet could be

resolved in the proton and deuteron spectra of these mixtures. However, the widths and the lineshapes of the peaks obviously indicated that they were not singlets. To separate out and study the relative contributions of the J-coupling, *i.e.*, multiplets, and the NMR experimental conditions, such as poor shimming, to the observed linewidths and lineshapes, a decoupling experiment was performed on one of these mixtures. The results showed that the decoupling of the other nucleus decreases the linewidths of the peaks associated with each nucleus by factors of about 2.0, and leaves well-defined peaks, with Lorentzian lineshapes. This experiment served also as a test for the NOE measurement discussed in Sec. 3.2.3.

Three HD–Ar mixtures, with 0.86%, 2.80% and 5.03% HD, were prepared. The relative error of the measured mole fraction of HD is estimated to be twice the sum of the errors in the measurments of the GHS pressure ($\simeq$0.5%), temperature ($\simeq$0.2%) and volume ($\simeq$0.2%) totalling $\simeq$1.8%. The effects of such (negligible) errors appear only at the time of extrapolation to infinite dilution. Because of the narrow range of mole fractions used in this work, and because of the weak dependence of the relaxation times on the mole fraction over such a narrow range, these errors can be safely neglected. Experiments on each mixture were performed at three different amagat densities, listed in Table 3.1, and for 8 to 21 temperatures between 180 and 420 K. For each mixture at each temperature NMR parameters were optimized on the one-dimensional spectra of the proton and deuteron before the T_1 measurements were made. The results of these one-dimensional spectra are presented below.

Table 3.1: Mole fractions of HD, x_{HD}, and amagat densities, ρ, of the HD–Ar mixtures studied in this work.

x_{HD}	0.86%		2.80%		5.03%	
	Mixture	ρ/amagat	Mixture	ρ/amagat	Mixture	ρ/amagat
	1	8.744	4	15.032	7	15.495
	2	4.784	5	8.340	8	8.383
	3	0.961	6	4.551	9	4.550

3.2.1 Analysis of the proton and deuteron NMR spectra of HD in HD–Ar mixtures

Typical proton and deuteron spectra of HD in these HD–Ar mixtures are shown in Figs. 3.1-(a) and (b), respectively. In these spectra the multiplet peaks of each nucleus, due to J-coupling to the other nucleus, are resolved. The excellent resolution of the spectra is due to sufficiently large T_2 values and well optimized experimental parameters, including NMR instrumental parameters, and the diffusion-restricted isothermal sample, which resulted mainly from the designs of the GHS and sample cell. A combination of these factors results in a sufficiently large value for T_2^*, which is essential for attaining high resolution. For various reasons no such resolution had been observed for HD under similar conditions in previous studies.[4,44] In Fig. 3.1 the singlet peak in the upper spectrum of each nucleus is obtained by decoupling the other nucleus.

For the highest density of each mixture, relatively strong signals (large S/N ratios) could be obtained at low temperatures after only a few hundred scans. The number of scans required to obtain an acceptable S/N ratio increased with tem-

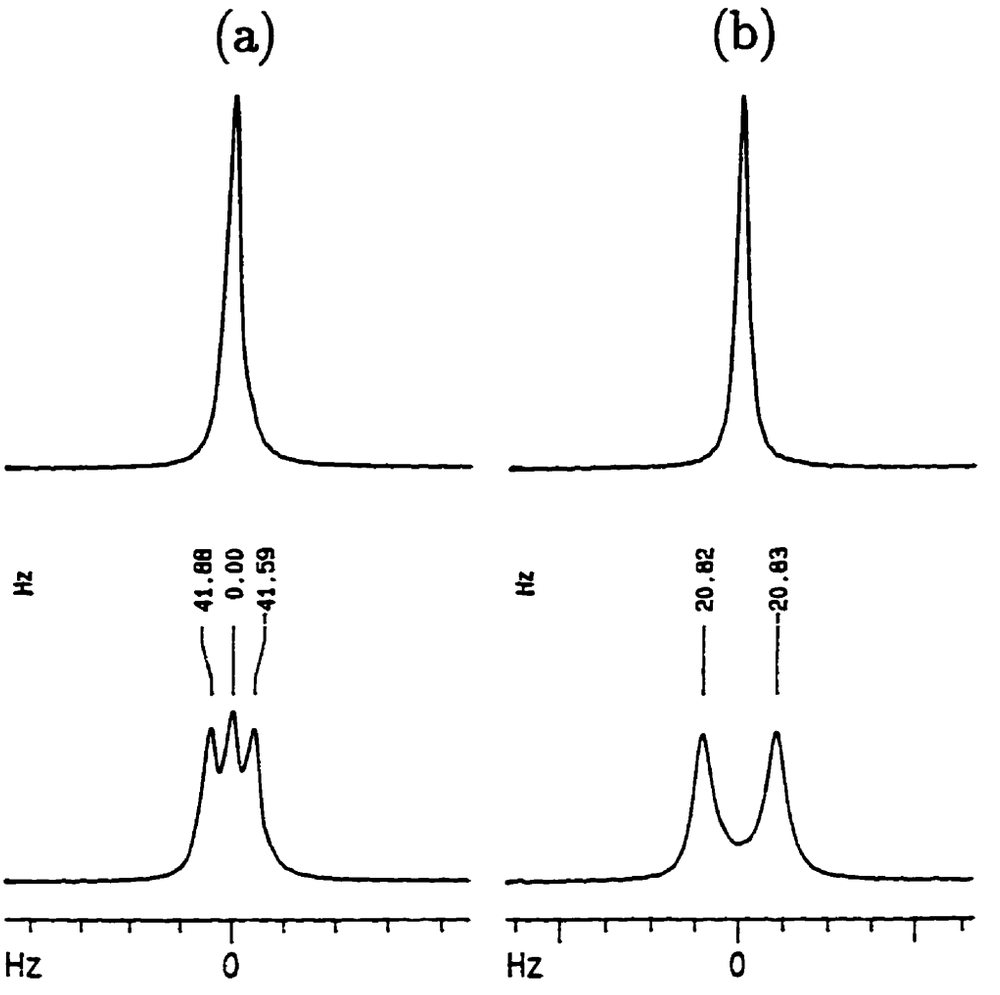

Figure 3.1: (a) Proton and, (b) deuteron spectra of HD in a mixture of 5.03% HD in Ar at 180 K and 8.38 amagat. Note the high resolution of the multiplet peaks. Both spectra were obtained with 128 scans. No window function has been used in processing these two spectra. Dwell times of 4.0 and 6.0 microseconds and relaxation delay times of 0.5 and 2.0 seconds were used for the proton and deuteron, respectively. The S/N ratios for a single peak were measured to be 7500 and 170 in the coupled, and 16440 and 680 in the decoupled spectra for the proton and the deuteron, respectively. The measured values of $^1J_{HD}$ from the proton and deuteron spectra are 41.74 and 41.66 Hz, respectively. The singlet peaks in (a) and (b) have been obtained by decoupling the other nucleus. See Sec. 3.2.3 for details. The tick spacing in (a) and (b) are 50 Hz and 25 Hz, respectively.

perature. There are two main reasons for such behavior. First, the population differences between the nuclear spin levels, which are responsible for nuclear magnetization, decrease with increasing temperature. This decreases the total magnetization and thus decreases the overall signal, which is proportional to it. Second, spin-spin relaxation times for both nuclei decrease with increasing temperature.[2] This leaves the experimentalist with a weak and rapidly decaying FID (free induction decay; the time-demain signal) with a low S/N ratio.

Quantitative information about temperature and density dependences of the S/N ratio would be quite useful in selecting the mole fractions and amagat densities at the beginning of this type of experiment. No such information has been reported on these systems in the literature. Tables 3.2 and 3.3 list the S/N ratios obtained for the peaks in the proton and deuteron spectra of HD in a mixture of 2.80% HD in Ar at 8.34 amagat and at different temperatures. Better S/N ratios can be obtained if window functions are used to suppress the contributions of the tail of the FID (which consists mostly of noise). But, at the same time, the use of window functions decreases the resolution of the spectrum. Collecting and including the tail of the FID is necessary for ultimate resolution of the multiplets. However, for T_1 measurements, for which such resolution is not necessary, a shorter acquisition time and a window function with an appropriate line-broadening factor can be used to improve the S/N ratio.

The widths of both the proton and the deuteron peaks increase with temperature, because T_2^* decreases with temperature. Linewidth and T_2^* are inversely related by Fourier transformation.[69] Increases in the widths of the multiplet peaks decrease the resolution such that the multiplet peaks cannot be resolved at higher temperatures. A typical example of the temperature dependence of the widths of the proton and deuteron peaks is shown in Figs. 3.2-(a) and (b), respectively. No

Table 3.2: Typical temperature dependence of signal-to-noise ratios, S/N, chemical shifts, δ, and peak widths, $\Delta\nu_{1/2}$, in the proton (^{1}H) spectra of HD in a mixture of 2.80% HD in Ar at 8.34 amagat. NS is the number of scans for each spectrum. The listed S/N ratio for each spectrum is calibrated for 256 scans, knowing that S/N is inversely proportional to the square root of the number of scans. No window function is used in the measurement of these quantities. The widths in the coupled spectra are the overall widths of the multiplet, *i.e.*, the sum of the widths of the three peaks of the triplet. See Fig. 3.2 for the spectra. The jumps in the values of the S/N ratios, widths, and chemical shifts at T = 298.4 K are due to changes in the shimming parameters.

	Deuteron-Coupled Spectra			Deuteron-Decoupled Spectra			
T(K)	NS	S/N	$\Delta\nu_{1/2}$(Hz)	NS	S/N	$\Delta\nu_{1/2}$(Hz)	δ(Hz)
180.7	128	4696	71.3	128	10667	19.1	0.0
194.9	128	3646	80.1	128	8316	15.3	9.7
209.8	256	2986	80.0	256	6948	19.1	14.1
225.9	256	2505	85.0	256	5125	22.9	18.9
243.2	256	1942	112.1	256	3642	26.7	24.8
261.2	512	1401	117.7	512	2771	34.3	29.8
279.7	1024	1220	124.3	1024	2217	38.2	39.2
298.4	128	1612	126.7	128	3251	38.2	76.4
324.0	256	926	132.2	256	1476	45.9	78.2
349.8	256	574	138.3	256	926	57.4	82.9
375.3	256	472	142.7	256	668	65.0	88.6
398.6	256	374	147.6	256	517	76.5	96.0
417.4	1024	314	153.0	1024	445	88.0	108.7

Table 3.3: Typical temperature dependence of signal-to-noise ratios, S/N, chemical shifts, δ, and peak widths, $\Delta\nu_{1/2}$, in the deuteron (^{2}H) spectra of HD in a mixture of 2.80% HD in Ar at 8.34 amagat. NS is the number of scans for each spectrum. The listed S/N ratio for each spectrum is calibrated for 256 scans, knowing that S/N is inversely proprotional to the square root of the number of scans. No window function is used in the measurement of these quantities. The widths in the coupled spectra are the overall widths of the multiplets, *i.e.*, the sums of the widths of the two peaks of the doublet. See Fig. 3.2 for the spectra. The jumps in the values of S/N ratios, widths, and chemical shifts at T = 298.4 K are due to changes in the shimming parameters.

	Proton-Coupled Spectra			Proton-Decoupled Spectra			
T(K)	NS	S/N	$\Delta\nu_{1/2}$(Hz)	NS	S/N	$\Delta\nu_{1/2}$(Hz)	δ(Hz)
180.7	512	189	19.7	512	387	6.2	0.0
194.9	512	138	24.4	512	313	6.2	1.0
209.8	1024	108	26.5	1024	262	6.3	1.3
225.9	1024	90	28.7	1024	226	5.9	2.3
243.2	1024	78	35.4	1024	193	9.6	2.6
261.2	1024	59	42.6	1024	163	9.7	2.9
279.7	1024	53	50.0	1024	139	9.5	4.5
298.4	512	71	58.4	512	158	9.0	11.1
324.0	1024	35	58.6	1024	84	8.9	11.3
349.8	1024	27	60.1	1024	55	9.5	11.6
375.3	1024	21	59.5	1024	49	10.4	12.5
398.6	1024	20	55.5	1024	46	11.4	12.9
417.4	1024	20	56.3	1024	39	12.5	16.4

window function is used in the processing of the spectra shown in these figures. Numerical values of the peak widths of the spectra are given in Tables 3.2 and 3.3. These widths are accurate to within $\pm$ 0.5 Hz. A study of the one-dimensional spectra of all mixtures at different temperatures shows that the peak widths are linearly proportional to temperature. This trend, however, is not observed at higher temperatures, at which the multiplet peaks overlap and can no longer be resolved. At these temperatures the reported widths are the overall widths of the multiplets, which are different from what the sums of the widths of the peaks of the multiplets would be if they could be measured. The overlap of the non-resolvable multiplet peaks causes a decrease in the measured widths of the multiplets.

The temperature dependence of the peak widths is consistent with the temperature dependence expected for T_2^{-1}. This suggests that the contribution of diffusion to the spin-spin relaxation time is very small. It can thus be concluded that diffusion has a negligible contribution to the spin-lattice relaxation processes and to the measured values of T_1 in this work. This conclusion is confirmed by the small values obtained for the widths of the deuteron peaks. Analysis of the values obtained for the deuteron T_1 (see the next section) suggests that the deuteron peak widths could have values of less than 1 Hz if the magnetic field was perfectly homogeneous over the sample. But, because it is not possible to shim the magnet perfectly, there is always a contribution from inhomogeneity of the magnetic field to the widths of the peaks. The minimum numerical value of this contribution is of the order of 5 Hz, and increases with decreasing shimming quality, which usually occurs when the temperature changes. Table 3.3 indicates that the widths of the deuteron peaks can be associated with contributions from the inhomogeneity of the magnetic field and from the spin-spin, or T_2 relaxation (*i.e.*, the natural linewidth). If the contribution of diffusion were significant, it should be observed more clearly for the

deuteron due to their having narrower linewidth. The results of T_1 measurements show that the deuteron relaxation times are longer than those for the proton by at least a factor 2. This means that diffusion could play a much more important role in the relaxation processes of the deuteron magnetization if its contribution was significant. Also, the widths of the deuteron peaks should increase rapidly with temperature. However, no such effects are observed in the values of the deuteron T_1. In other words, the measured values of T_1 in these experiments are *diffusion-free* values. In the gas phase, diffusion could be potentially the most important source of error in NMR measurements.

The decrease in the value of T_2^* that is responsible for the low resolution and the wide peaks can be due to a decrease in T_2, to poor shimming, to a change in the tuning of the LC circuit, or to an increase in the diffusion of the nuclei in and out of the effective volume of the coil. Thus, the values of the peak-widths depend on several experimental parameters. However, the quality of the data obtained in this work is such that the peak-widths still can be used to probe any contributions from diffusion in the measured spin-lattice relaxation times. This will be discussed later in this chapter. The temperature behavior of the peak-widths reported here can be used also as a guide for future NMR energetics, dynamics and relaxation experiments in these or similar systems. Beckett and Carr[70] reported a line width of 1.75 Hz for the deuteron peak of the HD gas at 40 K and 100 amagat. There is no other report on the peak widths of the proton or the deuteron in the HD gas.

Comparative analysis of one-dimensional spectra of the HD proton and deuteron in HD–Ar mixtures at different temperatures also shows that the chemical shifts of both the proton and deuteron peaks depend upon the temperature. This temperature dependence is due to the fact that chemical shielding of the nuclei depends on the rotational energy levels; the higher the rotational level, the lower the shielding

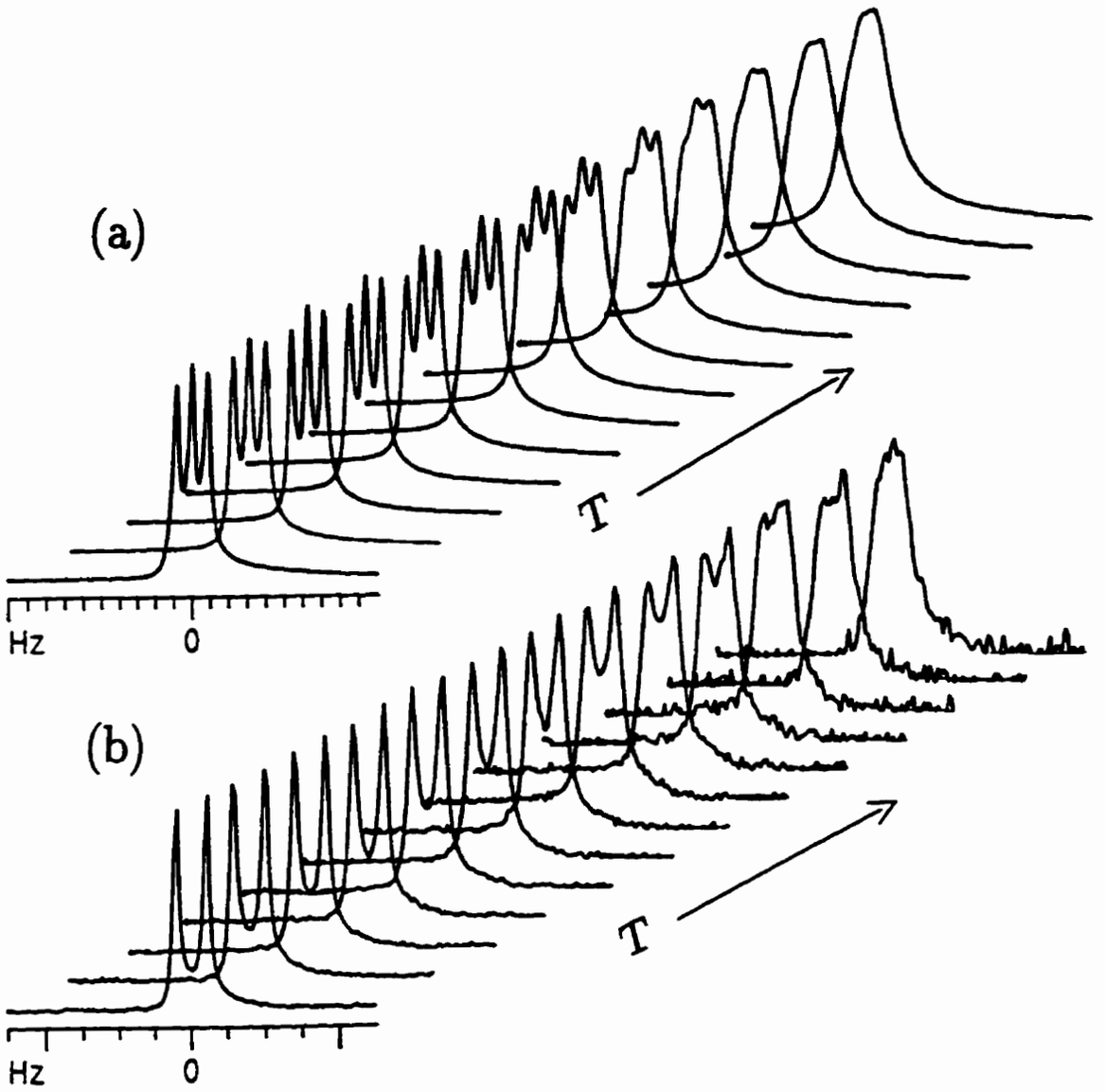

Figure 3.2: Typical temperature dependence of the peak widths of (a) the proton, and (b) the deuteron spectra of HD for 2.80% HD in Ar at 8.34 amagat. No window function is used in the processing of these spectra. The corresponding temperatures of these spectra, along with the number of scans and the numerical values of the widths and S/N ratios are listed in Tables 3.2 and 3.3.

of the nuclei. As the temperature increases, the populations of the higher rotational levels increase, and thus their contributions to the average shielding of the nuclei increase. This has an overall effect of decreasing the shielding of the nuclei, which is translated into increases in the chemical shifts.[71] Tables 3.2 and 3.3 list, respectively, the proton and deuteron chemical shifts of HD in a mixture of 2.80% HD in Ar at 8.34 amagat and at different temperatures to illustrate this temperature dependence. To locate the positions of the peaks in the measurement of these chemical shifts more accurately, exponential window functions with appropriate line-broadening factors are used in processing the spectra.

Assuming that the proton and deuteron are equalivalent so far as electronic properties are concerned, the temperature deshielding effects on the two nuclei are therefore also equal. However, since the magnetogyric ratio for the proton is $\simeq$6.5 times larger than that for the deuteron, any change in the chemical shift of the proton signal due to deshielding should be $\simeq$6.5 times larger than that of the deuteron signal. The observed chemical shifts for the HD proton and deuteron in HD–Ar mixtures, listed in Tables 3.2 and 3.3, are consistent with this fact.

The chemical shifts given in Tables 3.2 and 3.3 have error bars of the order of $\pm$0.5 Hz. However, they contain a systematic error which is introduced by the temperature dependence of the performance of the LC circuit and other components of the probe, as well as by shielding effects of the glass sample cell and the probe components, such as the glass inserts used to support the coils. In order to have error-free chemical shifts and quantitative results, the experiments should be carried out using a quartz cell and a new probe. Because of its rigid structure, the shielding effects of quartz show minimal and negligible temperature dependence. Use of a new probe would assure a perfect performance of the LC circuit and negligible temperature dependence of the shielding effects of the probe components. An

oscilloscope can be used to detect any temperature dependence of the LC circuit and the shielding effects of other probe components. Any changes in the shimming parameters should be avoided, unless corresponding changes in the field can be measured accurately and taken into account in the measurement of the chemical shifts. An example of the effect of changing the shimming parameters can be seen in Tables 3.2 and 3.3 at temperature 298.4 K.

The only anomaly that was observed in the HD proton spectra in HD–Ar mixtures was a very small peak which appeared at $\simeq -1800$ Hz with respect to the original peak. The intensity of this peak was between 0.1% and 0.8% of that of the original peak. In some mixtures, however, such an anomalous peak appeared farther from the original peak, and in some others it was not observed. The width of this peak depended upon the mixture, and was on the order of 70 Hz. Figure 3.3 shows the worst proton spectrum that has been obtained in this study, in which the anomalous peak can be observed. In this case the linewidth and the relative chemical shift and intensity of this anomalous peak are measured to be 86 Hz, -1785 Hz and 0.7%, respectively. Under the same conditions, the linewidth of the original peak is 159 Hz. Comparison of the chemical shift and the width of this peak with those of the original HD peak, suggests that an adsorbed species on the surface of the glass cell might be responsible for it. Because of its location and its negligible intensity, this peak does not affect signal or T_1 measurements on the original peak. The broad peak centered at -2750 Hz with respect to the original proton peak is the background peak of the empty probe. Hydrogenated species adsorbed onto different components of the probe are responsible for this peak: its position varied from one mixture to another, because of the different shimming parameters used for each mixture. The shimming parameters which set the magnetic field and its homogeneity at the position of the responsible species in the probe, define the

chemical shifts, as well as the widths of these peaks. In the shimming procedure which is performed on the lineshape sample, a solution of 3% chloroform and 0.2% TMS in acetone-d_6 in this study, the magnetic field homogeneity is adjusted only over the volume of the sample cell by probing and minimizing the widths of the peaks of the sample in the NMR tube. Improvement of the homogeneity of the magnetic field beyond the NMR tube is neither important nor possible. As the temperature increases, the intensity of the background peak of the probe increases, while its width decreases. In the worst case, which happens at the highest end of the temperature range of each series, the intensity of this peak is less than 5% of that of the original peak, while its width under the same conditions is about 1050 Hz, see Fig. 3.3. Because of its distance from the original peak, and its low S/N value, this peak interferes neither with the signal nor with the relaxation time measurement.

Since deuterated species are rare in the probe as well as in nature, no such background or adsorbed species peak is observed in the deuteron spectra.

3.2.2 NMR spin-lattice relaxation time measurements for the proton and deuteron of HD in HD–Ar mixtures

After optimizing all instrumental parameters, the inversion-recovery method was used to measure proton and deuteron spin-lattice relaxation times. In this method, as described in Sec. 1.2, the recovered magnetization is detected at different times, τ, after applying a π-pulse. Using a larger number of τ values will result in a more accurate relaxation time. However, a longer period of time is required to complete the experiment if a larger number of τ values is used. Because of time limitations, it is not practical to choose a large number of τ values. For most

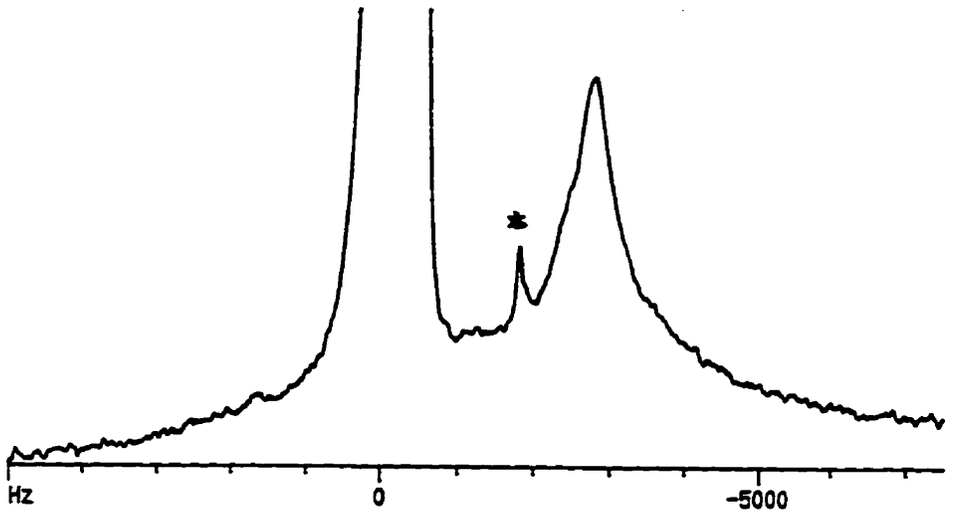

Figure 3.3: The anomalous peak in the proton spectrum of HD for the mixture with 2.80% HD for Ar at 417.4 K and 15.03 amagat. The maximum intensity of the peak is observed at the highest temperature of each series. In this case the intensity of the peak is $\simeq 0.7\%$ that of the original peak. The broad peak centered at -2750 Hz is the background peak of the empty probe.

systems with sufficiently large S/N ratios eight τ values are normally considered to be sufficient to obtain acceptable accuracy. Nonetheless, throughout the present studies sixteen τ values are used for all T_1 measurements on all mixtures. Further, a relaxation delay time on the order of $10\,T_1$ to $20\,T_1$ was used in all experiments. To set this relaxation delay, the value of T_1 was estimated using the T_1 values for previous experiments. An automatic calibration procedure, followed by a more accurate manual search for the first two null points, was used to calibrate the pulse lengths of the proton and deuteron channels. For each mixture this calibration was necessary at several temperatures, due to the temperature dependence of the performance of the coils.

The τ values and their corresponding detected magnetizations were fitted to an exponential function, given in equation (3.1) as

$$M_\tau/M_\infty = A - 2B\exp(-\frac{\tau}{T_1}). \tag{3.1}$$

In this equation M_τ and M_∞ are the recovered magnetization after τ and after a very long time, *e.g.*, $10\,T_1$, respectively, while A and B are adjustable parameters that account for the imperfections in pulse lengths, insufficient relaxation delay times, and inappropriate sets of τ values. The factor B also absorbs any effect of non-exponential relaxation processes. In an ideal experiment the values of both the A and B parameters should be exactly unity, see equation (1.4). Existence of any of the above-mentioned problems will result in deviations in the values of A and B from unity. For the majority of T_1 measurements reported herein, for both proton and deuteron, the fitted values of the A and B parameters were found to be between 0.98 and 1.02.

In addition to the values of the A and B parameters, standard deviations of the fits serve as measures of the quality of the experiments and of the measured relaxation times. The best fit has the lowest standard deviation as well as the closest values to 1.0 for each of the parameters A and B. In most of the experiments reported in this thesis the standard deviations of the fits were less than 0.2% and 1.0% for proton and deuteron, respectively. The error bars of the measurements were typically estimated to be six times the values of the standard deviations of the fits. This is, of course, a cautious estimate. Since T_1 measurements for all mixtures at all temperatures (with the exception of room temperature) were only performed once, no true error bar for the measured T_1 values can be reported. For each mixture a T_1 measurement at one temperature (usually room temperature) was performed

twice, once at the beginning, and once at the end of the experimental series on that mixture. Comparison of the results of these two experiments was used to probe any diffusion of hydrogen, here as HD, from the seals, or to see the effects of any changes in the features of the GHS, such as thermal expansion or changes in room temperature which might not be detected by the pressure gauge, *e.g.*, by cancelling one another. In all cases the results of both S/N ratio and T_1 measurements for the two experiments were in excellent agreement, *i.e.*, within the standard deviations for the two experiments. This test reassures us that no leakage of hydrogen, here as HD, happened during any of the experimental series. Hydrogen is more sensitive to breaks in the seals than is argon. Diffusion of hydrogen at low mole fractions cannot be easily detected by the pressure gauge unless a major fraction of it, *e.g.*, 10%, has leaked out through the GHS seals.

Both areas and intensities are employed in the curve-fitting procedure used to measure T_1. Generally, intensities gave better results, mainly because in most experiments the short dead-time, used to allow collection of the strong signal at the beginning of the FID, introduced a large baseline roll in the spectrum. Variation of this baseline from the spectrum for one τ value to that for another τ value introduces errors in using both peak areas and peak intensities in the T_1 measurement routine. It is important to note that these errors have a cumulative effect on the measured T_1 values obtained from peak areas.

For the proton, the effects of baseline distortion on the integrals caused by short dead-time are extremely small because the signals are so strong. Indeed, a very short dead-time was not needed for the proton measurements. The values of T_1 for the proton calculated from the peak areas and from the peak intensities are very close, considering the standard deviations of the two fits. In comparison, the difference between the two measured T_1 values for the deuteron is significant,

especially at higher temperatures. The minimum value of the dead-time for the deuteron channel was determined to be $\simeq$ 30 μsec (approximately half the dead-time needed for total avoidance of large baselines) for the Bruker broad-band probe used in these studies. Increasing the dead-time, *i.e.*, waiting longer before collecting the FID after the applied pulse, decreases the S/N ratio of the spectra considerably.

Intensities and areas of all individual multiplet peaks were used in the fitting procedure when they could be resolved, and their corresponding T_1 values could be measured. No significant difference was observed amongst the T_1 values obtained from different multiplet peaks.

Typical results of the inversion-recovery method for measurements of the proton and deuteron T_1 values for HD in HD–Ar mixtures are shown in Figs. 3.4 and 3.5, respectively. Measured proton and deuteron T_1 values for all HD–Ar mixtures, listed in Table 3.1, are plotted versus temperature in Figs. 3.6 and 3.7, respectively. These figures do not show the temperature error bar, which is $\pm$ 1 K for all experiments. Error bars for the T_1 values are estimated to be $\pm$ 3 SD or 6 SD with SD being the standard deviation of the fit. As can be seen in Figs. 3.6 and 3.7, most of the proton T_1 values and some of the deuteron T_1 values have error bars smaller than the sizes of the points. No good results for the deuteron T_1 values of the mixture with 0.86% HD in Ar could be obtained, because its S/N ratio was too low. Thus, no deuteron T_1 values are reported for this mixture.

An excellent data set is recognized by the feature that elimination of some of the τ values causes no effect on the measured value of T_1 and also decreases the standard deviation of the fit. All collected data, with the exception of the deuteron data sets for two HD–Ar mixtures, one with 0.86% HD at 8.74 amagat and the other with 5.03% HD at 15.5 amagat, at some temperatures, have this feature. A large standard deviation in the measured deuteron T_1 values for certain mixtures,

at some temperatures, was found upon investigation to be caused by a few points lying away from the general trend of the recovery curve, *i.e.*, statistical outliers. Normally, instrumental instabilities are responsible for such outlying data points. New T_1 values were determined by eliminating the outlier points. Two criteria were considered in the elimination of such outliers. Firstly, the fitting of the remaining data points to the inversion-recovery curve, equation (3.1), must result in improved values not only for the parameters A and B, but also for the standard deviation of the fit. Secondly, the best combination of the remaining points is the one that gives the closest (but not necessarily the same) T_1 values determined from both intensities and integrals (and from all multiplet peaks, where applicable).

Figures 3.6 and 3.7 show that both the T_1 value and the slope of the T_1 versus temperature curve generally decrease with increasing temperature. However, there are two exceptions to this trend. One exception is the behavior of the proton T_1 values for the mixture with 0.86% HD in Ar at 0.96 amagat. For this mixture the proton T_1 decreases very slowly, with essentially the same slope at all temperatures. This exceptional behavior is due to the very low amagat density of the mixture. For such a low density the system is close to the region of the T_1 minimum in a T_1 versus density plot. This would be more evident were the T_1/ρ values plotted versus temperature.[4] The other exception is the behavior of the deuteron T_1 values for the mixture with 0.86% HD at 8.74 amagat, which shows an increase in T_1 for the few temperatures at the upper end of the temperature range.

Except for the mixture with 0.86% HD at 8.74 amagat, which shows a local minimum at $\simeq$ 215 K, the proton T_1 curves for all mixtures show a smooth temperature dependence. According to Lemaire and Armstrong,[72] these local minima can be attributed to the formation of HD–Ar Van der Waals complexes. A trace of such a local minimum can be also seen in the proton T_1 curve for the mixture

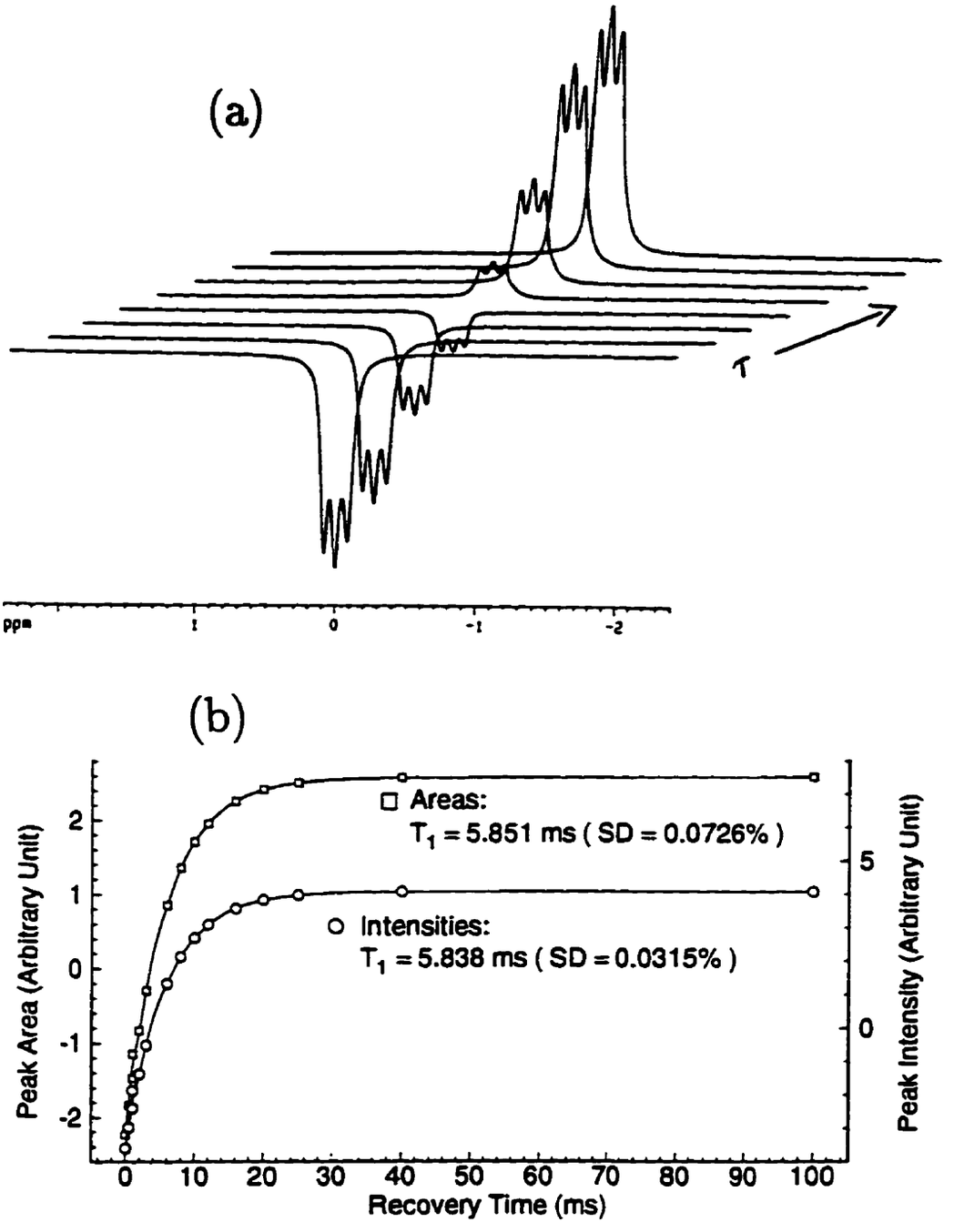

Figure 3.4: Typical inversion-recovery analysis of the proton magnetization for a sample of 5.03% HD in Ar at 375.3K and 4.55 amagat. (a) The stack-plot of the spectra at different recovery times, τ, and (b) fitting the areas and intensities of the peak into the inversion-recovery equation, Eq. (3.1). Note the values obtained for T_1 and the small standard deviations of the two fits.

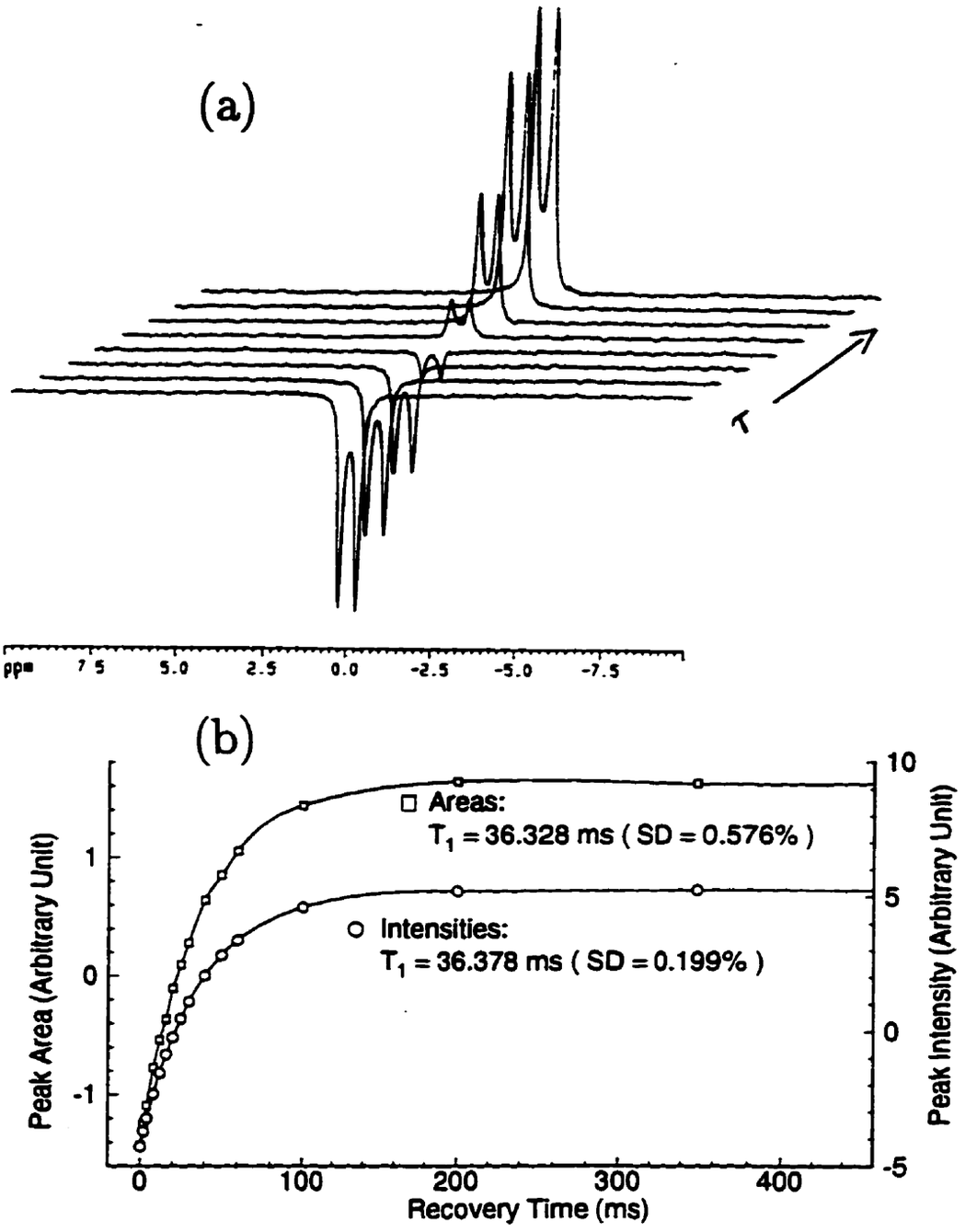

Figure 3.5: Typical inversion-recovery analysis of the deuteron magnetization for a sample of 5.03% HD in Ar at 243.2 K and 4.55 amagat. (a) The stack-plot of the spectra at different recovery times, τ, and (b) fitting the areas and intensities of the peak into the inversion-recovery equation, Eq. (3.1). Note the values obtained for T_1 and the small standard deviations of the two fits.

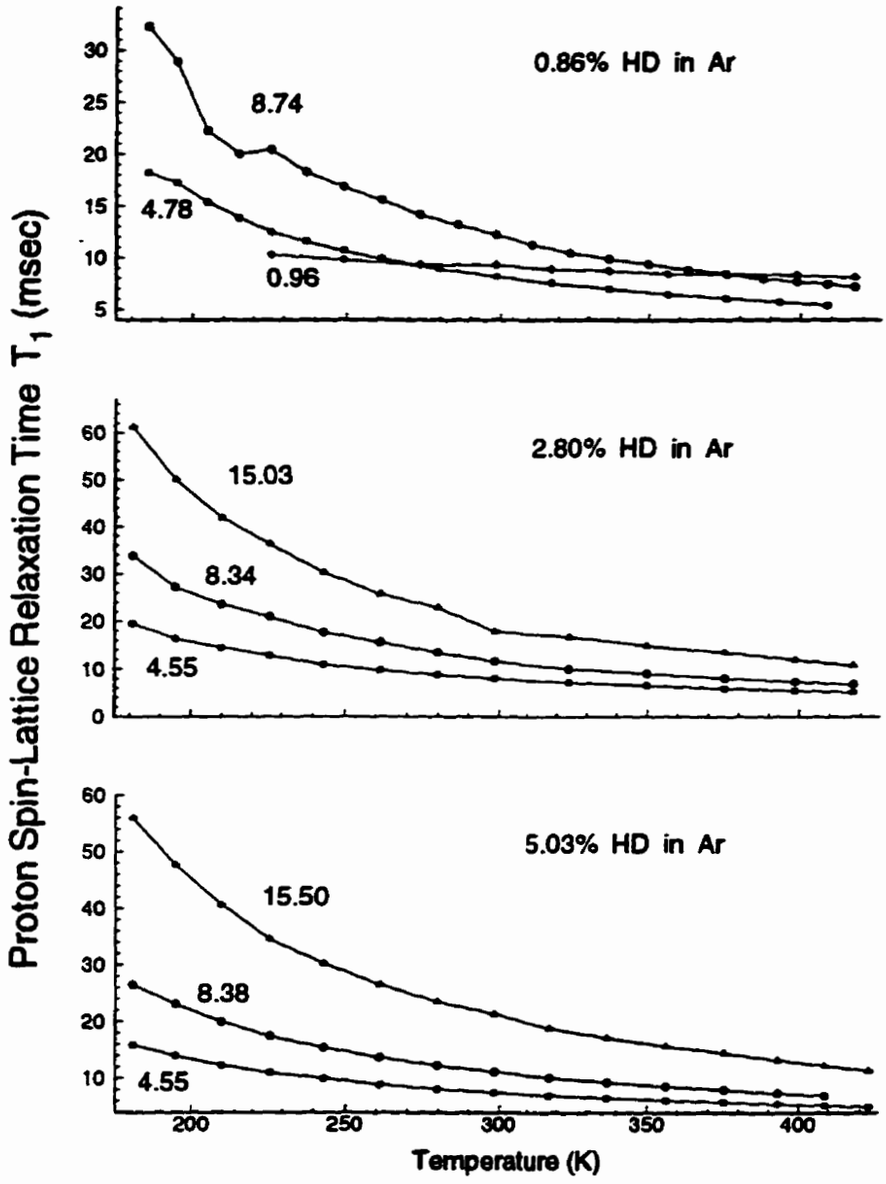

Figure 3.6: Proton spin-lattice relaxation times for HD in HD–Ar mixtures. The line-segments connecting the points serve as guides to the eye, and do not necessarily show the precise functional behavior of T_1. Numbers beside the curves represent the amagat densities of the mixture. Note the different temperature dependence of the proton T_1 for 0.86% HD at 0.96 amagat. See text for discussion on the minima observed in two of the T_1 curves. The horizontal error bars for all temperatures are about ± 1 K. See Appendix A.1 for numerical values of the temperatures and relaxation times (the T and $T_1^{(1)}$ columns, respectively).

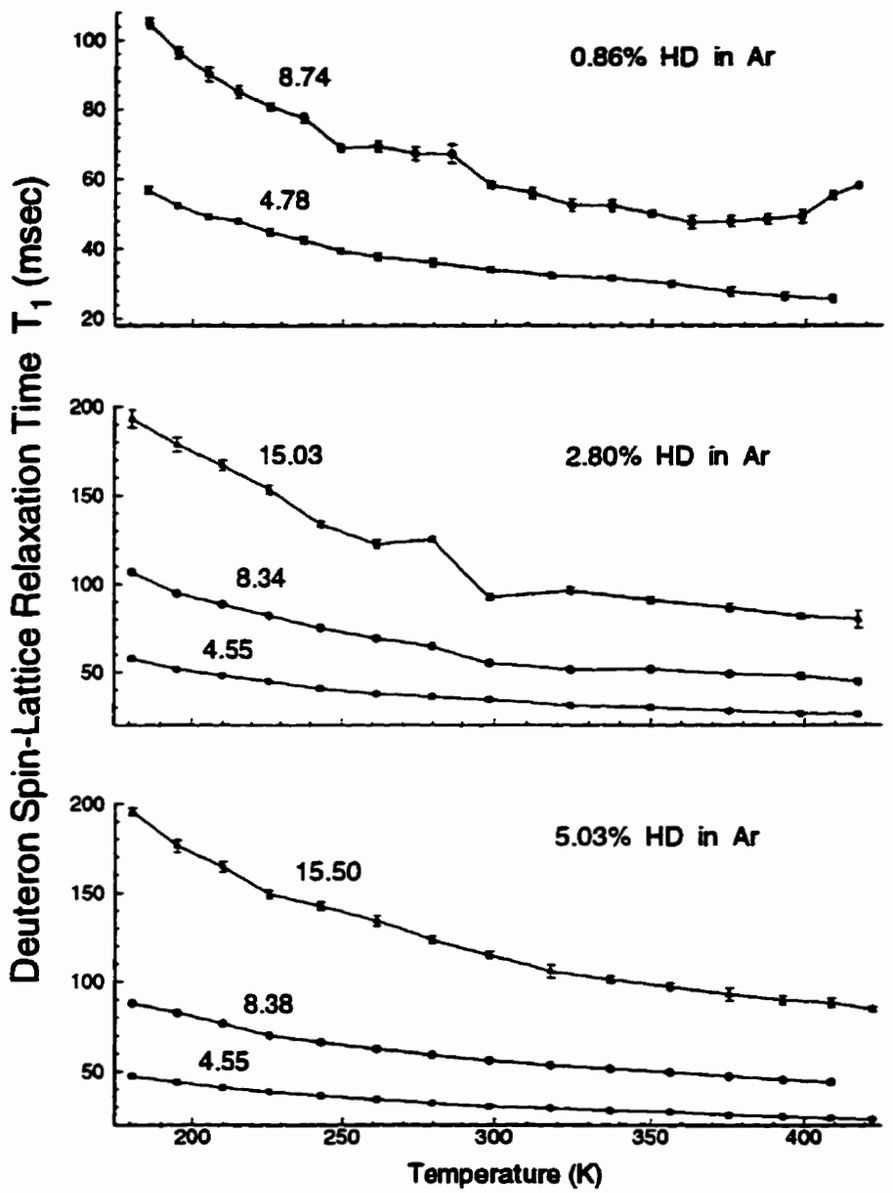

Figure 3.7: Deuteron spin-lattice relaxation times for HD in HD–Ar mixtures. The line-segments connecting the points serve as guides to the eye, and do not necessarily show the precise functional behavior of T_1. Numbers beside the curves represent the amagat densities of the mixture. The horizontal error bars for all temperatures are about ± 1 K. See Appendix A.2 for numerical values of the temperatures and relaxation times (the T and $T_1^{(1)}$ columns, respectively).

with 0.86% HD at 4.78 amagat at the lower end of the temperature range. A similar local minimum is observed in the T_1 curve for the mixture with 2.80% HD at 15.03 amagat at $\simeq$300 K. However, as only one point supports this local minimum, no firm conclusion can be made, however small its standard deviation. Inspection of the one-dimensional spectra for the proton and deuteron show that at a few temperatures close to this local minimum the shimming quality of the magnet was very poor, such that the peaks were wider than usual, and a shoulder, resembling a peak was found on the low frequency side. Normally, the results of the relaxation time measurements are not very sensitive to the shimming quality when the lineshape is not distorted. When the lineshape is distorted, however, significant effects may be expected on the measured T_1.

The behavior of the deuteron T_1 curves is much the same as that found for the proton, with only minor differences. Generally, the standard deviations of the deuteron T_1 values are larger than the corresponding proton T_1 values due to the smaller S/N ratios. No local T_1 minimum similar to that found for the proton is observed for the mixture with 0.86% HD at 8.74 amagat. However, abnormal behavior is observed for the mixture with 2.80% HD at 15.03 amagat for temperatures 279.7 and 298.4 K. This is the same place at which the corresponding proton T_1 curve show a local minimum. As mentioned above, one major source for this abnormal behavior is poor shimming. This observation shows that the effect of shimming on the T_1 measurement is larger when the S/N ratio is smaller. The deuteron T_1 curve for the mixture with 0.86% HD at 8.74 amagat shows a strange temperature dependence. As can be seen from Fig. 3.7, except for a short range of low temperatures, this curve is not smooth. The amplitude of the deviation is much higher than the standard deviation of the fit. No explanation has been found for this behavior.

For all mixtures at all temperatures the T_1 value for the deuteron is larger than

that for the proton by a factor between 3 and 8, depending upon the temperature and density (and slightly upon the HD mole fraction of the mixture). The T_1 values for both nuclei show a weaker temperature dependence at lower densities. These results are consistently observed for all mixtures, with the exception of the proton T_1 values for 0.86% HD in Ar at 0.961 amagat. The temperature and density dependence of the measured proton and deuteron T_1 values for HD in HD–Ar mixtures will be discussed in detail when they are compared to the theoretical calculations in Section 5.2.

Numerical values of the raw and adjusted (see Ch. 5) spin-lattice relaxation times obtained for the proton and deuteron of HD in HD–Ar mixtures can be found in Appendix A.1 and A.2, respectively.

3.2.3 Gas phase NOE measurements, and the contribution of the dipolar interaction to the proton and deuteron relaxation times of HD in HD–Ar mixtures

In a typical spin-lattice relaxation time measurement experiment, such as that discussed in the previous section, the measured quantity is the overall relaxation time, T_1. As described in Sec. 1.2, different independent mechanisms contribute to the relaxation of the nuclear magnetization, so that the overall relaxation rate (reciprocal relaxation time) is given by the sum of the corresponding relaxation rates, as in Eq. (1.14). No information can be obtained about individual contributions to the overall relaxation time in such an experiment. Approximate separation of the components of the spin-lattice relaxation time has been carried out routinely for many spin systems in the liquid phase.[7,73] Use of NOE measurements (for dipolar relaxation),[74,75] extrapolation of the field-dependent relaxation times to zero field-strength (for spin-rotation relaxation)[76] and lineshape analysis (for J-coupling relaxation)[77] are examples of the methods which sense the different mechanisms. Of course, not all of these methods are applicable for all systems.

There has been no attempt to measure directly the separate contributions from the different mechanisms to the total spin-lattice relaxation time in gaseous samples. This has been largely because of poor S/N ratio and the low resolution of gas phase spectra. From a theoretical point of view, however, it would be useful to be able to compare calculated values of individual components of the relaxation time directly with experimental results.

In the present studies an attempt has been made to measure separately each component of the spin-lattice relaxation times of both nuclei of HD in HD–Ar mixtures. The results of NOE measurements, which are used to separate the

dipolar contributions to the relaxation times of the proton and deuteron, are presented below. Attempts to measure the combined dipolar-quadrupolar relaxation time (towards complete separation of the contributing mechanisms) for the deuteron by use of the Jeener-Broekaert[14,78,79] method were unsuccessful due to poor S/N ratios.

The diagram of the spin levels and relaxation pathways for the nuclear spin system of HD is given in Fig. 3.8. In this diagram all fifteen possible transitions are shown by double-headed arrows. Only seven of these transitions are allowed, and thus observable, in single-quantum NMR experiments. These include two doubly degenerate transitions of the deuteron and three non-degenerate transitions of the proton. †

The rest of the transitions are not directly observable in NMR. However, all of the transitions contribute to the overall relaxation. The proton and deuteron peak intensities are proportional to the differences between populations of the energy levels associated with the corresponding transitions. An NMR transition changes these populations from their equilibrium values. The rate at which these populations return to their equilibrium values following a perturbation (*i.e.*, an rf pulse), is determined by the transition probabilities, $W_{k,l}$. As can be seen from Fig. 3.8, any perturbation in the population of one level will eventually result in a change in the populations of all other levels from their equilibrium values. This will change the peak intensities of the spectra obtained immediately after a perturbation has been applied. This phenomenon, which is called the Nuclear Overhauser Effect (or

† In general, for a two spin system AX, with spins I_A and I_X, the total number of transitions, N_t, and degeneracy, g_i, and multiplicity, m_i, of NMR transitions for nucleus i are given, respectively, by $N_t = N_l!/[2!(N_l-2)!]$, $g_i = 2I_i$ and $m_i = 2I_j + 1 (i \neq j)$, with $i, j = A, X$, while N_l, the total number of levels, is given by $N_l = (2I_A + 1)(2I_X + 1)$.

simply NOE), was first observed and described by Overhauser.[80] A mathematical formulation was given later by Solomon.[81] The Solomon method has been used to study NOE in a variety of systems.[74,75,82]

The perturbation that leads to equal populations for all spin levels of one of the two nuclei is called *saturation*. Once this perturbation has been applied, the total magnetization of the saturated nucleus vanishes, and its peak disappears from the spectrum. A corresponding change in the peak intensity of the other nucleus is then given by[82]

$$\eta_i\{j\} = \frac{I_i - I_i^0}{I_i^0} = \left(\frac{\gamma_j}{2\gamma_i}\right)\frac{T_{1t}}{T_{1D}}. \tag{3.2}$$

In this equation $\eta_i\{j\}$ is called the NOE enhancement; it gives the relative change in the peak intensity for nucleus i due to saturation of nucleus j. The quantities I_i and I_i^0 are peak intensities with, and without, saturation of the j nucleus, while T_{1D} is the dipolar contribution to the overall relaxation time for nucleus i. Equation (3.2) shows that values of T_{1D} for both nuclei can be obtained readily if NOE measurements can be carried out for both nuclei. This equation also shows that for the case of HD under similar conditions, the NOE enhancement for the deuteron should be $(\gamma_H/\gamma_D)^2$, or 42.25 times larger than that for the proton. Also, the limiting values of NOE enhancements for the proton and deuteron, which corresponds to a 100% contribution of dipolar relaxation, are +0.077 and +3.25, respectively.

Equation (3.2) is the limiting form of a more general equation[75] for the case in which the products of the rotational correlation time, τ_c, and the Larmor frequencies of the nuclei, ω_i, is negligible with respect to 1. This product for both nuclei of HD in its first rotational level is of the order of 10^{-7}. Thus, equation (3.2) can be applied to the NOE measurement of the HD system.

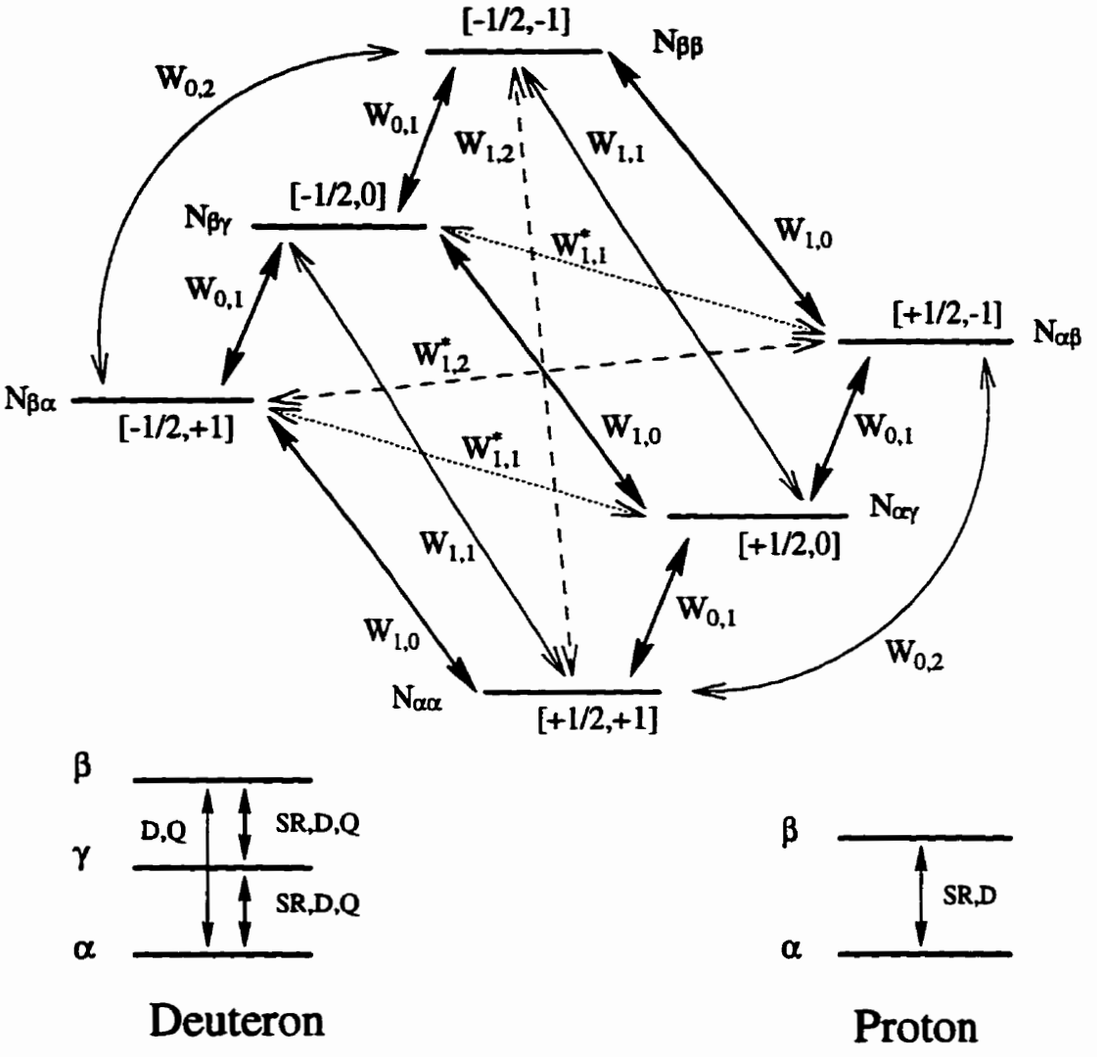

Figure 3.8: Nuclear spin levels and relaxation pathways for HD. $N_{i,j}$ represents the population of the level $[i,j]$ where $i = \alpha, \beta$ and $j = \alpha, \gamma, \beta$ represent the proton spin levels of $1/2$ and $-1/2$, and the deuteron spin levels of $1, 0$ and -1, respectively. In this diagram $W_{k,l}$ is the rate of the transition in which the proton and deuteron undergo k- and l-quantum changes, respectively. The asterisk on some of the $W_{k,l}$ denotes the opposite direction of change for the two nuclei. The solid arrows show the observable transitions in single-quantum NMR. The dotted and the thin arrows show double-quantum transitions. The dashed arrows indicate triple-quantum transitions. The proton and deuteron nuclear spin subsystems of HD and their NMR transitions are also shown. The labels SR, D and Q indicate, respectively, the spin-rotation, the dipolar and the quadrupolar interactions inducing the transitions.

One-dimensional NOE experiments can be performed in two different ways, namely, coupled and decoupled. Figure 3.9 shows the pulse sequences used in these two methods. Each method has its own advantages and disadvantages over the other.[75] None of these advantages and disadvantages are operative in gaseous HD, which has a single peak in each of its proton and deuteron spectra. The decoupled method has been used for all NOE measurements throughout this work. The characteristics of the decoupled spectra are used to analyze the temperature dependence of the peak widths and intensities, and thereby to probe any contributions from diffusion to the relaxation times. An example of such an analysis was presented in the previous section.

Based upon the above information, a series of decoupled NOE experiments were performed on the HD–Ar mixtures listed in Table 3.1 at several temperatures between 180 K and 420 K. Examples of the saturated (and decoupled) spectra obtained in these experiments for the proton and deuteron are shown in Fig. 3.1. As a further example, S/N ratios of the saturated spectra for the mixture with 2.80% HD at 8.34 amagat are compared with those of normal spectra in Tables 3.2 and 3.3 for the proton and deuteron, respectively. The NOE enhancements for both nuclei were calculated using the peak integrals. Because the decoupled method has been used, intensities cannot be used to calculate the NOE enhancements. The use of intensities will introduce significant error in the measured NOE enhancements when the coupled spectrum is used as reference and the multiplet peaks overlap (as is the case here). The results of these NOE measurements, which also represent the first NOE measurements performed in the gas phase,[‡] for the proton and deuteron are plotted versus temperature in Figs. 3.10-(a) and -(b), respectively. The measured

[‡]Based on a thorough survey of the Science Citation Index and Chemical Abstracts until August 1996. Gas phase NMR has been used in structural and kinetic studies based on the chemical shift measurements, and no polarization transfer or NOE measurement has been reported.[83–85]

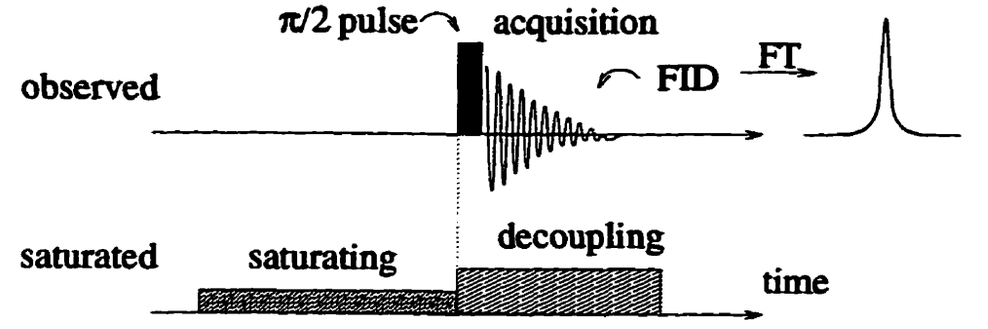

(a)

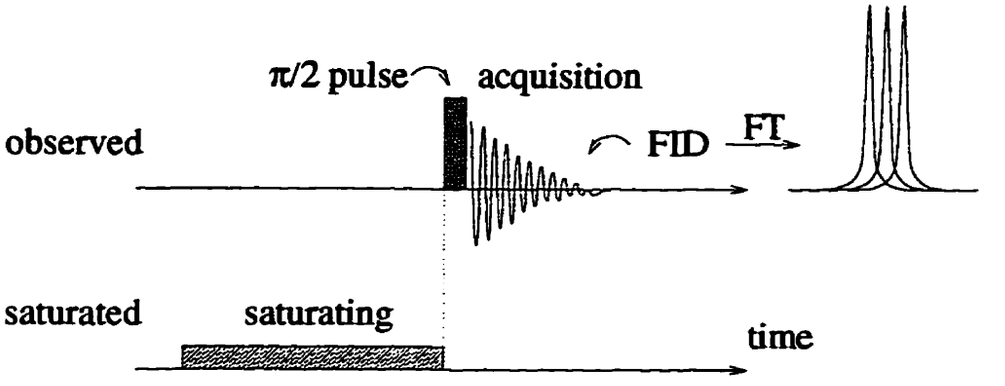

(b)

Figure 3.9: NMR pulse sequences for decoupled (a) and coupled (b) one-dimensional NOE experiments. The saturating pulse shown in this figure may be selective or non-selective (broad-band). The disadvantage of the decoupled method is that the decoupling pulse causes a Bloch-Siegert shift,[14] especially if the saturated and observed peaks have close chemical shifts. This happens more often for homonuclear NOE measurements on samples with crowded spectra. The disadvantage of the coupled method is that there should be a delay time after turning the saturating (or decoupling) pulse off and before applying the detecting pulse ($\pi/2$ pulse here) to the observed nucleus. This delay time is necessary in order that the electronics of the instrument settle down before acquisition, especially if the observed and saturated nuclei have close chemical shifts. The most serious problem is that the accumulated NOE may be lost during this delay time: if the T_1 of the saturated nucleus is sufficiently long, however, such a loss in NOE can be neglected.

NOE values have large error bars because of the experimental errors associated with NOE measurement,[75,86] especially the contributions of the baseline to the peak intensity and peak integrals. The effects of these errors are enhanced for the peaks with lower S/N ratios. The error bars for the measured NOE (NOE $= 1 + \eta_i\{j\}$) are estimated to be of the order of 5%. Within these large error bars, no distinct density or mole fraction dependence can be deduced from the results. However, as will be seen below, a study of the trend of the NOE enhancements gives a number of interesting results.

The first important result of these NOE measurements is the consistency between the relative values of η for the proton and deuteron, and the magnetogyric ratio dependence of the NOE enhancements, Eq. (3.2).

Another interesting result of these NOE measurements is that most of the measured values of η for the proton are negative. Neither the sign[74] nor the value[75] of the magnetogyric ratios supports negative values of η for the proton. Referring to the analysis of the proton and deuteron one-dimensional spectra discussed in the previous section, the observation of negative values of $\eta_i\{j\}$ can be attributed to the impurity peaks and the baseline of the spectra. These two sources of errors may also give rise to the divergence in the proton NOE enhancements observed at higher temperatures, since both become more important at higher temperatures. Because most of the measured NOE enhancements for the proton are negative, no T_{1D} could be obtained. As an example, an NOE enhancement of 0.01 for the proton corresponds to a value of 13% for the contribution of the dipolar interaction to the relaxation time.

Larger error bars are expected for the deuteron due to its poorer S/N ratio. However, the NOE enhancements can be distinguished from the effects of other errors because they are so large, and there is no interfering deuteron background signal.

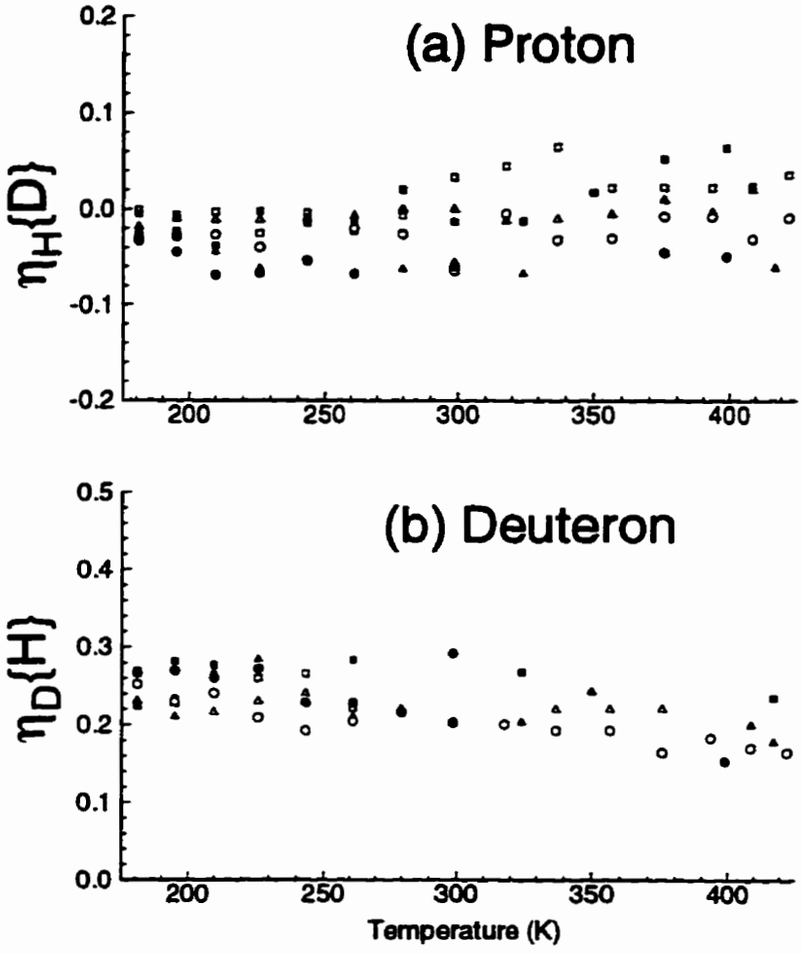

Figure 3.10: NOE enhancements for (a) the proton and (b) the deuteron of HD in HD–Ar mixtures. Hollow squares, triangles and circles represent the NOE enhancements for mixtures 4, 5 and 6, respectively, while solid squares, triangles and circles show those for mixtures 7, 8 and 9, respectively. See Table 3.1 for the specifications of these mixtures. The error bars of the measured NOE enhancements are estimated to be of the order of 0.05. However, for simplicity they are not shown in this figure.

Inspection of the values of η for the deuteron (neglecting deviations) shows that η decreases from $\simeq$0.25 at 180 K to $\simeq$0.18 at 420 K, which corresponds, respectively, to 7.7% and 5.5% for the contribution of the dipolar interaction to the relaxation time of the deuteron. This means that the contribution of the dipolar interaction to the relaxation of the deuteron magnetization decreases with temperature. No such behavior is observed for the proton. No conclusion can be made about the absolute values of the dipolar interaction between the proton and the deuteron, since no experimental evidence is available on the temperature dependence of the other interactions. Nevertheless, it is obvious that at higher temperatures, where a larger fraction of HD molecules is found in higher rotational levels, the dipolar interaction, which has a $\overline{r^{-3}}$ dependence is weaker because the inter-atomic distance r (bond length) is longer for the higher rotational levels. Further, the contribution of the spin-rotation interaction, which has a $(\overline{r^2})^{1/2}$ dependence, increases with temperature. It is therefore to be expected that the contribution of the dipolar interaction to the relaxation time should decrease with increasing temperature. Further discussion on the NOE results will be presented in Sec. 5.2, where the experimental and theoretical results for the HD–Ar system are compared.

To investigate the possible effects of saturation of one nucleus on the relaxation rate of the other nucleus, a series of proton T_1 measurement were carried out for HD in HD–Ar mixtures with the deuteron resonance saturated. The results of these T_1 measurements are compared with the results of the normal T_1 measurements in Fig. 3.11. Apart from the local minimum in the proton T_1 curve of the mixture with 0.86% HD, where the two T_1 values differ significantly, under almost all conditions the measured values of T_1 with saturation are larger than the normal values of T_1 by $2\,SD$ to $8\,SD$, with SD being the standard deviation of the measured values of T_1. The SD values for the two experiments are nearly the same. If the

local minimum in the proton T_1 curve of mixture 1 (see Table 3.1) is due to the formation of Van der Waals complexes, as described by Lemaire and Armstrong,[72] it can be concluded that the formation of such complexes introduces new relaxation mechanisms, which are sensitive to the perturbation in the population of the spin levels caused by saturation. However, no descriptive or analytical formulation is yet available to investigate how these new mechanisms behave under saturation conditions.[87] A good alternative approach to the study of the local minimum could be via a NOE measurement, if the formation of complexes significantly changes the contribution of the dipolar interaction to the relaxation time. Unfortunately, the NOE measurements carried out for this mixture could not be utilized, because different experimental parameters were employed for the two experiments.

Basically, the saturation pulse does not perturb the relaxation pathways or transition rates except for three cases. The first exception is the use of the nonselective inversion-recovery method for T_1 measurement of a nucleus coupled to other nuclei with very close chemical shifts or Larmor frequencies, such that they are affected by the pulses, *i.e.*, Bloch-Siegert effects.[14] The second exception is for those cases in which the contribution of the J-coupling to the relaxation is significant. This happens at low fields for strongly-coupled nuclei with similar Larmor frequencies,[88] especially if one of the nuclei relaxes very rapidly.[77] However, the largest contribution of J-coupling is of the order of a few percent. The last exception is the existence of interferences between different relaxation mechanisms.[89] In the case of such interferences the individual relaxation mechanisms do not act independently, and thus the overall relaxation rate, T_{1i}^{-1}, is no longer equal to the simple sum of the individual relaxation rates, T_{1i}^{-1}, *i.e.*, Eq. (1.14) is no longer valid. One important consequence of such interferences is that any perturbation in the nuclear spin of one nucleus affects the relaxation of other nuclei.[90] Another consequence of these

interferences is a non-exponential relaxation of the magnetization.[91]

The first of these exceptions does not apply to HD, since the Larmor frequencies of the proton and deuteron differ by a factor of 6.5. The second exception may at first glance seem especially relevant, as J-coupling produces unexpected negative values for NOE enhancements by contributing to zero-quantum transitions[75] (similar to those observed in the present study for proton NOE enhancements, see Fig. 3.10). These transitions are denoted by $W^{z}_{1,1}$ in Fig. 3.8. However, the HD–Ar system and the employed field do not meet the conditions required above for this contribution. Therefore, the only case which could *possibly* operate in the HD system is interference between relaxation mechanisms. Thus it can be said that if there is any difference between the measured values of the two T_1, it is due to interference between the relaxation mechanisms. Unfortunately, the differences in the measured values of the two T_1 are not large enough to attribute them to such interferences. To support the existence of such interferences, more accurate measurements will be required, such that the differences obtained between the two T_1 values can be resolved from their error bars. This kind of interference is extremely sensitive to the rotational properties of the molecule.[89] It is thus logically expected to see a large variation in the contribution of such interferences by changing the rotational properties of the molecule, say by the formation of Van der Waals complexes. There have been several reports on experimental studies of such interferences.[26,92,93] However, the existing relaxation theories have not been developed to allow the determination of values for such effects. The only suggestion which can be presented here is that an accurate and detailed study of simple systems such as HD, in the region of complex formation can provide an *order-of-magnitude* estimate of and trend for such effects. Such a study is beyond the scope of the present work, and has not been attempted.

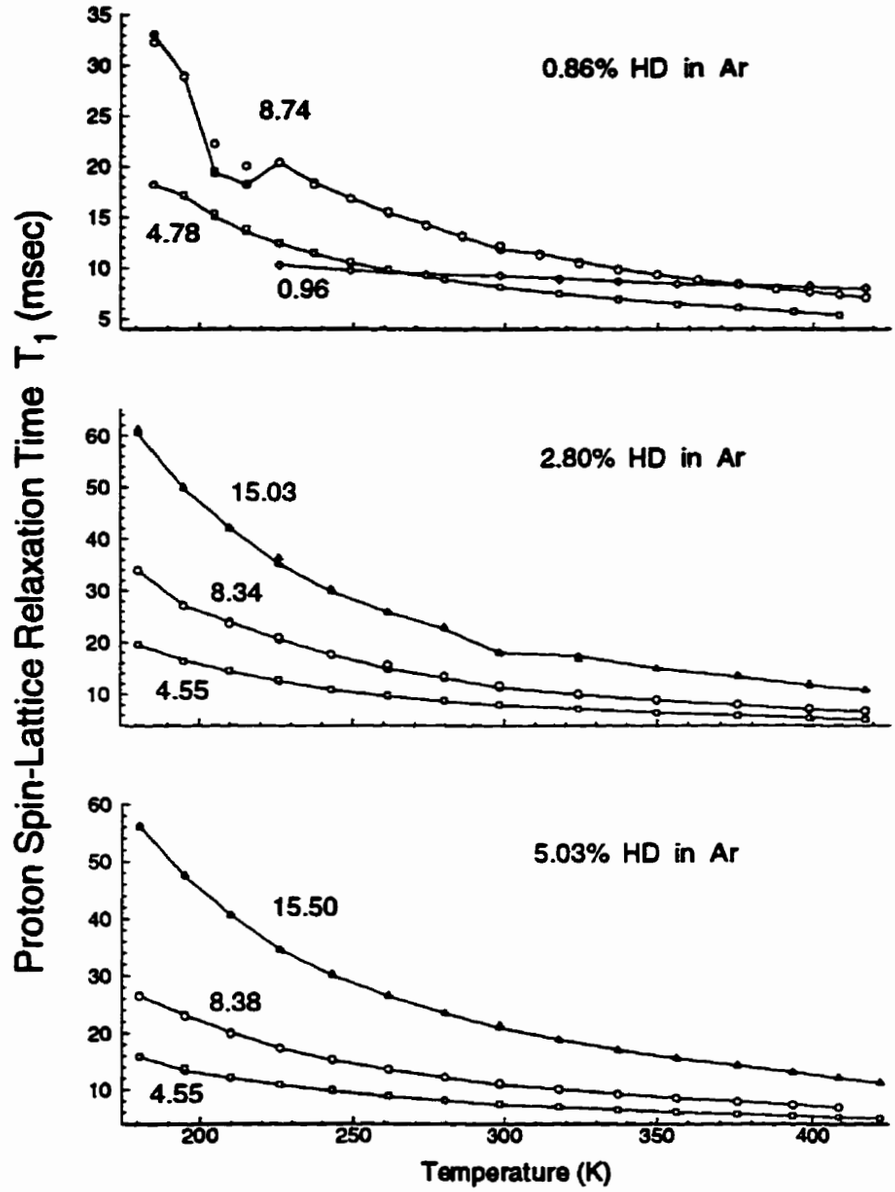

Figure 3.11: Deuteron-saturated proton spin-lattice relaxation times of HD in different HD–Ar mixtures. The solid points correspond to the deuteron-saturated values of T_1, and are connected by line-segments. The normal values of T_1 are represented by hollow points. Except for the abnormal local minimum at which the deuteron-saturated and normal proton T_1 values are significantly different, the two measured values of T_1 are almost equal within their common error bars. The horizontal error bars for all temperatures are about ± 1 K.

The only anomaly that is observed in the deuteron-decoupled proton spectra of HD in HD–Ar mixtures is a pair of satellite peaks. These two satellite peaks are located almost symmetrically around the original peak, with separation varying between 414 Hz and 420 Hz, *i.e.*, they are located at ±207 Hz to ±210 Hz with respect to the original peak, depending upon the temperature. Separation of the two satellite peaks slighly decreases with increasing temperature. The center of the pair of peaks differs from the original peak by less than one Hertz. The two peaks have the same relative intensity, which decreases with increasing temperature. The maximum intensity of these two peaks is about 1.1% of the original peak intensity, and is observed at the lowest temperature for each series. The two peaks have also exactly the same width, with a minimum value of about 60 Hz at the bottom end of the temperature range. As the temperature increases, the peak-widths increase rapidly. Their relative intensities decrease with increasing temperature, such that they are buried under the wide and growing shoulder of the original peak, and are no longer resolvable for temperatures above 250 K. The linewidths and intensities of these satellite peaks depend also on the HD mole fraction and density of the mixture. Fig. 3.12 expands one of the deuteron-decoupled proton spectra of HD in HD–Ar mixtures to show these satellite peaks. No such satellite peaks are observed in the proton-decoupled deuteron spectra. No explanation has been found for the observation of these satellite peaks in the deuteron-decoupled proton spectra.

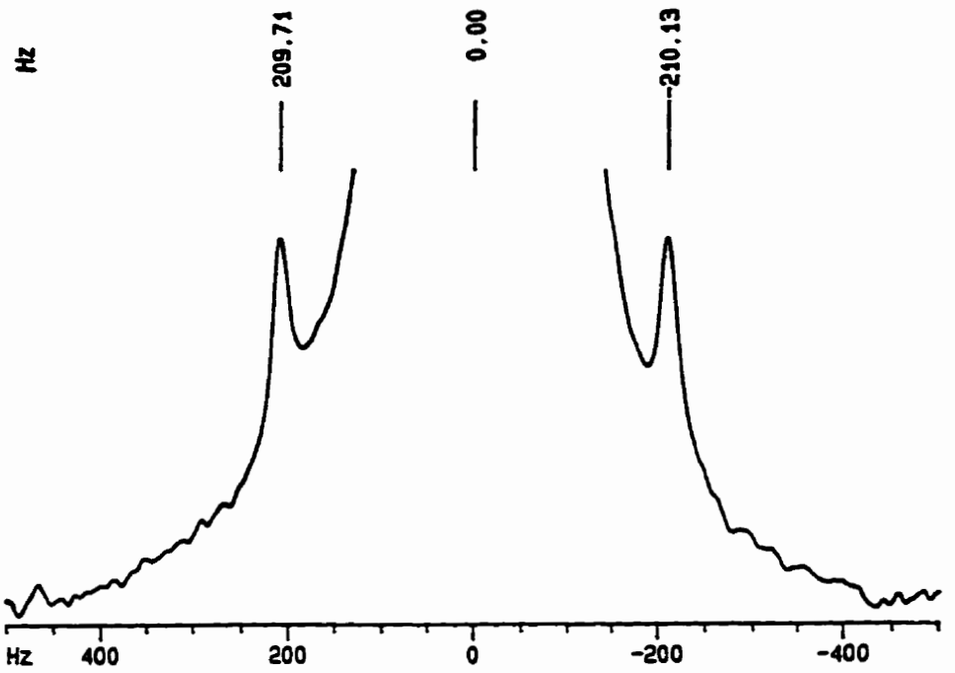

Figure 3.12: Satellite peaks observed in the deuteron-decoupled proton spectra of HD in HD-Ar mixtures. Note the equal intensity and symmetrical location of the satellite peaks with respect to the original peak. This spectrum is obtained for a mixture of 5.03% HD in Ar at 180 K and 4.55 amagat. Under these conditions the intensities of the satelite peaks both are 0.8% of that of the original peak. Linewidths of both satellite peaks are $\simeq$80 Hz. Under the same conditions the linewidth of the original peak is 40 Hz.

3.3 Gas phase NMR study of D_2–Ar mixtures

The D_2 gas was obtained from Cambridge Isotope Laboratories, with a stated purity of 99.6%, with the major impurity being HD, with H_2 a minor impurity. The gas was provided in a 460 cc carbon steel #12 lecture bottle (cylinder) with a CGA 110/170 brass angle valve under $\simeq$ 100 atm pressure. A CGA 110 to $\frac{1}{4}$ inch NPT brass adaptor was used to connect the cylinder to the GHS via $\frac{1}{4}$ inch copper tubing. The argon gas and the GHS setup used in these experiments were exactly the same as those used in the study of HD–Ar mixtures (See Sec. 3.2).

Two D_2–Ar mixtures were prepared, with 1.97% and 3.77% D_2. The relative error in the measured mole fractions for these mixtures is the same as that found for the HD–Ar mixtures, *i.e.*, about 1.8%. Experiments on each mixture were performed at three different amagat densities, as listed in Table 3.4, and for fifteen temperatures between 180 K and 420 K. For each mixture at each temperature NMR parameters were optimized on the deuteron one-dimensional spectrum prior to T_1 measurements. Analysis of the deuteron one-dimensional spectra is presented in the following section. The results of the T_1 measurements are presented and discussed in Sec. 3.3.2.

3.3.1 Analysis of the deuteron NMR spectrum of D_2 in D_2–Ar mixtures

Only one peak was observed in the deuteron spectrum for all D_2–Ar mixtures listed in Table 3.4 at all temperatures. A typical spectrum is shown in Fig. 3.13-(a). Analysis of the set of one-dimensional spectra shows a number of well-defined and interesting temperature dependences, which will be discussed below.

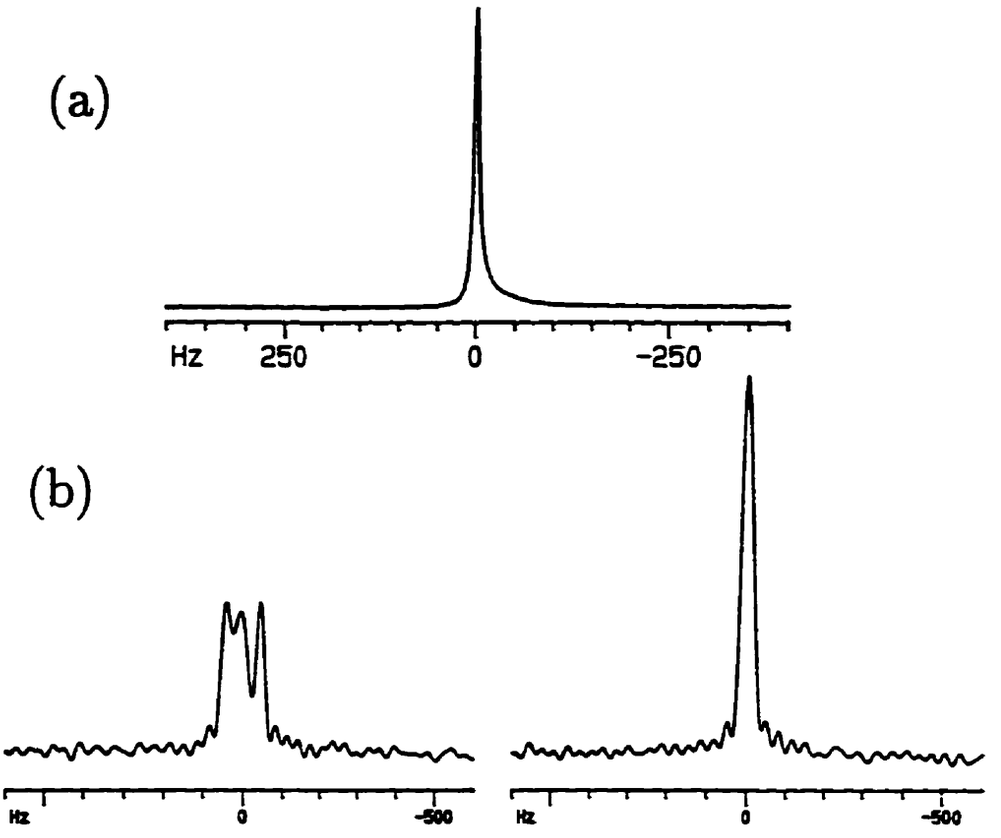

Figure 3.13: (a) A typical deuteron spectrum of D_2 for a mixture of 3.77% D_2 in Ar at 180 K and 13.99 amagat. The width and the S/N ratio of the deuteron peak under these conditions are 7.50 Hz and 1257 respectively. No other peak was observed in the deuteron spectrum. (b) Typical coupled (left) and decoupled (right) proton spectra for the same mixture and under the same conditions as in (a), used as an impurity test. This is the only observed peak in the proton spectrum. These spectra attest to the statement of the supplier that the major protonated impurity of their D_2 gas is HD. Under these conditions the proton-deuteron coupling constant in HD, J_{HD}, is measured to be 42.9 Hz. Also, the peak-widths and S/N ratios for the coupled and decoupled spectra are, respectively, 28 Hz and 21, and 35 Hz and 50. Under the same conditions the deuteron peak of the HD impurity would have widths of 10 Hz and 5 Hz, and S/N ratios of 1 and 2, for coupled and decoupled spectra, respectively. Proton decoupling had no observable effect on the deuteron spectra. The spectra in (a) and (b) are obtained with 256 scans.

Table 3.4: Mole fractions of D_2, x_{D_2}, and amagat densities, ρ, of the D_2–Ar mixtures studied in this work.

x_{D_2}	1.97%		3.77%	
	Mixture	ρ/amagat	Mixture	ρ/amagat
	1	13.84	4	13.99
	2	7.07	5	7.27
	3	3.55	6	3.58

Chemical shifts

One characteristic of the deuteron one-dimensional spectra that shows an interesting temperature behavior is the deuteron chemical shift. The deuteron chemical shifts for all of the D_2–Ar mixtures studied here are plotted versus temperature in Fig. 3.14. This figure shows that for all D_2–Ar mixtures the chemical shift of the deuteron peak increases with increasing temperature. This increase in the chemical shifts can be caused by two different processes, namely intramolecular and intermolecular processes.[41,71] As explained in Sec. 3.2.1, increasing the temperature increases the population of the higher rotational (and vibrational) levels, in which the (chemical) bond length between the two deuteron atoms of the molecule is longer. The shielding constant, which represents the effective electric charge circulation around the deuteron nuclei, decreases with increasing bond length.[§] In addition to intramolecular processes, such as the rovibrational averaging mentioned above, intermolecular interactions also contribute to the shielding constants of nuclei. This

[§]This is not the case for polar and ionic bonds, such as CH and LiF, where the shielding of one nucleus increases with increasing bond length while that of the other nucleus decreases.

contribution is called a collisional or dynamical chemical shift.[41,94,95]

Contributions of intramolecular processes to the temperature dependence of the deuteron chemical shifts for *ortho*-D_2 and *para*-D_2 have been calculated and plotted versus temperature in Fig 3.15-(b). These chemical shifts are all referenced to the chemical shift at 180 K. Figure 3.15-(b) shows that the difference between the chemical shifts of the two parity isomers is extremely small, and undetectable. This figure also shows that the chemical shifts of the two isomers increase linearly with temperature, with a positive slope of 0.01 Hz/K. Such a temperature dependence leads to a $\simeq$ 2.0 Hz increase in the deuteron chemical shift for a 200 K increase in temperature. Compared with corresponding experimental results obtained for different D_2–Ar mixtures, this increase is three to four times smaller (compare Figs. 3.14 and 3.15-(b)). This suggests that intramolecular processes are not the only sources of the temperature dependence of the deuteron chemical shift, and that their total contribution is much smaller than that of the intermolecular processes plus the contributions of possible experimental errors.

The intramolecular chemical shifts given in Fig. 3.15-(b) have been calculated in three steps. In the first step the eigenvalues of the D_2 bond length for the first fifteen rotational levels were calculated using the program LEVEL[96] with the Le Roy-Schwartz potential for the ground electronic state of D_2.[97] Numerical values of the potential were provided by Le Roy.[98] In the second step these eigenvalues were used to calculate isotropic chemical shieldings for the first fifteen rotational levels of D_2 using the *ab initio* program GAUSSIAN94.[99] Chemical shieldings have been calculated using a 6-31G* basis set at two different levels of theory, namely HF (Hartree-Fock) and B3LYP (Becke-style 3-parameter density functional theory using the Lee-Yang-Parr correlation function).[100] Isotropic chemical shieldings and the anisotropies of the chemical shielding tensor obtained from these calculations

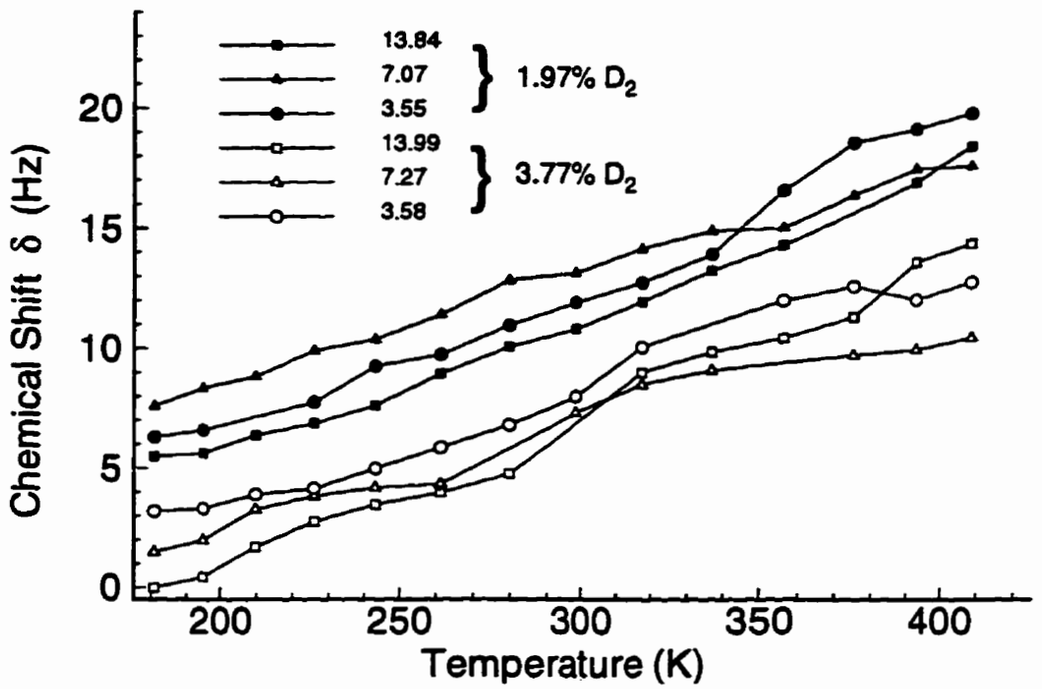

Figure 3.14: Chemical shifts for the deuteron peak of D_2 in D_2–Ar mixtures. Solid and hollow symbols correspond to mixtures with 1.97% and 3.77% D_2, respectively. The connecting line segments are guides to help follow the series of measurements on each mixture. The numbers in the figure represent the amagat densities of the mixtures. An exponential window function with a large line-broadening factor, and zero filling are used to locate the center of the peak more accurately. The breaks in the trends of chemical shifts are due to changes in the experimental parameters, such as the shielding effects of probe components. All measured chemical shifts are referenced to that of the mixture with 3.77% D_2 at 13.99 amagat and 180 K. The error bars of the measured chemical shifts are about ± 0.5 Hz. The horizontal error bar for all temperatures is about ± 1 K.

are plotted versus rotational quantum number j in Fig. 3.15-(a). It can be seen from this figure that for all rotational levels, calculations at the **HF** level give smaller isotropic chemical shielding. This figure also shows that the functional form of the j-dependence of the chemical shielding obtained at both levels of theory are essentially the same. For a general and more detailed comparison between the chemical shieldings obtained at these two levels of theory see Ref. 101. Calculations at both levels are based on the Born-Oppenheimer approximation, so that isotope effects on the electronic structure are ignored. For the present study this means that for a constant internuclear distance all isotopomers of hydrogen, *i.e.*, H_2, D_2, T_2, HD, HT and DT, have the same isotropic chemical shielding. In the third step, the isotropic chemical shieldings obtained for *even* and *odd* rotational levels are (thermally) averaged separately to calculate averaged isotropic chemical shieldings for *ortho*-D_2 and *para*-D_2, respectively. The rotational populations used for these averages have been obtained using the rotational energy eigenvalues of D_2 given in Ref. 102. In the last step, the averaged isotropic chemical shieldings of the two isomers obtained at the two levels of theory are multiplied by 76.775 Hz/ppm (corresponding to the deuteron resonance frequency at 11.75 Tesla) to calculate the corresponding deuteron chemical shifts in Hertz at temperatures between 180 K and 420 K. For each isomer, the chemical shifts at all temperatures are then referenced to that at 180 K. Fig. 3.15-(b) shows the temperature dependence of the chemical shifts obtained at both levels of theory for *ortho*-D_2 and *para*-D_2. Since the *ortho-para* conversion rate for D_2 is extremely slow, an ensemble average of the chemical shift in a mixture of the two isomers should not be carried out. Thus, the deuteron NMR spectrum of a mixture of the two spin modification should have two independent peaks, one corresponding to each spin modification. At both levels of theory, and at all temperatures, the chemical shift calculated for the *ortho*-D_2 isomer is slightly

larger ($\leq 0.02\,\mathrm{Hz}$) than that for *para*-D_2.

Evaluation of the contribution of the intermolecular processes, *i.e.*, collisional or dynamical chemical shifts, to the temperature dependence of the deuteron chemical shifts of D_2 in D_2–Ar mixtures would be an interesting research topic on its own. However, such a project is beyond the scope of the present study.

No clear density dependence can be deduced from the measured chemical shifts at different densities. This might be due to possible changes in the experimental parameters, such as the susceptibility properties of the probe components and the glass cell, from one mixture to another. Further, the field drift of the superconducting magnet contributes to the measured chemical shifts. This contribution, however, is small in the present study, since the spectrometer magnet has a very small field drift. Because no external reference has been used in the measurement of these chemical shifts, the effects of these sources of error on the measured chemical shifts cannot be precisely evaluated. The purpose of presenting these chemical shift data here is to provide us with an *order-of-magnitude* approximation of the temperature effects on the measured chemical shifts. As mentioned in Sec. 3.2.1, an accurate analysis of the chemical shifts would be possible if a quartz cell and a new probe were to be used together with an external frequency reference and an oscilloscope to measure and to probe changes in the carrier frequency more accurately. The breaks observed in the trend of the chemical shifts in Fig. 3.14 are due to changes in the experimental parameters mentioned above. The deviations at high temperatures are due to the larger widths and lower S/N ratios that enhance interference of the noise with the chemical shift measurements.

The difference between the deuteron chemical shifts for the two species responsible for the NMR signal, *ortho*-D_2 and *para*-D_2, is very small and cannot be detected under the conditions used in this study. The contribution to the error of the mea-

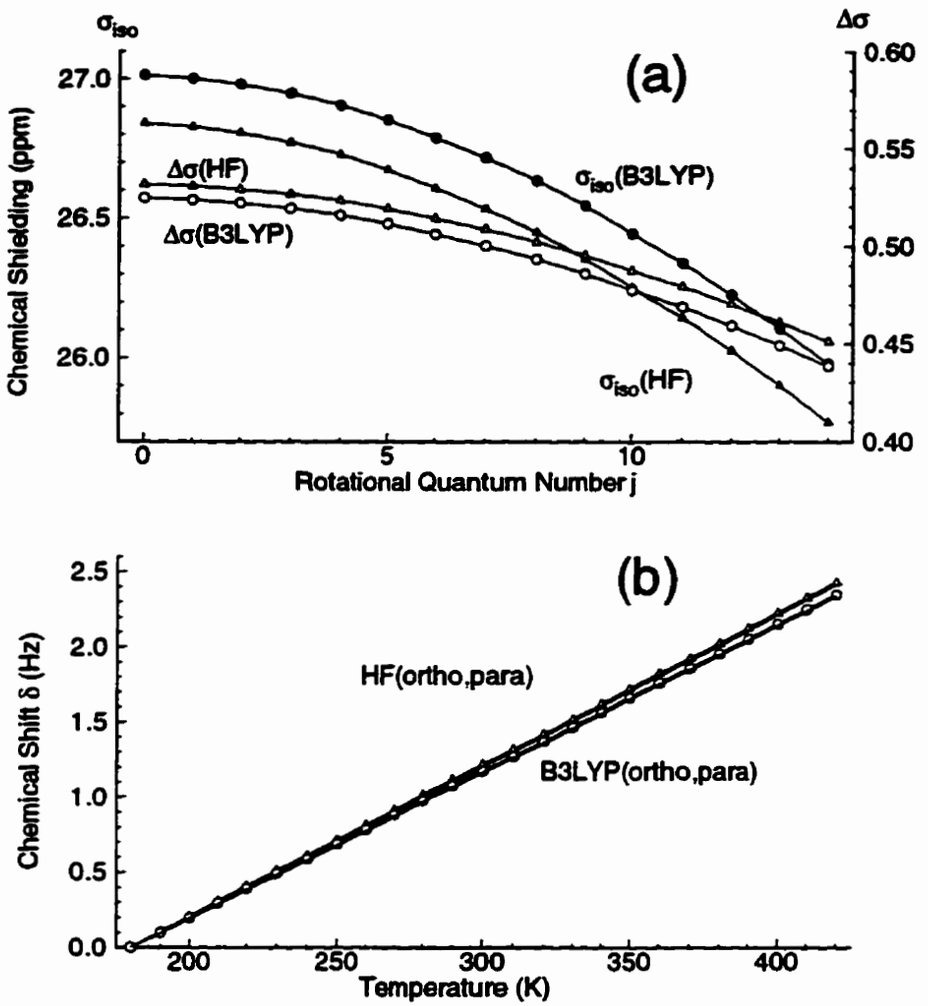

Figure 3.15: (a) Calculated isotropic chemical shieldings, σ_{iso}, and anisotropies of the chemical shielding tensor, $\Delta\sigma$, obtained for the first fifteen rotational levels of D_2 at the **HF** and **B3LYP** levels of theory. Note that both levels of theory result in the same functional form for the j-dependence of the two quantities, but with slightly different slopes. The anisotropy of the chemical shielding tensor is not observable in gas phase NMR. (b) Temperature dependence of the deuteron chemical shifts calculated for *ortho*-D_2 and *para*-D_2. At both levels of theory the chemical shifts of the two parity isomers are very close. The differences between the results of the **HF** and **B3LYP** calculations are within the expected range.[101]

sured chemical shifts from this difference is thus negligible.

Linewidths

Another interesting temperature dependence is observed for the width of the deuteron peak. Figure 3.16-(a) shows this temperature dependence for the D_2–Ar mixtures listed in Table 3.4. It can be seen from this figure that for almost all mixtures the deuteron peak-widths can be represented very accurately, within the experimental error bars of ± 0.5 Hz, by straight lines. Such a smooth temperature dependence shows the quality of the deuteron spectra obtained for the D_2–Ar mixtures. To present this result in a better way, the effective transverse relaxation times, T_2^*, are calculated from the measured peak-widths, and are plotted versus temperature in Fig. 3.16-(b). The fitted curves in this figure are essentially the inverse functions of the corresponding peak-width fitted lines. Such a temperature behavior for T_2^* for all mixtures suggests that only a single process contributes to the transverse relaxation of the deuteron magnetization. The error bar of the calculated values of T_2^* in msec, ΔT_2^*, can be calculated from

$$\Delta T_2^* = \frac{1000}{\pi}\left(\frac{1}{\Delta\nu_{1/2} - \delta\nu} - \frac{1}{\Delta\nu_{1/2} + \delta\nu}\right), \tag{3.3}$$

in which $\delta\nu$ is the uncertainty in the measured values of $\Delta\nu_{1/2}$, *i.e.*, $\delta\nu = 0.5$ Hz. The largest value of ΔT_2^*, which corresponds to the narrowest deuteron peak, for mixture 4 at 180 K, is about 5.5 msec, which is about 13% of the corresponding T_2^* value. However, the sizes of the deviations from the fitting curves are much smaller than the sizes of the error bars. Generally, experimental parameters, such as field inhomogeneity and diffusion, contribute to the measured values of T_2^*. The sum of these contributions sometimes is so large that the effective transverse relaxation

times are decreased by an order of magnitude. With an ideal experimental setup, and in the absence of diffusion, the value of T_2^* is equal to the natural transverse relaxation time, T_2. Thus, it is not possible to derive values of T_2 from the measured values of T_2^* unless the contributions of the field inhomogeneity and diffusion are precisely known.

Values of T_2 can be measured directly using the CPMG pulse sequence.[14] In this pulse sequence contributions to transverse relaxation of all dephasing processes (except for certain natural processes) are refocused at the time of acquisition. In the gas phase, however, the contribution of the magnetic field inhomogeneity cannot be removed, because of the large diffusion coefficient for molecules in this phase. Thus, the measured values of T_2 would also contain contributions from the field inhomogeneity and diffusion. It can therefore be said that for the deuteron peak of D_2 in D_2–Ar mixtures, for which no broadening due to heteronuclear J-coupling or shielding anisotropy exists, the values of T_2^* are as accurate as the values of T_2 would be.

To evaluate the quality of the deuteron NMR spectra obtained in this work, the measured values of T_2^* should be compared to the corresponding measured values of T_1. This comparison for mixtures 4, 5 and 6 is shown in Fig. 3.19. This figure shows that differences between the corresponding measured values of T_1 and T_2 are rather small. This result not only shows the high quality of the obtained spectra, but it also implies that the corresponding values of T_1 and T_2 are very close. Such a clean result, however, could not be obtained for mixtures 1, 2 and 3, for which the differences between the values of T_1 and T_2^* are quite large. The source of these larger differences arises from poorer shimming of the magnetic field. In the preparation step of the experiments on these three mixtures, the shimming quality of the field could not be improved to the same level as that for mixtures 4, 5 and 6.

In other words the measured values of T_2^* for these three mixtures had contributions from the field inhomogeneity, and resultant diffusion broadening. Diffusion of the molecules from the effective volume of the receiver coil, although negligible, exists for all mixtures and is unaffected by experimental parameters, except for the size and shape of the sample cell. The size of the sample cell is designed to be smaller than the effective volume of the coil to prevent such an experimental problem. The importance of the diffusion problem is tested below.

S/N ratios

The last property of the deuteron peak which shows an interesting temperature behavior is the S/N ratio. The S/N ratios of the deuteron peak obtained for the D_2–Ar mixtures listed in Table 3.4 are plotted versus temperature in Fig. 3.17-(a). This figure shows that for all mixtures, the S/N ratios decrease with increasing temperature. The functional form of this decrease is more or less the same for all mixtures, and can be expressed approximately by $S/N = a + bT^c$, where a and b are positive parameters while c is $\simeq -3.0$ for all mixtures examined. The S/N ratios for different mixtures cannot be compared directly because of the different densities and D_2 mole fractions. To compare the results for all mixtures, the raw values should be normalized to a constant number of nuclei per unit volume of the sample cell. This is done by multiplying the measured S/N ratios by the factor f given by

$$f = (\frac{T}{273.15})(\frac{1}{\rho x_{D_2}}), \tag{3.4}$$

in which T is the absolute temperature, while ρ and x_{D_2} are amagat density and D_2 mole fraction of the mixtures, as given in Table 3.4. In this factor the term in

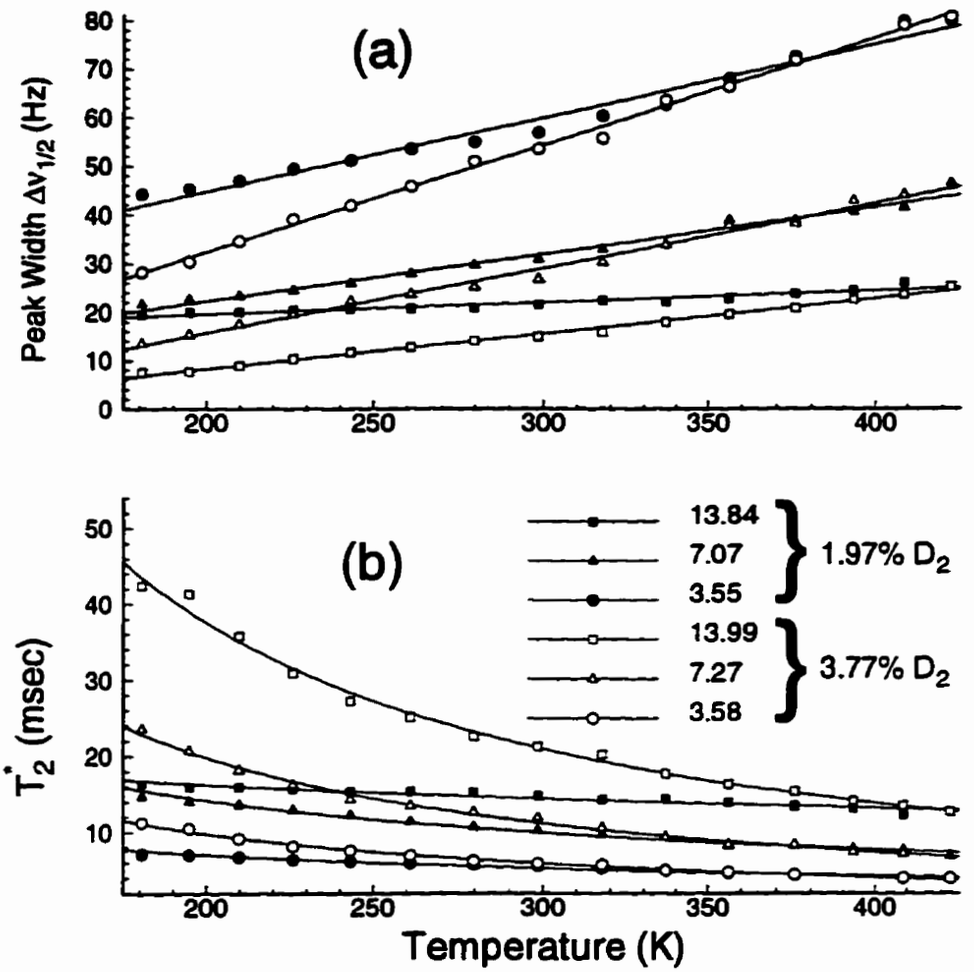

Figure 3.16: (a) NMR peak-widths, $\Delta\nu_{1/2}$, and (b) the effective transverse relaxation times, $T_2^* = (\pi\Delta\nu_{1/2})^{-1}$, for the deuteron of D_2 in D_2–Ar mixtures. Solid and hollow symbols correspond to the mixtures with 1.97% and 3.77% D_2, respectively. The fitting curves in (a) are straight lines. As can be seen, straight lines represent the temperature dependence of the deuteron peak-width for all mixtures (except for the mixture at 3.55 amagat) very accurately. The fitting curves in (b) are reciprocals of the corresponding fitting curves in (a). The error bars for the peak-widths are about ± 0.5 Hz. The error bars for the T_2^* values can be calculated accordingly. The horizontal error bar for all temperatures is about $\pm$ 1 K.

the first set of parentheses is the conversion factor from amagat density to number density. Multiplication by this factor normalizes the measured S/N ratios for 1% D_2 and number density L_0, or simply for $0.01L_0$ partial number density of D_2, with L_0 being Loschmidt's number (2.687×10^{25} molecule/m^3). This normalization removes the direct density dependence of the measured S/N ratios.

Further, the measured S/N ratios should be multiplied by the absolute temperature to normalize for the effect of the temperature dependence of the total magnetization (arising from the population difference between nuclear spin levels, Curie's law[13]) on the S/N ratio. In this normalization the direct temperature dependence of the measured S/N ratios is removed completely. Therefore, at this point the normalized S/N ratio should have contributions *only* from the relaxation processes (and possible experimental errors). These normalized S/N ratios are plotted versus temperature in Fig. 3.17-(b). This figure shows that the normalized S/N ratios have a well-defined temperature dependence, with a functional form very similar to that for the relaxation times. The temperature dependence of the normalized S/N ratios for the mixtures with 1.97% D_2 is in even better agreement with that of the T_1 values than is found for the T_2^* results. However, the standard deviations of the fits are larger, especially for the mixture with 1.97% D_2 at 13.84 amagat.

To complete the discussion on the measured S/N ratios, two more points should be considered. First, the loss of signal during the dead-time of the LC circuit is larger (in relative scale) when transverse relaxation is faster, *i.e.*, when the transverse relaxation time is shorter. Thus, the relative error due to this loss is larger at higher temperatures. Second, two species are responsible for the observed signal: these are *ortho*($I = 2$)- and *para*-D_2, so that the ratio of the total magnetizations, M_{ortho}/M_{para}, is equal to 5 at all temperatures used in these experiments. However, the loss of signal during the dead-time of the LC circuit is not constant, and de-

pends on the relative values of the relaxation times of the two species: the larger the difference in the relaxation times, the more unbalanced is the loss of the magnetization of the two species. Because the difference between the relaxation times of the two species is larger at lower temperatures (this will be discussed in detail later), relatively large deviations are to be expected for the temperature dependence of the normalized S/N ratios.

The error bars of the raw S/N ratios are of the order of ± 1. The relative error bars of the normalized S/N ratios are larger than those of the raw S/N ratios by the sums of the corresponding relative errors in the D_2 mole fraction and the mixture density, plus twice the relative error in the temperature, for a maximum relative error of $\simeq 4\%$. However, the calculated error bars do not cover the observed large deviations from a smooth temperature dependence in the normalized S/N ratios of the mixture with 1.97% D_2 at 13.84 amagat (and for a few points obtained for the other mixtures.) The major experimental error that could decrease the S/N ratios very effectively, if it occurs, is diffusion of the magnetization from the effective volume of the receiver coil. Such a process, which has an exponential temperature dependence, creates a bi-exponential relaxation of magnetization. From the normalized S/N ratios given in Fig. 3.17-(b), no sign of exponential temperature dependence is observable. The possibility of the contribution to the relaxation of magnetization from the diffusion process will be discussed in chapter 5. The difference between the chemical shifts of the *ortho*-D_2 and *para*-D_2 is very small, and has no measurable effect on the S/N measurement. Other experimental errors, such as errors in pulse length calibration, use of different acquisition times, and the temperature dependence of the noise level, contribute to error in the S/N measurement.

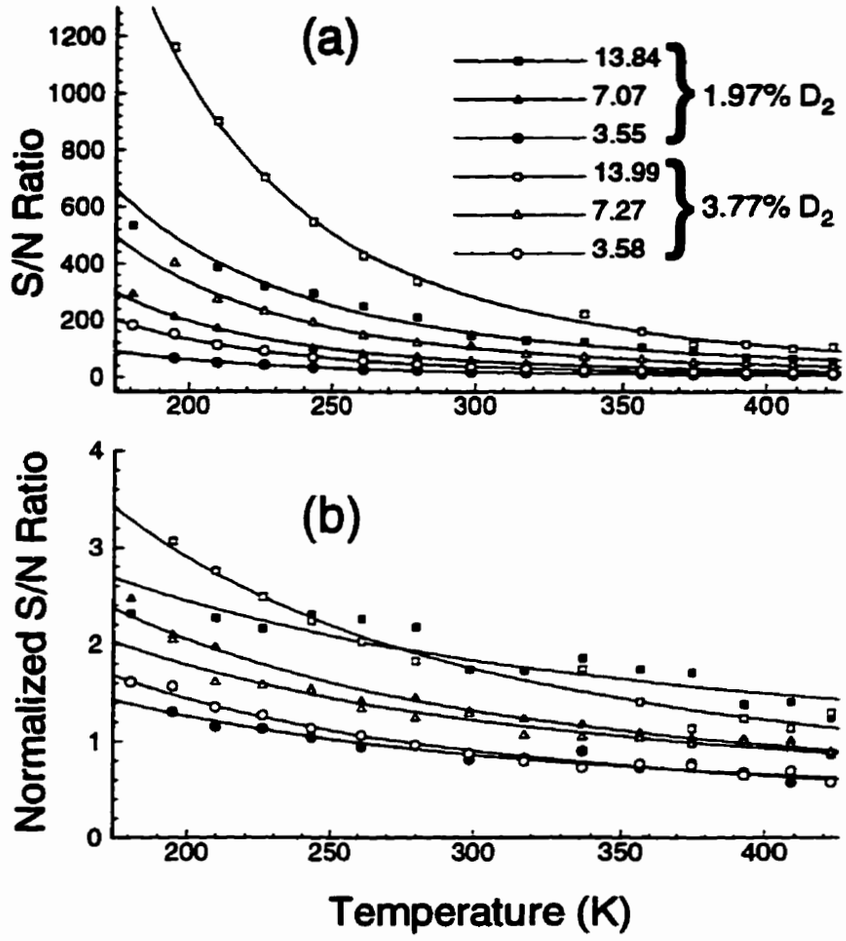

Figure 3.17: (a) Temperature dependence of the signal-to-noise ratios for the deuteron peak in D_2–Ar mixtures. (b) The same as (a) but normalized for one L_0 number density and 1% D_2 in Ar (equivalent to $0.01L_0$ partial number density for D_2), and for 1000 K temperature. Solid and hollow symbols are used for mixtures with 1.97% and 3.77% D_2, respectively. The fitting curves in (a) are of the form $y = a + bT^c$ in which a and b are positive parameters while c is more or less the same for all data sets, i.e $\simeq -3.0$. Compare the functional form of the normalized S/N ratios with the relaxation time curves in Fig. 3.16-(b). Both (a) and (b) are normalized for 256 scans. The error bars of the measured S/N ratios are of the order of ± 1. The error bars of the normalized S/N ratios can be calculated accordingly using the error bars of the amagat densities, the D_2 mole fractions and of the temperatures. The horizontal error bars for all temperatures are about ± 1 K.

Impurity test

As a test for possible impurities (whether original or from the sample preparation step) proton spectra were obtained at all temperatures for the mixture with 3.77% D_2 in Ar at 13.99 amagat. The only observable peak in these spectra was a very weak triplet. The maximum value of the S/N ratio for this peak, which happened at the bottom of the temperature range, was measured to be 21 for 256 scans. The S/N ratio and the resolution of these proton spectra decreased with increasing temperature, such that the triplet peaks could not be resolved for temperatures above 270 K, and vanished completely above 340 K. As mentioned earlier, according to the supplier of the D_2 gas, HD is the major impurity. Thus, the triplet peak in the proton spectra should be attributable to the HD impurity in the D_2 gas. This conclusion is supported by the measured values of the spacing between the triplet peaks, *e.g.*, 43 Hz at 180.67 K, which is consistent with the value of the proton-deuteron coupling constant, J_{HD}, measured from the proton and deuteron spectra of HD in HD–Ar mixtures (See Sec.3.2.1). As a further test, proton spectra were obtained while decoupling the deuteron. Decoupling of the deuteron replaced the proton triplet with a singlet peak located exactly at the center of the triplet, with a larger S/N ratio (at least doubled). Typical deuteron-coupled and deuteron-decoupled proton spectra for D_2–Ar mixtures are shown in Fig. 3.13-(b). Both spectra have been obtained with 256 scans. The S/N ratios and the peak-widths for the coupled and decoupled spectra are 21 and 28 Hz, and 50 and 35 Hz, respectively. Inspection of the coupled spectra shows that the spacing between the central and high frequency peaks was filled partially with another yet weaker peak which cannot be resolved from the HD triplet. However, it can be estimated that this peak is centered approximately halfway between the central and high frequency peaks of the triplet. According to Beckett and Carr,[70] the proton chemical shielding in HD is

about 0.036 ppm more than that in H_2 (see also Neronov *et al.*[42]). In the 11.75 Tesla field used in the present work, this is equivalent to a $\simeq +18$ Hz shift for the proton peak of H_2 with respect to the center of the HD triplet, which is approximately halfway between the central and high frequency peaks. This suggests that the non-resolvable peak overlapping the HD triplet can be attributed to the proton of an H_2 impurity.

The deuteron peak of the HD impurity could not be observed in the deuteron spectra. Further, decoupling of the proton had no observable effect on the deuteron spectra. This shows that the contribution of the HD deuteron to the signal is not observable, and hence is negligible. This was expected, since for HD the signal of the deuteron is at least 20 times weaker than that of the proton (See Tables 3.2 and 3.3). Thus, the deuteron peak would have a maximum S/N ratio of $\simeq 21/20$ or $\simeq 1$ (corresponding to the D_2–Ar mixture with 3.77% D_2 at 13.99 amagat and 180 K). Such a weak signal can hardly be resolved from the noise of the spectrum, especially when overlapping the very strong peak of the D_2 deuteron which has a S/N ratio of 1257 under the same conditions.

In conclusion, it can be said that these observations verify the impurities in the deuteron gas given by the supplier, and also show that no other species exist in the prepared mixtures. Another interesting result of these impurity test experiments is that HD-Ar mixtures containing as low as $0.4\% \times 3.77\%$ or 0.015% HD can be studied by proton NMR at low temperatures. This is in agreement with what had been predicted from the results of the preliminary studies on the HD–Ar mixtures (See Sec. 3.2). The experimental results obtained for such mixtures can be regarded as infinite dilution results, and should be directly comparable with theoretical results.

3.3.2 NMR spin-lattice relaxation time measurements for the deuteron of D_2 in D_2–Ar mixtures.

After optimizing the NMR parameters on the deuteron one-dimensional spectra of the D_2–Ar mixtures at each temperature, the inversion-recovery method was used to measure the deuteron longitudinal relaxation times. Since the D_2–Ar mixtures studied here contain *normal*-D_2, two species, namely *ortho*-D_2 and *para*-D_2, both contribute to the nuclear magnetization. Relative population, n_k, and the fractional contribution to the total magnetization, f_k, of the parity isomer k are given, respectively, by

$$n_k = \frac{g_k P_k}{\sum_l g_l P_l} \qquad \text{and} \qquad f_k = \frac{I_k(I_k+1) g_k P_k}{\sum_l I_l(I_l+1) g_l P_l}, \tag{3.5}$$

in which g_k, the nuclear spin multiplicity, is given by $g_k = 2I_k + 1$, and P_k is the sum of the pure rotational population factors for the levels coupled to the nuclear spin system of isomer k with spin I_k. For D_2, P_k is the total rotational probability either of the *even* rotational levels for *ortho*$(I = 0, 2)$-D_2, or of the odd rotational levels for *para*$(I = 1)$-D_2. Since only the ground vibrational level is accessible at the temperatures used in this study, vibrational averaging is not required in Eq. (3.5). At thermal equilibrium in the high temperature region, which starts at $\simeq 160$ K for D_2 (see Fig. 4.24), total probabilities for the *even* and *odd* rotational levels become equal. This results in the values $\frac{1}{9}, \frac{5}{9}$ and $\frac{3}{9}$ for the relative populations, and $\frac{0}{36}, \frac{30}{36}$ and $\frac{6}{36}$ (or $0, \frac{5}{6}$ and $\frac{1}{6}$) for the relative contributions to the total magnetization of *ortho*$(I = 0)$-D_2, *ortho*$(I = 2)$-D_2 and *para*$(I = 1)$-D_2, respectively. Since, of the two *ortho* isomers only *ortho*$(I = 2)$-D_2 contributes to the total magnetization, from now on, unless it is stated otherwise, the *ortho*$(I = 0)$-D_2 isomer is excluded from discussion and the *ortho*$(I = 2)$-D_2 isomer will be referred to for simplicity

as *ortho*-D_2. It should be mentioned here that all of the temperatures used in this study fall within the high temperature region. The population ratios and relative contributions to the magnetization would remain constant, even at lower temperatures , since the *ortho-para* conversion rate for D_2 is extremely slow,[67] and does not have any significant effect during the measurement period.

As mentioned in the previous section, the chemical shifts of *ortho*-D_2 and *para*-D_2 are so close that their peaks cannot be resolved in any of the one-dimensional deuteron spectra obtained for the D_2–Ar mixtures. However, the relaxation times of the two isomers are significantly different.[24,55] This difference depends on the temperature and density of the mixture.

In a system consisting of two or more species with the same Larmor frequency, but with different relaxation times, the total magnetization of the system recovered at a time τ in an inversion-recovery method is given by the sum of all individual magnetizations recovered at that time. For D_2 this summation gives

$$M_{t\tau} = \sum_i M_{i\tau} = M_{o\tau} + M_{p\tau}, \tag{3.6}$$

in which the subscripts o and p denotes the *ortho* and *para* isomers, respectively. Use of Eq. (1.4) for $M_{o\tau}$ and $M_{p\tau}$ gives the total magnetization as a function of τ as

$$M_{t\tau} = M_{o\infty}[1 - 2\exp(-\frac{\tau}{T_{1o}})] + M_{p\infty}[1 - 2\exp(-\frac{\tau}{T_{1p}})]. \tag{3.7}$$

Dividing the two sides by the total equilibrium magnetization, $M_{t\infty} = M_{o\infty} + M_{p\infty}$,

the above equation can be rearranged to give

$$\frac{M_{t\tau}}{M_{t\infty}} = 1 - 2f_o \exp(-\frac{\tau}{T_{1o}}) - 2f_p \exp(-\frac{\tau}{T_{1p}}), \tag{3.8}$$

in which, $f_o = \frac{M_{o\infty}}{M_{t\infty}}$ and $f_p = \frac{M_{p\infty}}{M_{t\infty}}$, the fractions of the total equilibrium magnetization produced by *ortho*-D_2 and *para*-D_2 are given by Eq. (3.5). For the temperature range used in the present study f_o and f_p are independent of temperature, and have the values $\frac{5}{6}$ and $\frac{1}{6}$, respectively, see Sec.4.5.3. Equation (3.8) shows that the relaxation of the total magnetization of D_2 in an inversion-recovery method is bi-exponential. Thus, in principle a bi-exponential function should be fitted to the inversion-recovery data points to extract the relaxation times of the two parity isomers correctly. However, a bi-exponential curve-fitting requires a larger number of parameters, which reduces the accuracy of the fitting procedure, and increases the standard deviation of the fit due to the non-linear relationship between the fitting parameters. This is especially the case when the difference between the two relaxation times is not sufficiently large (see Sec. 4.5). If a larger number of τ values is used, the accuracy of such a bi-exponential fitting will be increased. To decrease the standard deviation of the fitting by 50%, the number of data points of the recovery curve, *i.e.*, the number of τ values, should be increased by a factor four. This increases the total measuring time by the same factor. Timewise, such a solution seems to be uneconomical, even though it is the only way to extract the individual relaxation times of the two isomers more accurately. If the values of T_{1o} and T_{1p} are significantly different (by at least a factor of five), however, they can be extracted with a much smaller apparent standard deviation by dividing the recovery curve into two parts and fitting a single-exponential function of the form of Eq. (3.1) to each part. In such a case, increasing the number of τ values by a

factor two would allow extraction of the two relaxation times with the same degree of accuracy as is found for a single-exponential fit to the inversion-recovery curve of a single species system.

The values of T_1 obtained via fitting the inversion-recovery data to a single-exponential function do not have a corresponding theoretical expression derivable for the D_2 system. Such a relaxation time, which will be called T_1^*, is related to the individual relaxation times of the two isomers (and defined) by

$$\exp\left(-\frac{\tau}{T_1^*}\right) = f_o \exp\left(-\frac{\tau}{T_{1o}}\right) + f_p \exp\left(-\frac{\tau}{T_{1p}}\right). \tag{3.9}$$

Of course, such a relationship is valid only for a single value of τ, as Eq. (3.9) has a single root for τ. However, under two conditions this definition can be applied for all of the inversion-recovery data points within an acceptable approximation. One of these two conditions is that the values of the two individual relaxation times should be close to one another. The effect of this condition can be understood easily by considering the limiting case of equal relaxation times, which leads to $T_1^* = T_{1o} = T_{1p}$. The other condition is the use of a limited range for the τ values. A narrower range of τ values decreases the standard deviation of the single-exponential fit, but increases the deviation of the fitting parameters from their ideal values. Except for the limiting case of $T_1^* = T_{1o} = T_{1p}$, the measured T_1^* from a single-exponential fitting has no corresponding physical property, and serves only as an index for the relaxation of the overall magnetization. Since *ortho*-D_2 is the major contributor to the total magnetization (and has a longer relaxation time), the measured T_1^* can be also regarded as a rough estimate of the relaxation time of the *ortho*-D_2 isomer.

At this point it may seem that there is no way to compare directly the experi-

mental and theoretical results for the case of the D_2–Ar system. But, in Sec. 4.5.3 it will be shown that this is not quite the case; a comparison can be made in two different ways. One of these two ways is to generate single-exponential relaxation times, T_1^*, from the calculated relaxation times of the two isomers using the definition of T_1^* given in Eq. (3.9). These relaxation times can then be compared with corresponding experimental single-exponential relaxation times. The rest of this section deals with the details of the T_1^* measurement from the inversion-recovery curves.

One important point in establishing the NMR experimental parameters for these measurements is the estimate of the required relaxation delay times from the measured values of T_1^*. Since T_{1o} is longer than T_1^* under all experimental conditions, the relaxation delay time should be set such that the *ortho*-D_2 magnetization is recovered completely by the time the next scan starts. It can be estimated roughly that the ratios $\frac{T_{1o}}{T_1^*}$ and $\frac{M_{o\infty}}{M_{t\infty}}$ are of the same order of magnitude (but not essentially equal). Thus the relaxation delay time is set to be at least $20(\frac{6}{5})T_1^*$. This precaution seems not to be very critical, as the measured T_1^* and the longest T_1 of the component magnetizations are close to one another. However, for other systems with smaller fraction of the slow relaxing component, this may become very important.

Throughout these measurements, sixteen τ values have been used to map out the magnetization recovery curve from which the T_1^* values are measured by fitting to a single-exponential inversion-recovery function as given in Eq. (3.1). The deuteron T_1^* values obtained for the D_2–Ar mixtures are plotted versus temperature in Figs. 3.18. As can be seen from this figure, the measured values of T_1^* for all D_2–Ar mixtures show a well-behaved temperature dependence. Also, no local extrema or anomalous behavior is observed in the temperature dependence of the T_1^* curves. From Fig. 3.18 it can also be seen that the error bars of the T_1^* values are

rather small, even smaller than those obtained for the deuteron T_1 of the HD–Ar mixtures. As for the HD–Ar mixtures, these error bars are taken to be ± 3 (or 6) times the standard deviation of the single-exponential fit. Further, the values of the fitting parameters A and B obtained for these single-exponential fits are closer to the ideal value 1. These results show that the single-exponential relaxation times, T_1^*, describe the relaxation behavior of the total magnetization rather accurately. Thus, it can be concluded that the ratio $\frac{T_{1o}}{T_{1p}}$ is much smaller than the values that would lead to large error bars in the fitting of a single-exponential function to the original bi-exponential inversion-recovery curves (*i.e.*, less than 5). However, the error bars obtained for the values of T_1^* at low temperatures are unexpectedly large. The source of these large error bars cannot be the S/N ratio of the deuteron peaks, as they are sufficiently high at low temperatures. The source of these large error bars can thus only be the bi-exponential relaxation enhanced by the increasing difference between the two relaxation times T_{1o} and T_{1p} at low temperatures, which increases the standard deviation of the single-exponential fitting. This conclusion can be justified by considering the contribution of the rotational levels in the NMR relaxation of the two isomers. The lowest rotational level for *ortho*-D_2, the $j = 0$ level, has zero rotational angular momentum, and does not contribute directly to the relaxation of the nuclear magnetization. Decreasing the temperature decreases the populations of the higher rotational levels, *i.e.*, increases the population of the $j = 0$ levels. This decrease increases the relaxation time of *ortho*-D_2 significantly. For *para*-D_2, however, the lowest rotational level, $j = 1$, contributes directly to the relaxation of the nuclear magnetization at all temperatures, and no similar behavior can occur. The overall effect of the decrease in temperature is an unequal change in the relaxation times of the two isomers, which leads to a larger difference between the values of T_{1o} and T_{1p}. This larger difference between the two relaxation

times is undesirable in the T_1^* measurement, and thus increases the standard deviation of the fit. At higher temperatures, where the population of the $j = 0$ level of the *ortho* isomer becomes smaller, the two relaxation times become closer and hence the standard deviation of the single-exponential fit decreases, as can be seen from Fig. 3.18. At sufficiently high temperatures, in which the population profile is centered at higher rotational levels (*e.g.*, $j > 5$), the relaxation times of the two isomers are expected ideally to become equal. From comparing the rotational population profiles of the two isomers it can also be concluded that, in general, the deuteron relaxation time for *para*-D_2 is shorter than that for *ortho*-D_2.

To test the possibility of separation of the recovery curves of the *ortho*-D_2 and *para*-D_2, inversion-recovery experiments were performed on a mixture of 1.97% D_2 in Ar at 11.36 amagat (This mixture is not listed in Table 3.4.) for three temperatures: 237, 298 and 363 K. In these experiments 48 τ values were used. Using the relaxation-time information obtained in the previous experiments, these τ values were selected such that the recovery curves of both components are sampled perfectly. In the T_1 measurement process, the recovery data points were divided into two data sets such that each data set covers mostly the range of the recovery curve of one component. Next, a single-exponential fitting was used to extract the T_1^* value for each data set. For all three temperatures, the results obtained separately for the two parts of the recovery curve were close to that obtained by fitting the whole range of the recovery curve, but in each case with larger standard deviations. The same test experiment was performed on the D_2–Ar mixture with 3.77% D_2 at 3.58 amagat and 180 K, but with 32 τ values. In this case too, no acceptable results were obtained. Thus it can be said that, under the conditions of the present study, use of a larger number of τ values will not help separate the inversion-recovery curves of the two isomers of D_2.

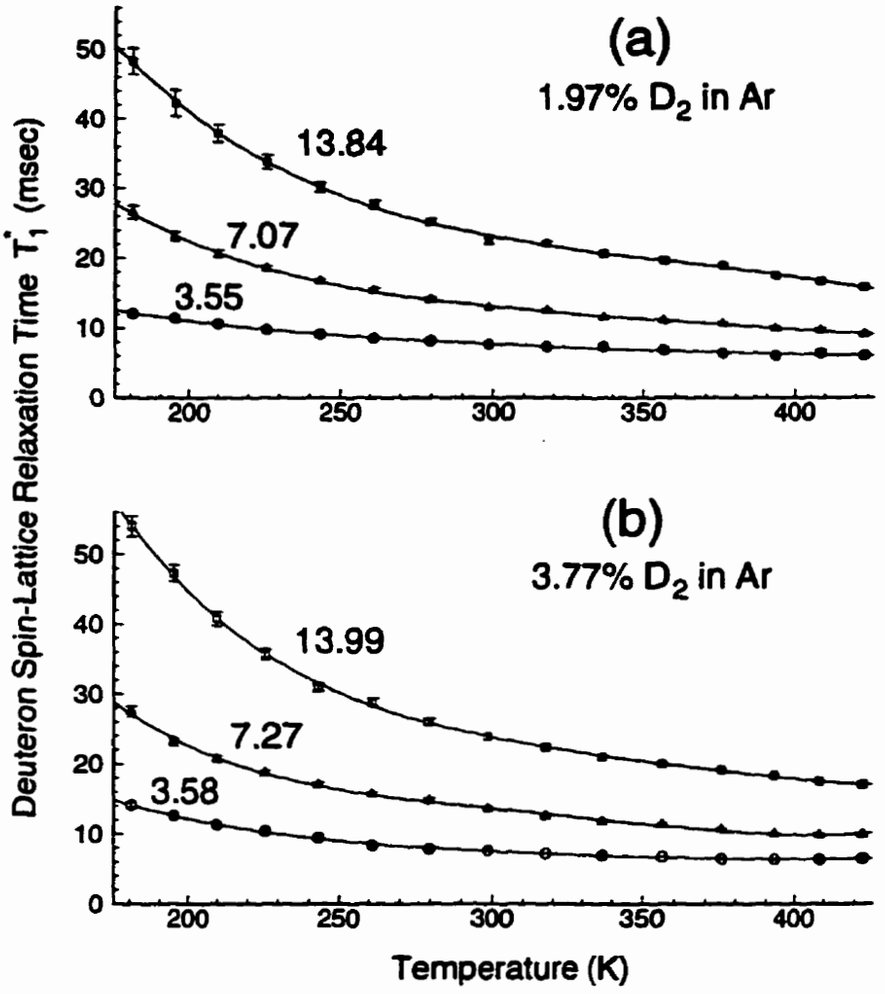

Figure 3.18: Spin-lattice relaxation times, T_1^*, for the deuteron of D_2 in D_2–Ar mixture obtained from single-exponential fits. The number beside each curve indicates the amagat density of the corresponding D_2–Ar mixture. These relaxation times are measured using the inversion-recovery method. See the text for the discussion of the trend of the error bars. The horizontal error bar for all temperatures is about ± 1 K. See Appendix A.3 for numerical values of the temperatures and relaxation times (the T and $T_1^{(1)}$ columns, respectively). The inversion recovery points, *i.e.*, the (τ, M_τ) pairs, from which these single-exponential (effective) relaxation times have been measured, can be found in the *ftp* site given in Ref. 103.

Figure 3.18 shows that the error bars obtained for the T_1^* values at lower densities are generally smaller. It can be concluded that the values of the relaxation times of the *ortho*-D_2 and *para*-D_2 are closer at lower densities. The error bars of the T_1^* values have the same temperature dependence at all densities, *i.e.*, increasing with decreasing temperature. Further discussion of the temperature and density dependences of T_1^* for the deuteron of D_2 in D_2–Ar mixtures will be presented in Sec. 5.3, where the experimental and theoretical results for the D_2–Ar mixtures are compared. The mole fraction dependence of the T_1^* values is discussed in Sec. 5.6.

Figure 3.19 compares values of T_1^* and T_2^* obtained for the D_2–Ar mixtures with 3.77% D_2 at three different amagat densities. This figure shows that T_1^* and T_2^* have almost the same temperature dependence. The agreement between the values of the two relaxation times is better at intermediate temperatures.

Numerical values of the raw and adjusted (see Ch. 5) single-exponential spin-lattice relaxation times obtained for the deuteron of D_2 in D_2–Ar mixtures can be found in Appendix A.3. The experimental raw data, *i.e.*, recovery delay times and normalized magnetizations in the form of (τ, M_τ) pairs, are saved in a computer data file which can be obtained via *ftp*.[103]

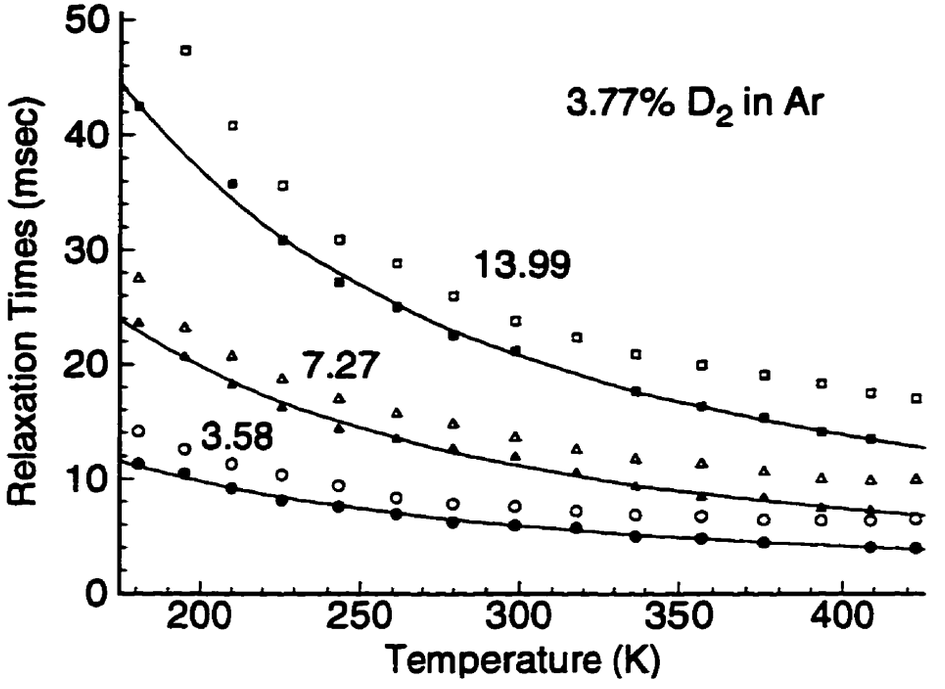

Figure 3.19: Comparison between the measured values of T_1^* and T_2^* for the deuteron of D_2 in a mixture of 3.77% D_2 in Ar at 13.99 amagat (squares), 7.27 amagat (triangles) and 3.58 amagat (circles) densities, respectively. The hollow and filled symbols show the measured values of T_1^* and T_2^*, respectively. The numbers beside each data set indicates the amagat density of the corresponding D_2–Ar mixture. The fitting curves connect the measured values of T_2^*. Note the agreement of the temperature dependences of the two relaxation times. Also note that the differences between them are (perhaps unexpectedly) small. Such small differences suggest that the experimental contribution to the effective transverse relaxation time is very small, and also that the values of T_1^* and T_2 are very close. This figure also shows that the agreement between the two values is better at intermediate temperatures. The error bars of the relaxation times are not shown for simplicity. The horizontal error bar at all temperatures is about ± 1 K.

Chapter 4

Theoretical Calculations of Spin-Lattice Relaxation Times for the HD–Ar and D_2–Ar Systems

In this chapter, procedures for and results of theoretical calculations of the spin-lattice relaxation times for the HD–Ar and D_2–Ar systems are presented. Explicit expressions for the various components of the spin-lattice relaxation times for the nuclei of the diatomic partner of the atom-diatom collision system will be presented and analyzed in Sec. 4.1. The governing parameters and their effects on the results of the calculations will be discussed briefly in Sec. 4.2. A description of the exchange-Coulomb (XC) potential energy surface XC(fit) determined by Bissonnette *et al.*[8] for the hydrogen–argon system is given in Sec. 4.3. This is the potential energy surface used in the present calculations. Close-coupled calculations of the opacities, effective cross sections and their thermal averages, and finally, calculations of the spin-lattice relaxation times for the proton and deuteron of HD in the HD–Ar system, and for the deuteron of the two parity isomers of D_2 in the D_2–Ar

system, are presented and discussed in Secs. 4.4 and 4.5, respectively. For each system, the dependence of the spin-lattice relaxation times on temperature, density and magnetic field strength is investigated separately. Calculation of the total magnetization and its relaxation time in mixtures of the two parity isomers of the D_2–Ar system are presented in Sec. 4.5.3.

4.1 Expressions for the relaxation times

Application of the kinetic theory briefly described in Ch. 1, to the atom-diatom system Z–XY results in the following equations for the components of the spin-lattice relaxation time for the X nucleus.[2,23]

$$(T_{1SR}^{X})^{-1} = \frac{2}{3}(\omega_{SR}^{X})^2 n\bar{c}_r \mathbf{d}_t^{(1)}.\boldsymbol{\sigma}_V.[(n\bar{c}_r)^2\boldsymbol{\sigma}_V.\boldsymbol{\sigma}_V + (\omega_B^{XY} - \omega_I^X)^2\boldsymbol{\delta}]^{-1}.\boldsymbol{\rho}.\mathbf{d}^{(1)}, \quad (4.1)$$

$$(T_{1D}^{X})^{-1} = \frac{2}{45} I_Y(I_Y+1)(\omega_D^{XY})^2 n\bar{c}_r \mathbf{d}_t^{(2)}.\boldsymbol{\sigma}_T.\{[(n\bar{c}_r)^2\boldsymbol{\sigma}_T.\boldsymbol{\sigma}_T + (\omega_B^{XY} - \omega_I^X)^2\boldsymbol{\delta}]^{-1} + 4[(n\bar{c}_r)^2\boldsymbol{\sigma}_T.\boldsymbol{\sigma}_T + 4(\omega_B^{XY} - \omega_I^X)^2\boldsymbol{\delta}]^{-1}\}.\boldsymbol{\rho}.\mathbf{d}^{(2)}, \quad (4.2)$$

$$(T_{1Q}^{X})^{-1} = \frac{1}{5}(\omega_Q^{X})^2 n\bar{c}_r \mathbf{d}_t^{(2)}.\boldsymbol{\sigma}_T.\{[(n\bar{c}_r)^2\boldsymbol{\sigma}_T.\boldsymbol{\sigma}_T + (\omega_B^{XY} - \omega_I^X)^2\boldsymbol{\delta}]^{-1} + 4[(n\bar{c}_r)^2\boldsymbol{\sigma}_T.\boldsymbol{\sigma}_T + 4(\omega_B^{XY} - \omega_I^X)^2\boldsymbol{\delta}]^{-1}\}.\boldsymbol{\rho}.\mathbf{d}^{(2)}, \quad (4.3)$$

in which superscripts X and Y denote the corresponding quantities for the X and Y nuclei, while subscripts SR, D and Q denote the corresponding quantities for the spin-rotation, dipolar and quadrupolar interactions, respectively. Also, I_Y is the spin quantum number of nucleus Y, and ω_i^X is the coupling constant of the interaction i (SR, D, Q) for nucleus X. The quantities ω_B^{XY} and ω_I^X are Larmor

(angular) frequencies of the precession of the rotational angular momentum of the diatom and spin angular momentum of the nucleus X around the direction of the static magnetic field, B_0, and are given respectively by $\omega_B^{XY} = (\mu_N g_{rot}^{XY}/\hbar)B_0$ and $\omega_I^X = (\mu_N g_I^X/\hbar)B_0$, in which μ_N is the nuclear magneton, while g_{rot}^{XY} and g_I^X are rotational and nuclear spin *g-factors*, respectively, and $\hbar$ is the Planck's constant divided by 2π. The nuclear spin g-factor is related to the magnetogyric ratio, γ, by $\gamma_X = \mu_N g_I^X/\hbar$. The average relative velocity, $\bar{c}_r$ is given by $(\frac{8kT}{\pi\mu})^{1/2}$, in which μ is the reduced molecular mass of the collision complex, $\mu = (m_{XY}^{-1} + m_Z^{-1})^{-1}$, and k is the Boltzmann constant. Also, n is the number density of Z.

The elements of the diagonal matrix $\boldsymbol{\rho}$ are per state fractional populations of the rotational states, *i.e.*,

$$\rho(j,j') = \delta_{j,j'}\frac{p(j)}{2j+1} = \delta_{j,j'}\left(\frac{\exp(-\frac{E_j}{kT})}{\sum_i (2i+1)\exp(-\frac{E_i}{kT})}\right), \tag{4.4}$$

with E_i being the energy of the ith rotational state. The jth elements of the $\mathbf{d}^{(1)}$ and $\mathbf{d}^{(2)}$ column vectors are given respectively by

$$d^{(1)}(j) = [(2j+1)j(j+1)]^{\frac{1}{2}} \tag{4.5}$$

$$d^{(2)}(j) = \left[\frac{(2j+1)j(j+1)}{6(2j+3)(2j-1)}\right]^{\frac{1}{2}}, \tag{4.6}$$

and $\mathbf{d}_t^{(1)}$ and $\mathbf{d}_t^{(2)}$ are row versions (transposes) of $\mathbf{d}^{(1)}$ and $\mathbf{d}^{(2)}$, respectively. Definitions of the cross section matrices $\boldsymbol{\sigma}_V$ and $\boldsymbol{\sigma}_T$ are given in Ch. 1.

For the case of the atom-homonuclear diatom system, the SR relaxation time is exactly the same as in Eq. (4.1). However, equations for the dipolar and quadrupolar relaxation times are different. For the *ortho* parity isomer of the homonuclear

diatom with a spin 1/2 nucleus, the dipolar relaxation time has the same form as Eq. (4.2) with the exception that the factor $I(I+1)$ is omitted. No quadrupolar interaction exists for a spin 1/2 nucleus. Note also that the *para* parity isomer of such a diatom is not NMR active. For the case of a homonuclear diatom with a spin 1 nucleus, the dipolar and quadrupolar intermolecular interactions between the nuclear spin and the rotational angular momenta are coupled (*i.e.*, they are not separable). The equation for the spin-lattice relaxation time of the coupled interaction, which is denoted by T_{1DQ}, has the same form as Eq. (4.3), with the difference that the quadrupolar coupling constant ω_Q^X is replaced by the coupled dipolar-quadrupolar (DQ) coupling constant ω_{DQ}^X. The DQ coupling constants for the *para* and *ortho* isomers are given respectively by[55]

$$\omega_{DQ}^X(para) = \omega_Q^X + 2\omega_D^{XX} \tag{4.7}$$

and

$$\omega_{DQ}^X(ortho) = \left[(\omega_Q^X)^2 + \frac{4}{5}\omega_Q^X\omega_D^{XX} + \frac{12}{5}(\omega_D^{XX})^2\right]^{\frac{1}{2}}. \tag{4.8}$$

Note that in the notations used here ω_Q is defined by $\omega_Q = (\frac{3}{2})e^2q_{zz}Q/\hbar$, in which e is the charge of electron, Q is nuclear quadrupole moment, and q_{zz} is the electric field gradient along the z-axis (*i.e.*, the direction of the static magnetic field) at the site of nucleus.

The functional form of the density-dependence of the relaxation times is very simple. Evaluation of the density-dependence of the T_1 equations at a fixed temperature and field strength shows that the relaxation times at the two limits of $n \to 0$ and $n \to \infty$ are linearly proportional to n^{-1} and n, respectively. This requires existence of a minimum point in the T_1-density curves. The position of this minimum

depends on temperature and field strength as well as on the interaction potential via the cross sections. Such a minimum point in the T_1 curves corresponds to a match between the frequency of the collisions leading to the relevant transitions, $n\bar{c}_r\sigma$, and the Larmor frequency of the rotational angular momentum in the frame rotating at the Larmor frequency of the nucleus, *i.e.*, $(\omega_B^{XY} - \omega_I^X)$. Obviously, the position of this minimum for the T_{1SR} curve is different from those for T_{1D} and T_{1Q}, which are the same.

In contrast to the density-dependence, the temperature-dependence of the relaxation times is more complicated, due to the complex temperature-dependences of the cross section (σ) and the population (ρ) matrices. However, it can be shown numerically that the relaxation times are generally decreasing functions of temperature.

Equations (4.1)-(4.3) show that the relaxation times are increasing functions of the magnetic field strength B_0. This behavior cannot be derived from the T_1 equations analytically, but can be shown numerically. For the low temperature region in which only the first contributing rotational level is occupied, however, this behavior can be shown explicitly. Under such circumstance, all of the matrices involved in the T_1 equations become scalar. This results in a linear dependence of the relaxation times on the square of the field strength. This shows the dramatic effects of the field on the density-behavior of the relaxation times. For a system with a specific interaction potential the relative contribution of the field-dependent term $(\omega_B^{XY} - \omega_I^X)$ to the relaxation times of the nucleus X depends on density, temperature, and the potential (via the cross section matrix elements) as well as on the field strength and on the g_{rot}^{XY} and g_I^X. When n is relatively large or B_0 is small, this contribution becomes very small, and can be neglected. Under these conditions the T_1 equations are considerably simplified, and become field-independent linear functions of den-

sity. The region at which the spin-lattice relaxation times are linearly dependent on density is called the *linear-regime*. At high magnetic field strengths and/or low densities the system is in the *nonlinear-regime*. The limit of the linear-regime depends on all of the specifications and experimental parameters of the system mentioned above. For example, in the HD–Ar system the contributions to the relaxation times of the field-dependent term for the proton is significantly larger than that for the deuteron due to the larger magnetogyric ratio of the proton ($\gamma_H/\gamma_D = 6.5$). Thus, it can be expected that the linear-regime behavior for the deuteron relaxation times in the HD–Ar system to start at significantly lower densities.

4.2 Computer programs and their parameters

In the present work, the MOLSCAT program of Hutson and Green[104] has been used to carry out the CC calculation of the S-matrix elements. The determining parameters of these calculations, which are directly related to the system under study, are as follows:

a) The R-parameters: The lower and upper limits and the step-size of the radial integration (R_{min}, R_{max} and *STEPS*, respectively). The parameter *STEPS* is the number of points used for integration over a half-wavelength of the asymptotic wave-function. In order to obtain converged integrals (and thus accurate S-matrix elements), within an acceptable time, these parameters should be optimized carefully.

b) The j-parameters: The minimum, maximum and step-size of j (j_{min}, j_{max} and Δj, respectively). The determination of the j_{min} and Δj values is based on the symmetry and the parity of the diatom (*i.e.*, homonuclear versus het-

eronuclear and *ortho* versus *para*). The value of j_{max} is determined by the value of the total energy, and the desired number of closed channels. In the present study, j_{max} is set so as to include at least one level above the highest rotational level accessible at the total energy of the system.

c) The J-parameters: The minimum, maximum and step-size of J (J_{min}, J_{max} and ΔJ, respectively). J_{min} is usually set to zero, and the values of J_{max} and ΔJ are optimized based on the inspection of the J-dependent opacities calculated by the SBE (see below) program.

The latter two sets of parameters determine which elements of the S-matrix should be calculated by the program, and do not affect the accuracy of the calculated S-matrix elements. However, the J-parameters (J_{min}, J_{max} and ΔJ), particularly J_{max}, determine the accuracy of the state-to-state energy-dependent cross sections which are calculated from an averaging over J of the state-to-state J-dependent opacities. Also, the value of J_{max} indirectly affects the convergence of the radial integration of the S-matrix, since the optimum value of R_{max} at a fixed total energy increases with increasing J. However, if R_{max} is set sufficiently large, convergence of the radial integration of the S-matrix will be independent of the value of J_{max}.

Calculations of the J-dependent opacities from the S-matrix are carried out using the SBE program of Green.[105] The only input parameters for this program are the corresponding values of K_l', K_j', K_l and K_j for the desired cross section. All other information needed for this step of the calculations comes from the output of the MOLSCAT program, including the S-matrix elements. This program also averages the J-dependent opacities over J to calculate the energy-dependent cross sections.

For thermal averaging of the state-to-state energy-dependent cross sections, the CRAVE program of Thachuk[31,106] is used after some modifications. The core of this program consists of an integrator which uses several quadrature techniques, along with some interpolation and extrapolation estimations, to evaluate the relevant integrals more accurately. The quality of the results of thermal averaging depends on the number and distribution of the values of total energies at which the S-matrix is calculated. This dependence is especially crucial if the effects of orbiting resonances[107,108] on the energy-dependent cross sections are significant, as is found to be the case for the systems studied in this work. The number and values of the total energies should be set such that the resulting curves for the energy-dependence of the cross sections are well-behaved and integrable, and allow error-free extrapolations and interpolations when needed. Since it is not economical to increase the number of total energies as desired, an accurate selection of the total energy values is needed in order to guarantee the required accuracy in the final results. Since CC calculation of the energy-dependent cross sections at the lower end of the energy range is not expensive, the minimum value of the total energy can be (and rather should be) set as small as possible. The maximum value of the total energy depends on the desired temperature at which the corresponding physical properties are to be calculated. An energy of 5-10 times the average thermal energy of the system at the maximum temperature is usually sufficient to obtain high accuracies for the calculated physical properties. In the absence of orbiting resonances,[107,108] the best selection of the total energy values is the one with an equal number of energies per energy spacing between the rotational levels of the diatom. For each rotational level this selection should also include two energies as close as possible, one below and the other above the threshold energy for the rotational channel. Such a selection allows a complete and uniform sampling of the energy-dependence curves for

all elements of the cross section matrix, which in turn results in accurate thermal averaging.

In the presence of orbiting resonances an additional number of total energies should be included in order to map the functional forms of the energy-dependence of the cross sections in the resonance ranges completely. Otherwise, the numerical extrapolation and interpolation techniques will give incorrect answers for the resonance ranges which leads to incorrect values for the thermally-averaged cross sections. The number of energies in the resonance ranges becomes especially important should the most probable energy, *i.e.*, the maximum of the Boltzmann distribution function for the total energy, of the system fall into one of the resonance ranges. However, if the orbiting resonances are not strong, and the resonance ranges are not wide, their total contribution to the thermally-averaged cross sections can be neglected. Possible problems introduced by such resonances in the integration process can be eliminated by excluding those points of the energy-dependent curves falling in the resonance ranges, and using the same interpolation and extrapolation techniques used for other parts of the curves, to cover the resonance ranges.

Except for defining the parameters mentioned above and the study of their corresponding effects on the convergence and accuracy of the final results, the MOLSCAT and the SBE programs have been used as "black boxes". Some minor modifications, however, have been made on the CRAVE program, as the list of cross sections of the original version did not include the σ_V and σ_T (NMR) cross sections, which were required in the calculation of the NMR spin-lattice relaxation times.

The last step of the calculations consists of the calculation of the spin-lattice relaxation times from the thermally-averaged cross sections via Eqs. (4.1)–(4.3). Two FORTRAN programs named HDT1 and D2T1 have been written to carry out

these calculations for the HD–Ar and D_2–Ar systems, respectively.

4.3 XC(fit) potential energy surface for the hydrogen–argon system

The calculations of the spin-lattice relaxation times for the HD–Ar and D_2–Ar systems are based upon the fitted exchange-Coulomb potential, the XC(fit) potential, determined by Bissonnette *et al.*[8] for the hydrogen–argon system. The XC(fit) potential is a full three-dimensional state-of-the-art, highly accurate potential energy surface recommended for the prototypical hydrogen–argon system. The XC(fit) potential has been determined by introducing a number of adjustable parameters into a theoretical model potential called the exchange-Coulomb XC(0) potential. The theoretical model potential XC(0) is based upon the calculation of the energies of the first-order Heitler-London interaction, and second- and higher-order Coulomb interactions (including dispersion and induction) from high quality Self-Consistent Field theory (SCF) wave-functions[109] of the isolated closed-shell hydrogen molecule and argon atom. The fitting parameters of the XC(fit) potential are then adjusted (*i.e.*, optimized) by fitting the theoretical values of some particular physical properties calculated from the potential to their corresponding experimental data obtained for the H_2–Ar and/or D_2–Ar system(s). These properties are the pressure-shifting coefficients for the Raman transitions of H_2 in Ar, the second virial coefficient of H_2–Ar mixtures, and the high resolution infra-red transitions of the H_2–Ar and D_2–Ar Van der Waals complexes. The quality of the optimized XC(fit) potential has then been tested by calculating two phenomena which were not used in the optimization procedure of the potential (the elastic and inelastic differential scattering cross sections for D_2–Ar, and the frequencies of the hyperfine transitions of

the H_2–Ar complex), and comparing their calculated values with the experimental data. The theoretical results from the XC(fit) potential gave excellent agreement with the experimental data for both phenomena. Compared with other available potentials for the hydrogen–argon system, the XC(fit) potential is not only optimized with respect to the most accurate experimental data obtained recently, but also yields excellent predictions of properties which were not included in the optimization process. For details of the calculation of the XC(0) model potential and the optimization procedures for the XC(fit) potential, and comparison with other potentials, see Ref. 8.

The analytical form of the XC(fit) potential contains terms which have fundamental physical meaning, but it does not directly display the anisotropy of the potential, which is the origin of many physical properties of the hydrogen–argon system such as the NMR spin-lattice relaxation times studied here. Thus, it seems useful to convert this analytical form to a more suitable form for the present study. This conversion is explained below.

The XC(fit) potential can be described briefly as a function of three variables R, ξ and θ. The intermolecular distance R is the distance between the argon atom and the center-of-mass of the hydrogen molecule. The reduced stretching-length ξ is defined by $\xi = (r - r_0)/r_0$, in which r is the hydrogen bond-length and $r_0 = 1.448739a_0$ is the expectation value of r for H_2 in its ground rovibrational level. The angle θ is the orientation of $\mathbf{R}$ relative to the hydrogen bond-axis. The three variables are illustrated in Fig. 4.1 for the generic Z–XY system. Dependence of the XC(fit) potential on these variables is such that the analytical form of the potential can be expanded as

$$V(R,\theta,\xi) = \sum_{k=0}^{4} \xi^k U_k(R,\theta). \tag{4.9}$$

The variable ξ depends only on the vibrational motion of the diatomic molecule. Since the time scale of that vibrational motion is orders of magnitude shorter than that of the translational and rotational motions involved in the scattering process, the ξ^k terms in the expansion of V can be replaced safely by their quantum mechanical averages over the vibrational motion. For temperatures sufficiently high that excited vibrational levels of the hydrogen molecule are significantly occupied, a different potential may be calculated for each vibrational level for a given set of R and θ values, because the averages of ξ^k for different vibrational levels are different. An ensemble average over the occupied vibrational levels is valid only for those physical properties with longer time scales than that of the collision-induced transitions between vibrational levels. Since the maximum temperature used in the experimental part of the present study is much lower than that required for occupation of higher vibrational levels, such an ensemble averaging is not needed.

Replacing the ξ^k terms by their expectation values removes any bond-length dependence of the potential, and reduces the potential to $V(R,\theta)$. One useful analytical form which can be used to represent this potential is the expansion of the potential in terms of Legendre polynomials of $\cos\theta$ with R-dependent coefficients, *i.e.*,

$$V(R,\theta) = V(R,\cos\theta) = \sum_{\lambda} V_\lambda(R) P_\lambda(\cos\theta), \tag{4.10}$$

in which $P_\lambda(\cos\theta)$ is the Legendre polynomial of order λ. This form of the potential has a number of advantages, all due to the parity and orthonormality properties of the Legendre functions.[110] Symmetry of the potential with respect to the plane perpendicular to the diatom bond at its center-of-mass can be characterized by the parity of the Legendre components of the potential. A zero value for all odd

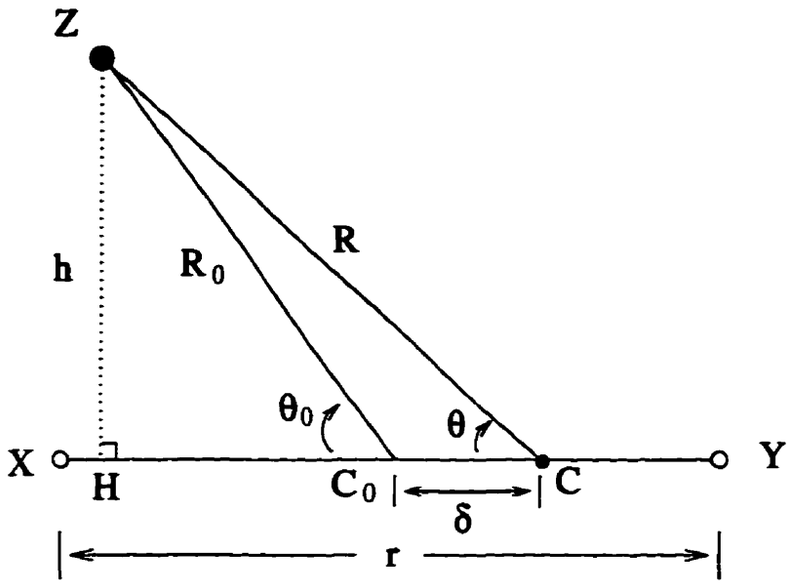

Figure 4.1: Internal coordinates for the generic atom-diatom system Z–XY; Variables of the XC(fit) potential. The subscript 0 represents the corresponding variables for a homonuclear diatom. In this figure δ is the displacement of the center-of-mass for the heteronuclear diatom (C) relative to that for the homonuclear isotopomers (C_0), which is the midpoint of the diatom bond (C_0).

Legendre components requires a mirror plane perpendicular to the diatom bond at its center-of-mass; this happens only for homonuclear diatoms, *e.g.*, the H_2, D_2 and T_2 isotopomers of hydrogen. The orthonormality of the Legendre functions eases the expansion of the potential, and also allows the potential to be used directly in the MOLSCAT program suite which makes extensive use of analytical properties of these polynomials in the calculations. Using orthonormality of the Legendre polynomials, the R-dependent coefficients of the Legendre expansion of the potential, $V_\lambda(R)$, which are also called radial strength functions, can be calculated using any

standard numerical integration technique via

$$V_\lambda(R) = \int_{-1}^{+1} V(R, \cos\theta)(\lambda + 0.5) P_\lambda(\cos\theta) d(\cos\theta), \tag{4.11}$$

in which the $(\lambda+0.5)$ factor is the normalization factor for the Legendre polynomial of order λ. The number of terms required in the Legendre expansion of the XC(fit) potential depends upon the accuracy required for the calculations. A four-term expansion gives accuracies better than 0.1%, which is sufficient for the present study. For heteronuclear diatoms, however, two additional terms are needed to obtain the same accuracy in the calculations.

To expand the XC(fit) potential in terms of the Legendre functions, the FORTRAN code of the subroutine generating the $U_k(R, \theta)$ coefficients of Eq. (4.9) has been obtained from LeRoy.[98] This subroutine was then incorporated into a FORTRAN program to generate numerical values of the potential for a given set of (R, θ) pairs for all isotopomers of hydrogen. The expectation values of the ξ^k terms required for these calculations were calculated by the program LEVEL.[96] Next, to carry out the integration given in Eq. (4.11), a Gauss-Legendre quadrature technique was used with 24 points (*i.e.*, 24 values for $\cos\theta$) equally spaced over the interval $(-1, +1)$. Numerical values of the potential were then calculated for wide ranges of R and θ, both from the original analytical form of the potential and from its Legendre-expanded form. For almost all values of R and θ the differences between the values of the potential obtained by these two procedures were less than 0.05% for all six isotopomers of hydrogen; four terms ($\lambda = 0$ to 6 and $\Delta\lambda = 2$) of the Legendre-expanded form were used for homonuclear, and seven terms ($\lambda = 0$ to 6 and $\Delta\lambda = 1$) for heteronuclear isotopomers.

For the homonuclear isotopomers of hydrogen, all odd-λ terms of the Legendre

expansion of the potential should be zero due to the symmetry of the potential with respect to the center-of-mass of the diatom (the midpoint of the bond). This can be regarded as a test for any potential proposed for an atom-diatom system, and a check point for the expansion procedure of the potential. The Legendre expansion of the XC(fit) potential derived for all three homonuclear isotopomers of hydrogen showed this property.

It should be noted here that the original analytical form of the potential was obtained for homonuclear hydrogen. Thus, for the Legendre expansion of the potential for the heteronuclear hydrogen isotopomers, *i.e.*, HD, HT and DT, it is necessary to transform the heteronuclear coordinates R and θ to the corresponding homonuclear coordinates denoted by R_0 and θ_0 in Fig. 4.1, from which the value of the potential is calculated as described above. This value is then used in Eq. (4.10) to derive radial strength functions $V_\lambda(R)$. All other terms in Eq. 4.1 are calculated using the heteronuclear coordinates.

Transformation of the coordinates of the XC(fit) potential from the heteronuclear case to the homonuclear case is carried out simply (See Fig. 4.1) via

$$R_0 = \sqrt{R^2 + \delta^2 - 2\delta R\cos\theta}, \qquad \cos\theta_0 = \frac{R\cos\theta - \delta}{R_0}. \tag{4.12}$$

In these equations δ is the displacement of the center-of-mass of the heteronuclear isotopomer with respect to the midpoint of its bond, and is given by

$$\delta = (\frac{r}{2})\frac{m_h - m_l}{m_h + m_l}, \tag{4.13}$$

in which r is the value of the bond-length (the same variable that appeared in the definition of ξ given above) while m_h and m_l are, respectively, the atomic masses of the heavier and the lighter atoms of the heteronuclear diatom. Values of δ for

HD, HT and DT are 0.1271, 0.1901 and 0.0755 Å, respectively.

Radial strength functions, V_λ, of the Legendre expansions of the XC(fit) potential derived for the D_2–Ar and HD–Ar systems are plotted versus R in Figs. 4.2 and 4.4, respectively. The dotted curves in these figures show the corresponding functions for an older version of the potential.* In part (b) of these figures the subsequent improvement in the Legendre expansion of the potential is plotted against R. As can be seen from these figures, the differences between the two versions of the XC(fit) potential are negligible for the region of the potential well and at long range. However, the two versions differ significantly at very short range, especially below 2.5 Å (far up the repulsive wall), which is thermally accessible only for very high temperatures. These parts of the curves are not shown in the figures. Relative values of the radial strength functions V_λ for a given value of the intermolecular distance R show the anisotropy of the potential at that distance: the larger the values of the higher-order radial strength functions the more anisotropic the potential. As can be seen from Figs. 4.2 and 4.4, the anisotropy of the potential decreases with increasing intermolecular distance.

A better view of the anisotropy of the potential may be obtained by analysis of the angular dependence of the potential at a few constant intermolecular distances, and analysis of the distance dependence of the potential at a few constant orientation angles. Angular and distance dependences of the XC(fit) potential for the D_2–Ar and HD–Ar systems (as representatives of homo- and heteronuclear isotopomers of the hydrogen–argon system) are shown in parts (a) and (b) of Figs. 4.3 and 4.5, respectively. These figures show directly the anisotropy of the XC(fit) potential for the two systems. A comparison between Figs. 4.3 and 4.5 shows that rotation of the diatom has a larger effect on the XC(fit) potential for the HD–Ar

*Unpublished August 1995 version of the potential.

system than it does on that for the D_2–Ar system, as can be expected. Figure 4.3-(a) explicitly shows the symmetry of the XC(fit) potential with respect to the plane normal to the diatom bond (corresponding to a vertical line at $\theta = 90°$) for the homonuclear diatom D_2. The same plot for the HD–Ar system does not show such a symmetry. Obviously, the potential for both systems has a cylindrical symmetry with respect to the diatom bond axis.

The intermolecular potentials for the vast majority of systems are anisotropic; the principal exception is the case of two closed-shell atoms. The degree of anisotropy of the intermolecular potential energy surface depends on the electronic structure of the interacting particles.

The FORTRAN program written for evaluation of the Legendre expansion coefficients in this section has been developed to be used as a potential read-in subroutine, called POTENL.F, for the MOLSCAT program. The subroutine returns the potential specifications in the first call, and the coefficients of the Legendre expansion of the potential for a specified distance R in subsequent calls by the main program. As mentioned above, this subroutine can be used for all isotopomers of hydrogen. A copy of this subroutine may be obtained from the *ftp* site set up by Le Roy.[111]

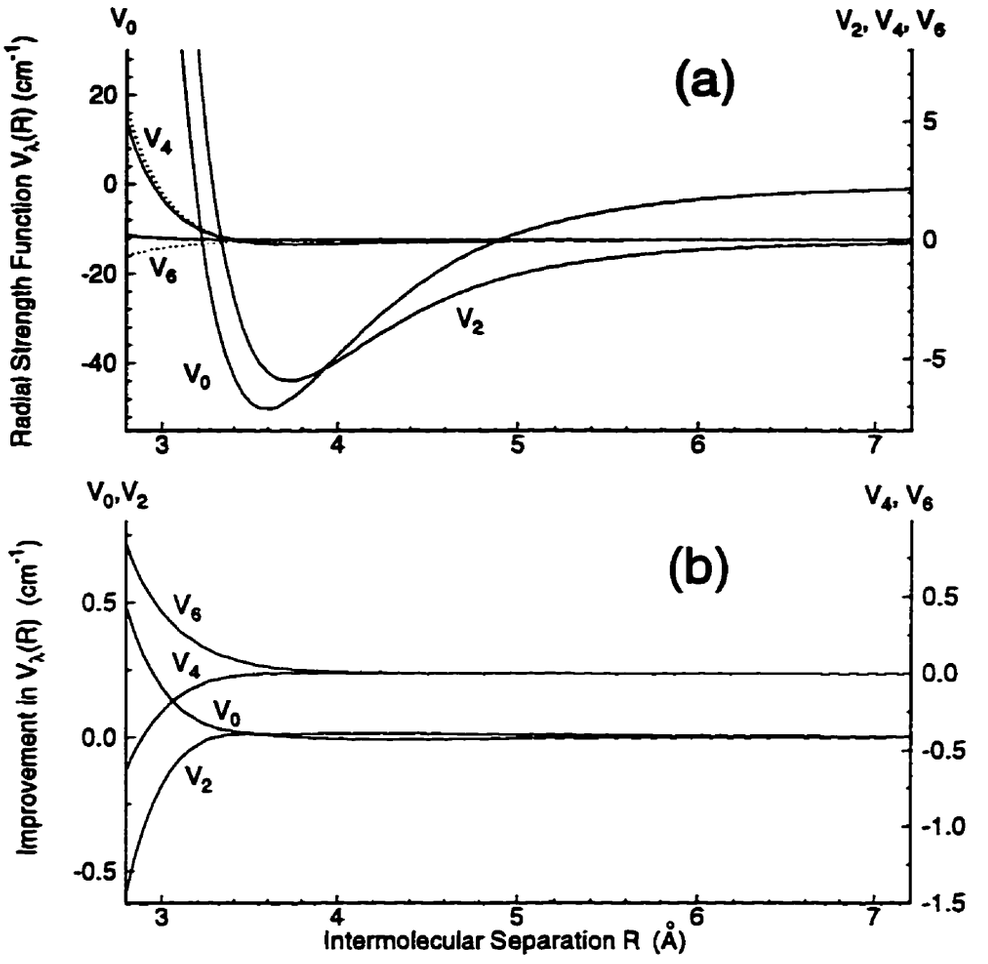

Figure 4.2: (a) Radial strength functions for the Legendre expansion of the XC(fit) potential for the D_2–Ar system. The dotted curves are the corresponding radial strength functions V_λ for an older version of the potential. Note the relative values of the functions, and their R-dependences. The total contribution to the potential of the higher-order Legendre components, that are not shown in this figure is of the order of a few percent of the contribution of the V_6 term for the region shown in this figure. This contribution is larger at shorter range. (b) Improvement in the potential, V(new) $-V$(old), in terms of the radial strength functions in cm^{-1}. It can be seen from this figure that the differences between the two versions of the potential at long range and on the attractive part of the potential well are negligible. At short range, however, this difference is significantly larger. Note the different scales used for individual components in both (a) and (b).

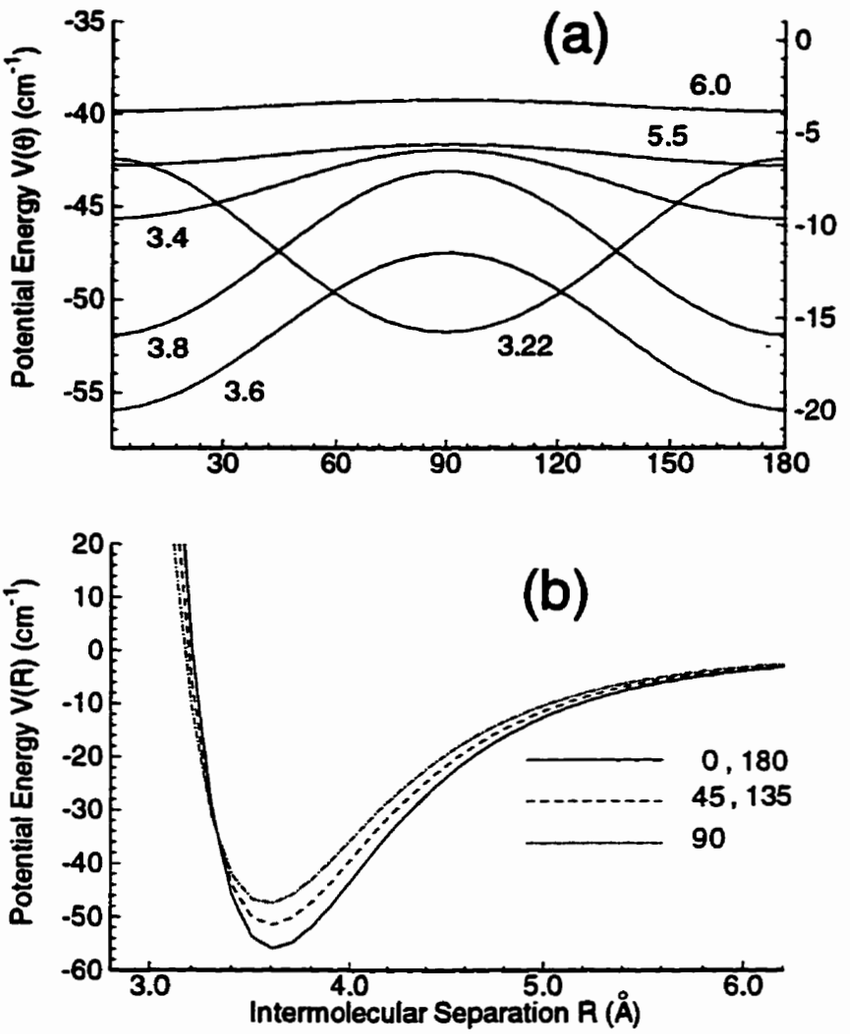

Figure 4.3: Anisotropy of the XC(fit) potential for the D_2–Ar system. (a) Angular dependence of the potential at different intermolecular distances. These curves show the effect of rotation of the D_2 molecule on the intermolecular potential. Note the symmetry of the potential with respect to the orientation angle $\theta = 90°$. The left- and right-hand side vertical axes scale the potential at 3.4, 3.6 and 3.8 Å, and 3.22, 5.5 and 6.0 Å, respectively. (b) Distance dependence of the potential for different orientation angles.

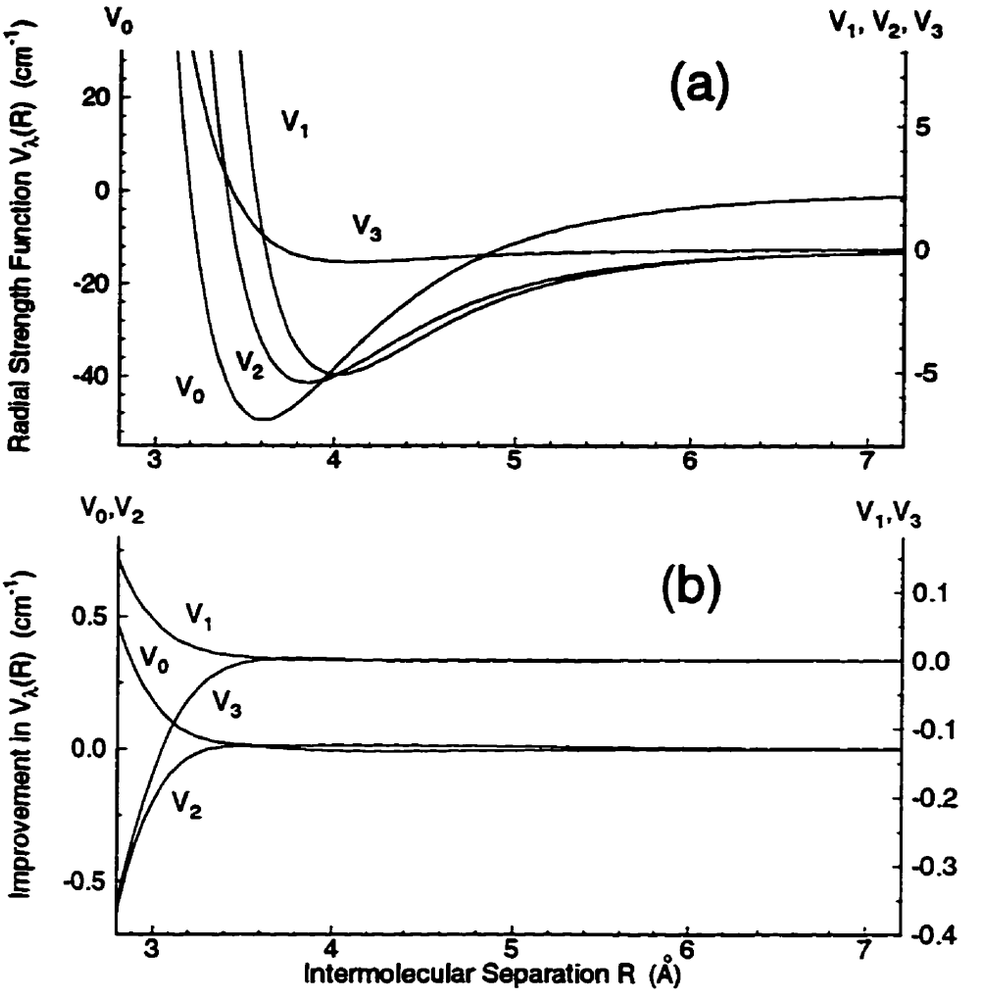

Figure 4.4: (a) Radial strength functions V_λ for the Legendre expansion of the XC(fit) potential for the HD–Ar system. The differences between the corresponding radial strength functions of the two versions of the potential are so small that they cannot be seen with the scales used in this figure. Note the relative values of the functions, and their R-dependence. The total contribution to the potential of the higher-order Legendre components, not shown in this figure, is of the order of 50% of that of the V_3 term for the region shown in this figure. This contribution is larger at shorter range. (b) Improvement in the potential, V(new) − V(old), in terms of the radial strength functions in cm^{-1}. It can be seen from this figure that the differences between the two versions of the potential at long range and on the attractive part of the potential well are negligible. At short range, however, this difference is significantly larger. Note the different scales used for the different components in both (a) and (b).

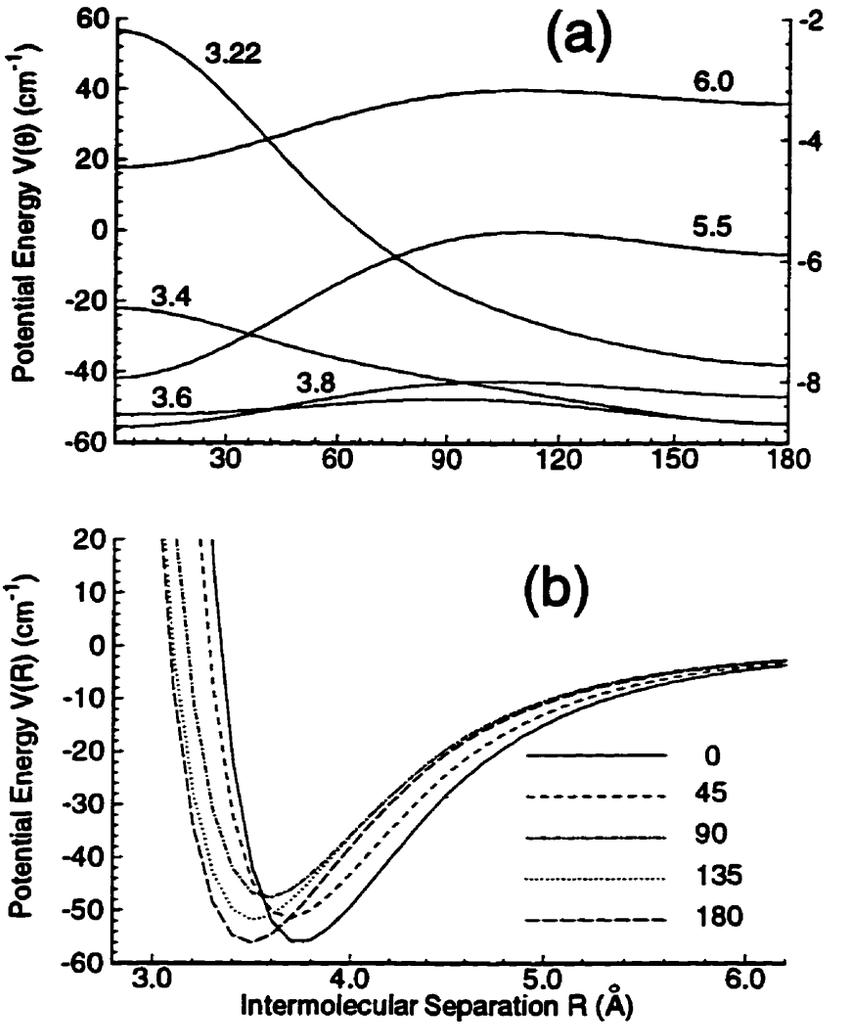

Figure 4.5: Anisotropy of the XC(fit) potential for HD–Ar system. (a) Angular dependence of the potential at different intermolecular distances. These curves show the effect of rotation of the HD molecule on the intermolecular potential. Note the larger effects for shorter R. The left- and right-hand side vertical axes scale the potential at 3.22, 3.4, 3.6 and 3.8 Å, and at 5.5 and 6.0 Å, respectively. (b) Distance dependence of the potential for different orientation angles. Compare this figure with Fig. 4.3-(b).

4.4 Calculations of spin-lattice relaxation times for the proton and deuteron of HD in HD–Ar system

In this section results of the calculations of the proton and deuteron spin-lattice relaxation times for HD in the HD-Ar system will be presented. For these calculations, thermally-averaged σ_V and σ_T state-to-state cross sections will be calculated first, using the XC(fit) potential for the hydrogen–argon systems. Results and details of these calculations are presented in Sec. 4.4.1. Spin-lattice relaxation times will be calculated from these cross sections using the equations given in Sec. 4.1. Results of the calculations of the spin-lattice relaxation times and the effects of physical parameters, such as temperature, density and magnetic field strength on these results will be presented in Sec. 4.4.2.

4.4.1 CC calculations of the σ_V and σ_T cross sections for the HD–Ar interaction

Close-coupled calculations of the S-matrix elements for the HD–Ar system have been carried out for 984 values of the total energy, ranging from 1 to 6800 cm^{-1}, using the MOLSCAT program suite and the potential subroutine described in the previous section. Steps of 10, 50, 100 and 200 cm^{-1} have been used for total energies below 1000, between 1000 and 3000, between 3000 and 5000, and above 5000 cm^{-1}, respectively. At all energies at least one closed channel was included in order to guarantee the required accuracy of the calculations. A new closed channel was added when the total energy of the system was within a few cm^{-1} below the previous closed channel. Including an additional closed channel did not significantly affect

the results of the calculations, apart from increasing the calculation time. A fine mesh of energies with a step-size of $0.5\,\mathrm{cm}^{-1}$ has been used for the resonance ranges of the first eight rotational levels. This fine mesh extends from a few cm^{-1} below to at least 50 cm^{-1} above each rotational level.

Values of J_{min} and ΔJ were set to their lowest possible values, *i.e.*, 0 and 1, respectively. The well-behaved J-dependences of the opacities calculated with these parameter choices suggests that a J-step of $\Delta J = 2$ would have also given much the same accuracy. The same results also showed that the most appropriate value for J_{min} was zero at each energy. The J_{max} value was first optimized for six total energies, from 1000 to $6000\,\mathrm{cm}^{-1}$ with a step-size of $1000\,\mathrm{cm}^{-1}$ (see Table 4.1). A 0.01% convergence in the averaged (over J) values of the diagonal elements of the J-dependent opacity matrices (*i.e.*, the diagonal elements of the energy-dependent cross section matrices) was considered as the criterion for these optimizations. The optimized J_{max} values for off-diagonal opacities were generally smaller than those for the corresponding diagonal elements by about 5–10, depending on their distance from the diagonal. The optimized J_{max} value for higher diagonal elements was usually smaller. The best values of J_{max} for other energies were then estimated carefully from interpolation or extrapolation of the optimized J_{max} values.

Values of R_{min} and R_{max} were set to 1 Å and 15 Å, respectively. However, the control parameters of the program were set such that the limits of the radial integration could be extended beyond these values, if necessary, to obtain the desired convergence in the wave-functions. Monitoring the results of the calculation of the S-matrix elements step-by-step (from the high-level output channel) showed that such an extension for the upper limit (R_{max}) was needed only for certain energies at large values of J. For the lower limit (R_{min}), however, such an extension was not required. Evaluation of the potential at short range shows that even for the highest

total energy used in these calculations the value $R_{min} = 2\,\text{Å}$ would be sufficient. The parameter *STEPS* (number of steps used per half-wavelength of the asymptotic wave-function) was set to the value 10 throughout these calculations. The rest of the calculational parameters were set to the default values recommended by the authors of the MOLSCAT program.[104]

To calculate scattering cross sections for each total energy, the output of the MOLSCAT program (including the S-matrix elements) was input to the SBE program. No extra parameter of the system is needed for running this program. This program first calculates the J-dependent opacities, and then averages them over J. Optimization of the J-parameters can be checked by inspection of the J-dependent opacities (see Eq. (1.39)). Figures 4.6 and 4.7 show, respectively, the J-dependence of the typical state-to-state elements of the $\mathcal{P}_V(J;j,j')$ and $\mathcal{P}_T(J;j,j')$ opacity matrices for the HD–Ar system at total energies between 200 and 2000 cm^{-1} in steps of 100 cm^{-1}. These figures show that at all energies and for all components, partial opacities exhibit a well-behaved J-dependence. These figures also show that the functional form of the J-dependence is similar for all components at all energies. However, different functional forms and abnormal values are obtained for the corresponding opacities at total energies lying slightly above the rotational threshold energies for the HD molecule. This exceptional behavior is due to the phenomenon of orbiting resonances.[108,112] Figures 4.6 and 4.7 also show that the partial opacities at all total energies have converged effectively to zero at J-values well below the corresponding J_{max}. The other interesting feature of the J-dependence curves is that at all energies apart from the resonance ranges, they have a single maximum. As can be seen from Figs. 4.6 and 4.7, the position and value of the maximum of each curve depends upon the total energy. An increase in the total energy moves the position of the maximum monotonically towards higher values of J. The rate

of this move is larger at lower energies. Increasing the total energy up to a certain value increases the value of the maximum opacity; above this total energy, however, a further increase in the total energy decreases the value of the maximum opacity. As for location, the rate of change in the value of the maximum opacity itself is larger at lower energies. For all other elements that are not shown in Figs. 4.6 and 4.7 for brevity, the same behavior has been observed for the J- and E-dependences.

The total energy at which the direction of the changes in the maximum value of the magnitude of the opacities is reversed will be called the *turning point energy* (*TPE*) and will be denoted by E^*. The value of E^* depends upon the type of opacity and varies with j and j'. For a specified (j,j') element of the opacity $\mathcal{P}$, the *TPE* will be denoted specifically by $E^*_{\mathcal{P}}(j,j')$. For example, Fig. 4.6 shows that the values of $E^*_{\mathrm{V}}(1,1)$ and $E^*_{\mathrm{V}}(1,3)$ are $\simeq 800$ and $\simeq 1800$ cm^{-1}, respectively. The *turning point energy* $E^*_{\mathcal{P}}(j,j')$ is a unique point in the $(J, E, \mathcal{P}(J;j,j'))$ space; that is the extremum (maximum or minimum, depending on whether the opacity element is diagonal or off-diagonal) point of the $\mathcal{P}(J;j,j')$ opacity surface. In terms of analytical algebra, this point is the root of the complete derivative of the $\mathcal{P}(J;j,j')$ opacity with respect to its two variables J and E. For a given system, the value of $E^*_{\mathcal{P}}(j,j')$ depends only upon the interaction potential. It is thus suggested that this point can be used to differentiate between different potentials recommended for a system (of course, at the level of theory only, since the properties of this point cannot be measured experimentally).

As mentioned above, the SBE program carries out the averaging (over J) of the J-dependent opacities $\mathcal{P}_{\mathrm{V}}(J,j,j')$ and $\mathcal{P}_{\mathrm{T}}(J,j,j')$ to calculate the energy-dependent state-to-state cross section elements of $\sigma^E_{\mathrm{V}}(j,j')$ and $\sigma^E_{\mathrm{T}}(j,j')$, respectively. Results of these calculations for certain diagonal and off-diagonal elements of the σ_{V} and σ_{T} cross section matrices are illustrated in Figs. 4.8 and 4.9, respectively. These figures

show a number of similar behaviors for the two energy-dependent cross sections. These similar behaviors will be discussed below.

The first interesting behavior is the effect of orbiting resonances on the values of different elements of the two cross section matrices. As can be seen from Figs. 4.8 and 4.9, these effects are significant, and cannot be neglected for the present system. From these figures it can be seen also that orbiting resonances of a specific rotational level affect all elements of the two cross section matrices involving rotational levels up to this level (*i.e.*, it has no effect on the elements involving higher levels only). However, these effects are at least two orders of magnitude smaller for the elements involving lower levels only. Two other general trends are observed for the effects of orbiting resonances of a specific level on the elements involving that level. The first of these two trends is that the effect on diagonal elements is larger than that on off-diagonal elements. The second trend is that the effect on the elements corresponding to the transitions to this specific rotational level is at least two orders of magnitude larger than that on the elements corresponding to the transition from this level. Details of the structure of the resonance ranges for the diagonal elements of the σ_V and σ_T cross section matrices are shown in Fig 4.10-(a) and (b), respectively. It can be seen from these figures that the effect of orbiting resonances on both opacities, in terms of the number of peaks and their relative heights, has the same structure for all diagonal elements. This figure also shows that the effect for both cross sections decreases with increasing j. The rate of this decrease is, however, different for the two cross sections. Figure 4.10 shows also that the fine mesh used for the total energies in the resonance ranges has covered them completely. Although a finer mesh would be needed to map out details of the fine structures of the sharp peaks, the functional forms obtained for the cross sections in these ranges are sufficiently well-behaved to allow an error-free

integration in the process of thermal averaging of the cross sections.

The second interesting behavior observed for the energy-dependence of the two cross sections, see Figs. 4.8 and 4.9, is that at all total energies out of the resonance ranges the values of the diagonal cross sections are larger for lower j elements. These values increase with total energy to a common asymptotic value for all diagonal elements. At all total energies the off-diagonal elements of the cross section matrices which belong to one column (*i.e.*, having a common j') decrease with the variable of the column j. The elements belonging to a particular row do not show any specific trend. The functional form of the absolute values of the off-diagonal elements differs from that for the diagonal elements in that with increasing total energy of the system it passes through a maximum before reaching the asymptotic value. The asymptotic values of the pair of elements corresponding to the two transitions (with opposite direction) between a pair of rotational levels are the same.

The thermal averages of the state-to-state cross sections were calculated at temperatures between 50 and 500 K in steps of 5 K using the CRAVE program.[106] The program employs an appropriate integration scheme for a width of 50 cm^{-1} above each threshold energy. The results of these calculations for typical elements of the thermally-averaged (temperature-dependent) $<\sigma_V>$ and $<\sigma_T>$ cross section matrices are plotted versus temperature in parts (a) and (b) of Fig. 4.11, respectively. This figure shows that all elements of the two cross section matrices are well-behaved functions of temperature. The form of these functions for the off-diagonal elements differs from that for the diagonal elements. This figure also shows that the absolute values of the diagonal and their lower nearest off-diagonal elements are of the same order of magnitude at all temperatures. The absolute values of other off-diagonal elements are, however, very small at low temperatures, but become significant at higher temperatures. From these observations it can be concluded

that the contributions to the final results (*i.e.*, spin-lattice relaxation times) of off-diagonal elements may be significant, but still much smaller than those of the diagonal elements.

Since the potential has a well-defined functional form, the errors associated with the calculation of the S-matrix elements is minimal, and is limited to the errors of numerical techniques used in the integrations. Calculations of the energy-dependent cross sections from the S-matrix elements (by the SBE program) have errors as small as the floating points of the real variables of the program, which are negligible. The major calculational errors of the results are introduced at the thermal averaging step. This error, as mentioned above, might arise from integration over the resonance ranges. Thus, it is expected to have larger errors at lower temperatures for which the contribution of the resonance ranges are larger. The maximum value of these errors in the thermally-averaged cross section elements obtained for the HD–Ar system was less than 1%. However, at a few temperatures, the thermal averaging resulted in outlier points for some elements, which were replaced by interpolation of the remaining normal points. The number of these outliers was the same for both cross sections, and varied with the element, from 2 to a maximum of 5 points over the entire range of temperatures that is used in these calculations, *i.e.*, from 50 to 500 K. These outlier points are not shown in Fig. 4.11.

In conclusion, the analysis presented above shows that the results of the CC calculations obtained for the HD–Ar system are indeed high-quality results.

4.4.2 Calculation of proton and deuteron spin-lattice relaxation times for HD in the HD–Ar system

The spin-lattice relaxation times for the proton and deuteron of HD in the HD–Ar system have been calculated using thermally-averaged σ_V and σ_T cross section matrices calculated and studied in the previous section, via the T_1 equations given in Sec. 4.1, Eq. (4.1)-(4.3). In these calculations spin-rotation, dipolar, and quadrupolar coupling constants of Code and Ramsey[113] for the $j = 1$ rotational level of the HD molecule have been used.

In the theoretical calculations presented in this chapter, it is assumed that the coupling constants are independent of the rotational levels of the HD molecule. Validity of this assumption, which implicitly requires a rigid-rotor assumption, and the effects of non-rigidity of the HD molecule on the relaxation times will be discussed in Sec. 5.5.

As can be seen from the T_1 equations, the experimental parameters of the spin-lattice relaxation times consists of temperature, density and the magnetic field strength. Dependence of the relaxation times on these parameters was discussed generally in Sec. 4.1. As mentioned in that section, dependence on density and the field strength are explicit, but dependence on temperature is complicated. In the following, the dependence of the components and the overall relaxation times of the proton and the deuteron on these experimental parameters will be demonstrated numerically, and will be studied briefly.

Temperature-dependence

Figure 4.12 shows the temperature effects on the components and the overall relaxation times calculated for the proton and deuteron of HD in the HD–Ar system at ρ=1 amagat and B_0=11.75 Tesla. These figures show that the components and

the overall relaxation times of both nuclei are well-behaved functions of temperature. Comparison between the results obtained for the proton and for the deuteron shows that the overall relaxation time of the proton is significantly shorter than that of the deuteron at all temperatures. Over the temperature range shown in Fig 4.12 the SR and the Q interactions are the dominant relaxation pathways for the proton and deuteron, respectively. The functional forms of the T_{1D} and T_{1Q} curves are essentially the same, and are different from that of the T_{1SR} curve (compare Eqs. (4.2) and (4.3) with Eq. (4.1)). The difference between the functional forms of the T_{1D} and T_{1Q}, and the T_{1SR} curves depends upon both the density and the field strength. As can be seen from Fig. 4.12, the temperature-dependence of the overall relaxation time has a simple functional form, which is similar to that of one of the components (*i.e.*, that of the dominant interaction). This observation is not general, however, especially under conditions in which the contributions of the SR and the combined D and Q interactions are comparable. The functional form of the overall relaxation curves under such conditions is more complicated, and contain characteristic temperature behavior of both sets of relaxation times. Increasing the temperature increases the contribution of the SR relaxation for both nuclei. The increase for the deuteron is such that at very high temperatures the SR and Q relaxations become competitive. For both nuclei the dipolar interaction has a small contribution to the overall relaxation time. This small contribution, however, increases with decreasing temperature.

As is shown in Fig. 4.13, and will be discussed next, for $\rho = 1$ amagat the proton relaxation times are well inside the nonlinear-regime, while the deuteron relaxation times are close to the linear-regime. This difference explains the significant difference between the temperature-behaviors of the T_{1D} curve for the proton and deuteron shown in Fig. 4.12. In the linear-regime, however, the T_{1D} values for

the two nuclei are simply related by the factor $\frac{I_D(I_D+1)}{I_H(I_H+1)} = 2.67$ at all temperatures. This can be seen clearly in the small windows of Fig. 4.13.

Density-dependence

A typical density-dependence of the components and the overall relaxation times of the proton and the deuteron at $T = 300\,K$ and $B_0 = 11.75$ Tesla are shown in parts (a) and (b) of Fig. 4.13, respectively. This figure shows that the density behavior for all components and the overall relaxation times of the two nuclei have the same functional form. As observed for the temperature-dependence, the SR and Q interactions are the dominant relaxation pathways for the proton and the deuteron, respectively. Relative contributions of the different components change with density, but much more slowly than the rate of change with temperature. The most interesting feature of the density-dependence of the relaxation times of the two nuclei can be seen at higher densities, and shown in the smaller windows of Fig. 4.13. Comparison between the high density results for the two nuclei shows clearly that the region of the linear-regime behavior for proton relaxation starts at densities above $\simeq$18 amagat, while for the deuteron this regime starts at densities as low as $\simeq$3 amagat. This significant difference is due to the large difference between the Larmor frequencies of the two nuclei ($\frac{\omega_H}{\omega_D} = \frac{\gamma_H}{\gamma_D} = \simeq 6.5$). The lower limits of the linear-regime regions for both nuclei is moved rapidly towards larger densities with increasing the field strength B_0, and moves towards smaller densities with increasing temperature (see also Eqs. (4.1)-(4.3)). In conclusion, Fig. 4.13 shows how a linear-regime assumption can introduce dramatic errors in the calculated values of the spin-lattice relaxation times for the proton, even at intermediate densities. For the deuteron however, the linear-regime assumption is valid for densities down to 3 amagat at 11.75 Tesla.

Field-dependence

It was shown above that the proton relaxation at $B_0 = 11.75$ Tesla is well inside the nonlinear-regime at intermediate densities, and that the deuteron relaxation is in the nonlinear-regime at densities up to 3 amagat. It is worth mentioning here again that the linear-regime behavior is implicitly equivalent to field-independent relaxation times, or alternatively, being in a nonlinear regime means that the relaxation times are field-dependent. Although the field effects on the relaxation times can be studied analytically, based on the algebraic forms of the T_1 equations, to have a better physical understanding and to visualize the magnitude of these effects, it seems to be useful to study them numerically. Figures 4.14 shows the field effects on the relaxation times of the proton and deuteron of HD in the HD–Ar system at $T = 300$ K and $\rho = 1$ amagat. As expected, this figure shows that functional forms of the field-dependence of all of the components and of the overall relaxation times of both nuclei are the same. All relaxation times decrease to their respective asymptotic values with decreasing field strength. The rate of this decrease is, however, larger for the proton than it is for the deuteron. For example, decreasing the field strength from 10 T to 5 T decreases the proton relaxation times by a factor $\simeq$ 2, (still in nonlinear-regime). While, the same change in the field strength decreases the relaxation times of the deuteron by a factor of 2% (almost in the linear-regime). The slopes of the field-dependence of the relaxation times obviously depend on the temperature and density. The dominant relaxation mechanisms for the proton and the deuteron over the entire range of the field strengths are the SR and the Q interactions, respectively. Figure 4.14 shows also that compared with that of proton, the relaxation of the deuteron approaches the linear regime behavior at higher field strengths. The open circles in Fig 4.14 show the corresponding relaxation times at $B_0 = 11.75$ Tesla which is the field employed in the experimental part of the present

research. Comparison between the actual relaxation times (curves) and their corresponding linear-regime (field-independent) relaxation times (straight lines) shows the size of errors introduced by a linear-regime assumption.

The NOE enhancements

In the experimental part of this research the possibility of NOE measurements in the gas phase was examined, and some results of the first NOE measurements in the gas phase obtained for the proton and the deuteron of HD in HD–Ar mixtures were presented (see Figs. 3.10). These preliminary results suggest that it will be useful to calculate the NOE enhancements, $\eta_i\{j\}$, and to study their dependence on the experimental parameters of the system. Since the NOE experiment is totally independent of the relaxation time measurements, comparison between the theoretical and the measured values of the NOE enhancements, $\eta_i\{j\}$, can be regarded as an independent test of the theoretical results for the relaxation times.

In the calculation of the maximum NOE enhancements Eq. (3.2) has been utilized. As mentioned in Sec. 3.2.3, this equation is valid only for the liquid phase at the extreme narrowing-regime (*i.e.*, the linear-regime). The results presented above showed that the proton relaxation times are not in the linear-regime. However, Eq. (3.2) will still be used in the calculation of the NOE values, because the appropriate frequency-dependent formulae for the NOE enhancement in the gas phase have not yet been derived.[†] Typical temperature, density, and field effects on the calculated maximum NOE enhancements are shown in Fig. 4.15. Part (a) of Fig. 4.15 shows that although the NOE enhancements for both nuclei decrease with temperature, they do so at different rates and following different functional forms. The dependence on density of the NOE enhancements is very weak, except

[†]Formulation of the NOE effect in the gas phase using kinetic theory is underway.

for that for the proton at low densities. This weak dependence could be predicted by inspecting Fig. 4.13, which shows the same functional form and the same slope for the density dependence of the relaxation time components. Part (b) of Fig. 4.15 shows that the field effect on the NOE enhancement for the deuteron, $\eta_D\{H\}$, at $\rho = 1$ amagat is so weak that it is not observable at low temperatures. The field-dependence for the proton, however, is relatively strong, and depends upon the temperature. The asymptotic value of the $\eta_H\{D\}$ at $B_0 \rightarrow 0$ is either a maximum or a minimum, depending upon the temperature. Figure 4.15 shows also that the calculated values of the proton NOE enhancement, overwhelmingly determined by the magnetogyric ratios factor (the $\frac{\gamma_D}{2\gamma_H}$ factor in Eq. (3.2)), is very small under all conditions. Such small values for the NOE enhancement are not detectable in typical NOE experiments, which have typical error bars as large as ± 0.05 for the peaks with good S/N ratios. The calculated values of the NOE enhancements for the deuteron are, however, large enough to be observed in typical NOE experiment.

The theoretical results obtained for the relaxation times and the NOE enhancements for the proton and the deuteron of HD in the HD–Ar system will be compared with experimental results in Sec. 5.2.

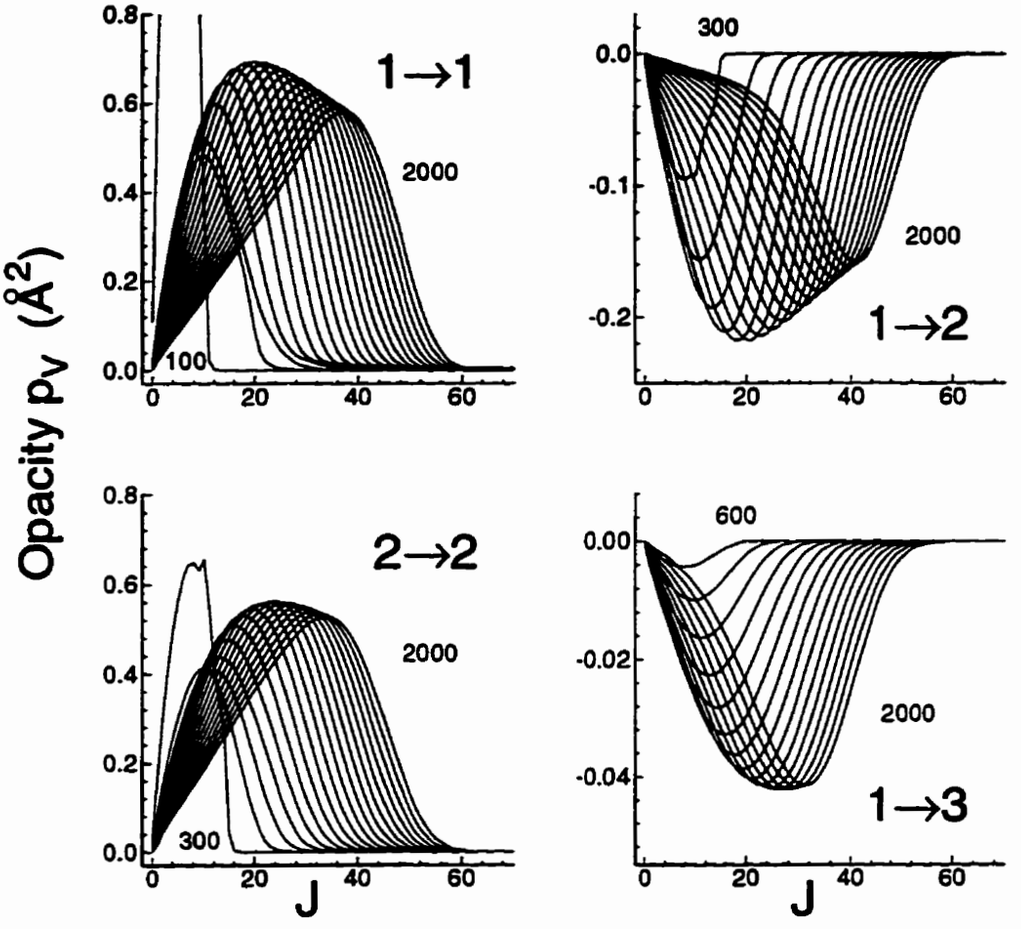

Figure 4.6: Typical J-dependence of the state-to-state $\mathcal{P}_V(J;j,j')$ opacity for the HD–Ar system for a series of total energies in steps of $100\,cm^{-1}$. For simplicity, only the two curves for the lowest and the highest total energies are labeled. As can be seen, state-to-state $\mathcal{P}_V(J;j,j')$ opacities at all energies show well-behaved J-dependence. The different behavior observed at some of the lower energies is due to orbiting resonances corresponding to the resonance ranges of the $j = 1$ and $j = 2$ levels. Note the changes in the position and height of the maximum with the change in the total energy of the system. Note also the different scales used for the different elements.

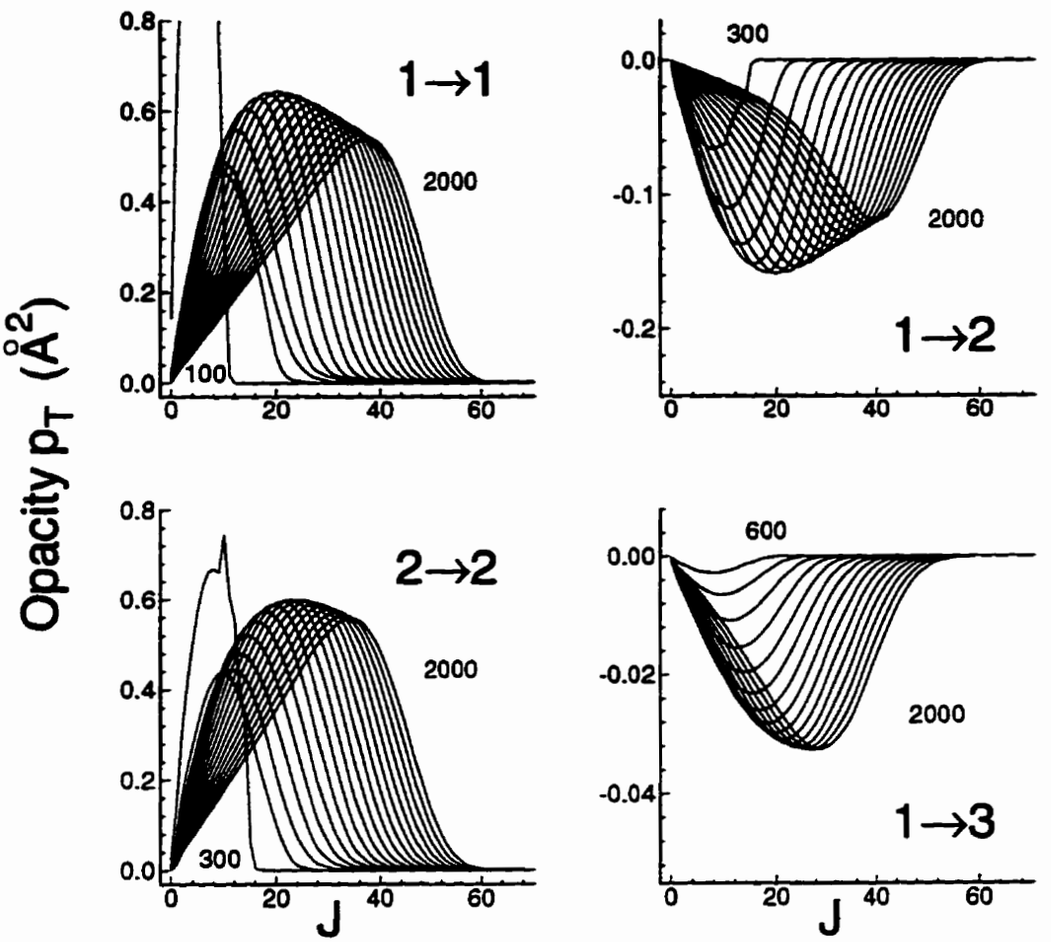

Figure 4.7: Typical J-dependence of the state-to-state $\mathcal{P}_T(J;j,j')$ opacity for the HD–Ar system for a series of total energies in steps of $100\,cm^{-1}$. For simplicity, only the two curves for the lowest and highest total energies have been labeled. As can be seen, state-to-state $\mathcal{P}_T(J;j,j')$ opacities at all energies show well-behaved J-dependence. The different behavior observed at some of the lower energies is due to orbiting resonances corresponding to the resonance ranges of the $j = 1$ and $j = 2$ levels. Note the changes in the position and height of the maximum with the change in the total energy of the system. Note also the different scales used for the different elements.

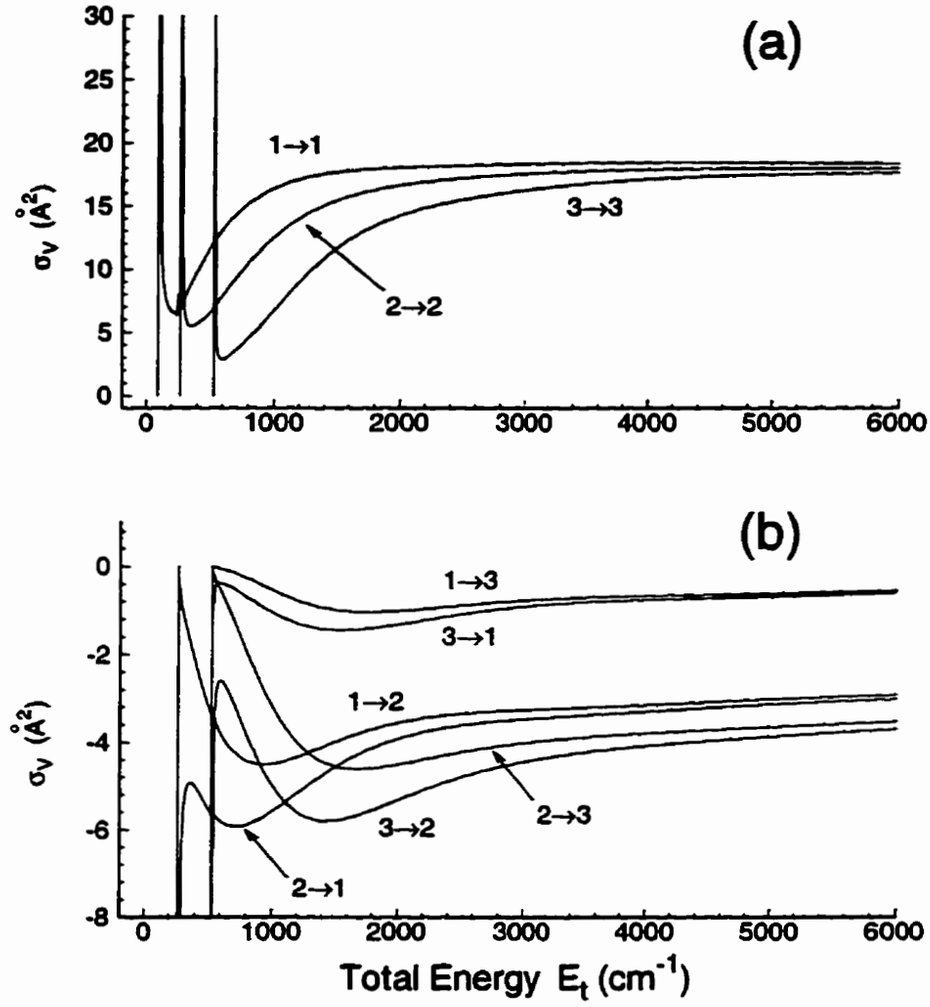

Figure 4.8: Energy-dependence of some (a) diagonal and (b) off-diagonal state-to-state $\sigma_V^E(j,j')$ cross sections for the HD–Ar system. Note the relative values of the two sets of elements, and the significant effects of orbiting resonances on them. The resonance ranges are expanded in Fig. 4.10-(a) to show these effects in more detail. Note also the j-dependence of the two sets of elements.

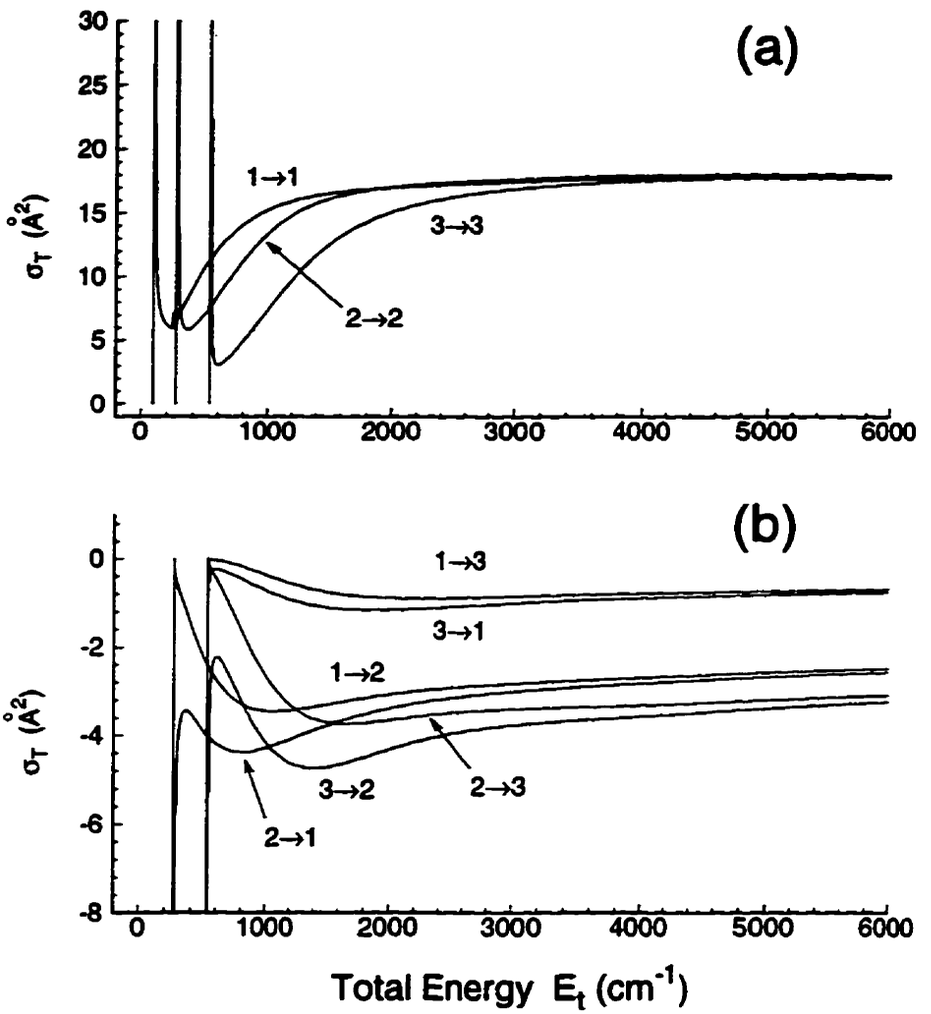

Figure 4.9: Energy-dependence of some (a) diagonal and (b) off-diagonal state-to-state $\sigma_T^E(j,j')$ cross sections for the HD–Ar system. Note the relative values of the two sets of elements, and the significant effects of orbiting resonances on them. The resonance ranges are expanded in Fig. 4.10-(b) to show these effects in more detail. Note also the j-dependence of the two sets of elements.

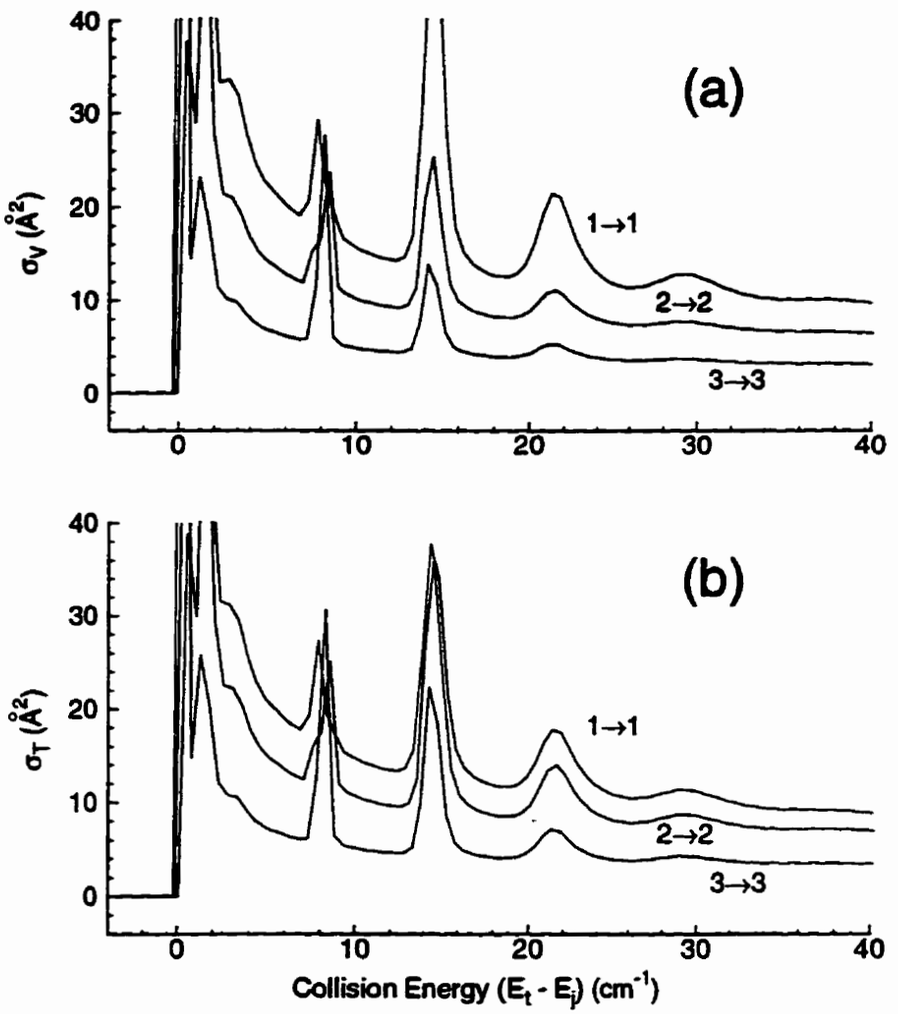

Figure 4.10: Effects of orbiting resonances on energy-dependent state-to-state $\sigma_V^E(j,j')$ (a) and $\sigma_T^E(j,j')$ (b) cross sections for the HD–Ar system. To have a common energy axis all elements of the two opacities have been plotted versus collision energy $(E_t - E_j)$. Calculations of the cross sections for the resonance range of each rotational level have been carried out with a fine mesh of 0.5 cm^{-1} starting from a few wavenumbers below, up to at least 50 wavenumbers above the threshold for each rotational level. Note the similar structures of the two cross sections and their different j-dependence.

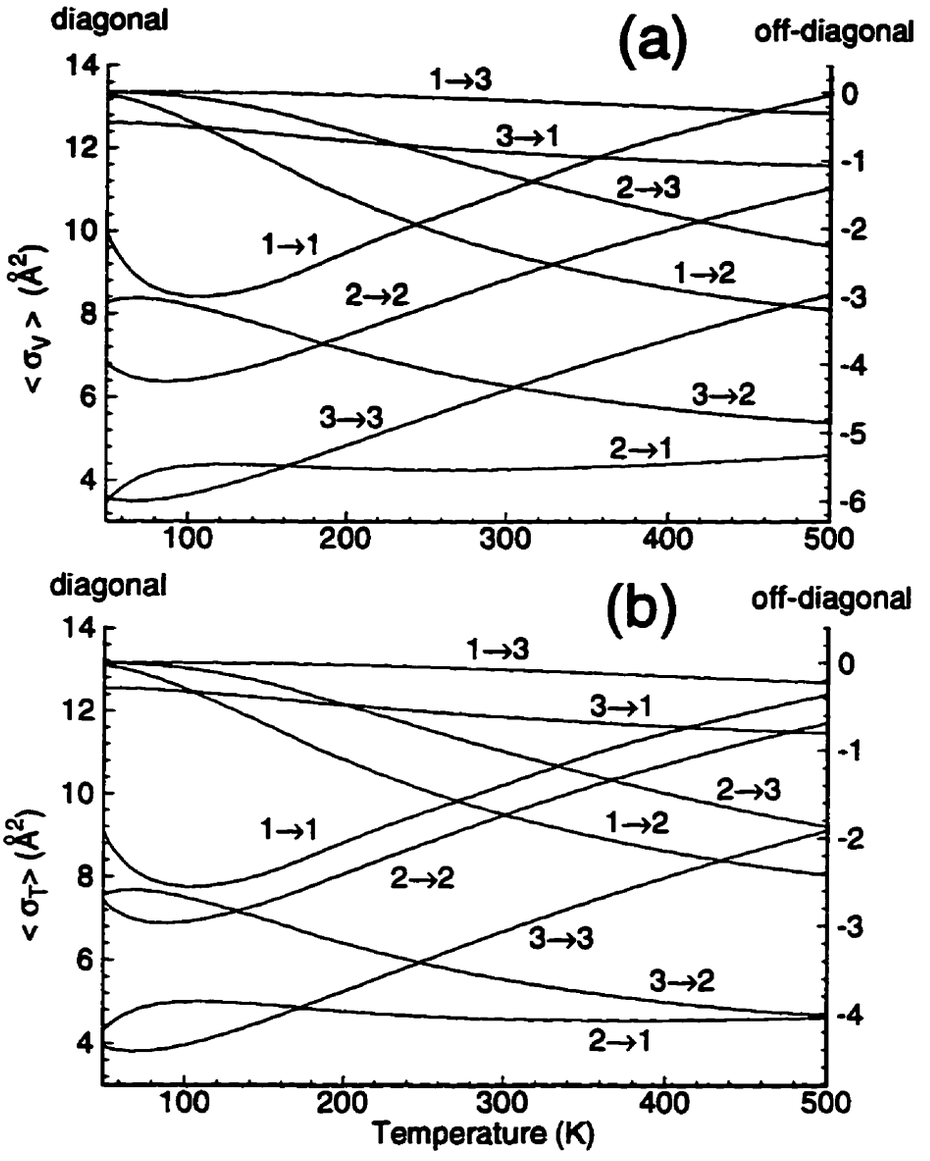

Figure 4.11: Temperature-dependence of the thermally-averaged state-to-state $\sigma_V(j,j')$ (a) and $\sigma_T(j,j')$ (b) cross sections for the HD–Ar system. Note the different scales used for the diagonal and off-diagonal elements. Calculations have been carried out for temperatures between 50 and 500 K in increments of 5 K.

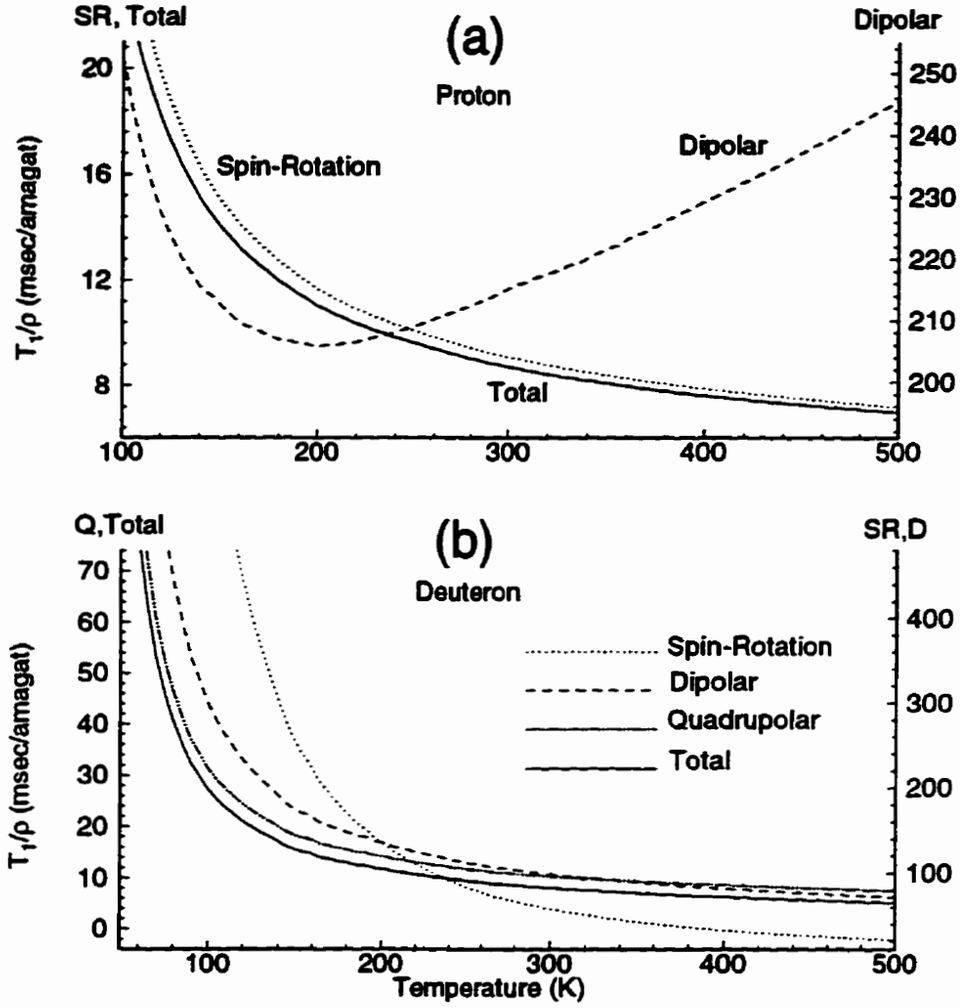

Figure 4.12: Temperature-dependence of the different components of the spin-lattice relaxation time for (a) the proton and (b) the deuteron of HD in the HD-Ar system at $\rho = 1$ amagat and $B_0 = 11.75$T. Note the different scales used for the different components. Note also how the different components change with temperature.

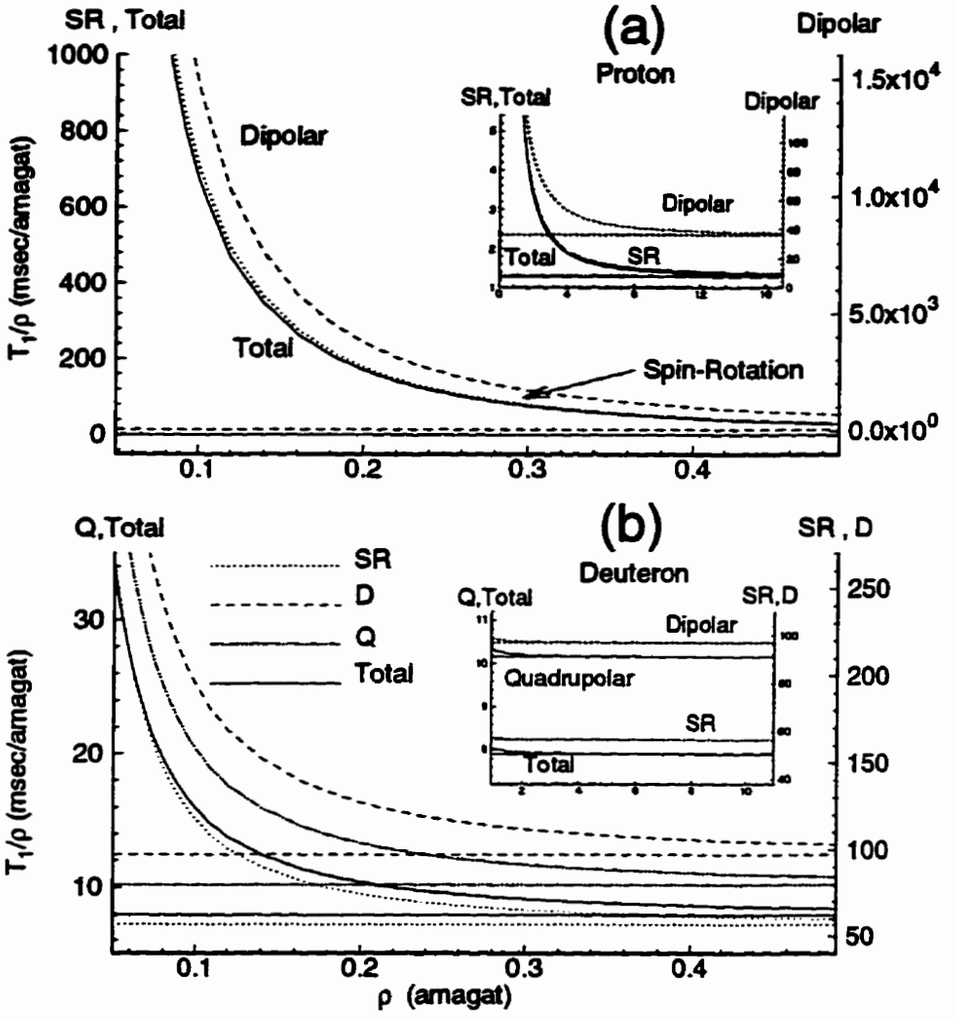

Figure 4.13: Density-dependence of the different components of the spin-lattice relaxation times for (a) the proton and (b) the deuteron of HD in the HD-Ar system at $T = 300\,\mathrm{K}$ and $B_0 = 11.75\mathrm{T}$. The straight lines show the corresponding linear-regime relaxation times. The small window in each part shows the density-dependence at large densities. Note that the deuteron relaxation times are in linear-regime above $\simeq 3$ amagat, while the linear-regime behavior for the proton starts at significantly higher density which is not shown in this figure (*ca.*, above 18 amagat). Note the different scales used for the different components.

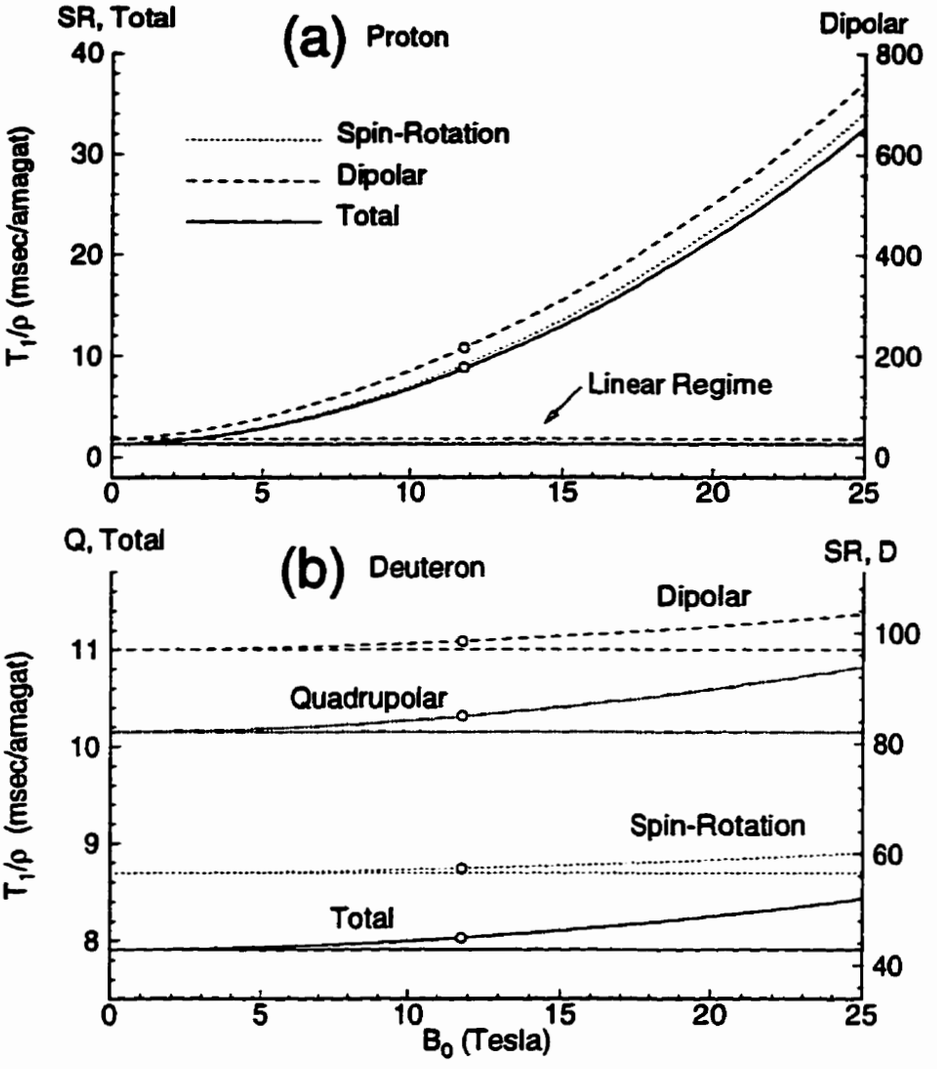

Figure 4.14: Field-dependence of the different components of the spin-lattice relaxation time for (a) the proton and (b) the deuteron of HD in the HD-Ar system at $\rho = 1$ amagat and $T = 300$ K. Note the different scales used for different components. The straight lines show the corresponding linear-regime relaxation times. The open circles show the corresponding relaxation times at $B_0 = 11.75$T, which is the field strength used in the experimental part of the present research.

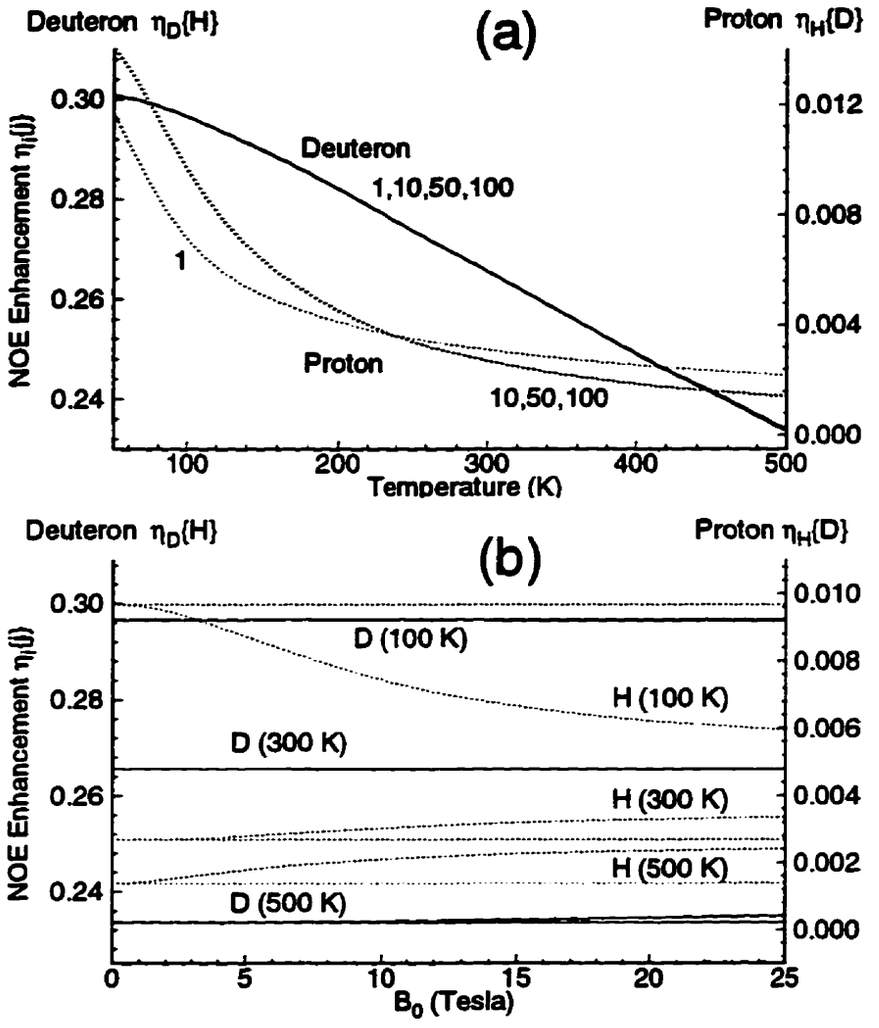

Figure 4.15: (a) Temperature-dependence and (b) field-dependence of the NOE enhancements for the proton and deuteron of HD in the HD-Ar system. The numbers in (a) show the amagat densities. The superposition of the deuteron curves is due to the linear-regime behavior of its relaxation times at all densities. All of the NOE enhancements in (a) are calculated for $B_0 = 11.75$ Tesla. The NOE enhancements in (b) are calculated for $\rho = 1$ amagat. The letters D and H in (b) denote the corresponding curves for the deuteron and proton, respectively. The straight lines in (b) show the corresponding linear-regime curves. Note the different scales used for the two nuclei. Note also the significant field-dependence of the proton NOE enhancements.

4.5 Calculations of spin-lattice relaxation times for the deuteron of D_2 in D_2–Ar system

Since the two parity isomers of D_2 are not interconvertible by scattering processes at the low energies (compared with the energy separation between the ground and excited electronic states) studied here, relaxation of their nuclear spin magnetizations induced by collisional reorientation of their rotational angular momenta occur independently. Therefore, calculations of the scattering cross sections and the deuteron spin-lattice relaxation times for the two parity isomers of the D_2–Ar system shall be dealt with separately. However, throughout this section, separate results of the calculations of the S-matrices, the NMR cross sections and deuteron spin-lattice relaxation times for the two parity isomers of the D_2–Ar system will be presented in parallel. An appropriate method for calculating the overall relaxation time of the deuteron in a mixture of the two parity isomers (from the relaxation times calculated in this section) will be presented and discussed in Sec. 4.5.3.

4.5.1 CC calculations of the σ_V and σ_T cross sections for the D_2–Ar interaction

Close-coupled calculations of the S-matrix elements for the *ortho*-D_2–Ar and *para*-D_2–Ar systems have been carried out, respectively, for 696 and 576 values of the total energy, ranging from 1 to 6800 cm^{-1}, using the MOLSCAT program suite and the potential subroutine described in Sec. 4.2. Steps of 20, 50, 100 and 200 cm^{-1} have been used for total energies below 1000, between 1000 and 3000, between 3000 and 5000, and above 5000 cm^{-1}, respectively. Because of the larger spacings between the rotational energy levels of each parity isomer of D_2 a larger step-size

than that used for the HD–Ar calculations has been used for both isomers for energies below 1000 cm^{-1}. At all energies at least one closed channel was included in order to guarantee the required accuracy of the calculations. A new closed channel was added when the total energy of the system was within a few cm^{-1} below the previous closed channel. As for the the HD–Ar calculations, the inclusion of an additional closed channel did not significantly affect the results, apart from increasing the calculation time.

A fine mesh of energies with a step-size of 0.5 cm^{-1} has been used to cover the resonance ranges above the first four rotational levels for each isomer; $j = 2, 4, 6$ and 8 for the *ortho*, and $j = 1, 3, 5$ and 7 for the *para* systems, respectively. This fine mesh extends from a few cm^{-1} below to at least 50 cm^{-1} above each rotational level.

Values of J_{min} and ΔJ were set to their lowest possible values, *i.e.*, 0 and 1, respectively. The well-behaved J-dependence of the opacities obtained with these parameter choices suggests that a J-step of $\Delta J = 2$ would also have given much the same accuracy. The same results also showed that the most appropriate value for J_{min} was zero for each energy. The J_{max} value was first optimized for five total energies, from 1000 to 5000 cm^{-1} with a step-size of 1000 cm^{-1}. The best values of J_{max} for other energies were then estimated carefully from interpolation or extrapolation of these optimized J_{max} values. A 0.01% convergence in the averaged (over J) values of the diagonal elements of the J-dependent opacity matrices (*i.e.*, the diagonal elements of the energy-dependent cross section matrices) was considered as the criterion for these optimizations. The optimized J_{max} values for off-diagonal opacities were generally smaller than those for the corresponding diagonal elements. Table 4.1 compares the optimized J_{max} values obtained for the *ortho*-D_2–Ar, *para*-D_2–Ar and HD–Ar systems. It can be seen from this table that the optimized values

Table 4.1: Comparison between the optimized values of J_{max} for the HD–Ar, *ortho*-D_2–Ar and *para*-D_2–Ar systems. The criterion considered in the optimization of the J_{max} values was a 0.01% convergence in the averaged (over J) values of the diagonal elements of the J-dependent opacity matrices.

Total Energy (cm^{-1})	Optimized J_{max}		
	$o$$D_2$–Ar	$p$$D_2$–Ar	HD–Ar
1000	80	76	70
2000	101	96	88
3000	115	109	102
4000	126	119	115
5000	136	126	126

of J_{max} for the HD–Ar system are generally smaller than those for the D_2–Ar system. The smaller values of J_{max} obtained for the HD–Ar system are due partially to the fact that at a fixed total energy, the rotational index (j) of the highest accessible level for HD is smaller than that for either of the two parity isomers of D_2. Table 4.1 shows also that within the D_2–Ar system the optimized values of J_{max} for the *ortho*-D_2–Ar system are larger by 5-8% than those for the *para*-D_2–Ar system, depending on the total energy.

The R-parameters were set to the same values as used in the CC calculations for the HD–Ar system (*i.e.*, R_{min} = 1 Å, R_{max} = 15 Å and *STEPS*=10). Also, unless stated otherwise, the values for the remaining parameters and conditions used in the MOLSCAT, SBE and CRAVE programs employed, respectively, for the calculations of the S-matrix elements, effective cross sections and thermal averaging, are the same as those used for the HD–Ar system as discussed in Sec. 4.4.1. The

results obtained from these calculations will be presented below.

Figures 4.16 and 4.17 demonstrate, respectively, the J-dependence of some typical elements of the opacity matrices $\mathcal{P}_V(J;j,j')$ and $\mathcal{P}_T(J;j,j')$ for the D_2–Ar system. The elements selected for this demonstration represent the first diagonal and the first off-diagonal elements of the opacity matrices, which contribute to the deuteron NMR spin-lattice relaxation for each parity isomer of the D_2–Ar system. As can be seen from Figs. 4.16 and 4.17, at all total energies, except for the resonance ranges, elements of the opacities for both parity isomers are well-behaved functions of J. The functional forms of the diagonal opacities are different from those of the off-diagonal ones in that they have an extra peak (*i.e.*, they have two maxima). This extra peak, which does not appear in the J-dependent opacities obtained for the HD–Ar system, is narrower than the original peak, and is centered at a higher J-value. The intensity of this second peak for the 1→1 element (*para*) for the $\mathcal{P}_V$ opacity (*i.e.*, $\mathcal{P}_V(J;1,1)$, is higher than that for the $\mathcal{P}_T$ opacity (*i.e.*, $\mathcal{P}_T(J;1,1)$). This trend is the opposite to that found for the 2→2 element (*ortho*). At a given energy the height of this peak is larger for the *para*-D_2–Ar system than that for the *ortho*-D_2–Ar system, while its width is smaller. This observation suggests that the appearance of this second peak is partially responsible for the higher values of the optimized J_{max} obtained for *ortho*-D_2–Ar (in comparison with those for *para*-D_2–Ar) and for the generally higher J_{max}-values for the D_2–Ar system (in comparison with those for HD–Ar), see Table 4.1. Except for a few low energies for the 1→1 element, the height of this second peak is several times smaller than that of the original peak, and decreases rapidly with increasing energy. Increasing the total energy also displaces the positions of both peaks towards higher values of J. This displacement is larger for the second peak.

The *turning point energy* (*TPE*), $E_p^*(j,j')$, of the original peak for both parity

isomers of the D_2–Ar system is generally very large; much larger than the corresponding $E^*_{\mathcal{P}}(j,j')$ for the HD–Ar system. For example, the *TPE*'s of the first diagonal and the first off-diagonal elements of the $\mathcal{P}_V$ opacity matrix for the *para*-D_2–Ar system, $E^*_V(1,1)$ and $E^*_V(1,3)$, are $\simeq$4800 and $\simeq$4200 cm^{-1}, respectively. The corresponding values for the $\mathcal{P}_T$ opacity, $E^*_T(1,1)$ and $E^*_T(1,3)$, are slightly larger. The *TPE*'s for the equivalent elements of the same opacity matrices for the *ortho*-D_2–Ar system are generally larger. The *turning points* of the second peak when they appear occur at very low energies, close to the corresponding rotational threshold energies. A detailed study of the *TPE* of this peak was not possible because of alterations introduced by orbiting resonances.

The averages over J of the (J-dependent) opacities of the two parity isomers have been carried out using the SBE program. Typical energy-dependent elements of the σ_V and σ_T cross section matrices for the *ortho*-D_2–Ar and *para*-D_2–Ar systems obtained from this averaging are plotted versus total energy in Figs. 4.18 and 4.19, respectively. These figures show that the energy-dependent cross sections are well-behaved functions of total energy. The rate at which the state-to-state cross sections approach their asymptotic values is much slower than was found for the HD–Ar calculations. The minimum points in the energy-dependence curves of the off-diagonal opacities are located at very high energies (much higher than those observed for the HD–Ar system). Within the cross section matrices of each parity isomer, the value of the diagonal elements decrease with increasing j for a fixed value of the total energy. This trend is, of course, interrupted in the resonance ranges. The small windows in Figs. 4.18 and 4.19, which expand the resonance ranges for typical elements of the cross section matrices, show that the effect of orbiting resonances on the diagonal elements is significantly larger than that on the off-diagonal elements. For each parity isomer the intensities of the resonance peaks

for the σ_T cross section are generally larger than those for the σ_V cross section. This could be seen also by comparing part (c) of Figs. 4.16 and 4.17. The changes with j in the structure and intensity of the resonance peaks is much larger than those found for the HD–Ar system (compare the resonance windows of Figs. 4.18 and 4.19 for D_2–Ar with Fig. 4.10 for HD–Ar).

The thermally-averaged cross section matrices $<\sigma_V>$ and $<\sigma_T>$ are calculated for 91 temperatures, ranging from 50 to 500 K in increments of 5 K, from the energy-dependent cross sections by using the CRAVE program. For each parity isomer a special integration scheme was used for a width of (at least) $50\,cm^{-1}$ above the first four rotational energy thresholds to cover the possible effects of orbiting resonances. The results of the thermal averaging for the two parity isomers of the D_2–Ar system are presented together in Fig. 4.20. This figure shows that all elements of the two cross section matrices are well-behaved functions of temperature, and show the same behavior as observed for those for the HD–Ar system. However, the j-dependence of the cross sections does not follow the same pattern observed for the HD–Ar system. For example, compare part (b) of Figs. 4.20 and 4.11, especially for the $\sigma_T(1,1)$ and $\sigma_T(2,2)$ cross sections. This behavior is not unexpected, since the two parity isomers of D_2–Ar are independent systems. For each parity isomer, however, the expected j-dependence is followed normally.

From the figures and the analysis presented in this section it can be concluded that the NMR cross section matrices calculated for the two parity isomers of the D_2–Ar system are high-quality results.

4.5.2 Calculation of deuteron spin-lattice relaxation times for D_2 in the D_2–Ar system

Deuteron spin-lattice relaxation times for D_2 in the *para*-D_2–Ar and *ortho*-D_2–Ar systems have been calculated separately from their thermally-averaged σ_V and σ_T cross section matrices via the equations for T_1 given in Sec. 4.1, Eq. (4.1)-(4.3). The spin-rotation, dipolar, and quadrupolar coupling constants of Code and Ramsey[113] for the $j = 1$ and the $j = 2$ rotational levels of D_2 have been used (for *para*-D_2–Ar and *ortho*-D_2–Ar, respectively) in these calculations. The coupling constants for the combined dipolar-quadrupolar interaction, ω_{DQ}, for the two parity isomers are obtained via Eqs. (4.7) and (4.8). In the present calculations it is assumed that the coupling constants do not depend on the rotational levels of D_2. It will be shown in Sec. 5.5 that although this assumption is not quite valid, the errors introduced by it are negligible for the temperature range involved in the present study. The way in which the calculated deuteron relaxation times depend upon the physical parameters of the system, including temperature, density and magnetic field strength, will be discussed below.

Temperature-dependence

Temperature effects on the components and the overall relaxation times for the deuteron of D_2 in the *ortho*-D_2–Ar and *para*-D_2–Ar systems for $\rho = 1$ amagat and $B_0 = 11.75$ Tesla are illustrated in Fig. 4.21-(a). This figure shows that all components, as well as the overall relaxation times, are well-behaved functions of temperature. As expected, the dominant relaxation mechanism for both isomers over the entire temperature range studied in the present work is the DQ interaction. As can be seen from Fig. 4.21-(a), however, the contribution of the SR mechanism to the overall relaxation time increases with temperature. Comparison between the

two isomers shows that their SR relaxation curves have the same functional forms. Also, their T_{1SR} values are very close, especially at the higher temperatures. The functional forms and the numerical values of the DQ relaxation times of the two isomers are, however, significantly different, particularly at low temperatures. The difference between the DQ relaxation times of the two isomers is a consequence of two factors, whose effects will be discussed in detail below.

The first factor causing a difference between the DQ (and hence overall) relaxation times of the deuteron for the two parity isomers is the difference between the ground rotational levels of the *para*-D_2 and *ortho*-D_2 molecules. The ground rotational level for the *ortho* isomer has zero rotational angular momentum (*i.e.*, $j = 0$), so that the intra-molecular interaction with the nuclear spin vanishes. Thus, molecules populating this level, which constitutes a significant fraction at low temperatures, does not contribute to the deuteron relaxation of D_2 in the *ortho*-D_2–Ar. By contrast, the ground level of the *para* isomer has a non-zero rotational angular momentum (*i.e.*, $j = 1$), and contributes significantly to the deuteron relaxation of D_2 in *para*-D_2–Ar (to see this compare the (1,1) element with other elements of the σ_V and σ_T cross section matrices for the *para*-D_2–Ar isomer in Fig. 4.20). Thus, at low temperatures the deuteron relaxation times for *para*-D_2–Ar are significantly shorter than those for *ortho*-D_2–Ar. At those temperatures for which the population of the higher rotational levels of the *ortho* isomer is negligible, the theory predicts extremely long relaxation times for the deuteron in the *ortho*-D_2–Ar system. Under similar conditions, no significant change is predicted for the deuteron relaxation times in the *para*-D_2–Ar system. However, at extremely low temperatures, the decrease of temperature is expected to increase the deuteron relaxation times for the *para*-D_2–Ar isomer via the average relative velocity factor, $\bar{c}_r$. The average velocity equally affects the already very long relaxation times for the *ortho*-

D_2–Ar isomer at these temperatures. It is obvious that the effect of the first factor decreases with increasing temperature, and becomes negligible at temperatures in which the population of the $j = 0$ level is insignificant (*e.g.*, above $T = 400\,\mathrm{K}$), see Fig. 4.24.

The difference in the DQ coupling constants of the two isomers is another factor introducing a difference between the deuteron relaxation times for them. This factor remains equally effective for all temperatures, so long as the the DQ interaction is the dominant relaxation mechanism. At high temperatures, for which the effect of the first factor becomes negligible, the ratio of the DQ relaxation times for the two isomers, $\frac{T_{1DQ}(ortho)}{T_{1DQ}(para)}$ is approximately equal to $(\frac{\omega_{DQ}(para)}{\omega_{DQ}(ortho)})^2 = 1.33$, see Eq. (4.3). In this approximation the values of the matrix products in the T_{1DQ} equation for the two isomers are assumed to be equal. Assuming a negligible SR contribution, one obtains the same value for the ratio of the overall relaxation times, *i.e.*, $\frac{T_{1\rho}}{T_{1\rho}} = 1.33$. At those temperatures for which the SR and the DQ relaxations are comparable, the above assumption is not, however, valid. As can be seen from Fig.4.21-(a), increasing the temperature increases the contribution of the SR relaxation for both isomers. This increase does not affect the high temperature value of the $\frac{T_{1DQ}(ortho)}{T1_{1DQ}(para)}$ ratio, but does decrease the $\frac{T_{1\rho}}{T_{1\rho}}$ ratio. For very high temperatures, at which the SR relaxation dominates the overall relaxation times for both isomers, the $\frac{T_{1\rho}}{T_{1\rho}}$ ratio approaches $\frac{T_{1SR}(ortho)}{T_{1SR}(para)}$, which is given approximately by $(\frac{\omega_{SR}(para)}{\omega_{SR}(ortho)})^2 = 1.063$. Here also, it is assumed that the matrix products in the T_{1SR} equation for the two systems are equal. Note that the T_{1SR} values for the two isomers are very close at all temperatures, see Fig. 4.21-(a). Since the difference between the SR coupling constants for the two systems is very small, it can be concluded that the difference between the values of the matrix products in the T_{1SR} equations for the two systems is negligible. This justifies the above assumption.

Non-rigidity of the D_2 molecule introduces an additional temperature dependence to the relaxation times; its effects will be discussed in Sec. 5.5.

Density-dependence

The density-dependences of the components and the overall relaxation times of the deuteron for the two parity isomers of D_2 in the D_2–Ar system at 300 K and 11.75 Tesla are shown in Fig. 4.21-(b). This figure shows that T_1/ρ for each component, as well as for the overall relaxation times for each isomer, are decreasing functions of density. Figure 4.21 shows also that the DQ interaction is the dominant relaxation mechanism at all densities. The contribution of the SR interaction is not, however, negligible. Increasing the density slightly increases the SR contribution to the overall relaxation time for each isomer. The rate of this increase is larger for the *ortho*-D_2–Ar system. The asymptotic contributions of the SR interaction to the relaxation times for the *ortho*-D_2–Ar and *para*-D_2–Ar systems at 300 K and 11.75 Tesla are approximately 20% and 10%, respectively.

In comparison with the HD–Ar system, the rate at which the relaxation times approach their asymptotic (linear-regime) values is significantly slower for both parity isomers of the D_2–Ar system. The density-dependence of the relaxation times becomes linear at densities above 25 amagat for both isomers of the D_2–Ar system. The significant difference between the density-behaviors of the deuteron relaxation times for the HD–Ar and D_2–Ar systems is due to: a) the larger *g-factor* for the D_2 molecule; b) the smaller average relative velocity, $\bar{c}_r$; c) the significantly smaller cross sections for the D_2–Ar system. These differences result in a significantly larger contribution of the frequency-dependent term to the relaxation times. This enhances the density-dependence of the relaxation times, and hence extends the nonlinear-regime.

Field-dependence

In addition to the extension of the nonlinear-regime discussed above, the relatively large contributions of the field-dependent terms enhance the field-dependence of the deuteron relaxation times for both parity isomers of the D_2–Ar system. The field-dependence of the components and the overall relaxation times for the deuteron of D_2 in the *ortho*-D_2–Ar and *para*-D_2–Ar systems at 300 K and 1 amagat are shown in Fig. 4.22. This figure indicates a much stronger field-dependence of the deuteron relaxation times for both systems than is observed for the HD–Ar system, compare Figs 4.14 and 4.22. For extremely low field-strengths, *i.e.*, below 0.1 Tesla, the relaxation times are, however, field-independent. The dominant relaxation mechanism is the DQ interaction for both systems over the entire range of the field-strengths. Figure 4.22 shows also that changing the field-strength does not significantly change the relative contributions of the SR and DQ relaxations.

4.5.3 Relaxation of the total magnetization in mixtures of *ortho* and *para*-D_2–Ar systems

It has been pointed out in Sec. 3.3.2 that it is not possible to measure individual relaxation times for the deuteron of *ortho*-D_2 and *para*-D_2 in a mixture of the two isomers when the ratio of their deuteron relaxation times is very small.[‡] Under this condition the experimental data which can be obtained from a T_1 experiment is limited to the inversion-recovery points for the total magnetization, and a decay index found by fitting a single-exponential function to them. This decay index will be called the effective relaxation time, and will be denoted by T_1^*. Since no theoretical method has been devised so far to calculate the inversion-recovery curve of the total magnetization for a mixture of two parity isomers, this limitation has been an obstacle for the evaluation of the theoretical results under the above-mentioned condition. Consequently, in most of the NMR studies that have been carried out on mixtures of *ortho*-D_2 and *para*-D_2 under this condition, this problem has been dealt with either by neglecting the contribution of the *para*-D_2 isomer to the NMR signal,[6] or by using *ad hoc* methods, *e.g.*, writing the total relaxation rates as a weighted sum of the individual relaxation rates of the two isomers with adjustable parameters.[55] In this section a simple theoretical method will be proposed to calculate the inversion-recovery curve for the total magnetization. The calculated inversion-recovery curve can be compared directly with the experimental inversion-recovery points for the total magnetization. Once the theoretical inversion-recovery curve for the total magnetization is at hand, a second comparison can be made between

[‡]When the deuteron relaxation times for the two isomers are significantly different, say by a factor of 5 or more, however, they can be measured separately by fitting a bi-exponential function, similar to Eq. (3.8), to the inversion-recovery curve for the total magnetization. See, for example, Refs. 24, 114, 115.

the theoretical and experimental results by calculating the single-exponential decay index for this curve (*i.e.*, the effective relaxation time T_1^*). Thus, a comparison between the experimental and theoretical results for a mixture of the two parity isomers is possible via two methods. These two methods are, however, correlated, and cannot be regarded as independent methods. It should be noted also that neither of these methods allows a detailed evaluation of the theoretical results obtained for individual isomers.

a) The inversion-recovery curve for the total magnetization

The normalized total magnetization for a mixture of *ortho*-D_2–Ar and *para*-D_2–Ar at each instant τ in the inversion-recovery experiment can be calculated via Eq. (3.7) using the relaxation times obtained for the individual components. For equilibrium mixtures of the two parity isomers the fractions of the total magnetization produced by *ortho* and *para* isomers, f_o and f_p, appearing in Eq. (3.7), are generally temperature-dependent due to the temperature dependence of the fractional populations, see Eq. (3.5). Since the conversion rate between the two parity isomers of D_2 is extremely slow,[67] however, these fractions can be considered constant during a series of typical variable temperature T_1 experiments. In other words, a mixture consisting of certain mole fractions of the two parity isomers of D_2 retains its original composition during a typical NMR experiment. Such a mixture is called a *frozen-out* mixture. The fractions f_o and f_p for a frozen-out mixture are determined by the temperature at which the mixture is prepared (or by the temperature at which the prepared mixture is stored for a long period of time). The temperature-dependence of the ratio $\frac{M_{\infty o}}{M_{\infty p}} = \frac{f_o}{f_p}$, along with the rotational populations for equilibrium and high-temperature frozen-out mixtures of the two parity isomers of D_2 are calculated, and are shown in Fig. 4.24-(b). It can be seen from

this figure that the $\frac{f_o}{f_p}$ ratio for the equilibrium mixture decreases with increasing temperature and reaches its asymptotic value (*i.e.*, 5) at approximately 160 K. It can be concluded that the chemical preparation of D_2 gas at any temperature above 160 K results in a mixture with asymptotic fractional magnetizations for the two parity isomers, which are $f_o = \frac{5}{6}$ and $f_p = \frac{1}{6}$, respectively.

The commercial D_2 gas used in the NMR experiments, is usually a room temperature frozen-out mixture of the *ortho* and *para* parity isomers, for which, according to the above discussion (see also Fig. 4.24), $f_o = \frac{5}{6}$ and $f_p = \frac{1}{6}$. Thus, for practical purposes it is useful to calculate and present the total magnetization for the room temperature frozen-out mixture of the two parity isomers of the D_2–Ar system. Note that the results for equilibrium and room temperature frozen-out mixtures are, however, the same for all temperatures above 160 K.

Figure 4.23-(a) shows the simulated inversion-recovery curves for the normalized deuteron magnetization in the *ortho*-D_2–Ar and *para*-D_2–Ar systems (calculated by using Eq. (1.4) and the T_1 values for the individual systems) at 1 amagat and 11.75 Tesla for the temperatures 100 and 500 K. The corresponding normalized total deuteron magnetizations for a room temperature frozen-out mixture of the two parity isomers are calculated point-wise for each value of τ using Eq. (3.8), and are shown in Fig. 4.23-(a). In the simulation of these inversion-recovery curves a large number of τ values has been used in order to cover completely the recovery curves for the total magnetization. Figure 4.23-(a) shows that the behavior of the recovery curves for the total magnetization is very similar to that for the *ortho* isomer. This similarity increases as the temperature increases, due to the fact that the difference in the relaxation times for the two parity isomers decreases with increasing temperature, see Fig. 4.21.

b) The effective relaxation time T_1^*

The effective relaxation time, T_1^*, for each simulated inversion-recovery curve for the total magnetization is calculated by fitting it into a single-exponential function of the form of Eq. (3.1). Values of the function $\ln(\frac{2M_\infty}{M_\infty - M_\tau})$ calculated from the simulated inversion-recovery points are plotted in Fig. 4.23-(a) in order to visualize the quality of this fitting procedure. For a true single-exponential relaxation process this function should be linear in τ, with a slope of T_1^{-1}. As can be seen from this figure, under the specified conditions the values of this function for the total magnetization can be well characterized by a straight line for both temperatures. This means that the relaxation of the total magnetization can be described by a single-exponential decay function similar to that used for the recovery of the magnetizations of the individual isomers. Fitting a single-exponential function to the total magnetization points, which are generated originally from a bi-exponential function, *i.e.*, Eq. (3.1), introduces some error to the calculated effective relaxation times in the form of standard deviation of the fit. The standard deviation obtained for the single-exponential fitting procedures in this study was of the order of 1-3% depending on the ratio of the relaxation times of the two parity isomers.

The values of the effective relaxation times T_1^* obtained for the relaxation of the total magnetization in a room temperature frozen-out mixture of the *ortho*-D_2–Ar and *para*-D_2–Ar systems at 11.75 Tesla and at 1 and 10 amagat densities are plotted versus temperature in Fig. 4.23-(b). For both densities, and for the entire temperature range shown in this figure, the condition that the value for the ratio of the deuteron relaxation times for the two isomers be small is valid. It can be seen from this figure that the values of the relaxation times for the total magnetization and for the *ortho* system differ by 10-20%. This observation indicates that neglecting the contribution of the *para* isomer to the total magnetization results

in errors several times larger than the typical errors for the experimental results. Thus, neglecting the contribution of the *para* isomer to the total magnetization represents an incorrect evaluation of the theoretical results.

In conclusion, it can be said that the two new methods proposed in this section, *i.e.*, the method of inversion-recovery curves for the total magnetization and the method of effective relaxation times, provide reliable means for evaluation of the theoretical results. The advantage of the former method is that it does not introduce any error to the evaluation process, whereas the assumption of a single-exponential relaxation for the total magnetization in the latter method introduces some errors to the final results (in the form of the standard deviation of the fitting procedure). These errors, however, can be evaluated exactly, and can be taken into account in the calculation process. As mentioned before, neither of these two methods can be used, however, to evaluate theoretical results obtained for individual isomers.

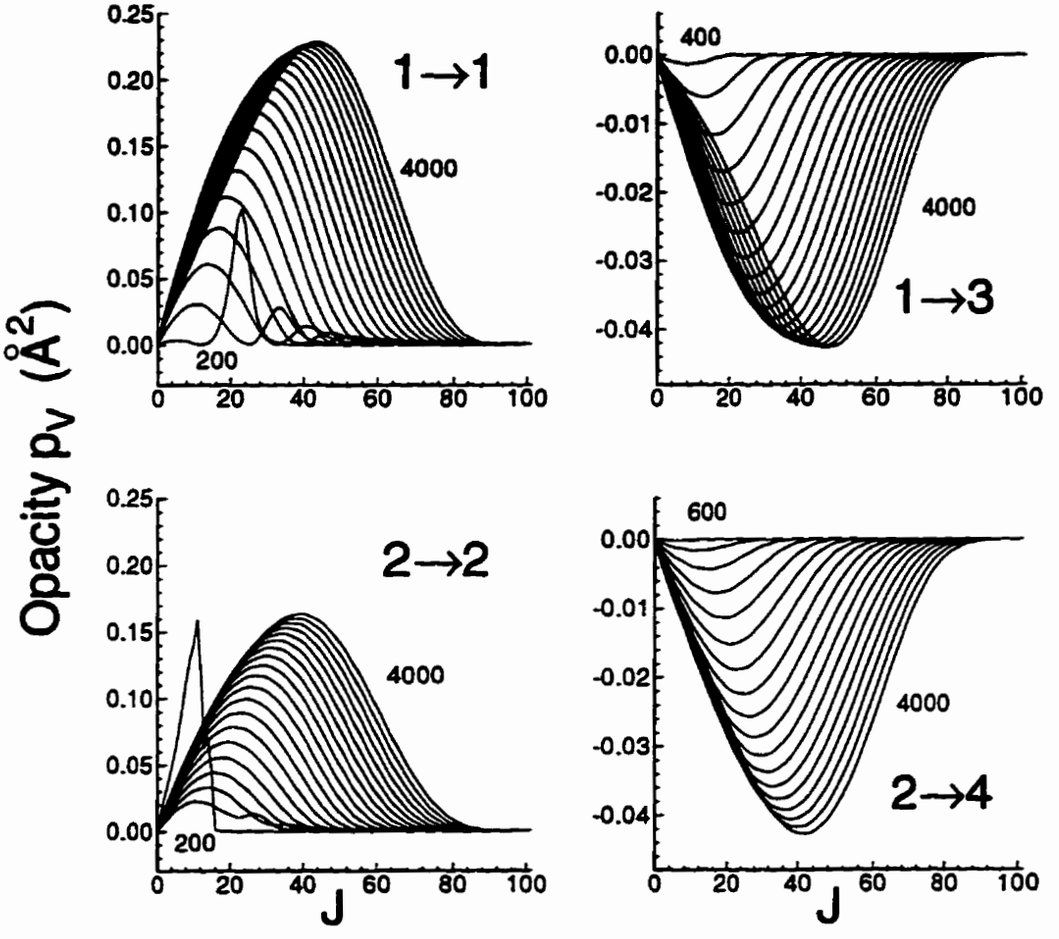

Figure 4.16: Typical J-dependence of the state-to-state $\mathcal{P}_V(J;j,j')$ opacity for the *para*-D_2–Ar, (a) and (b), and *ortho*-D_2–Ar systems, (c) and (d), for a series of total energies in steps of $200\,cm^{-1}$. For simplicity only the two curves for the lowest and highest total energies have been labeled. As can be seen, state-to-state $\mathcal{P}_V(J;j,j')$ opacities at all energies show well-behaved J-dependences. The different behavior observed for the 2→2 element at the lowest energy is due to orbiting resonances in the *ortho*-D_2–Ar system, corresponding to the $j = 2$ resonance range. Note the different scales used for different elements.

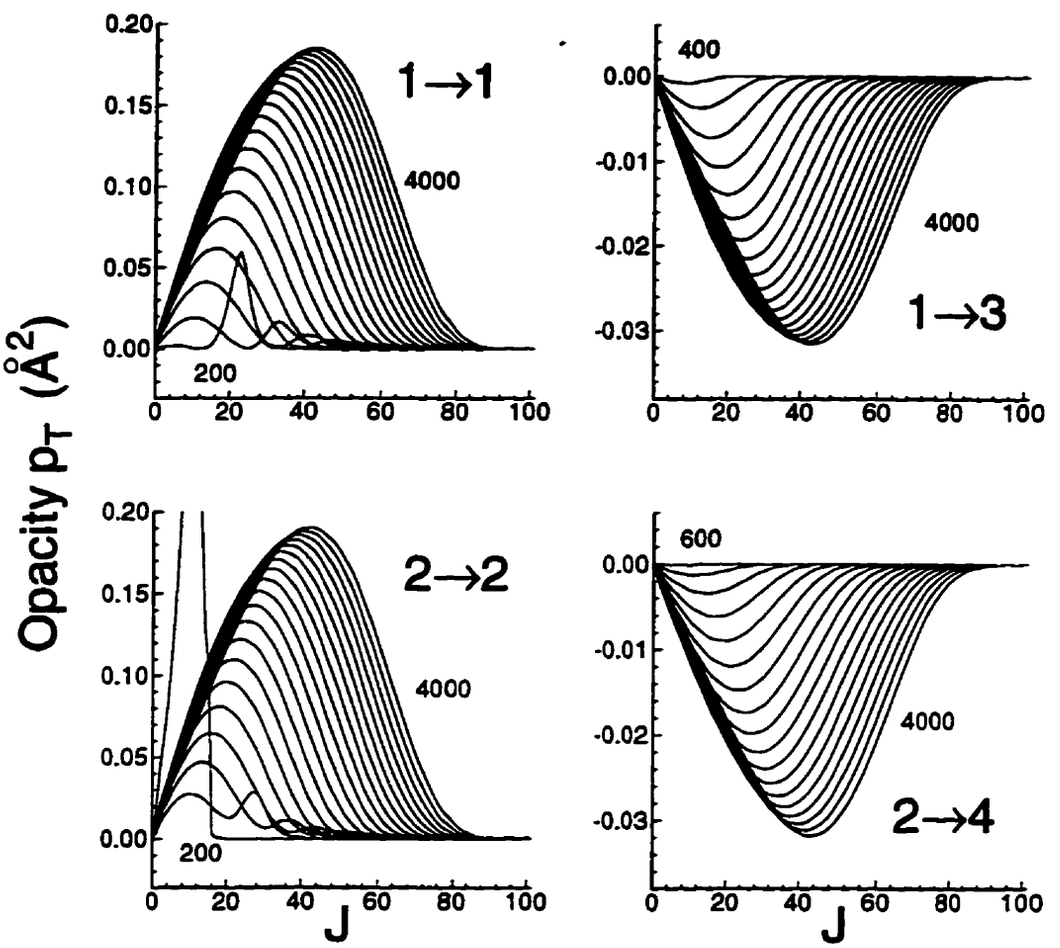

Figure 4.17: Typical J-dependence of the state-to-state $\mathcal{P}_T(J;j,j')$ opacity for the *para*-D_2–Ar, (a) and (b), and *ortho*-D_2–Ar systems, (c) and (d), for a series of total energies in steps of 200 cm^{-1}. For simplicity only the two curves for the lowest and highest total energies have been labeled. As can be seen, state-to-state $\mathcal{P}_T(J;j,j')$ opacities at all energies show well-behaved J-dependences. The different behavior observed for the 2→2 element at the lowest energy is due to orbiting resonances in the *ortho*-D_2–Ar system, corresponding to the $j = 2$ resonance range. Note the different scales used for different elements.

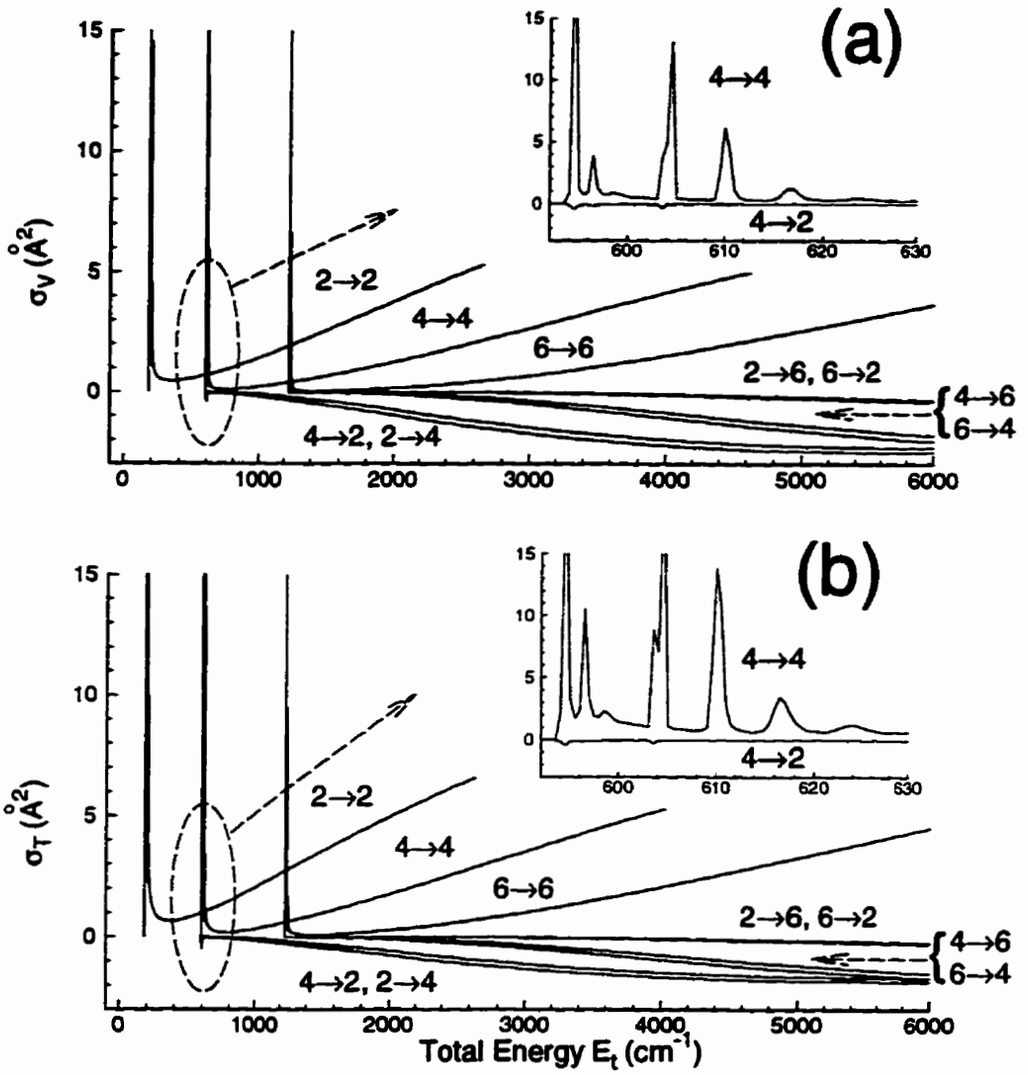

Figure 4.18: Energy-dependence of some state-to-state $\sigma_V^E(j,j')$ (a) and $\sigma_T^E(j,j')$ (b) cross sections for the *ortho*-D_2–Ar system. Note the significant effect of orbiting resonances on the diagonal elements of each cross section. The small window in each part expands the resonance range above the $j = 4$ rotational level. Calculations of the cross sections for the resonance range of each rotational level have been carried out with a fine mesh of 0.5 cm^{-1} starting from a few wavenumbers below, up to at least 50 wavenumbers above the rotational threshold energy. Note the similarities and differences between the two cross sections in the resonance range. Note also the small effects of orbiting resonances on the off-diagonal elements.

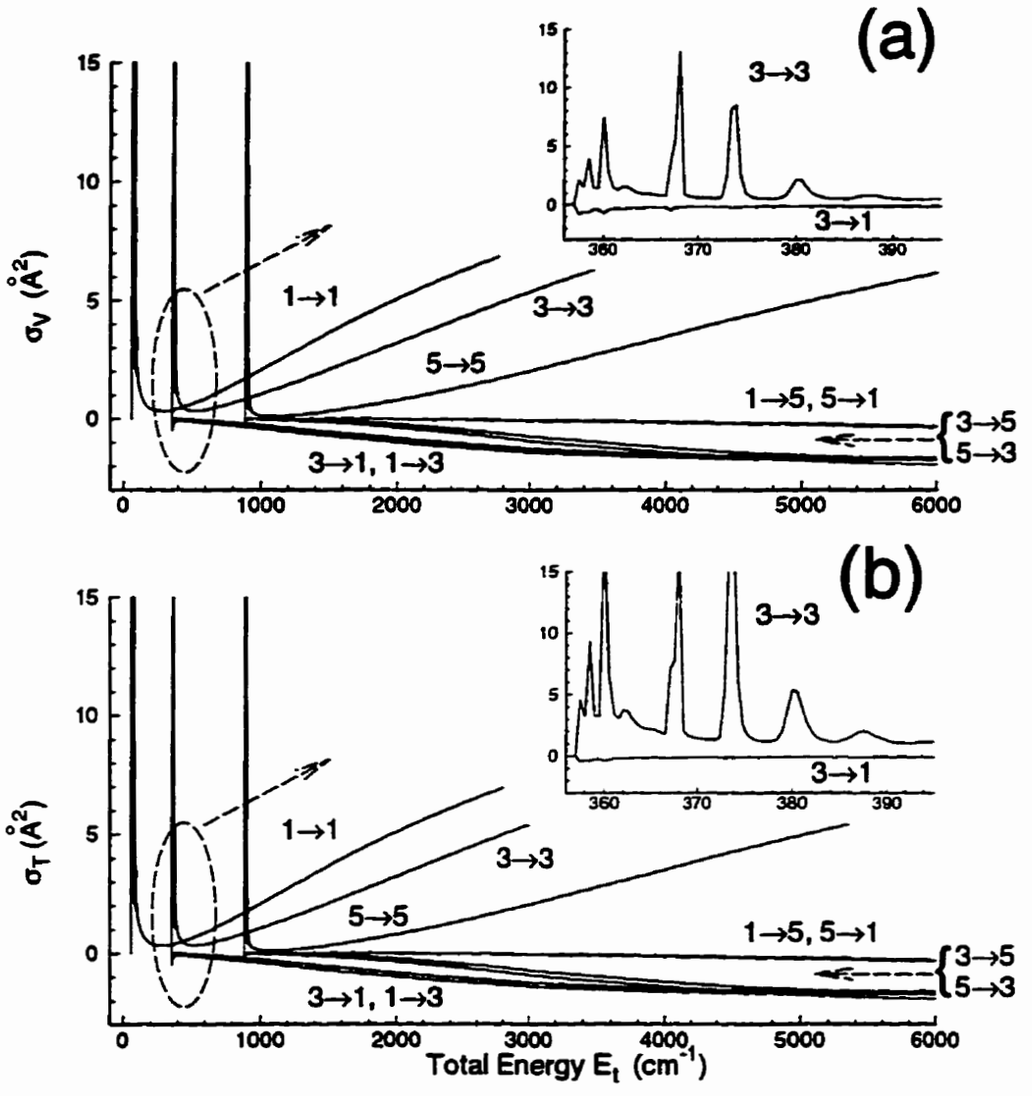

Figure 4.19: Energy-dependence of some state-to-state $\sigma_V^E(j,j')$ (a) and $\sigma_T^E(j,j')$ (b) cross sections for the *para*-D_2–Ar system. Note the significant effect of orbiting resonances on the diagonal elements of each cross section. The small window in each part expands the resonance range above the $j = 3$ rotational level, and shows that the effects of the orbiting resonances on the off-diagonal elements is very small. Note the similarities and differences between the two cross sections in the resonance range.

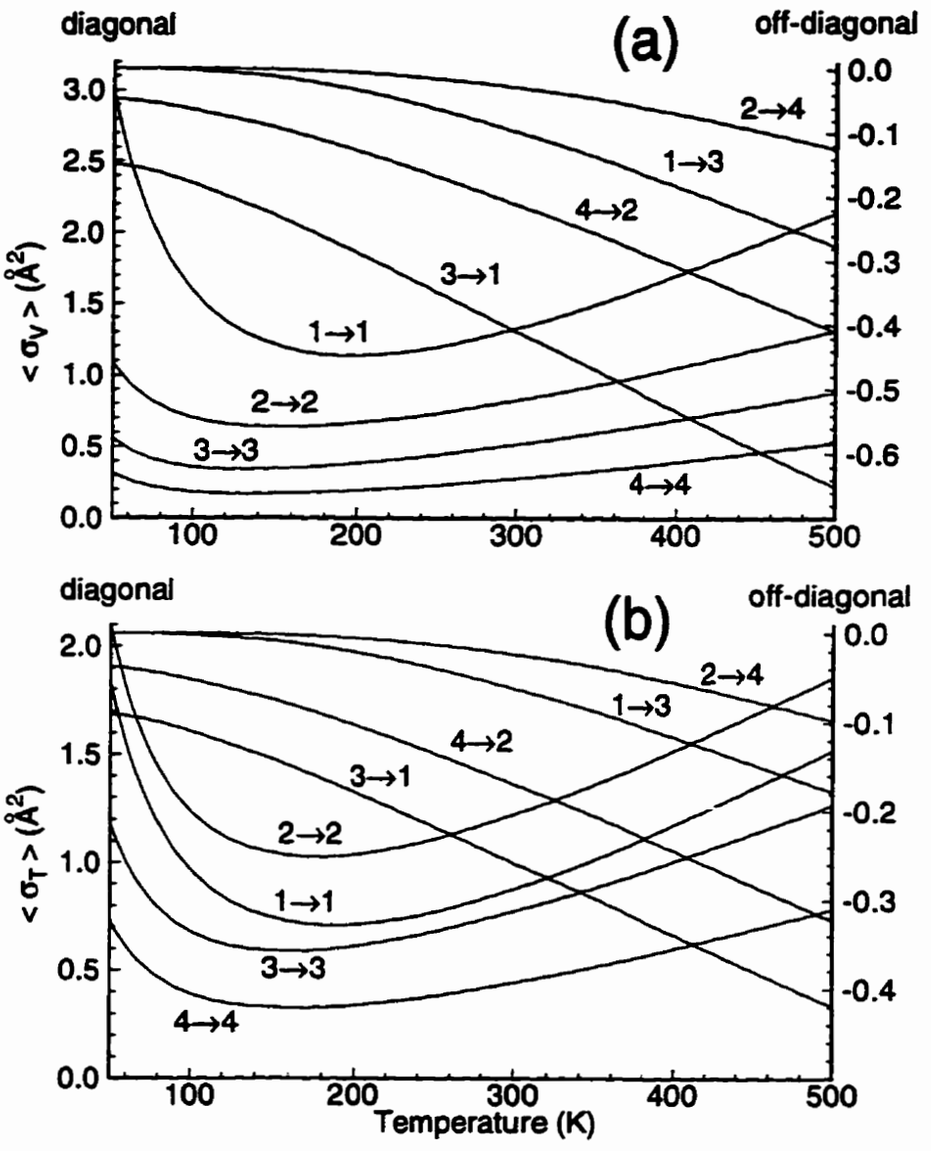

Figure 4.20: Temperature-dependence of the thermally-averaged state-to-state $\sigma_V(j,j')$ (a) and $\sigma_T(j,j')$ (b) cross sections for the D_2–Ar system. Note the different scales used for the two sets of elements. Calculations have been carried out for temperatures between 50 and 500 K in increments of 5 K.

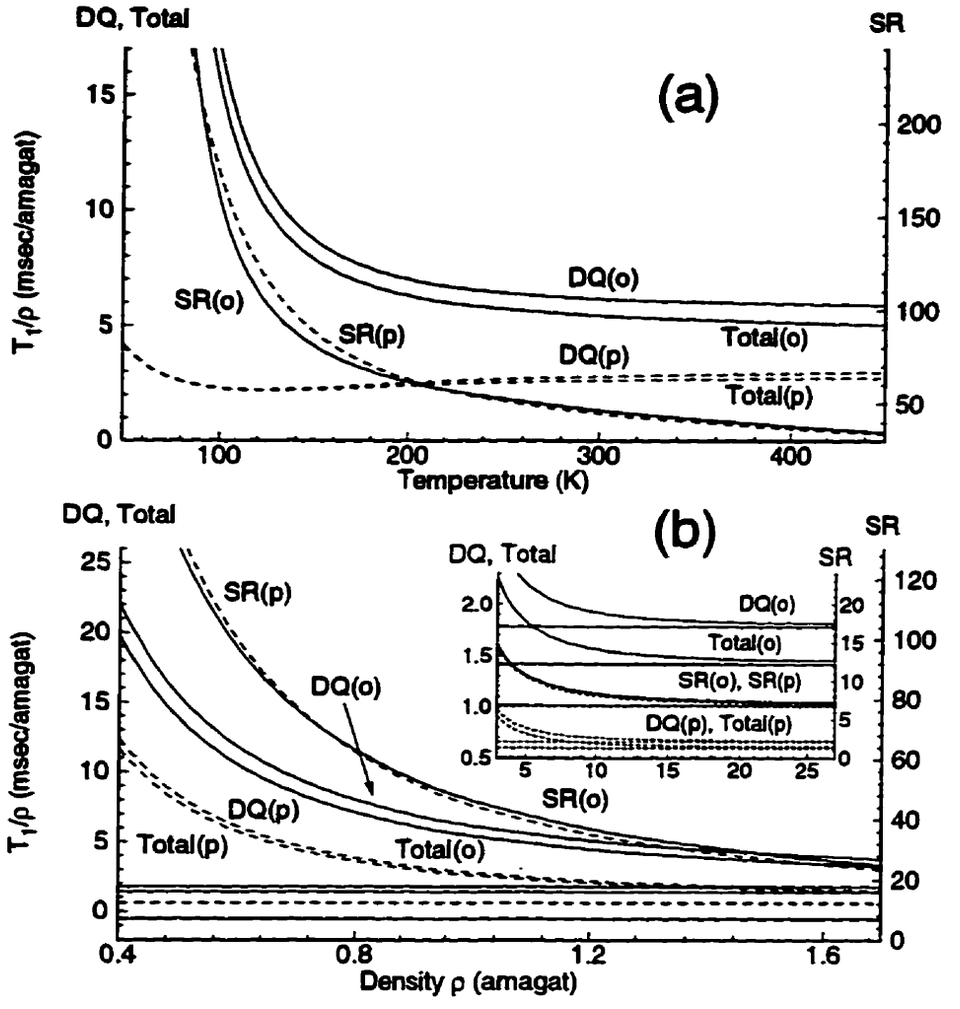

Figure 4.21: (a) Temperature- and (b) density-dependence of the different components of the spin-lattice relaxation time for the deuteron of the two parity isomers of D_2 in the D_2–Ar system. The T_1/ρ values in (a) are calculated for $B_0 = 11.75$ Tesla and $\rho = 1$ amagat, while the T_1/ρ values in (b) have been obtained for $B_0 = 11.75$ Tesla and $T = 300$ K. The letters o and p in the brackets denote the corresponding components for the *ortho* and *para* isomers, respectively. The dashed line-pattern has been used for the corresponding relaxation times of the *para* isomer. The straight lines in (b) show the corresponding linear-regime relaxation times. The small window in (b) shows the density-dependence of the relaxation times at higher densities. Note the different scales used for the various components.

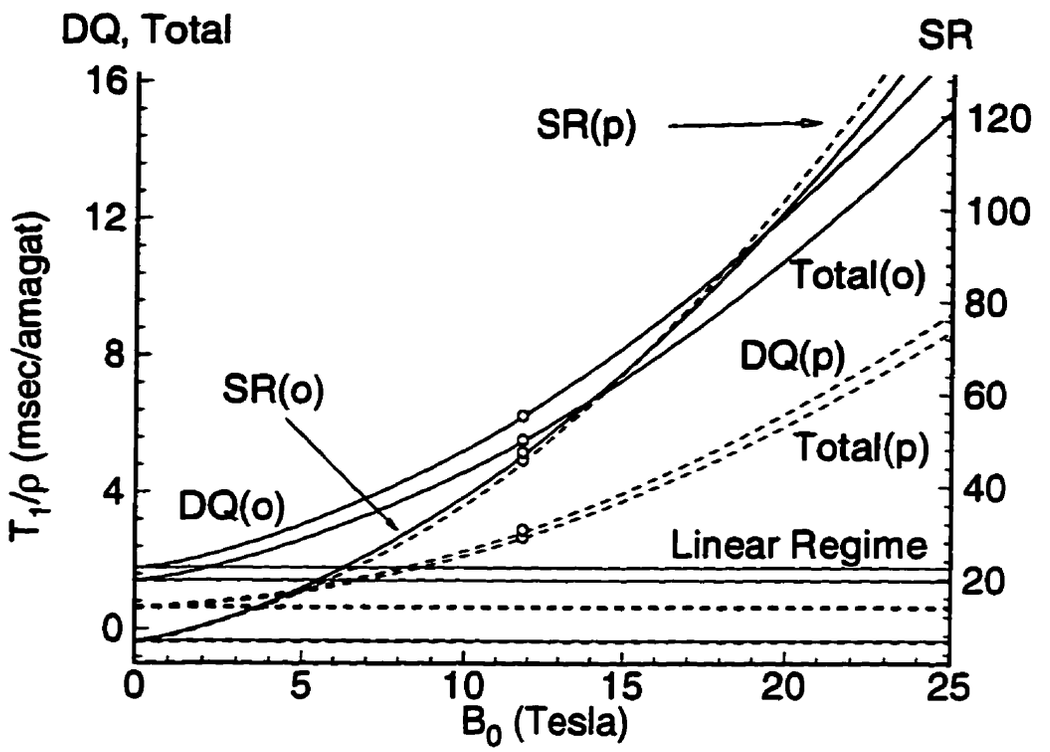

Figure 4.22: Field-dependence of the components of the spin-lattice relaxation time for the deuteron of D_2 in the D_2–Ar system at $\rho = 1$ amagat and $T = 300$ K. The letters o and p in the brackets denote the corresponding components for the *ortho* and *para* isomers, respectively. The dashed line-pattern has been used for the corresponding relaxation times of the *para* isomer. The straight lines show the corresponding linear-regime relaxation times. The open circles show the relaxation times at $B_0 = 11.75$T, which is the field strength used in the experimental part of the present research. Note that the relaxation times are field-dependent for field strengths as low as 0.1 Tesla. Note also the different scales used for the various components.

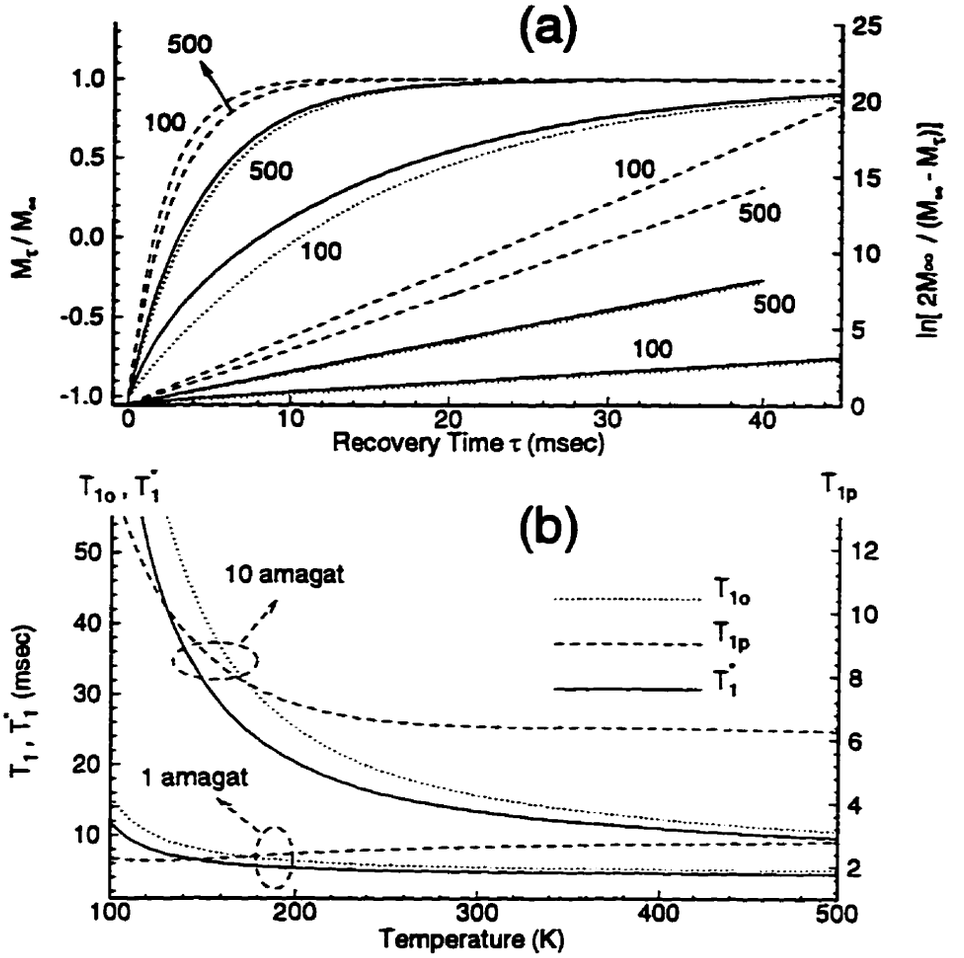

Figure 4.23: (a) Simulated inversion-recovery curves and (b) the temperature-dependences of the relaxation times for *ortho*-D_2–Ar, T_{1o} (dotted curves), *para*-D_2–Ar, T_{1p} (dashed curves), and the total magnetization in a room temperature *frozen-out* mixture of *ortho*-D_2–Ar and *para*-D_2–Ar, T_1^* (solid curves) at 1 amagat and 11.75 Tesla. Numbers in (a) represent the temperatures of the mixture. The straight lines in (a) show the values of the recovery function $\ln(\frac{2M_\infty}{M_\infty - M_\tau})$; their slopes are equal to the T_1^{-1} values. The linearity of the recovery function obtained for the total magnetization justifies a single-exponential fit to the corresponding experimental inversion-recovery curves under these conditions, see Sec.3.3.2. The values of the deuteron relaxation times obtained for *ortho*, *para* and the frozen-out mixture are 2.27, 15.28 and 11.65 for $T = 100$ K, and 2.79, 4.97 and 4.49 msec for $T = 500$ K.

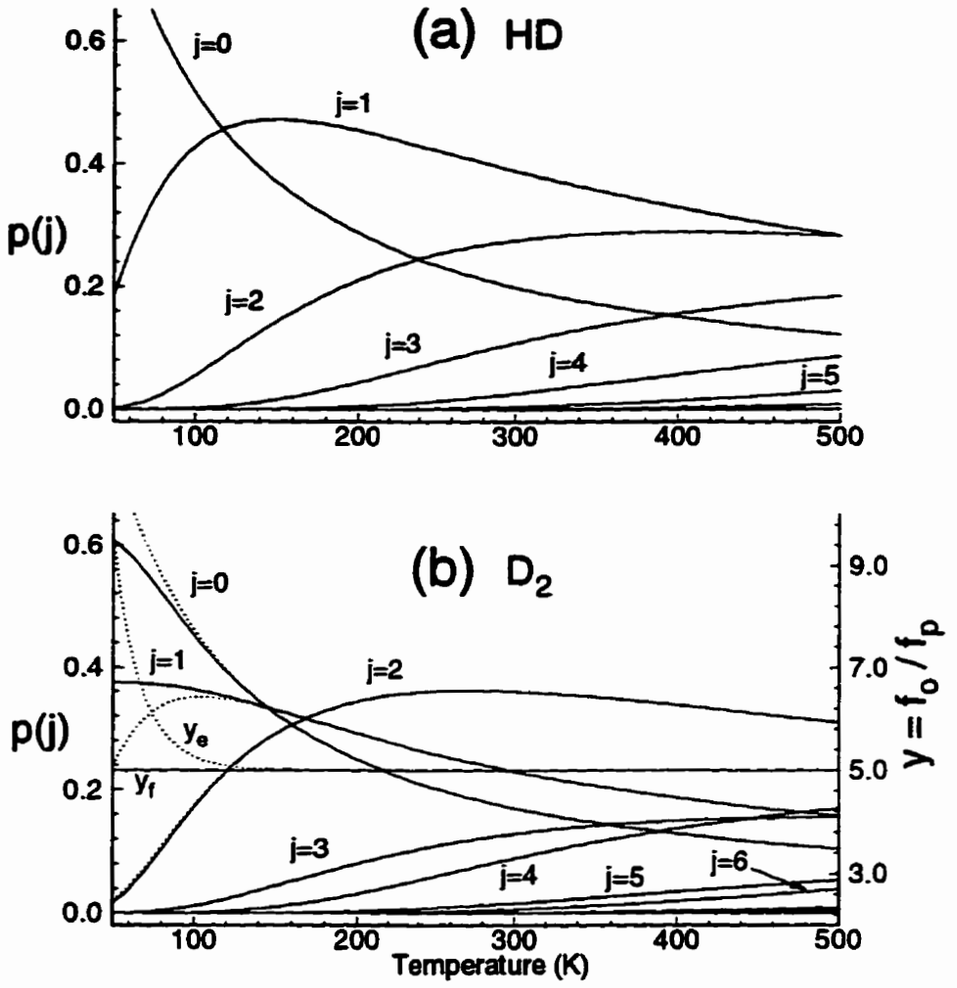

Figure 4.24: Temperature dependences of the relative populations of the rotational states for (a) HD and (b) D_2. The dotted and solid curves in (b) show, respectively, the corresponding populations of the equilibrium and the frozen-out room temperature *ortho-para* mixtures. Since the $I = 0$ modification of the *ortho* isomer is not NMR active, only the $I = 2$ modification of the *ortho* isomer is included in the calculation of these populations. The curves labeled y_e and y_f in (b) show the temperature-dependences of the $y = \frac{M_{\infty o}}{M_{\infty p}} = \frac{f_o}{f_p}$ ratio for the equilibrium and frozen-out room temperature mixtures of *ortho*- and *para*-D_2, respectively.

Chapter 5

Comparison of Experimental and Theoretical Results; Discussion and Conclusion

In this chapter, experimental and theoretical results are compared with one another and the results of this comparison are discussed. The general considerations for converting the theoretical and experimental data to comparable quantities will be discussed in Sec. 5.1. These conversions and the comparisons between the two data sets for the HD–Ar and D_2–Ar mixtures will be presented in Secs. 5.2 and 5.3, respectively. Based on the results obtained in these sections, the XC(fit) potential for the hydrogen-argon system used in the calculations of this study will be evaluated in Sec. 5.4. Discussions on the calculations and experiments, including possible sources of error and their effects on the final results, will be discussed in Secs. 5.5 and 5.6, respectively. Finally, the chapter will be concluded by an overall evaluation of the experimental and theoretical results.

5.1 Conversion of experimental and theoretical results into comparable quantities; General considerations.

The experimental spin-lattice relaxation times obtained for the HD–Ar and D_2–Ar systems presented in Ch. 3 are raw data, and cannot be compared directly with the theoretical results. In order to process the experimental data and convert them into quantities directly comparable to the theoretical results, it is necessary to review both the assumptions made in the derivation of the T_1 equations and the experimental conditions. The major assumptions used in the formulations of the T_1 equations, Eqs. (4.1)-(4.3), are: (a) isolated atom-diatom binary collisions and (b) uncorrelated successive collisions. From the experimental point of view the former assumption is critical since the experimental conditions should be set such that only atom-diatom binary collisions contribute to the relaxation of the nuclei under study. As pointed out in Sec. 3.1, this assumption is satisfied only for mixtures with hydrogen (or the diatom, in general) at infinite dilution, for which direct NMR measurements are not possible, because of S/N ratio considerations. It was mentioned also in Sec. 3.1 that such a study can be carried out indirectly by extrapolation of the results obtained for mixtures with small concentrations of the diatom to infinite dilution. Experiments on mixtures with different mole fractions of the diatom should be carried out under the same conditions, including the temperature and total density. It is not uncommon that for practical reasons the same sets of experimental conditions are not reproduced exactly for mixtures with different mole fractions. The experimental data obtained in such cases should be normalized, or corrected, to produce corresponding results for the required conditions.

Under certain experimental conditions the collision atom-diatom pair form a relatively long-lived Van der Waals complex. The formation of such long-lived complexes may have large effects on the measured spin-lattice relaxation times.[72] It is obvious that the inclusion of the data obtained under such conditions may introduce significant errors into the extrapolated results due to the fact that the concentrations and life-times of these complexes, and hence their contributions to the measured relaxation times, depend strongly upon the mole fraction.

At intermediate and high densities, the major unwanted contributions to the NMR relaxation times arise from collisions between two diatomic molecules. These collisions, which will be called *self-collisions*, induce NMR relaxation via the same mechanisms as atom-diatom collisions (*i.e.*, *non-self collisions*) do. The contribution of the self-collisions to the relaxation times depends upon the intermolecular potential between the diatomic molecules. Once the formulation of the relaxation times for the self-collisions is known, and a reliable potential is available, it is also possible to calculate the contributions from these collisions. Thus, it would be possible to calculate directly the relaxation times for the finite dilution mixtures, and compare them with the experimental results. The atom-diatom results obtained using such a method would clearly be equivalent to the infinite dilution results. The computer time needed for such theoretical calculations is much longer than that needed for the calculations for the atom-diatom system, because of the additional variables introduced by the diatomic collision partner (*e.g.*, the rotational states of the second diatom). This makes the proposed method uneconomical at present.

Another alternative method to deal with the problem of the self-collisions is to run a set of experiments on the pure diatomic gas. These experiments should be carried out under conditions such that the frequency of self-collisions in the pure gas is the same as that in the mixture. The condition of the equal collision

frequencies is met if the number density of the diatomic gas is the same in the two sets of experiments. Subtraction of the relaxation rate measured for the pure diatomic gas from that obtained for the mixture should give the pure contribution of the desired non-self (atom-diatom) collisions. The results obtained via this simple subtraction of the relaxation rates is valid only if the self and non-self collisions are not correlated (*i.e.*, assumption (b) above). With this assumption, the relaxation of the nuclear magnetization can be described as a set of two parallel first-order process, which justifies the subtraction.

According to Gordon[20] and Jameson,[116] even in the absence of correlations between the two sets of collisions, the separate contributions of the self and non-self collisions are additive only at the level of the collision frequencies, and not at the level of relaxation rates (see also Ref. 117). However, a simple algebraic analysis of the T_1 equations shows that at the limits of low densities and high magnetic field strengths, the two methods give precisely the same results. Also, when the mole fraction of the diatomic gas, x, in the mixture is small, *e.g.*, $x = 0.05$, the difference in the results obtained for the contribution of the self-collisions from the two methods is of the order of $100x\%$. Such small differences introduce negligible or relatively small errors into the evaluation of the contribution of the non-self collisions via the subtraction method.

One important disadvantage of this method is the enhanced contribution of *wall-collisions* to relaxation of the nuclei in the pure diatomic gas. It can be shown that the contribution of wall-collisions to the relaxation times of the nuclei in the pure diatomic gas is larger than that in the mixture by a factor of $\frac{1-x}{x}$. The enhanced contribution of wall collisions becomes more important at lower total densities and when the relaxation times of the nuclei are long. The wall-collision contribution to the relaxation process is inversely proportional to the cross section and to the

number density of the collision partner. For a given mixture at a constant density, the contribution of the wall-collisions increases with the ratio $\frac{A}{V}$, in which A and V are the area of the internal surface and volume of the cell. This ratio is inversely proportional to the dimensions of the cell. Thus, for small sample cells, such as the one used in the experimental part of the present study, the contribution of wall-collisions might be significant in the relaxation of the nuclei in the pure diatomic gas at low densities.

From the above discussion it can be concluded that the most reliable method for derivation of the isolated contribution of the atom-diatom collisions to the relaxation times is the method of extrapolation to infinite dilution. Experimental points corresponding to the region of complex formation should be excluded from the extrapolation process, however.

In the method of extrapolation to infinite dilution used in the present study, the problem of reproducibility of the temperatures has been dealt with by using interpolation or extrapolation of the data in order to measure the corresponding relaxation times at the required (common) temperatures. The maximum distance between the actual and interpolated points on the temperature scale in this study is less than 10 K. Generally, there are two methods for the interpolation or extrapolation within a data set. In the first method the *lever rule* is used to calculate the relaxation time at the desired point. This is equivalent to finding the relaxation times by locating the desired temperature on the line-segment connecting the two surrounding points (or the first two adjacent points when extrapolating). The minimum errors in the interpolated relaxation times can be evaluated from the errors in the temperature measurements and the relaxation times at these two points. The actual errors, which cannot be evaluated, can be quite large when the temperature dependences of the relaxation times are non-linear, especially if

larger temperature steps have been used. In the second method, the interpolation process is based on the best-fit curve for the entire data set. The advantage of this latter method is that the assumption of a linear temperature dependence is not necessary. Further, the actual errors can be evaluated, since the precise functional forms of the relaxation times are mapped out by the entire data set. The actual errors introduced into the interpolated results in this method is the sum of the minimum errors calculated in the first method and the corresponding errors of the fitted curves (*e.g.*, $\pm 3SD$, in which SD is the standard deviation of the fit). This means that all of the points in a data set contribute to the values and errors of the interpolated relaxation times. The accuracy of this method is independent of the actual functional forms of the relaxation times. Using the fitted curves in the interpolation processes introduces experimentally unrealistic smoothness into the infinite dilution results. This unrealistic smoothness is, however, compensated by the additional realistic errors introduced by the curve-fitting processes (in the form of standard deviations). The smoother results may, however, better represent the actual temperature behavior of the relaxation times. When the temperature dependence of the relaxation times is non-linear, which is the case for the present study, this method is the only logical choice.

The adjustment of the results for all mixtures to a common set of total densities, when required, is carried out by assuming a linear dependence on density for the relaxation times over the narrow interval between the actual and the desired densities. The maximum difference between the actual and desired density for the experimental part of the present work is about 2.5%. The errors introduced into the adjusted data by assuming a linear dependence on density over such a small interval are negligible, even if the measurements have been made in a non-linear regime. Obviously, such an assumption has absolutely no effect on the adjusted data in a

linear-regime, *e.g.*, for the deuteron relaxation times in the HD–Ar system at all densities above 3 amagat. When the agreement between theory and experiment is reasonably good, a more reliable estimate for the correction factor for the density adjustment can be extracted from the corresponding theoretical data points. Both of these methods fail to give reasonable results in the nonlinear regime when the difference between the desired and actual densities is large, *e.g.*, of the order of 10%. In these cases the problem of reproducibility should be solved by carrying out experiments for additional densities, and using a curve-fitting method, such as that described above for the temperature adjustment. The total errors introduced by the density adjustments and temperature interpolations for a reasonable experimental data set should not be larger than 1-2%.

The infinite dilution results are obtained simply by linear extrapolation of the relaxation times for the mixtures with two different small mole fractions. The errors introduced into the infinite dilution results in the extrapolation step can be quite large. Using geometric relations, it can be shown readily that for a two-point linear extrapolation the maximum error bar of the extrapolated result is given by

$$\Delta_0 = \frac{a\Delta_b + b\Delta_a}{|a-b|}, \tag{5.1}$$

in which a and b are the mole fractions of the two mixtures, and Δ_x is the error bar of the relaxation time at mole fraction x. In the derivation of this formula it has been assumed that errors in the mole fractions are negligible. When these errors are significant, they contribute an amount Δ_0' to the error bar of the extrapolated results, which is given by

$$\Delta_0' = \frac{a\delta_b + b\delta_a}{2|a-b|} \sum_{\pm} \frac{2|T_1(a) - T_1(b)| \pm (\Delta_a + \Delta_b)}{2|a-b| \pm (\delta_a + \delta_b)}, \tag{5.2}$$

with δ_x being the error bar associated with mole fraction x, and $T_1(a)$, $T_1(b)$ the measured relaxation times at mole fractions a and b, respectively. Equations (5.1) and (5.2) show that the extrapolation errors increase rapidly with increasing mole fractions of the diatomic gas. Also, when the two mole fractions are very close, these equations predict large errors.

For all of the experimental data obtained in the present study Δ_0' is very small, and can be neglected in comparison with Δ_0. Thus, the error bars reported herein consist solely of Δ_0 values. It can be seen from comparing the error bars of the extrapolated and finite dilution results, that the contribution of the extrapolation procedure to the error bars of the final results are relatively large, and non-negligible.

Many experimental results are reported with error bars for the extrapolated data estimated to be equal to those for the data point with the minimum abscissa. The two equations above show that this assumption is valid only when a (or b) is very close to zero and the errors in the mole fraction are negligible. Equations (5.1) and (5.2) show that under these conditions Δ_0 approaches Δ_a (or Δ_b), and Δ_0' vanishes.

To suppress the effect of the linear density factor on the relaxation times they are divided by density, and are thus converted to T_1/ρ values. The T_1/ρ values are more suitable for comparing the temperature dependence of the relaxation times for different densities at the same time. Also, the approach of the relaxation times towards the linear regime can be visualized more clearly in T_1/ρ versus ρ and T_1/ρ versus B_0 diagrams. It was for this reason that the demonstrations of the theoretical results throughout Ch. 4 were based on the T_1/ρ values.

5.2 Comparison of theoretical and experimental results for the HD–Ar System

Spin-lattice relaxation times

Temperature interpolations have been necessary for HD–Ar mixtures prior to extrapolation of the relaxation times to finite dilution, because different temperatures have been used for different mixtures. The outlier points of each data set, which do not represent the pure collisional relaxation processes, were not included in the curve-fitting procedure required for the interpolation. The total numbers of outliers for the proton and deuteron data sets are 4 and 8, respectively. Except for the deuteron data set for the mixture with 0.86% HD at 8.74 amagat, the standard deviations of the best-fit curves were very small. The proton and deuteron relaxation times have been interpolated for 13 values of temperatures between 180 K and 420 K with a step-size of 20 K.

The pairs of data sets used for extrapolation, and their common densities for which the data sets have been adjusted are as follows (see Table 3.1 for specifications of the mixtures); mixtures 1 and 5 at 8.54 amagat, mixtures 2 and 6 at 4.67 amagat, and mixtures 4 and 7 at 15.26 amagat. A linear dependence on density has been assumed for the adjustments of the relaxation times to a common density for each pair of data sets. The maximum adjustment of the densities corresponds to the pair of mixtures 2 and 6, and is about 2.5%. The above assumption for such small adjustments introduces no error into the final results for the deuteron, since its relaxation times are in the linear-regime at all three densities. This is true also for the proton at 15.26 amagat. The proton relaxation times at the other densities are not in the linear-regime, but are still far from the minimum of their T_1 versus density curves. However, the errors introduced by using a linear interpolation over

such small intervals are so small that they can be neglected.

The proton data set for the mixture with 0.86% HD at 0.96 amagat cannot be used in the extrapolation process, since no experiments have been made for the other mixtures at the same density (see Sec. 3.2.2). However, this data set will be treated as infinite dilution data, and will be included in the comparison with the theoretical results. Since the theory predicts a non-linear behavior for the relaxation of the proton of HD in the HD–Ar mixture at 0.96 amagat, it would be useful to use this experimental data set as a check point for the low density behavior of the relaxation times predicted by theory. However, in the comparison process it should be kept in mind that the contributions from the self-collisions to the relaxation times have not been corrected for this data set.

The infinite dilution relaxation time at each temperature has been obtained by linear extrapolation of the corresponding pair of the adjusted relaxation times to zero mole fraction of HD. The extrapolation error for each data point has been calculated via Eq. (5.1), neglecting the contributions from the relatively small errors in the mole fractions. The infinite dilution (*i.e.*, extrapolated) results for the proton and deuteron are compared with the theoretical results in part (a) of Figs. 5.1 and 5.2, respectively. As can be seen from these figures, and has been discussed generally in the previous section, the errors introduced in the extrapolation step are significant when compared with the original experimental errors (compare the error bars in these figures with those in Figs. 3.6 and 3.7, respectively). A comparison between the experimental (infinite dilution) and theoretical values of T_1/ρ for the proton and deuteron are given in part (b) of Figs. 5.1 and 5.2, respectively.

Figure 5.1 shows that the experimental and theoretical results obtained for the proton spin-lattice relaxation times in the HD–Ar mixtures are in excellent agreement. Even for the data set corresponding to 0.96 amagat, which has not been

corrected for self-collisions (*i.e.*, it is a finite dilution data set), the experimental and theoretical results are in relatively good agreement (*i.e.*, within a few percent). The differences between the experimental and theoretical results for this density are due mainly to the contribution of self-collisions to the relaxation processes.

The agreement between the experimental and theoretical results for the deuteron is relatively good, but not as much as it is for the proton. Figure 5.2 shows that the experimental spin-lattice relaxation times for the deuteron are generally shorter than those predicted by theory. Assuming ideal experimental conditions, the processes responsible for the systematically shorter experimental relaxation times obtained for the deuteron are possibly diffusion of the HD molecules into and out of the effective volume of the rf coil, contributions from wall-collisions, and J-coupling to the fast relaxing proton. All of these processes, which result in a faster decay of the nuclear magnetization, become more effective when the relaxation time is longer. In the first look, Fig. 5.2-(b) suggests that the experimental T_1/ρ values for the deuteron at the densities used in the experiments are in a nonlinear regime, as opposed to the theoretical results which predict linear-regime relaxation times for the same densities. But, the order of the experimental T_1/ρ values for the three densities is not consistent with theory. Also, the displacements of the experimental data points with respect to the density of the mixtures is much smaller than the error bars. These observations mitigate against the possibility of a systematic nonlinear dependence on the density for the experimental relaxation times obtained for the deuteron.

A comparison between the T_1 and T_1/ρ plots for the proton and deuteron shows that the agreement between experiment and theory for the deuteron is better at the two extreme temperatures, while for the proton agreement is better at the intermediate temperatures. A closer look at the plots shows that both observations

arise from the fact that at all densities the curvatures of the theoretical curves are slightly smaller than those of the experimental curves. A similar behavior can be observed in the results reported previously for the HD–He system.[4]

In comparison with the HD–He system, the agreement between the experimental and theoretical results obtained in the present work for the HD–Ar system is the same for the proton but significantly better for the deuteron. The error bars reported for the HD–He system are, however, significantly smaller: this is because they were not evaluated properly, in the sense that Eq. (5.1) has not been used. The relative values of T_1/ρ for both nuclei are generally larger in the HD–Ar system than in the HD–He system. A minimum in the T_1/ρ versus temperature curve could not be observed for the deuteron in the HD–Ar system over the temperature range used in the present work; this contrasts with the observation of a minimum in the HD–He case, and is due to the higher magnetic field strength employed in the present experiments. The minima of the T_1/ρ curves for the proton occur at significantly higher temperatures for both systems, due to the larger magnetogyric ratio of the proton. It should be noted here that a direct comparison between the functional forms of the T_1/ρ curves reported for the proton and deuteron in the HD–He system is not valid due to the different field strengths used for the two nuclei.

The effects of the extrapolation to infinite dilution on the final error bars can be visualized clearly by comparing Figs. 5.1 and 5.2 with Figs. 3.6 and 3.7, respectively. As could be predicted by Eq. (5.1), these effects are quite significant.

NOE enhancements

Because of relatively large errors associated with the NOE measurements, an extrapolation to infinite dilution leads to uneven curves for the temperature dependence of the NOE enhancements, which are in poor agreement with the theoretical results. The finite dilution NOE enhancements are, however, comparable with the theoretical results. For this comparison only the experimental data for the mixture with 5.03% HD at 8.38 and 4.55 amagat densities, which show the best (*i.e.*, the smoothest) temperature behavior have been chosen, (see Fig. 3.10). The theoretical values of the NOE enhancements for the proton and deuteron have been calculated for these two densities using Eq. (3.2), and are compared with the experimental results in Fig. 5.3-(a) and (b), respectively. It can be seen from this figure that the agreement between the theoretical and experimental results within the typical error bars of the NOE measurements, are relatively good, especially for the proton. Figure 5.3 shows also that the theoretical NOE enhancements are generally larger for both nuclei. The temperature dependence of the theoretical and experimental NOE enhancement for the deuteron are relatively in good agreement. The agreement for proton is better, even though the temperature dependence for the experimental results cannot be distinguished from the error bars. It has been pointed out above that the spin-lattice relaxation times for the proton is in a nonlinear regime at 8.38 and 4.55 amagat densities. This means that the NOE values for the proton at these densities are not the maximum NOE values. Thus, the proton NOE enhancements calculated via Eq. (3.2) do not correspond to the measured values. Since the correlation times for the different mechanisms are not the same in the gas phase, the NOE values under non-extreme-narrowing condition cannot be evaluated from the NOE formulations for the liquid phase. It was mentioned in Sec. 4.4.2 that the formulation of the NOE for the gas phase is not available at present. How-

ever, based on the distance of the relaxation times from their linear-regime values, Fig. 5.1-(b), it can be said that the differences between the calculated and the actual NOE enhancements are relatively small. For the deuteron, however, the calculated NOE enhancements from Eq. (3.2) correspond to the measured values due to deuteron relaxation times being in the linear regime. From the comparison presented here it can be said that the NOE enhancements provide an independent ground for checking the theoretical results at the qualitative level. An accurate (quantitative) evaluation of the theoretical results is not, however, possible due to the typically large error bars associated with the measured NOE enhancements. Once the NOE effect in the gas phase is formulated, and more accurate measurements are made, the NOE enhancements can be used to evaluate the theoretical results for the components of the relaxation times separately, which is ideal.

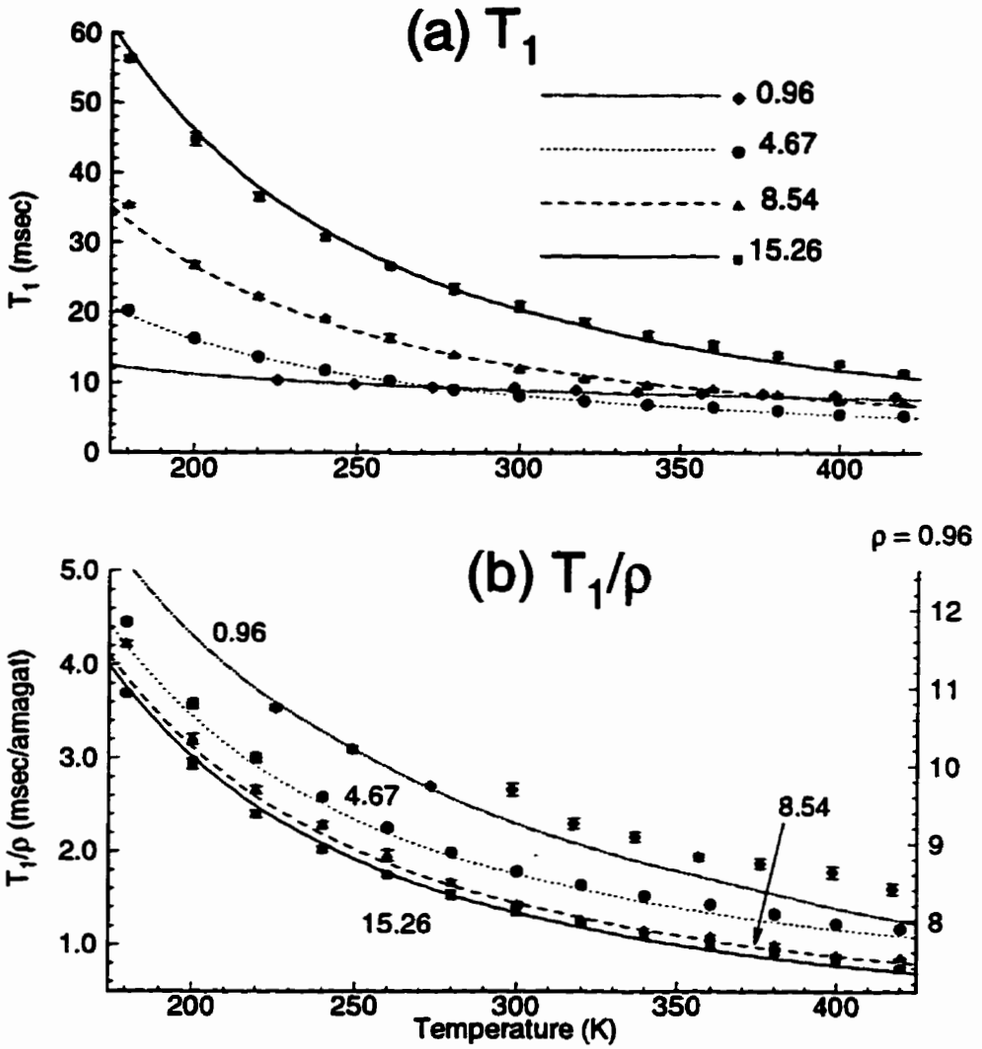

Figure 5.1: Comparison between experimental and theoretical results obtained for the infinite dilution proton spin-lattice relaxation times in the HD–Ar system. The same line patterns and symbols have been used in (a) and (b). The numbers in (a) and (b) denote the amagat densities of the mixtures. Note the different scale used for the proton T_1/ρ at 0.96 amagat. The considerably different values of T_1/ρ for this mixture shows that the proton relaxation time in this mixture is significantly far from the linear-regime. The horizontal error bars associated with the experimental data points at all temperatures are about ± 1 K.

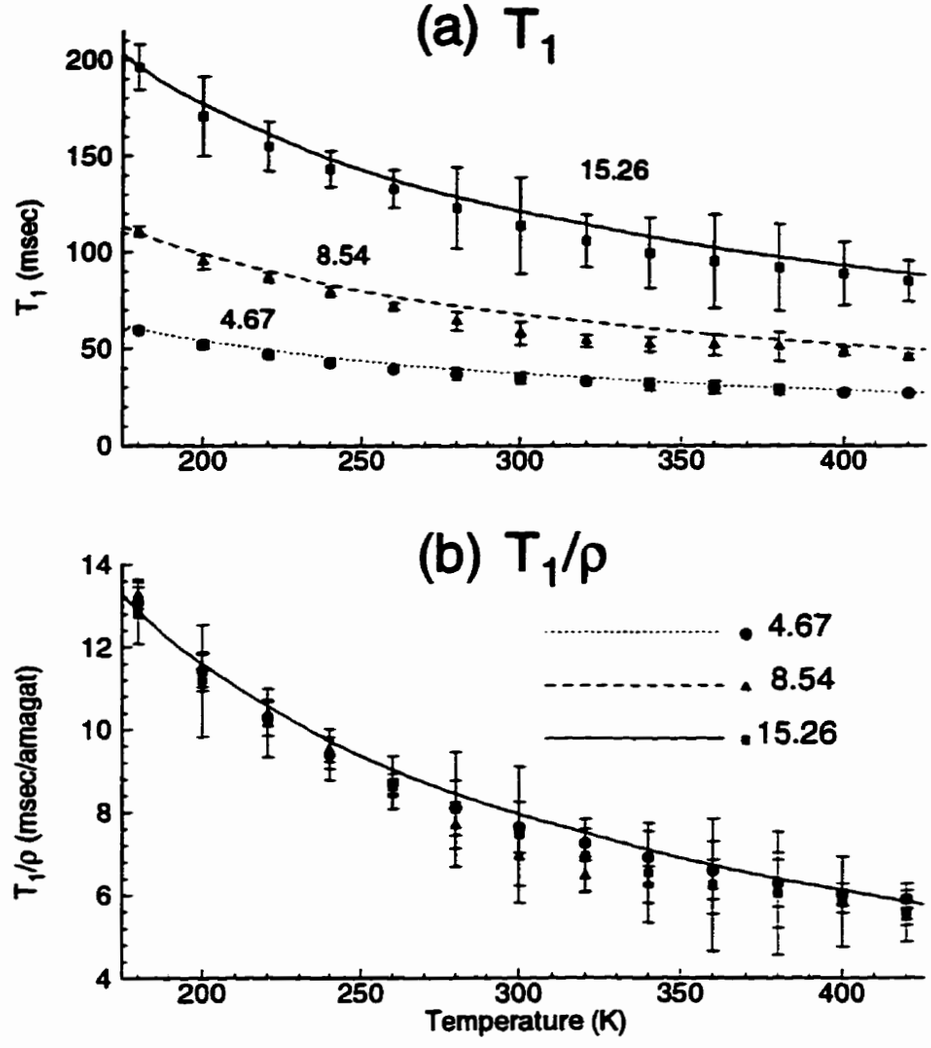

Figure 5.2: Comparison between experimental and theoretical results obtained for the infinite dilution deuteron spin-lattice relaxation times in the HD–Ar system. The numbers in (a) and (b) denote the amagat densities of the mixtures. The same line patterns and symbols have been used in (a) and (b). All of the theoretical T_1/ρ curves for the deuteron overlap due to being in the linear-regime at the specified densities in an 11.75 Tesla magnetic field, see Sec. 4.5.2. The horizontal error bars associated with the experimental data points at all temperatures are about ± 1 K.

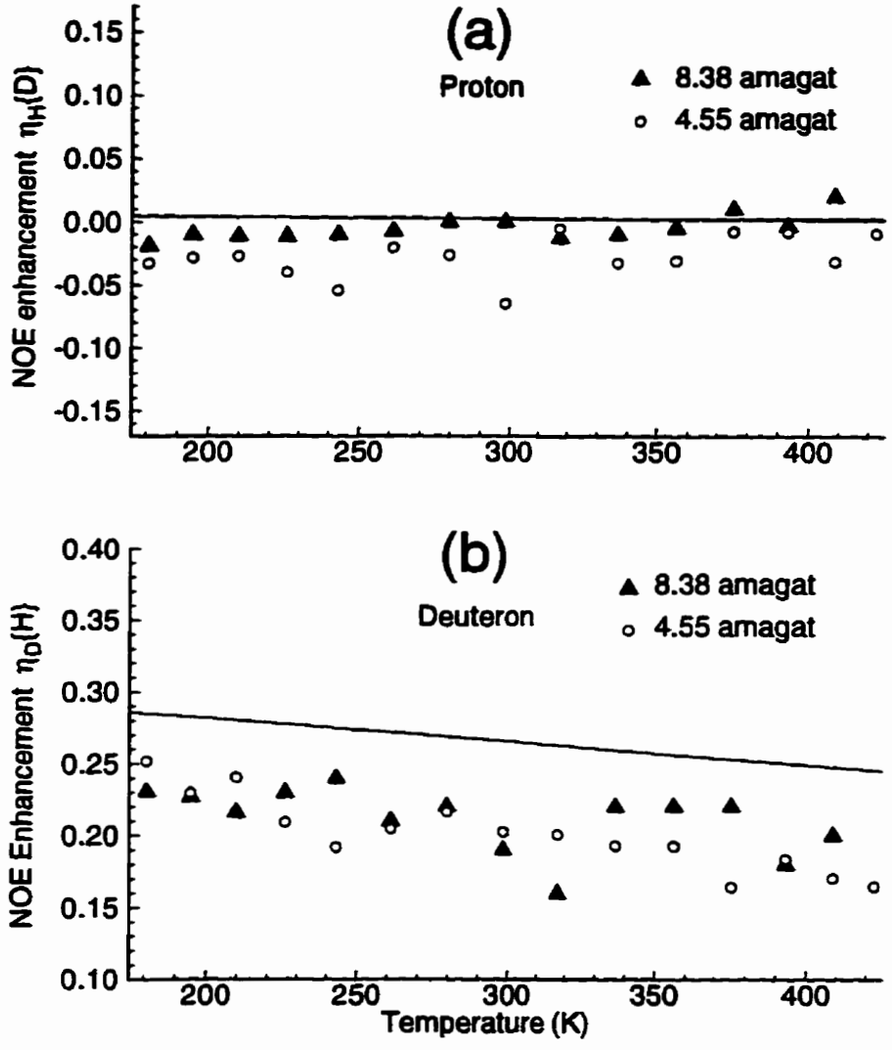

Figure 5.3: Comparison between experimental and theoretical NOE enhancements for (a) the proton and (b) the deuteron of HD in the HD–Ar system. Triangles and circles in (a) and (b) show the experimental results for the HD–Ar mixture with 5.03% HD at 8.38 and 4.55 amagat, respectively. For both nuclei the theoretical values of the NOE enhancements at the two densities are so close that they cannot be distinguished within the scales used in this figure. Note the different scales used in (a) and (b). Note also the similar temperature behaviors of the experimental and theoretical results. Typical error bars for the experimental values of the NOE enhancement are approximately 0.05. The horizontal error bars associated with the experimental data points at all temperatures are about ± 1 K.

5.3 Comparison of theoretical and experimental results for the D_2–Ar System

In the comparison of the theoretical and experimental results for the D_2–Ar system, the method of effective relaxation times has been used, because this method provides us with a numerical measure of the agreement (or disagreement) between the two sets of results. The deuteron spin-lattice relaxation times for the *ortho*-D_2–Ar and *para*-D_2–Ar systems have been calculated separately for the three densities for which the experimental results have been adjusted, over a temperature range extending from 150 K to 450 K. The effective relaxation times for the room temperature frozen-out mixture of the two parity isomers under the same sets of conditions have been calculated using the method described in Sec. 4.5.3. The calculated relaxation times for the individual isomers and the effective relaxation times for the frozen-out mixture are plotted versus temperature in Fig. 5.4. It can be seen from this figure that the $\frac{T_{1\rho}}{T_1}$ ratio increases with decreasing temperature. The minimum and maximum values of this ratio over the temperature range used in the experimental part of the present study are 1.8 and 3.9, corresponding respectively to 420 K and 180 K at 13.91 amagat. These results explain why, in spite of larger S/N ratios, and the smoother recovery curves, the standard deviations of the single-exponential fits used for derivation of the T_1^* values are systematically larger at lower temperature. According to what was discussed in Sec. 4.5.3 these values for the $\frac{T_{1\rho}}{T_1}$ ratio are not large enough to allow accurate separation of the recovery curves for the two parity isomers or to fit bi-exponential decay functions to them. The simulated inversion-recovery curves, which have not been presented here for brevity, attest to this conclusion.

The deuteron spin-lattice relaxation times measured for the D_2–Ar mixtures

with 1.97% D_2 at 3.55, 7.07 and 13.84 amagat, and 3.77% D_2 at 3.58, 7.27 and 13.99 amagat have been adjusted for 3.57, 7.17 and 13.91 amagat, respectively; with a maximum of 1.4% adjustment in the densities. In these adjustments it has been assumed that the relaxation times are linearly dependent on density over the narrow intervals limited to the actual and desired densities. No temperature interpolation has been necessary prior to extrapolation to zero mole fraction, since the same set of temperatures have been used for all D_2–Ar mixtures. At each temperature, a linear extrapolation has been used to find the corresponding infinite dilution relaxation times. The error bars due to extrapolation process have been calculated using Eq. (5.1). The infinite dilution relaxation times have been compared with the theoretical results in Fig. 5.5. This figure shows that the experimental relaxation times are significantly larger than the theoretical results. The agreement between the two sets of results is, however, better at higher temperatures. It can be seen from part (b) of Fig. 5.5 that both the theoretical and experimental relaxation times for the deuteron in the D_2–Ar mixtures are in a nonlinear regime. At a few low temperatures, the experimental T_1^*/ρ values obtained for the D_2–Ar mixture at 3.57 amagat is not, however, consistent with theory. This inconsistency is due only to unexpectedly shorter experimental relaxation times obtained at temperatures below 215 K.

A detailed comparison between the results obtained for the D_2–Ar system in this study and those reported for the D_2–He system[6] is not possible, because too few data points have been reported for the D_2–He system. However, a comparison with the available data for the D_2–He system shows that the experimental T_1^*/ρ values for the two systems are relatively close to one another. As opposed to the D_2–He system the experimental relaxation times obtained in the present study for the deuteron of D_2 in the D_2–Ar system are in a nonlinear regime. In comparison

with the D_2–He system, the minima in the theoretical T_1/ρ curves for both parity isomers of the D_2–Ar system occur at significantly higher temperatures. This is due partly to the higher magnetic field used in the present study. Based on the T_1^* values estimated for the D_2–He system from the reported relaxation times for its two parity isomers (Fig. 2 of Ref. 6), it can be said that for both the D_2–He and D_2–Ar systems the experimental values obtained for the effective relaxation times are larger than those predicted by theory. Also, the agreement between theory and experiment is better for the D_2–He system. The linearity of the density dependence of the calculated relaxation times for the two systems cannot be compared, since in the study of the D_2–He system the theoretical calculations are based on linear-regime formulae.

A comparison between the infinite dilution spin-lattice relaxation times for the HD–Ar and D_2–Ar systems indicates the effect of the curve-fitting procedure used in the temperature interpolation step for the HD–Ar system on the smoothness of the extrapolated data points.

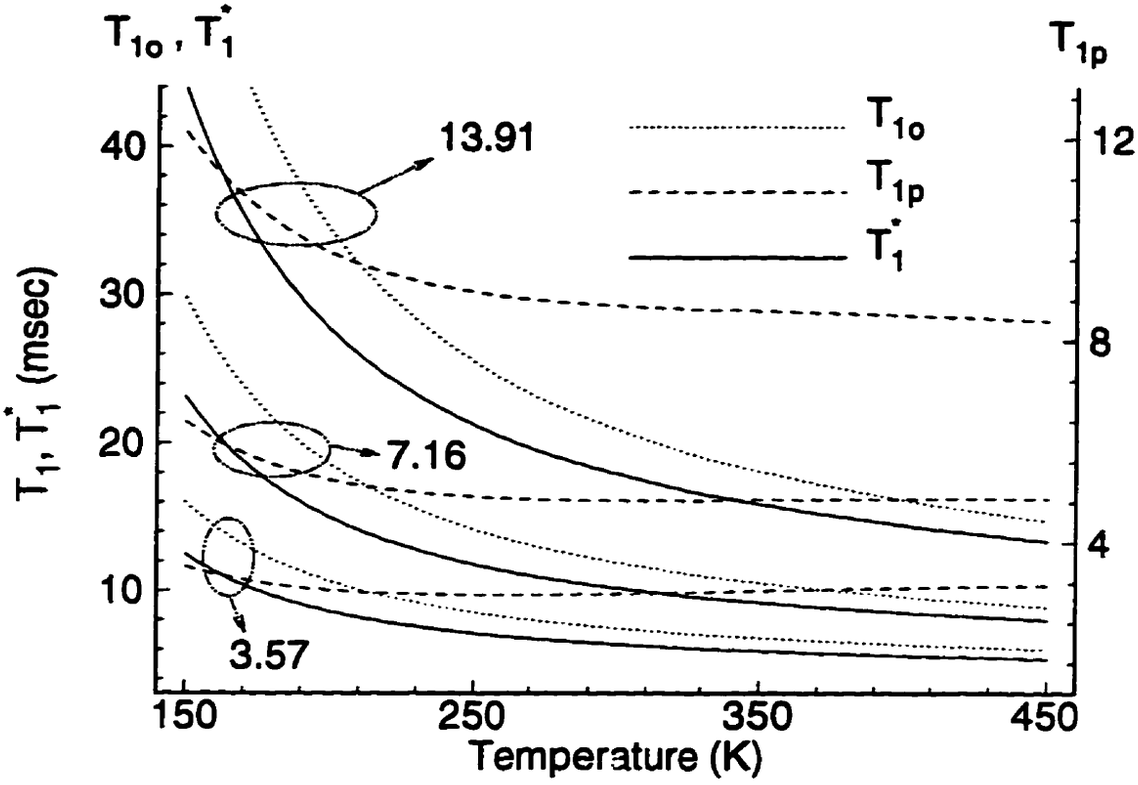

Figure 5.4: Deuteron spin-lattice relaxation times for *ortho*-D_2–Ar, T_{1o} (dotted curves), *para*-D_2–Ar, T_{1p} (dashed curves), and room temperature frozen-out mixtures of *ortho*-D_2–Ar and *para*-D_2–Ar, T_1^* (solid curves) corresponding to the conditions used in the experimental study of the D_2–Ar mixtures. The numbers in this figure represent the total amagat densities. Note that only the T_1 curves for the *para*-D_2–Ar at 3.57 and 7.16 amagat show a minimum in the temperature window shown in this figure. The minimum and maximum values of the ratio of the relaxation times for the two parity isomers, which both belong to the mixture at 13.91 amagat and correspond to 450 K and 150 K temperatures, are 1.7 and 4.7, respectively.

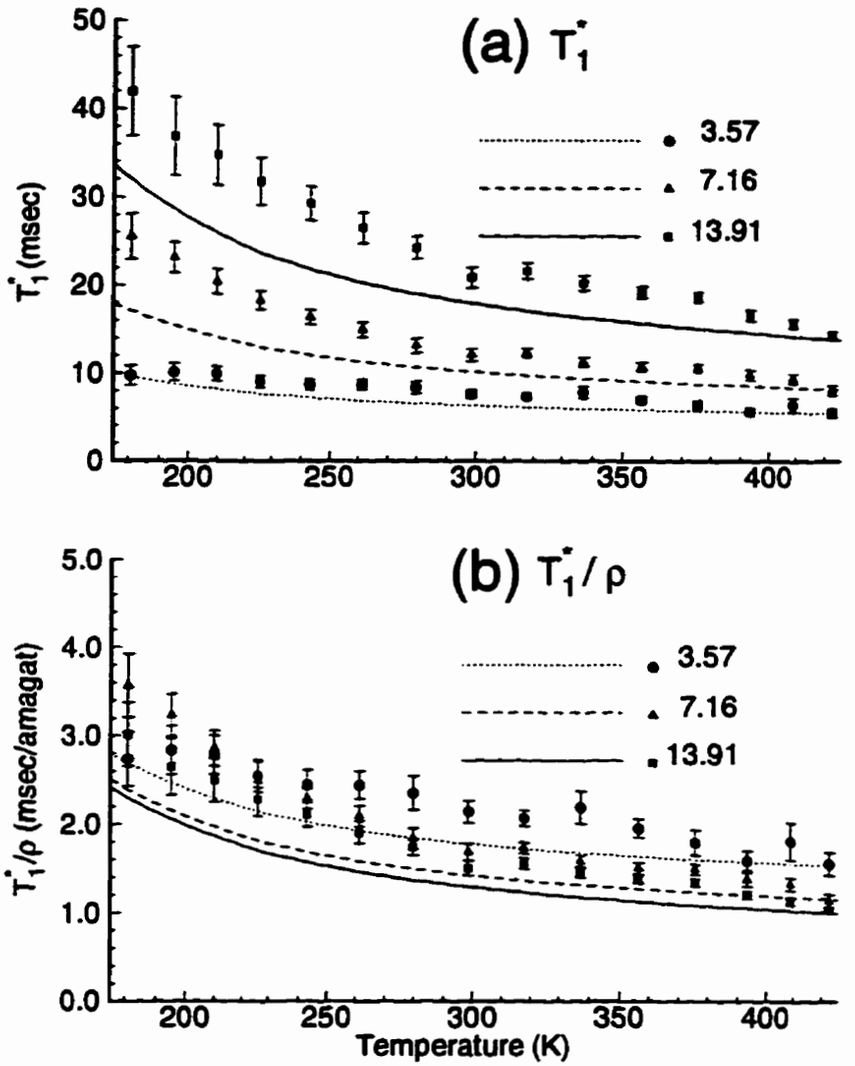

Figure 5.5: Comparison between experimental and theoretical results obtained for the infinite dilution deuteron spin-lattice relaxation times in the room-temperature frozen-out mixtures of *ortho* and *para* isomers of the D_2–Ar system. The numbers in (a) and (b) denote the amagat densities of the mixtures. The theoretical results for T_1^*/ρ show that the deuteron relaxation time is in the non-linear regime at the specified densities in an 11.75 Tesla magnetic field. The horizontal error bars associated with the experimental data points at all temperatures are about ± 1 K.

5.4 Evaluation of the XC(fit) PES for hydrogen-argon system

From comparisons of theoretical and experimental spin-lattice relaxation times presented in the previous two sections it can be said that the XC(fit) PES represents the interaction between the HD molecule and Ar atom in the HD–Ar system fairly accurately, while the same PES shows poor quality for the D_2–Ar system. Since the interaction potential for the HD–Ar system has been derived from the same PES which has been used directly for the D_2–Ar system, these results seem, at first, to be inconsistent with one another. Assuming the same accuracy for the experimental results obtained for the two systems, and correct formulations for the relaxation times, the different behaviors of the XC(fit) PES for homonuclear and heteronuclear hydrogen isotopomers can be attributed only to the transformation of the potential. In the following it will be explained how the transformation of the potential from the homonuclear to heteronuclear system may change the quality of the potential.

In the numerical method used for the transformation of the XC(fit) PES from the homonuclear isotopomer to the heteronuclear isotopomer (see Sec.4.3), the individual Legendre components of the transformed potential cannot be traced. However, it is obvious that this transformation mixes all components of the homonuclear potential. For numerical evaluation of the contributions of each Legendre component of the homonuclear potential to the values of the individual components of the transformed potential the integration of Eq. (4.11) should be carried out piecewise for each contributing term of the homonuclear potential. This evaluation will not be carried out here. Instead, the results of the analytical method of Kreek and LeRoy[118] will be used to present a descriptive discussion. This discussion will be

focussed only on the V_1 and V_2 terms of the heteronuclear potential, as they are the leading terms of the anisotropic part of the potential which determines NMR relaxation. Figure 4.4 shows that these two terms have very similar values on the attractive part of the potential. This figure shows also that the value of the V_1 term at short range, below the potential minimum, is significantly larger than the value of the V_2 term.

Thus, it can be concluded that at low temperatures these two terms contribute about equally to the NMR relaxation in the heteronuclear system, while at higher temperatures the NMR relaxation is dominated by the V_1 term of the PES. The sum of the contributions of all other anisotropic terms to the potential, and hence to the NMR relaxation times, is at least one order of magnitude smaller than the contribution of either of these two terms. The accuracy of the NMR relaxation times calculated for the heteronuclear HD–Ar system is thus determined predominantly by the accuracies of the V_1 and V_2 components.

Kreek and LeRoy[118] have shown that, except for a very narrow range of intermolecular distances on the repulsive wall, the V_0 term of the homonuclear potential contributes to the value of the V_1 term of the heteronuclear potential dominantly, and is the second contributor to the V_2 term.* This means that the accuracy of the theoretical NMR relaxation times for the HD–Ar system depends strongly upon the accuracy of the V_0 term of the homonuclear potential; this behavior should be compared with that for the D_2–Ar system, for which the accuracy of the V_2 term of the homonuclear potential determines the accuracy of the calculated NMR

*As a nice example, consider a totally isotropic potential for the homonuclear system, for which V_2 and all higher terms are zero. Equations (A1) and (A2) of Ref. 118, give expressions for the V_1 and V_2 terms of the heteronuclear potential, which depend totally on the V_0 term of the isotropic potential for the homonuclear system. In other words, the anisotropic part of the potential for the heteronuclear system is generated entirely from the isotropic potential for the homonuclear system in this example.

relaxation times. Thus it can be concluded that the calculated relaxation times obtained for the HD–Ar and D_2–Ar systems would have the same accuracy *if and only if* the V_0 and V_2 terms evaluated for the homonuclear potential (from the relevant experimental data) had the same accuracy. In principle, the uncertainty in the values of the anisotropic terms evaluated from the spectroscopic data is much higher than that of the isotropic term. Further, many of the experimental data used to refine the potential are not particularly sensitive to the anisotropic components of the potential. It can then be expected that the overall uncertainties in the values of the V_2 and higher terms of the homonuclear potential are much higher than the uncertainty in the value of the V_0 term. This leads to the final conclusion that the anisotropic part of the interaction potential for the HD–Ar system is much more accurate than is for the D_2–Ar system. Consequently, it is expected that the uncertainties in the calculated spin-lattice relaxation times obtained for the D_2–Ar will be much larger than those for the HD–Ar system. This conclusion can be tested if NMR T_1 measurements could be made at temperatures low enough for the contributions of the V_1 and V_2 terms to the NMR relaxation times to be comparable. For such temperatures it can be anticipated that the agreement between experimental and calculated spin-lattice relaxation times for the D_2–Ar and HD–Ar systems would be comparable.

In conclusion, it can be said that the difference in the agreement between experimental and calculated relaxation times obtained for the D_2–Ar and HD–Ar systems is due to uncertainties in the V_2 term of the homonuclear PES. Based on this conclusion it is predicted that the same level of agreement should also be observed between experiment and theory for the remaining homonuclear systems H_2–Ar and T_2–Ar. A comparison between the theoretical relaxation times calculated for the proton of H_2 in the H_2–Ar system, using an older version of the XC(fit) PES[119]

(see Figs. 4.2 and 4.4), and the experimental results of Lemaire and Armstrong,[68] which shows relatively poor agreement between theory and experiment, supports this prediction.

5.5 Discussions on the calculations

Sensitivity of the NMR cross sections

Although NMR spin-lattice relaxation times cannot be used to analyze the detail of the functional forms and parameters of the PES's, they are, however, the most sensitive physical properties to the overall anisotropy of the PES's. This sensitivity has already been used to distinguish between different PES's suggested for a system.[4] Since the higher quality of the XC(fit) PES is evident at the level of other physical properties,[8] the results of a comparative NMR study of the XC(fit) and other PES's suggested for the hydrogen-argon system are obvious, and such a study might appear not to be necessary. Rather, a comparison of the two different versions of the XC(fit) PES at the final stage of the refinements of the potential will be provided to show the sensitivity of the NMR spin-lattice relaxation times to subtle changes in the PES. This comparison is based on the elements of the thermally averaged NMR cross section matrices, σ_V and σ_T, calculated from the two versions of the potential using the same method that was described in Ch.4.

Figure 5.6-(a) shows the typical sensitivity of the NMR cross sections to subtle changes in the anisotropy of the XC(fit) potential for elements of the σ_V cross section matrix for the *ortho*-D_2–Ar system. As can be seen from this figure, the effects of an improvement of the anisotropic components of the XC(fit) potential of the magnitude shown in Fig.4.2, as small as they are, are quite visible. The differences between values of the diagonal elements of the cross sections calculated

from the two versions of the potential are very small at intermediate temperatures and increases for higher and lower temperatures. For off-diagonal elements of the cross sections the differences are small at low temperatures and increase with increasing temperature. The difference in the comparative behaviors of the diagonal and off-diagonal elements at low temperatures is due to the higher sensitivity of the orbiting resonances, which have significantly larger contributions to the values of the diagonal elements, to the changes in the potential. These typical changes in the values of the cross section elements lead to approximately similar changes in the values of the relaxation times, with a maximum change of about 1.5%. Although such changes are smaller than the typical error bars associated with the experimental values of spin-lattice relaxation times, they are significantly larger than the changes observed for other properties calculated from the two versions of the potential.[98] Similar changes with almost the same magnitude, have been observed for the σ_T cross sections. The NMR cross sections for the *para*-D_2–Ar and HD–Ar systems also show similar sensitivity.

Contribution of the resonance ranges

As pointed out in Sec. 4.1, and shown in Secs. 4.4 and 4.5, the distribution of the total energy values becomes important for systems which exhibit orbiting resonances. To show this importance explicitly, the contribution of the resonance ranges to the thermally averaged NMR cross sections for the *ortho*-D_2–Ar system have been calculated, and are plotted versus temperature in Fig. 5.6-(b). It can be seen from this figure that these contributions are significantly larger at low temperatures, and decrease rapidly with increasing temperature. Figure 5.6-(b) shows also that the resonance contributions for off-diagonal elements are significantly smaller, and vanish at lower temperatures (see also the discussion on Figs. 4.11 and 4.20).

The contributions of the resonance ranges to the calculated spin-lattice relaxation times are almost the same as those to the cross sections. The contributions of the resonance ranges to the NMR cross sections have been found to be slightly larger for the HD–Ar system. It should be noted here that for systems with no orbiting resonances a less careful selection of the total energy values can still lead to incorrect values for the thermally averaged cross sections if the narrow ranges above the rotational thresholds are not covered properly. This is due to the near-threshold behavior of the energy-dependent cross sections. The contribution of the near-threshold behavior is, however, rather small, and rapidly vanishes with increasing temperature.

From the results obtained here it can be concluded that, because of its sensitivity, NMR relaxation time measurements at low temperatures may provide an excellent probe for the study of orbiting resonances.

j-dependence of the coupling constants

The spin-rotation, dipolar and quadrupolar coupling constants are proportional respectively to $(\overline{r^2})^{\frac{1}{2}}$, $\overline{r^{-3}}$ and q_{zz},[14,120] where r is the bond length, and q_{zz} is the electric field gradient along the direction of the magnetic field. All of these quantities, and hence the coupling constants, depend implicitly upon the rotational quantum number j. When the coupling constants are functions of j, they should be replaced with their thermally-averaged values in the T_1 equations, Eqs. (4.1)-(4.3). This introduces small changes as well as additional temperature dependences to the spin-lattice relaxation times, since the average values of the coupling constants are temperature-dependent. As will be shown below, the magnitudes of these changes are small for low temperatures, and increase with increasing temperature. It should be noted here that if the diatom was rigid, all expectation values of the r-dependent

functions remain independent of temperature, and all of the j-dependences vanishes. Thus, j-dependence of the coupling constants is valid only for non-rigid diatoms.

As for any other physical property, the average values of the coupling constants can be calculated from their values at each rotational level by using the fractional populations of the rotational levels. The values of the quadrupolar coupling constants for the deuteron of D_2 and of HD in different rotational levels have been calculated by Vojtik *et al.*[121,122] Moreover, the values of spin-rotation and dipolar coupling constants for the lowest rotational level ($j = 1$ or 2) have been measured for D_2 and for HD by Code and Ramsey.[113] The corresponding values of the coupling constants for higher rotational levels have been calculated using the expectation values $\overline{r^2}$ and $\overline{r^{-3}}$, which are calculated by the program LEVEL.[96] Table 5.1 lists the j-dependent values of the coupling constants for HD, *ortho*-D_2 and *para*-D_2. It can be seen from this table that the dipolar and quadrupolar coupling constants are decreasing functions of j, while the spin-rotation coupling constant is an increasing function of j. It can thus be anticipated that the overall relaxation time for the proton of HD in the HD–Ar system, which is dominated by the spin-rotation interaction, decreases with increasing temperature, while those for the deuteron in the HD–Ar system and in the D_2–Ar system increase with temperature, due to their domination by the quadrupolar interaction. When the contributions of the spin-rotation and quadrupolar interactions are comparable, the overall temperature dependence of the relaxation times due to the j-dependence of the coupling constants lies between these two extreme behaviors. Table 5.2 shows the typical effects of the j-dependences of the coupling constants on the calculated relaxation times for the HD–Ar system and the two parity isomers of the D_2–Ar system. This table shows that at 450 K and 11.75 Tesla the j-dependences of the coupling constants change the overall relaxation times for the proton and deuteron of HD in the

HD–Ar system at 15.26 amagat by −0.6% and +2.3%, respectively. The changes for the deuteron in the *ortho*-D_2–Ar and *para*-D_2–Ar systems under the same conditions, but at 13.91 amagat, are +1.9% and +2.6%, respectively. These changes results in a +2.0% change in the deuteron T_1^* in a frozen-out room temperature mixture of the two systems. As pointed out above, these effects are smaller for lower temperatures.

It should be mentioned here that the actual j-dependence of the spin-rotation coupling constants is complicated,[123] and its study is beyond the scope of this work. What has been reported here is based only on the direct dependence of the spin-rotation coupling constant on the bondlength of the diatomic molecule.

Possible sources of error in the calculations

Other than possible inaccuracies and uncertainties in the derivation of the XC(fit) potential, the number of sources of error in the calculations are very limited. The most important source of error in the present calculations has been found to be associated with the evaluation of the thermally averaged cross sections. As has been pointed out in Sec. 4.1, when the system exhibits orbiting resonances the functional forms of the cross sections in the resonance ranges become complicated. In such cases a special integration scheme is required to handle the integration accurately. Such a scheme should use a variety of standard functional forms observed for the resonance peaks in order to evaluate the integrals more accurately. The thermal-averaging program used for the calculation of the relaxation times in this study, is not equipped with such a scheme. In the present study a large number of total energies have been used to overcome this limitation of the program. However, the program has resulted in some outliers, as well as some small ridges, in the temperature-dependent curves of the thermally-averaged cross sections. The sizes

of the ridges are, however, very small, and cannot be seen easily within the scales used in the T_1 versus temperature diagrams presented in Ch.4.

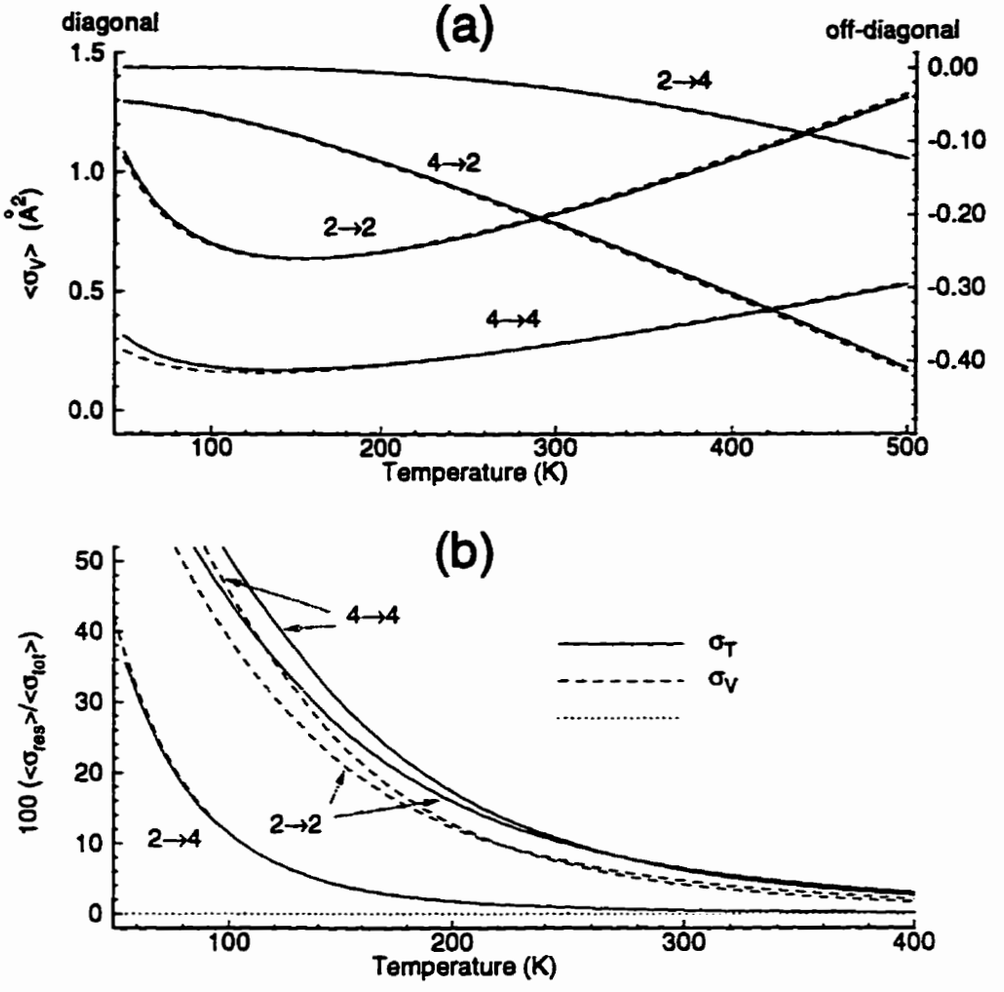

Figure 5.6: (a) Typical sensitivity of the NMR cross sections to subtle changes in the anisotropy of the XC(fit) potential. The solid and dashed curves in (a) show the corresponding cross section elements calculated from the older and the newer versions of the potential, respectively. Figure 4.2 compares the two versions of the XC(fit) potential. Note the different scales used for the diagonal and off-diagonal cross section elements. (b) Contributions of the resonance ranges to the NMR cross sections for the *ortho*-D_2–Ar system. In this figure σ_{res} and σ_{tot} denote the contribution of the resonance range (a width of 50 cm^{-1} above each threshold) and the total cross section, respectively. This figure emphasizes the importance of proper selection of the values and distribution of the total energies used for the calculation of the cross sections.

Table 5.1: j-dependence of the coupling constants for HD, *ortho*-D_2 and *para*-D_2. The ω_Q values have been taken from Refs. 121, 122. The values of ω_{SR} and ω_D have been calculated respectively using the expectation values $\overline{r^2}$ and $\overline{r^{-3}}$ for each rotational level. The ω_{DQ}^D values for *ortho*-D_2 and *para*-D_2 have been calculated via Eq. (4.8) and (4.7), respectively. All coupling constants are angular frequencies given in s^{-1}.

HD : j	$\omega_{SR}^H/10^6$	$\omega_{SR}^D/10^5$	$\omega_D^{D,H}/10^7$	$\omega_Q^D/10^7$
1	0.5377	0.8242	0.1674	0.2112
2	0.5390	0.8279	0.1651	0.2089
3	0.5408	0.8334	0.1617	0.2055
4	0.5432	0.8408	0.1573	0.2011
5	0.5461	0.8500	0.1521	0.1957
6	0.5497	0.8611	0.1461	0.1894
7	0.5538	0.8740	0.1396	0.1825
8	0.5583	0.8888	0.1325	0.1749
9	0.5636	0.9053	0.1252	0.1668
10	0.5693	0.9237	0.1176	0.1584
11	0.5755	0.9440	0.1100	0.1489

o-D_2 : j	$\omega_{SR}^D/10^5$	$\omega_D^D/10^6$	$\omega_Q^D/10^7$	$\omega_{DQ}^D/10^7$
2	0.5481	0.1284	0.2100	0.2058
4	0.5510	0.1264	0.2048	0.2006
6	0.5554	0.1233	0.1967	0.1928
8	0.5614	0.1192	0.1872	0.1836
10	0.5690	0.1145	0.1743	0.1709
12	0.5780	0.1091	0.1649	0.1618
14	0.5883	0.1033	0.1508	0.1479

p-D_2 : j	$\omega_{SR}^D/10^5$	$\omega_D^D/10^6$	$\omega_Q^D/10^7$	$\omega_{DQ}^D/10^7$
1	0.5509	0.1290	0.2117	−0.2374
3	0.5530	0.1275	0.2078	−0.2330
5	0.5567	0.1249	0.2010	−0.2253
7	0.5620	0.1213	0.1919	−0.2147
9	0.5688	0.1169	0.1805	−0.2017
11	0.5771	0.1118	0.1695	−0.1890
13	0.5869	0.1062	0.1602	−0.1777

Table 5.2: Typical effects of the j-dependence of the coupling constants on the calculated relaxation times. The relaxation times for the proton and deuteron of HD in the HD–Ar system, and for the deuteron of D_2 in the D_2–Ar system have been calculated for 450 K and 11.75 Tesla, and 15.26 and 13.91 amagat, respectively. Rigid and non-rigid terms have been used here to denote, respectively, the j-independent and j-dependent coupling constants. The changes in the relaxation times due to the j-dependence of the coupling constants decreases rapidly with decreasing temperature. All relaxation times are given in msec.

HD–Ar :	Proton			Deuteron			
	T_{1SR}	T_{1D}	T_1	T_{1SR}	T_{1D}	T_{1Q}	T_1
Rigid	9.770	456.3	9.566	381.4	1128	118.1	83.48
Non-rigid	9.707	465.5	9.509	378.9	1151	121.9	85.36
% Diff.	−0.7	+2.0	−0.6	−0.7	+2.0	+3.2	+2.3

D_2–Ar :	*ortho*			*para*			
	T_{1SR}	T_{1DQ}	T_{1o}	T_{1SR}	T_{1DQ}	T_{1p}	T_1^*
Rigid	54.70	20.14	14.72	53.67	9.945	8.390	13.35
Non-rigid	54.43	20.71	15.00	53.33	10.27	8.613	13.62
% Diff.	−0.5	+2.8	+1.9	−0.6	+3.3	+2.6	+2.0

5.6 Discussions on the experiments

Mole fractions

From comparisons of the measured spin-lattice relaxation times for mixtures at different mole fractions under the same conditions, it can be seen that the contributions of the self-collisions to the relaxation times depend upon temperature and density, and become significant at specific temperatures and densities. The results for the HD–Ar system show that these contributions do not depend linearly upon the mole fraction of HD, in spite of the fact that the mole fractions used in the experiments are rather small. Such a non-linear dependence on the mole fraction would give rise to incorrect infinite dilution relaxation times if higher mole fractions had been used in the experiments. For example, extrapolation of the results at the lower densities for the two HD–Ar mixtures with higher mole fractions, to infinite dilution changes the final results by factors up to about 5%, depending upon the temperature. The magnitude of such changes would be significantly larger had larger mole fractions been used in the experiments. Large effects are not expected for the higher densities, such as the highest density used for the HD–Ar mixtures, for which the individual contributions of both self- and nonself-collisions are in the linear regime. It can be shown analytically that if the contributions of inelastic collisions can be neglected, only in the linear regime, and when either the spin-rotation or the combined dipolar-quadrupolar interaction dominates, the relaxation times depend linearly upon the mole fraction of the diatomic hydrogen.[41] When the system is in an extreme nonlinear regime, *i.e.*, at very high magnetic field strength and/or very low density, the relaxation rates, T_1^{-1}, become linear functions of mole fractions, so that an extrapolation to zero mole fractions should be carried out for the relaxation rates rather than the relaxation times. For intermediate conditions

the dependences both of relaxation times and of relaxation rates on the mole fraction are weaker. The solution to this problem is to carry out experiments for a larger number of low mole fraction mixtures, and map out precisely the actual functional forms of the mole fraction dependences of the relaxation times. An extrapolation of the relaxation times based on these functional forms would give accurate infinite dilution results. This solution is, of course, not economical.

For the D_2–Ar system an additional complexity arises because of possibly different mole fraction dependences of the deuteron relaxation times for the two parity isomers.

The above discussion has been presented here to complement similar discussions presented in the relevant contexts of Chs.3 and 4, and to stress the importance of the mole fractions of the diatomic component in such studies. Fortunately, the mole fractions used in the experimental part of the present study are small enough to neglect the problems discussed briefly above.

Contributions of impurities

In the analysis of the one-dimensional spectra obtained for the HD–Ar and D_2–Ar mixtures it was shown that the contributions of the impurities to the signal are negligible. This, however, does not necessarily require that the contributions of the impurities to the relaxation times should be neglected. Rather, the evaluation of such contributions should be based on the effectiveness and the fraction of the collisions with the impurity molecules. In general, contributions of the impurities of the hydrogen gases (HD and D_2) to the measured relaxation times are smaller than those of the Ar gas by a factor of x^{-1}, where x is the mole fraction of hydrogen in the mixture. The isotopic impurities of the hydrogen gas contribute to the measured relaxation times by changing the fraction of self-collisions (to impurity nonself-

collisions) with the same interaction potential, but with different reduced masses of the collision complexes. Considering the very low concentrations of the hydrogenic impurities (*i.e.*, 3% for HD and 0.4% for D_2), such changes can be neglected. The direct contributions of the hydrogenic impurities to the NMR signal appear as a very small increase in the standard deviation of the measured relaxation times. The total concentration of the non-hydrogenic impurities is less than 10 ppm for both HD and D_2 gases.

In contrast to the role of impurities from the hydrogen gas, impurities from the argon gas are considerably more important, as the argon molecules constitute a major fraction of the collision partners for diatomic hydrogen. For this reason an UHP (ultra-high purity) grade argon gas has been used in the present experiments. The stated total concentrations of the impurities in the UHP grade argon gas is less than 20 ppm. Obviously, the contributions of this small concentration of the impurities can safely be neglected. While the contribution of (paramagnetic) oxygen, which constitutes 10% of the non-hydrogenic impurities, might seem to be a real concern. The number of collisions between diatomic hydrogen and oxygen molecules is at least five orders of magnitude less than that between diatomic hydrogen molecules and argon atoms. Furthermore, this trace amount of oxygen is usually adsorbed at the active surfaces of the gas handling system, *e.g.*, the copper tubes. Oxygen impurity is the major problem with the isotopic hydrogen gases prepared locally via chemical or electrochemical reactions. The UHP argon gas may contain a trace of the ^{36}Ar isotope, which can also be regarded as an impurity. The actual concentration of this isotopic impurity in the UHP argon gas is much smaller than the natural abundance of the ^{36}Ar isotope (*i.e.*, 0.34%), due to the method by which UHP argon gas is prepared. Further, within the Born-Oppenheimer approximation the differences between the contributions to bulk

mixture properties of hydrogen-^{36}Ar and hydrogen-^{40}Ar collisions are entirely due to the difference between their reduced masses, which is very small (*e.g.*, for the D_2–Ar system this difference is less than 1%). Moreover, as the isotopic impurity of the argon gas is negligible, its contribution to the measured NMR relaxation times can be neglected safely.

In conclusion, it can be said that the contributions of the impurities to the measured relaxation times in the present study are very small.

Possible sources of error in the experiments

In the gas phase NMR experiments, except for closed sample cells with dimensions confined to the effective volume of the rf coil, diffusion of gases into and out of this volume is usually one of the most important sources of error in the measured values of the relaxation times. When the sample cell is open and is connected to a large reservoir (GHS) by a capillary, such as that used in the present study, diffusion[†] of the molecules from the effective volume of the rf coil through the capillary gives rise to an additional decay of the nuclear magnetization. The rate constant of this decay, which is equivalent to an inverse relaxation time, is proportional to $T^{\frac{1}{2}}A_c/V$, with V the volume of the sample cell and A_c the capillary cross section. In order to minimize the contribution of diffusion to the measured values of the relaxation times, this factor should be kept as small as possible. This means that a larger sample cell and a narrower capillary are preferred. It was argued in Secs. 3.2.1 and 3.3.1 that diffusion does not play an important role under the conditions used in the present study. However, for higher temperatures at which molecular diffusion rates are larger, significant contributions from diffusion may be expected. For such temperatures a closed sample cell should be used in order to confine the molecules

[†]In this case *effusion* may be a more suitable terminology[21]

within the effective volume of the rf coil. The trivial solution of using a larger sample cell at such temperatures is not practical due to cell size and increased difficulty in shimming of the probe (see Ch. 2). When the magnetic field is not homogeneous, diffusion of molecules both inside the sample cell and into and out of the sample cell becomes another source of decay in the magnetization, and thus contributes to the measured relaxation time.

Another problem associated with an open sample cell is that large amounts of gases are needed to prepare the desired mixture in the sample cell, which has a maximum volume of $1\,cm^3$. This can be a real disadvantage, especially when studying expensive gases. Further, changes in the density of the reservoir (due to variation of its temperature) affect the total density of gases in the sample cell. On the plus side, however, an open sample cell allows one to probe the pressure of the gases instantaneously and continuously to check for possible leaks.

Temperature instability and inhomogeneity over the sample cell, which depend on the temperature control unit and the design of the probe, are other important sources of error in gas phase T_1 measurements. Besides increasing the standard deviation of the measured relaxation time, temperature inhomogeneity and instability can lead to convection (a homogeneous diffusion) in the gas mixture in the sample cell, the capillary and the connecting tubes to the gas handling system. This introduces yet another source of error.[124] The convection of gases in a closed sample cell has no effect on the measured relaxation time when the magnetic field is homogeneous.

Contribution of wall-collisions to the decay of nuclear magnetization, as discussed briefly in Sec. 5.1, is another source of error which becomes important only for nuclei with extremely long relaxation times (*e.g.*, at very low temperatures), for dilute gases,[15] and/or for small sample cells.

Formation of Van der Waals complexes may not always be detected easily, especially when it occurs at the limits of the temperature range. The temperature range over which these complexes are formed, and the magnitudes of their effects on the relaxation times of the nuclei depend upon the physical properties of both the atom and the diatom making up the complex, the most important of which is their interaction PES.[72] These effects on the T_1 versus temperature curves may be so smooth that they cannot be distinguished from the general temperature behavior of the relaxation times. In such cases, comparison between experiment and theory could result in incorrect conclusions being drawn. A T_1 measurement study of the atomic component of the mixture (when it is NMR active) can be used to map out the regions in which these complexes are formed. The effects of the formation of Van der Waals complexes on the relaxation times of the atomic species are dramatic, because they introduce much more effective interactions (*i.e*, intramolecular interactions) to the relaxation of the nuclear magnetizations in atoms, which otherwise relax via the much weaker intermolecular interactions.[15,16] Unfortunately, the Ar nucleus is not NMR active, and thus does not allow such a study to be carried out for the HD–Ar and D_2–Ar systems.

The low S/N ratios usually obtained for the gaseous samples generally decrease the accuracy of the T_1 measurements. For heteronuclear diatomic samples, such as HD in the HD–Ar system, when observation of the structure of the peaks are not of interest, decoupling of the other nucleus during the acquisition time can be used to increase the S/N.

5.7 Conclusion

A reliable gas handling system and a sample cell have been designed to fit the standard solution probes of a commercial NMR instrument, and they have been used successfully in the NMR study of HD–Ar and D_2–Ar gas mixtures.

For the first time, NMR one-dimensional and spin-lattice relaxation time studies for HD–Ar and D_2–Ar gas mixtures have been carried out over a wide range of temperatures at several mole fractions and densities. Analysis of the one-dimensional spectra for both the HD–Ar and D_2–Ar mixtures showed that diffusion of molecules, which might be an important source of error in T_1 measurements with an open sample cell, is not significant for the conditions used in this study. However, it should be noted here that the open sample cell setup should not be used at very high temperatures, as diffusion of molecules at these temperatures will contribute significantly to the relaxation times. The chemical shifts of the peaks in the one-dimensional spectra showed well-behaved temperature dependences. The contribution of the j-dependence of the intramolecular interactions to the temperature dependence of the deuteron chemical shifts in the D_2–Ar system (*i.e.*, through rovibrational averaging) was calculated using *ab initio* methods. The results of these calculations showed that the intramolecular interactions cannot be responsible for the large temperature dependences of the chemical shifts observed in the D_2–Ar system, and it thus appears that intermolecular interactions are likely responsible for the observed relatively strong temperature dependences. The deuteron linewidths obtained for the D_2–Ar mixtures illustrate the high quality of the experimental data obtained in these studies. The theoretical results suggest that the difference between the measured values of T_1^* and T_2^* for the deuteron of D_2 in D_2–Ar mixtures is due partially to the deuteron relaxation times for the two parity isomers under the experimental

conditions used in this study being in the non-linear regime in which T_2 is shorter than T_1.citemccourt1

Close-coupled S-matrix elements, opacities, and the σ_V and σ_T cross sections have been calculated for both systems. The quality of the results of each step of the calculations have been tested in detail. A turning-point energy has been observed for the maximum in the J-dependent opacities. Such a turning-point has not been reported previously for similar systems. The turning-point energies for the D_2–Ar system occur at significantly higher energies in comparison with those for the HD–Ar system. It has been shown that the main source of error in the results of the calculations arises from the thermal-averaging step. It has been suggested that a better technique should be used in the resonance ranges, in which a known lineshape function is employed in the curve-fitting step of the integrations over these ranges. Such an improvement in the thermal averaging routine is not moot, since it has been shown that the contributions of orbiting resonances to the relaxation times are not negligible for the HD–Ar and D_2–Ar systems, and become quite significant at low temperatures. Thus, a careful selection of the total energies is required for systems exhibiting such resonances. It is also clear that NMR T_1 measurements at low temperatures can be used to study the contribution of orbiting resonances to such phenomena.

Two general methods have been proposed to provide means for comparison of the experimental and theoretical spin-lattice relaxation times for *ortho-para* mixtures of a homonuclear diatomic gas when the relaxation times of the two parity isomers are so close that they cannot be measured separately. Under such conditions, an accurate and quantitative comparison of the theoretical and experimental results is not, otherwise, possible. One of these methods, the method of effective relaxation times, has been employed successfully for the study of the D_2–Ar sys-

tem, after all efforts to obtain separate measurements of the relaxation times of the deuteron in the the *para*-D_2–Ar and *ortho*-D_2–Ar systems failed. The theoretical results confirmed that such separate measurements are not possible, because the values of the relaxation times of these two parity isomers are indeed very close.

The theoretical spin-lattice relaxation times for the HD–Ar system show excellent agreement with the experimental results for all conditions, while for the D_2–Ar system relatively good agreement could be obtained only at higher temperatures. The source of the difference between the theoretical results for the two systems has been attributed to possible inaccuracies in the anisotropic components of the XC(fit) PES for the homonuclear hydrogen-argon systems. It was concluded that the anisotropic parts of the transformed PES, and hence the NMR relaxation times, for the heteronuclear hydrogen-argon systems are predominantly determined by the isotropic part of the homonuclear PES. For the HD–Ar system the agreement between experimental and theoretical results for the deuteron was not as good as that for the proton. This can be due to experimental errors and/or possible involvement of other mechanisms in the relaxation of the deuteron magnetization. The comparative results for different isotopic hydrogen-helium[6] systems reported previously, cannot be generalized to hydrogen-argon systems. Also, any potential-related problems, such as inaccuracies in the transformation of the PES from the homonuclear to heteronuclear system mentioned by Armstrong *et al.*,[6] should lead to the same level of agreement (or disagreement) for both nuclei of the heteronuclear system (assuming the same accuracies for all coupling constants). Thus, attribution of the difference in the agreements between theory and experiment reported for the proton and deuteron spin-lattice relaxation times in the HD-He system does not seem to be justified.

Both the experimental and the theoretical results showed that the relaxation

times for the proton of HD in the HD–Ar system, and of the deuteron of D_2 in the D_2–Ar system lie in a non-linear regime. These results are a consequence of the strong magnetic field employed in this study. Based on these results, it is recommended that the use of the linear-regime formulae for the relaxation times should be based on the exact evaluation of the numerical values of the relevant frequencies, rather than on the assumptions. This will be especially important in future when even higher magnetic field strengths may be used in such studies.

Although it has been a long time since double resonance techniques have been employed in gas phase NMR studies,[125] no NOE measurement has previously been reported in the literature for gaseous samples. For the first time, the possibility of NOE measurements in gas phase samples has been examined in the present study. It has been shown also that the the results of the NOE measurements can be used as an independent source for the evaluation of the theoretical results. In the present study, the NOE measurements have been carried out for both the proton and the deuteron of HD in HD–Ar mixtures. The theoretical values of the NOE enhancements have also been calculated using the NOE formulae developed originally for the liquid phase.[81,88] Within the typical error bars of the NOE measurements, the experimental and theoretical NOE enhancements showed good qualitative agreements. However, the large error bars of the NOE enhancements did not allow a quantitative comparison between the theoretical and experimental results. A proper formulation of the NOE phenomena should be derived directly using kinetic theory arguments, but this has still to be done.

Sensitivity of the gas phase NMR relaxation cross sections to the PES has been examined for two different versions of the XC(fit) potential. While the two versions of the PES gave essentially the same results for all other physical properties of the system, they resulted in slightly different values for the NMR relaxation cross

sections.

NMR spin-lattice relaxation times and the NOE measurements provide a powerful tool for the study of intermolecular potential energy surfaces. Sensitivity of these physical properties to the anisotropic part of the PES's is a unique tool for further refinements of these PES's, which will lead eventually to a better understanding of the nature of interactions between atoms and molecules. It is proposed that a NMR quality test, if feasible, should be a must for the final ranking of any proposed PES for atom-diatom systems.

Chapter 6

Future Studies

Some plans for future studies will be presented in this chapter. In Sec. 6.1 some other possible experiments whose results will complement the results obtained in this study are discussed. A miniature gas handling system that has been designed, built, and tested, and has already been used in some preliminary experiments on HD–Ar mixtures, will be introduced in Sec. 6.2.

6.1 Other experiments and other systems

Further study of the HD–Ar mixtures

As a final step in the study of the HD–Ar system, it would be useful to investigate the possible effects of saturation (decoupling) of the proton on the spin-lattice relaxation times of the deuteron. This study will aim, especially, to determine the effects of the formation of Van der Waals complexes on the relaxation processes with and without decoupling of the other nucleus. It will also allow the investigation of possible interferences between different relaxation mechanisms.[89,93]

Pure *ortho*-D_2–Ar and *para*-D_2–Ar mixtures

It is obvious that the problems associated with the study of the *ortho-para* mixtures of the D_2–Ar system, *i.e.*, difficulties in obtaining separate measurements of the spin-lattice relaxation times for the individual *ortho*-D_2–Ar and *para*-D_2–Ar systems, will not arise if pure gases of the two parity isomers of D_2 are employed in the preparation of the D_2–Ar gas mixtures. Thus, NMR spin-lattice relaxation time studies of pure *para*-D_2–Ar and *ortho*-D_2–Ar mixtures will provide data which can be used directly in the evaluation of the theoretical results. Since pure *ortho*-D_2 and *para*-D_2 gases are not commercially available, they should be prepared locally. The *ortho-para* conversion rate for D_2 is extremely slow in the absence of catalysts or magnetic materials,[67] and therefore it can be neglected safely if appropriate cautions are taken. The results of such studies under conditions in which the deuteron relaxation times for the two pure systems are close to one another can be used to verify the two methods proposed in this thesis for the study of the *ortho-para* mixtures of the D_2–Ar system.

Collisional chemical shift

Analysis of the one-dimensional spectra obtained for HD–Ar and D_2–Ar mixtures showed that the measured chemical shifts are well-behaved functions of temperature. For the D_2–Ar mixtures it has been established that the intra-molecular processes can account for only 10-15% of the observed temperature-dependence of the deuteron chemical shift. In order to study the contribution of the inter-molecular processes (*i.e.*, the collisional or dynamical chemical shift) accurately, contributions from experimental problems, such as instability and temperature dependence of the carrier frequency of the LC-circuit, should be excluded from the measured chemical shifts. To accomplish this an oscilloscope should be employed as a standard fre-

quency reference during the experiments. This would allow the contribution of the inter-molecular interactions to the measured temperature dependence of the chemical shifts to be determined. Development of the formalism linking the dynamical chemical shift to the PES of the system, starting from Eq. (1.18), would provide another NMR-based method for the evaluation of the PES. Such a method requires shorter experimental times than does the measurement of the NMR relaxation times themselves.

HT–Ar mixture

The conclusions drawn for the XC(fit) PES based on comparisons of the theoretical and experimental results obtained for the HD–Ar and D_2–Ar systems can be further examined by studying the HT–Ar system. If the transformation of the PES from the homonuclear to a heteronuclear system improves the anisotropic part of the potential, the agreement between the theoretical and experimental results for the HT–Ar system should be of the same quality as that for the HD–Ar system. A study of the HT–Ar system has also a number of advantages to be discussed below.

The tritium nucleus (or triton) has the highest magnetogyric ratio of any known nucleus; it is over 6.7% higher than that of proton, *i.e.*, $\gamma_T = 28.5336\,T^{-1}\,s^{-1}$.[86] This means that the S/N ratio for the triton peak will be even higher than that for the proton peak. Thus, it is possible to study mixtures with mole fractions much lower than those used in the current study of the HD–Ar and D_2–Ar mixtures. Consequently, problems associated with extrapolation to infinite dilution will be alleviated considerably.

The relaxation mechanisms for the proton and triton of HT in the HT–Ar system are the same (*i.e.*, spin-rotation and dipolar interactions). This allows a cleaner study to be made of sources of possible differences in the agreement

between theoretical and experimental results for the two nuclei, if they are found. It also has the potential of leading to an understanding of the observed differences in the agreement between the theoretical and experimental results for the proton and deuteron of HD in the HD–Ar system.

The values of the NOE enhancements for the proton and triton of HT in the HT–Ar system should be close to one another, because the magnetogyric ratios of the two nuclei are very close. Further, the contribution of the dipolar interaction to the relaxation times of the nuclei of HT in the HT–Ar system is comparable with that of the spin-rotation interaction (the dipolar interaction between the nuclei of HT is about 7 times larger than that of HD). Thus, an NOE study of the HT–Ar system, especially at low temperatures, for which the contribution of the dipolar interaction to the relaxation times is larger, would provide further experimental results for evaluation of the NOE formulae to be derived for the gas phase. The HT molecule in the gas phase is indeed the simplest and neatest system for which the validity of the NOE formulation can be tested.

Another unique feature of the HT–Ar system is that it should be possible to measure values of the σ_V and σ_T cross sections from the measured values of the spin-lattice relaxation times for the proton and triton at temperatures sufficiently low that only the $j = 0$ and $j = 1$ rotational levels of the HT molecule are occupied. When this happens, the NMR cross section matrices are reduced to scalar quantities. Should such temperatures not be attainable, a set of multi-field experiments would allow evaluation of the elements of the cross section matrices from experimental results. No other isotopomer of hydrogen has this feature. The number of magnetic field strengths required for such a study is given by $N_f = \frac{1}{2} j_{max}(j_{max} + 1)$, where j_{max} is the rotational quantum number for the highest significantly occupied level. For example, when $j_{max} = 2$, three field strengths are needed to measure

values of all cross section elements.

Radioactivity of the tritium nucleus requires some health and environmental precautions. No special setup is needed for a triton NMR study, except that the probe should be equipped with a LC circuit which can resonate at the triton Larmor frequency. A tritium NMR study is nowadays a routine experiment.[126-128] Also the half-life of the triton is sufficiently long that the effects of the radioactive decay of the triton on the chemical composition, temperature and electronics of the LC circuit of the probe can be safely neglected.* The required HT gas can be prepared from lithium tritide (LiT) in a substitution reaction with H_2O. The lithium tritide compound can be obtained from the U.S. National Tritium Facility.[129]

The only problem with the above proposed study of the HT–Ar system is that HT gas is exceedingly expensive, so that the gas handling system used in the study of the HD–Ar and D_2–Ar mixtures cannot be used, since such a gas handling system requires large amount of the constituent gases. The solution to this problem is the use of a closed sample cell. In the following section a miniature gas handling system will be introduced which can be used as a sample cell for the study of HT–Ar mixtures. With this special sample cell, a maximum amount of 50 mg of HT gas would be sufficient to carry out a complete set of T_1 measurements, such as that has been carried out for HD–Ar mixtures in this study.

---

*The tritium nucleus undergoes a 0.0186 MeV β decay with a half-life of 12.6 years. The average diffusion length of the generated β particles in the gas phase at 1 atm pressure is about 1 cm. The electric current produced by the β particles, if all can be collected before being absorbed by the $^3He^+$ and H^+ ions produced in the radioactive decay, is of the order of 5 pA for a 1 cm^3 sample of 1% HT in Ar at 1 atm. The chemical composition of the gas mixture after a 10-day experiment, for example, will change only by 0.15%, with non-interfering and clean ^3He and H_2 impurities.

6.2 A miniature gas handling system for gas phase NMR experiments

It was pointed out in Ch. 5 that the gas handling system (GHS) and sample cell setup employed in the study of HD–Ar and D_2–Ar mixtures cannot be used in NMR studies at high temperatures due to the increased contribution of diffusion to the measured relaxation times. It was also mentioned that temperature gradients along the probe and magnet bore and variation of the temperature in the spectrometer room introduce errors into the measured values of the relaxation times. The requirement of large amounts of gases is also another disadvantage of this setup, especially for expensive gases. Different existing closed sample cells (as alternative solutions) and their advantages and disadvantages have been reviewed in Ch. 2, where it was also indicated that none of these sample cells is a good choice for hydrogen-containing gas mixtures.

A new set of detachable compact coaxial valves (DCCV) has been designed to be used with special glass tubes for gas phase measurements, and to fit the standard solution probes used in commercial NMR instruments. The role of the DCCV is to connect the sample cell to the GHS in which the gas mixtures are prepared, and to seal it. Multiple seals, minimal dead volume and piston effects (associated with all valves), convenient connection to and disconnection from the GHS, easy access to all parts for inspection, repair or replacement when required, and reliability are features of this new set of valves. The assembly of the DCCV and the glass tube can be regarded as a miniature GHS, which can be used to store and even to carry gas mixtures safely from one laboratory to another. Figure 6.1 shows an axial cross section of this miniature GHS, which has a weight of $\simeq$400 g, a length of $\simeq$40 cm and a maximum diameter of 2.4 cm. This GHS can hold pressures up to 50 atm over

a temperature range of 250-350 K. A trial version of this GHS has been made by the Science Shop at the University of Waterloo, and has passed a 24-hour pressure test with helium gas at 80 atm. This GHS has also been used successfully in NMR test experiments on H_2–Ar and HD–Ar gas mixtures. More details of the DCCV will appear in a technical report soon.

The miniature GHS described above will be used primarily in the study of HT–Ar mixtures. This GHS will also allow T_2 measurements, which require closed cells, on some hydrogen-argon mixtures under specified conditions. The results of the T_2 measurements can be used in the same way that T_1 measurements have been used to obtain further information about the relaxation processes and the interaction PES in these systems. The miniature GHS introduced here can also be used for other types of spectroscopic techniques.

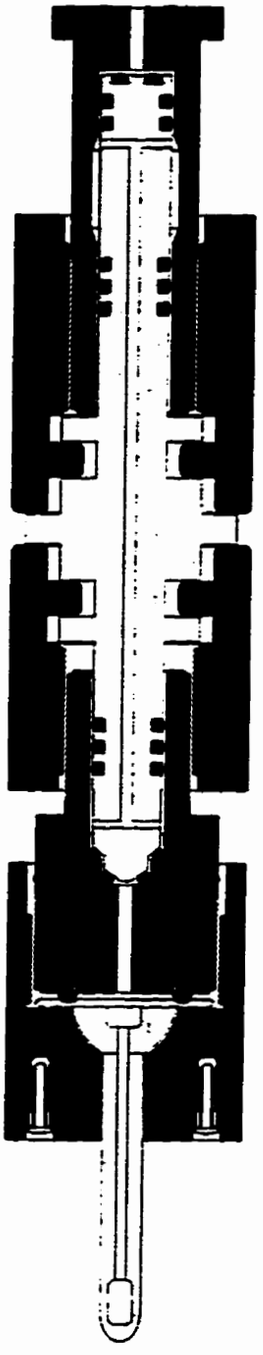

Figure 6.1: DCCV (detachable compact coaxial valve), a miniature gas handling system designed for the NMR study of gases at high pressures. This gas handling system, which is used as a sample cell, can hold pressures up to 50 atm over a temperature range of 250-350 K

Appendix A

Experimental Data

As discussed in Ch. 5, the raw relaxation times for each series of measurements at different temperatures are adjusted to a single pressure corresponding to the probe temperature 273.15 K. To extrapolate to infinite dilution for each temperature, the relaxation times for mixtures at different mole fractions are adjusted to a single density. The header of each table in this appendix identifies the mole fraction of the hydrogen component (D_2 or HD), the amagat density of the gas mixture at temperature 273.15 K, ρ_1, to which the raw relaxation times for each series are adjusted, and the amagat density ρ_2, to which the relaxation times of the corresponding series at different mole fractions are adjusted in order to extrapolate to infinite dilution. Columns of the tables from left to right include probe temperatures T, mixture total pressure P, raw relaxation times $T_1^{(0)}$, pressure-adjusted relaxation times $T_1^{(1)}$, density-adjusted relaxation times $T_1^{(2)}$, and the percent standard deviation of the relaxation times SD. All temperatures are given in Kelvin, pressures in atmosphere and relaxation times in msec. The last table in each section lists the values of the infinite dilution relaxation times and their error bars (both in msec) derived from the raw data using the procedures discussed in detail in Ch.5.

A.1 Proton relaxation times for HD in HD–Ar mixtures

$x_{HD} = 0.86\%$		$\rho_1 = 8.74$ amagat		$\rho_2 = 8.54$ amagat	
T	P	$T_1^{(0)}$	$T_1^{(1)}$	$T_1^{(2)}$	SD
185.46	8.56	31.86	32.28	31.78	0.219
194.93	8.58	28.61	28.92	28.47	0.125
204.70	8.59	22.06	22.27	21.93	0.315
215.01	8.60	19.89	20.06	19.75	0.143
225.90	8.61	20.30	20.45	20.13	0.170
237.30	8.62	18.16	18.28	18.00	0.069
249.10	8.65	16.83	16.88	16.62	0.126
261.18	8.67	15.59	15.61	15.36	0.125
273.46	8.68	14.23	14.21	13.99	0.107
285.89	8.73	13.33	13.25	13.04	0.137
298.45	8.77	12.38	12.25	12.06	0.066
311.13	8.77	11.42	11.29	11.11	0.135
323.95	8.78	10.59	10.47	10.30	0.451
336.88	8.78	10.00	9.88	9.73	0.254
349.84	8.78	9.53	9.41	9.27	0.282
362.72	8.78	8.97	8.86	8.72	0.149
375.33	8.78	8.56	8.45	8.32	0.219
387.40	8.78	8.05	7.96	7.83	0.147
398.65	8.79	7.79	7.69	7.57	0.265
408.74	8.79	7.56	7.46	7.35	0.247
417.41	8.79	7.26	7.16	7.05	0.241

proton of HD in HD–Ar mixtures

$x_{HD} = 0.86\%$ $\rho_1 = 4.78$ amagat $\rho_2 = 4.67$ amagat

T	P	$T_1^{(0)}$	$T_1^{(1)}$	$T_1^{(2)}$	SD
185.46	4.71	18.03	18.21	17.86	0.126
194.93	4.72	17.11	17.28	16.94	0.040
204.70	4.73	15.31	15.41	15.11	0.038
215.01	4.74	13.84	13.90	13.63	0.066
225.90	4.75	12.48	12.52	12.27	0.079
237.30	4.75	11.54	11.57	11.35	0.062
249.10	4.76	10.67	10.68	10.47	0.046
261.18	4.77	9.89	9.88	9.69	0.055
279.65	4.76	8.97	8.97	8.80	0.061
298.45	4.77	8.21	8.20	8.04	0.051
317.53	4.77	7.55	7.54	7.39	0.041
336.88	4.77	7.00	6.98	6.84	0.055
356.30	4.78	6.51	6.49	6.36	0.071
375.33	4.79	6.09	6.06	5.94	0.108
393.15	4.80	5.75	5.71	5.59	0.112
408.74	4.81	5.45	5.40	5.29	0.071

proton of HD in HD–Ar mixtures

$x_{HD} = 0.86\%$ $\rho_1 = 0.96$ amagat $\rho_2 = 0.96$ amagat

T	P	$T_1^{(0)}$	$T_1^{(1)}$	$T_1^{(2)}$	SD
225.90	0.96	10.32	10.32	10.32	0.103
249.10	0.96	9.84	9.81	9.81	0.130
273.46	0.96	9.36	9.36	9.36	0.076
298.45	0.96	9.28	9.31	9.32	0.264
317.53	0.96	8.89	8.89	8.90	0.229
336.88	0.97	8.79	8.73	8.74	0.228
356.30	0.97	8.54	8.48	8.48	0.153
375.33	0.96	8.43	8.40	8.40	0.236
398.65	0.97	8.35	8.30	8.30	0.284
417.41	0.97	8.17	8.09	8.09	0.266

proton of HD in HD–Ar mixtures

$x_{HD} = 2.80\%$ $\rho_1 = 15.03$ amagat $\rho_2 = 15.26$ amagat

T	P	$T_1^{(0)}$	$T_1^{(1)}$	$T_1^{(2)}$	SD
180.67	14.69	60.62	61.25	62.98	0.040
194.93	14.69	49.56	50.05	51.47	0.071
209.78	14.74	41.72	42.00	43.19	0.159
225.90	14.77	36.16	36.34	37.37	0.161
243.16	14.79	30.19	30.30	31.16	0.184
261.18	14.80	25.70	25.76	26.49	0.101
279.65	14.85	22.95	22.94	23.59	0.064
298.45	14.87	17.92	17.88	18.39	0.065
323.95	14.90	16.91	16.84	17.32	0.158
349.84	14.94	15.04	14.94	15.37	0.079
375.33	14.95	13.65	13.55	13.93	0.494
398.65	14.97	12.11	12.00	12.34	0.102
417.41	15.00	10.92	10.81	11.11	0.107

proton of HD in HD–Ar mixtures

$x_{HD} = 2.80\%$ $\rho_1 = 8.34$ amagat $\rho_2 = 8.54$ amagat

T	P	$T_1^{(0)}$	$T_1^{(1)}$	$T_1^{(2)}$	SD
180.67	8.20	33.62	33.93	34.99	0.045
194.93	8.22	27.00	27.20	28.06	0.084
209.78	8.23	23.50	23.63	24.38	0.132
225.90	8.25	20.90	20.97	21.63	0.158
243.16	8.26	17.65	17.70	18.25	0.145
261.18	8.26	15.59	15.63	16.12	0.630
279.65	8.27	13.50	13.52	13.95	0.107
298.45	8.32	11.72	11.66	12.03	0.193
323.95	8.32	10.12	10.07	10.38	0.130
349.84	8.33	9.07	9.01	9.30	0.166
375.33	8.35	8.14	8.07	8.33	0.143
398.65	8.34	7.37	7.32	7.55	0.190
417.41	8.33	6.84	6.80	7.01	0.114

proton of HD in HD–Ar mixtures

$x_{HD} = 2.80\%$ $\rho_1 = 4.55$ amagat $\rho_2 = 4.67$ amagat

T	P	$T_1^{(0)}$	$T_1^{(1)}$	$T_1^{(2)}$	SD
180.67	4.47	19.31	19.58	20.17	0.074
194.93	4.49	16.23	16.40	16.89	0.051
209.78	4.50	14.47	14.58	15.02	0.131
225.90	4.51	12.82	12.88	13.26	0.217
243.16	4.52	10.90	10.94	11.27	0.119
261.18	4.52	9.79	9.81	10.11	0.150
279.65	4.55	8.87	8.84	9.11	0.201
298.45	4.56	8.02	7.98	8.22	0.026
323.95	4.57	7.21	7.16	7.37	0.083
349.84	4.59	6.58	6.50	6.69	0.138
375.33	4.59	6.01	5.94	6.12	0.114
398.65	4.60	5.57	5.49	5.65	0.113
417.41	4.60	5.24	5.16	5.32	0.127

proton of HD in HD–Ar mixtures

$x_{HD} = 5.03\%$ $\rho_1 = 15.50$ amagat $\rho_2 = 15.26$ amagat

T	P	$T_1^{(0)}$	$T_1^{(1)}$	$T_1^{(2)}$	SD
180.67	15.14	55.40	56.00	55.85	0.049
194.93	15.16	47.22	47.65	47.52	0.088
209.78	15.19	40.33	40.63	40.52	0.072
225.90	15.25	34.44	34.56	34.47	0.047
243.16	15.26	30.20	30.30	30.21	0.056
261.18	15.29	26.51	26.53	26.46	0.078
279.65	15.31	23.52	23.50	23.43	0.076
298.45	15.30	21.35	21.35	21.29	0.127
317.53	15.31	18.83	18.83	18.78	0.157
336.88	15.34	17.15	17.11	17.06	0.096
356.30	15.34	15.68	15.64	15.60	0.136
375.33	15.35	14.44	14.39	14.35	0.064
393.15	15.39	13.28	13.20	13.17	0.098
408.74	15.39	12.30	12.23	12.20	0.061
422.50	15.40	11.39	11.32	11.29	0.117

proton of HD in HD–Ar mixtures

$x_{HD} = 5.03\%$ $\rho_1 = 8.38$ amagat $\rho_2 = 8.54$ amagat

T	P	$T_1^{(0)}$	$T_1^{(1)}$	$T_1^{(2)}$	SD
180.67	8.26	26.25	26.47	27.15	0.057
194.93	8.27	22.90	23.06	23.66	0.059
209.78	8.29	19.83	19.92	20.43	0.079
225.90	8.30	17.33	17.39	17.84	0.048
243.16	8.31	15.36	15.39	15.79	0.073
261.18	8.32	13.62	13.63	13.98	0.059
279.65	8.33	12.24	12.24	12.55	0.070
298.45	8.34	11.19	11.17	11.45	0.178
317.53	8.34	10.15	10.14	10.40	0.094
336.88	8.34	9.32	9.30	9.54	0.051
356.30	8.35	8.62	8.59	8.81	0.049
375.33	8.37	7.98	7.94	8.15	0.038
393.15	8.39	7.46	7.40	7.59	0.042
408.74	8.40	7.00	6.93	7.11	0.044

proton of HD in HD–Ar mixtures

$x_{HD} = 5.03\%$ $\rho_1 = 4.55$ amagat $\rho_2 = 4.67$ amagat

T	P	$T_1^{(0)}$	$T_1^{(1)}$	$T_1^{(2)}$	SD
180.67	4.52	15.85	15.88	16.36	0.061
194.93	4.53	13.89	13.91	14.33	0.136
209.78	4.53	12.29	12.29	12.66	0.143
225.90	4.54	10.98	10.97	11.30	0.163
243.16	4.52	9.97	9.99	10.29	0.160
261.18	4.53	8.89	8.90	9.17	0.069
279.65	4.54	8.15	8.14	8.39	0.048
298.45	4.57	7.60	7.54	7.77	0.032
317.53	4.57	7.05	7.00	7.21	0.082
336.88	4.57	6.60	6.55	6.74	0.074
356.30	4.57	6.20	6.15	6.33	0.062
375.33	4.58	5.84	5.78	5.96	0.032
393.15	4.57	5.55	5.50	5.67	0.072
408.74	4.58	5.28	5.23	5.39	0.067
422.50	4.58	5.03	4.98	5.13	0.059

Infinite dilution relaxation times for the proton of HD in HD–Ar mixtures

	4.67 amagat		8.54 amagat		15.26 amagat	
T(K)	T_1	ΔT_1	T_1	ΔT_1	T_1	ΔT_1
180.0	20.256	0.119	35.266	0.246	56.347	0.307
200.0	16.291	0.221	26.769	0.452	44.836	0.917
220.0	13.663	0.205	22.214	0.308	36.642	0.552
240.0	11.743	0.093	19.061	0.273	30.833	0.421
260.0	10.239	0.081	16.324	0.485	26.633	0.263
280.0	9.045	0.049	13.869	0.249	23.452	0.703
300.0	8.128	0.098	11.878	0.262	20.891	0.717
320.0	7.452	0.050	10.492	0.168	18.721	0.455
340.0	6.945	0.085	9.634	0.185	16.853	0.482
360.0	6.504	0.090	9.005	0.150	15.271	0.643
380.0	6.042	0.103	8.262	0.198	13.962	0.342
400.0	5.572	0.092	7.368	0.139	12.805	0.231
420.0	5.332	0.034	7.119	0.057	11.461	0.227

A.2 Deuteron relaxation times for HD in HD–Ar mixtures

$x_{HD} = 0.86\%$ $\rho_1 = 8.74$ amagat $\rho_2 = 8.54$ amagat

T	P	$T_1^{(0)}$	$T_1^{(1)}$	$T_1^{(2)}$	SD
185.46	8.56	103.50	104.85	103.23	0.491
194.93	8.58	95.27	96.29	94.80	0.544
204.70	8.59	89.24	90.09	88.70	0.749
215.01	8.60	84.27	84.98	83.66	0.673
225.90	8.61	80.13	80.74	79.49	0.443
237.30	8.62	76.96	77.46	76.26	0.558
249.10	8.65	68.64	68.82	67.75	0.465
261.18	8.67	69.24	69.29	68.22	0.708
273.46	8.68	67.28	67.21	66.17	0.962
285.89	8.73	67.59	67.16	66.12	1.302
298.45	8.77	58.92	58.27	57.37	0.555
311.13	8.77	56.58	55.94	55.07	0.883
323.95	8.78	53.08	52.46	51.65	1.095
336.88	8.78	52.93	52.32	51.51	1.006
349.84	8.78	50.59	49.98	49.21	0.541
362.72	8.78	48.04	47.47	46.73	1.192
375.33	8.78	48.30	47.70	46.96	1.002
387.40	8.78	49.04	48.43	47.68	0.973
398.65	8.79	49.84	49.21	48.45	1.209
408.74	8.79	55.96	55.22	54.37	0.695
417.41	8.79	58.86	58.09	57.19	0.187

deuteron of HD in HD–Ar mixtures

$x_{HD} = 0.86\%$ $\rho_1 = 4.78$ amagat $\rho_2 = 4.67$ amagat

T	P	$T_1^{(0)}$	$T_1^{(1)}$	$T_1^{(2)}$	SD
185.46	4.71	56.08	56.67	55.56	0.603
194.93	4.72	51.69	52.19	51.17	0.352
204.70	4.73	48.76	49.09	48.13	0.461
215.01	4.74	47.68	47.88	46.95	0.305
225.90	4.75	44.55	44.67	43.80	0.683
237.30	4.75	42.35	42.47	41.63	0.748
249.10	4.76	39.25	39.27	38.51	0.549
261.18	4.77	37.71	37.69	36.95	0.871
279.65	4.76	36.03	36.03	35.33	0.999
298.45	4.77	33.99	33.94	33.28	0.688
317.53	4.77	32.34	32.30	31.67	0.683
336.88	4.77	31.57	31.50	30.88	0.522
356.30	4.78	29.99	29.89	29.30	0.832
375.33	4.79	27.75	27.58	27.04	1.514
393.15	4.80	26.56	26.34	25.83	1.289
408.74	4.81	25.73	25.50	25.00	1.220

$x_{HD} = 0.86\%$ $\rho_1 = 0.96$ amagat $\rho_2 = 0.96$ amagat

No acceptable data due to poor S/N ratio

deuteron of HD in HD–Ar mixtures

$x_{HD} = 2.80\%$ $\rho_1 = 15.03$ amagat $\rho_2 = 15.26$ amagat

T	P	$T_1^{(0)}$	$T_1^{(1)}$	$T_1^{(2)}$	SD
180.67	14.69	191.18	193.15	198.63	0.872
194.93	14.69	176.79	178.54	183.60	0.736
209.78	14.74	165.73	166.84	171.58	0.547
225.90	14.77	152.77	153.52	157.88	0.536
243.16	14.79	133.19	133.67	137.46	0.348
261.18	14.80	122.14	122.44	125.92	0.606
279.65	14.85	125.27	125.21	128.77	0.323
298.45	14.87	92.69	92.50	95.13	0.529
323.95	14.90	96.71	96.31	99.04	0.633
349.84	14.94	91.53	90.90	93.48	0.618
375.33	14.95	87.32	86.67	89.13	0.786
398.65	14.97	82.43	81.69	84.00	0.492
417.41	15.00	80.81	79.96	82.23	2.037

deuteron of HD in HD–Ar mixtures

$x_{HD} = 2.80\%$ $\rho_1 = 8.34$ amagat $\rho_2 = 8.54$ amagat

T	P	$T_1^{(0)}$	$T_1^{(1)}$	$T_1^{(2)}$	SD
180.67	8.20	105.82	106.79	110.15	0.244
194.93	8.22	93.99	94.70	97.68	0.222
209.78	8.23	88.01	88.50	91.28	0.262
225.90	8.25	81.87	82.13	84.71	0.228
243.16	8.26	74.80	74.98	77.34	0.286
261.18	8.26	68.85	69.01	71.18	0.289
279.65	8.27	64.45	64.55	66.58	0.212
298.45	8.32	55.25	54.99	56.72	0.420
323.95	8.32	51.63	51.36	52.98	0.640
349.84	8.33	51.94	51.62	53.24	0.581
375.33	8.35	49.39	48.98	50.52	0.818
398.65	8.34	48.19	47.86	49.37	1.079
417.41	8.33	44.85	44.58	45.98	0.777

deuteron of HD in HD–Ar mixtures

$x_{HD} = 2.80\%$ $\rho_1 = 4.55$ amagat $\rho_2 = 4.67$ amagat

T	P	$T_1^{(0)}$	$T_1^{(1)}$	$T_1^{(2)}$	SD
180.67	4.47	56.88	57.67	59.42	0.316
194.93	4.49	51.08	51.60	53.16	0.247
209.78	4.50	47.73	48.08	49.53	0.289
225.90	4.51	44.70	44.89	46.25	0.366
243.16	4.52	40.28	40.43	41.65	0.329
261.18	4.52	37.62	37.70	38.84	0.302
279.65	4.55	36.20	36.10	37.19	0.728
298.45	4.56	34.65	34.47	35.52	0.656
323.95	4.57	31.34	31.09	32.03	0.419
349.84	4.59	30.37	29.97	30.88	0.792
375.33	4.59	28.49	28.12	28.97	0.734
398.65	4.60	26.97	26.58	27.39	0.367
417.41	4.60	26.42	26.04	26.83	0.474

deuteron of HD in HD–Ar mixtures

$x_{HD} = 5.03\%$ $\rho_1 = 15.50$ amagat $\rho_2 = 15.26$ amagat

T	P	$T_1^{(0)}$	$T_1^{(1)}$	$T_1^{(2)}$	SD
180.67	15.14	193.43	195.53	194.99	0.338
194.93	15.16	174.52	176.11	175.62	0.619
209.78	15.19	163.24	164.44	163.98	0.590
225.90	15.25	148.73	149.27	148.86	0.465
243.16	15.26	142.02	142.45	142.05	0.508
261.18	15.29	134.01	134.13	133.75	0.675
279.65	15.31	123.66	123.58	123.23	0.499
298.45	15.30	114.98	114.98	114.66	0.561
317.53	15.31	105.83	105.81	105.52	1.113
336.88	15.34	101.44	101.20	100.92	0.546
356.30	15.34	97.38	97.15	96.88	0.616
375.33	15.35	93.25	92.95	92.69	1.268
393.15	15.39	90.42	89.88	89.63	0.800
408.74	15.39	88.81	88.30	88.06	0.861
422.50	15.40	85.21	84.64	84.41	0.511

deuteron of HD in HD–Ar mixtures

$x_{HD} = 5.03\%$ $\rho_1 = 8.38$ amagat $\rho_2 = 8.54$ amagat

T	P	$T_1^{(0)}$	$T_1^{(1)}$	$T_1^{(2)}$	SD
180.67	8.26	87.34	88.07	90.34	0.172
194.93	8.27	82.14	82.73	84.86	0.210
209.78	8.29	76.34	76.67	78.65	0.192
225.90	8.30	70.06	70.28	72.09	0.165
243.16	8.31	66.08	66.22	67.92	0.188
261.18	8.32	62.45	62.50	64.11	0.172
279.65	8.33	59.21	59.19	60.71	0.174
298.45	8.34	56.27	56.16	57.61	0.176
317.53	8.34	53.53	53.47	54.84	0.121
336.88	8.34	51.64	51.53	52.86	0.106
356.30	8.35	49.73	49.60	50.87	0.171
375.33	8.37	47.59	47.35	48.57	0.155
393.15	8.39	45.88	45.52	46.70	0.170
408.74	8.40	44.52	44.12	45.26	0.207

deuteron of HD in HD–Ar mixtures

$x_{HD} = 5.03\%$ $\rho_1 = 4.55$ amagat $\rho_2 = 4.67$ amagat

T	P	$T_1^{(0)}$	$T_1^{(1)}$	$T_1^{(2)}$	SD
180.67	4.52	47.28	47.39	48.82	0.318
194.93	4.53	43.96	44.03	45.36	0.262
209.78	4.53	40.92	40.92	42.16	0.235
225.90	4.54	38.70	38.67	39.84	0.214
243.16	4.52	36.38	36.46	37.56	0.198
261.18	4.53	34.06	34.11	35.14	0.205
279.65	4.54	32.30	32.28	33.25	0.223
298.45	4.57	30.71	30.49	31.41	0.281
317.53	4.57	29.72	29.51	30.40	0.306
336.88	4.57	28.38	28.15	29.00	0.225
356.30	4.57	27.62	27.38	28.21	0.126
375.33	4.58	25.98	25.73	26.51	0.139
393.15	4.57	25.13	24.91	25.66	0.260
408.74	4.58	24.16	23.93	24.66	0.210
422.50	4.58	23.41	23.18	23.88	0.243

Infinite dilution relaxation times for the deuteron of HD in HD–Ar mixtures

	4.67 amagat		8.54 amagat		15.26 amagat	
T(K)	T_1	ΔT_1	T_1	ΔT_1	T_1	ΔT_1
180.0	59.533	1.679	110.852	2.660	196.204	11.762
200.0	52.088	1.906	95.145	3.716	170.619	20.659
220.0	46.802	1.971	86.741	2.406	155.015	12.680
240.0	42.765	1.585	79.543	2.465	143.445	9.345
260.0	39.527	1.087	71.836	1.742	133.093	9.828
280.0	36.884	2.992	64.201	4.667	123.146	21.123
300.0	34.730	2.807	57.930	5.852	113.873	24.983
320.0	32.958	1.506	53.954	3.061	105.906	13.502
340.0	31.431	2.876	52.262	3.696	99.724	18.327
360.0	30.003	3.199	51.840	5.426	95.335	24.361
380.0	28.599	2.574	51.106	7.543	92.174	22.569
400.0	27.358	1.222	48.849	2.292	89.186	16.596
420.0	26.827	0.955	45.678	1.651	85.128	10.611

A.3 Single-exponential relaxation times for the deuteron of D_2 in D_2–Ar mixtures

$x_{D_2} = 1.97\%$ $\rho_1 = 13.84$ amagat $\rho_2 = 13.91$ amagat

T	P	$T_1^{(0)}$	$T_1^{(1)}$	$T_1^{(2)}$	SD
180.67	13.63	47.29	47.42	48.24	1.320
194.93	13.64	41.49	41.58	42.30	1.506
209.78	13.65	37.20	37.27	37.91	1.112
225.90	13.64	33.15	33.23	33.80	1.004
243.16	13.65	29.59	29.64	30.16	0.778
261.18	13.66	27.26	27.28	27.75	0.654
279.65	13.68	24.80	24.78	25.21	0.581
298.45	13.61	21.95	22.05	22.43	0.732
317.53	13.63	21.58	21.66	22.03	0.428
336.88	13.65	20.26	20.29	20.64	0.499
356.30	13.66	19.27	19.30	19.63	0.420
375.33	13.66	18.57	18.59	18.91	0.360
393.15	13.69	17.22	17.20	17.50	0.385
408.74	13.72	16.42	16.37	16.65	0.340
422.50	13.73	15.56	15.50	15.76	0.325

deuteron of D_2 in D_2–Ar mixtures

$x_{D_2} = 1.97\%$ $\rho_1 = 7.07$ amagat $\rho_2 = 7.16$ amagat

T	P	$T_1^{(0)}$	$T_1^{(1)}$	$T_1^{(2)}$	SD
180.67	6.98	25.89	26.05	26.55	1.207
194.93	6.98	22.60	22.73	23.17	0.951
209.78	6.99	20.10	20.20	20.59	0.742
225.90	7.00	18.12	18.19	18.54	0.602
243.16	7.00	16.33	16.39	16.70	0.488
261.18	7.01	15.04	15.07	15.36	0.624
279.65	7.02	13.74	13.75	14.01	0.812
298.45	7.01	12.61	12.63	12.87	0.463
317.53	7.00	12.19	12.23	12.46	0.402
336.88	6.98	11.24	11.31	11.53	0.534
356.30	6.98	10.76	10.83	11.04	0.413
375.33	6.99	10.37	10.43	10.63	0.518
393.15	6.99	9.67	9.72	9.90	0.886
408.74	6.99	9.44	9.49	9.67	0.736
422.50	6.99	8.83	8.88	9.05	0.845

deuteron of D_2 in D_2–Ar mixtures

$x_{D_2} = 1.97\%$ $\rho_1 = 3.55$ amagat $\rho_2 = 3.57$ amagat

T	P	$T_1^{(0)}$	$T_1^{(1)}$	$T_1^{(2)}$	SD
180.67	3.51	11.83	11.94	12.03	0.881
194.93	3.52	11.25	11.32	11.41	1.171
209.78	3.53	10.51	10.56	10.64	0.833
225.90	3.53	9.65	9.69	9.76	0.757
243.16	3.53	9.00	9.03	9.10	1.036
261.18	3.54	8.46	8.47	8.54	0.777
279.65	3.55	8.07	8.06	8.12	1.020
298.45	3.55	7.59	7.57	7.63	0.686
317.53	3.55	7.24	7.23	7.28	0.578
336.88	3.55	7.30	7.28	7.34	1.192
356.30	3.55	6.82	6.80	6.85	0.843
375.33	3.56	6.38	6.36	6.41	1.131
393.15	3.55	5.99	5.97	6.02	0.946
408.74	3.55	6.37	6.36	6.41	1.595
422.50	3.55	5.99	5.98	6.02	0.964

deuteron of D_2 in D_2–Ar mixtures

$x_{D_2} = 3.77\%$ $\rho_1 = 13.99$ amagat $\rho_2 = 13.91$ amagat

T	P	$T_1^{(0)}$	$T_1^{(1)}$	$T_1^{(2)}$	SD
180.67	13.77	53.47	53.71	54.03	0.901
194.93	13.80	46.94	47.04	47.31	0.822
209.78	13.82	40.55	40.57	40.81	0.798
225.90	13.83	35.45	35.45	35.65	0.712
243.16	13.84	30.77	30.75	30.93	0.605
261.18	13.83	28.70	28.70	28.87	0.644
279.65	13.82	25.88	25.89	26.04	0.487
298.45	14.01	23.99	23.69	23.82	0.425
317.53	13.97	22.47	22.24	22.37	0.414
336.88	13.94	21.01	20.84	20.96	0.359
356.30	13.90	19.97	19.86	19.97	0.306
375.33	13.90	19.09	19.00	19.11	0.290
393.15	13.92	18.30	18.18	18.29	0.333
408.74	13.93	17.53	17.41	17.51	0.283
422.50	13.93	17.04	16.91	17.01	0.203

deuteron of D_2 in D_2–Ar mixtures

$x_{D_2} = 3.77\%$ $\rho_1 = 7.26$ amagat $\rho_2 = 7.16$ amagat

T	P	$T_1^{(0)}$	$T_1^{(1)}$	$T_1^{(2)}$	SD
180.67	7.14	27.41	27.70	27.46	0.888
194.93	7.16	23.19	23.38	23.19	0.701
209.78	7.19	20.80	20.90	20.72	0.713
225.90	7.20	18.81	18.86	18.70	0.591
243.16	7.21	17.10	17.13	16.98	0.521
261.18	7.22	15.84	15.84	15.71	0.538
279.65	7.23	14.92	14.90	14.78	0.506
298.45	7.23	13.73	13.70	13.59	0.601
317.53	7.24	12.68	12.65	12.54	0.365
336.88	7.26	11.89	11.84	11.74	0.417
356.30	7.25	11.44	11.39	11.29	0.452
375.33	7.25	10.73	10.69	10.60	0.328
393.15	7.26	10.10	10.04	9.96	0.452
408.74	7.26	10.00	9.94	9.86	0.469
422.50	7.31	10.12	10.01	9.92	0.438

deuteron of D_2 in D_2–Ar mixtures

$x_{D_2} = 3.77\%$ $\rho_1 = 3.58$ amagat $\rho_2 = 3.57$ amagat

T	P	$T_1^{(0)}$	$T_1^{(1)}$	$T_1^{(2)}$	SD
180.67	3.58	14.13	14.10	14.11	0.835
194.93	3.58	12.61	12.59	12.59	0.696
209.78	3.58	11.32	11.30	11.30	0.717
225.90	3.58	10.39	10.37	10.37	0.626
243.16	3.57	9.45	9.44	9.44	0.499
261.18	3.57	8.38	8.38	8.38	0.649
279.65	3.57	7.86	7.86	7.86	0.845
298.45	3.57	7.61	7.61	7.61	0.585
317.53	3.56	7.17	7.19	7.19	0.395
336.88	3.55	6.86	6.90	6.90	0.843
356.30	3.53	6.66	6.73	6.73	0.425
375.33	3.52	6.33	6.42	6.42	0.657
393.15	3.49	6.21	6.36	6.36	0.542
408.74	3.46	6.18	6.37	6.37	1.070
422.50	3.44	6.22	6.46	6.46	0.716

Infinite dilution single-exponential relaxation times for the deuteron of D_2 in D_2–Ar mixtures

	3.57 amagat		7.16 amagat		13.91 amagat	
T(K)	T_1	ΔT_1	T_1	ΔT_1	T_1	ΔT_1
180.669	9.772	1.0781	25.546	2.5426	41.948	5.0544
194.932	10.120	0.9790	23.144	1.7188	36.845	4.4555
209.785	9.930	0.7934	20.442	1.4151	34.752	3.3770
225.903	9.090	0.6454	18.357	1.0521	31.793	2.6655
243.158	8.721	0.5991	16.384	0.8185	29.310	1.9167
261.177	8.717	0.5550	14.972	0.8394	26.540	1.7382
279.655	8.406	0.6843	13.176	0.8369	24.299	1.2585
298.446	7.649	0.4485	12.088	0.7074	20.919	1.1625
317.529	7.377	0.3137	12.378	0.4499	21.654	0.8841
336.877	7.817	0.6462	11.303	0.5065	20.288	0.8024
356.302	6.972	0.3647	10.754	0.4683	19.252	0.6466
375.327	6.401	0.4962	10.651	0.3957	18.699	0.5646
393.149	5.653	0.3956	9.836	0.5652	16.639	0.5986
408.740	6.448	0.7456	9.468	0.5201	15.717	0.4926
422.500	5.540	0.4673	8.104	0.5209	14.406	0.3814

References

1. R. Tyco, How does nmr probe molecular dynamics, in *Nuclear Magnetic Resonance Probes of Molecular Dynamics*, edited by R. Tyko, pages 1–26, Kluwer Academic, The Netherland, 1994.

2. F. R. W. McCourt, J. J. M. Beenakker, W. E. Köhler, and I. Kuščer, *Nonequilibrium Phenomena in Polyatomic Gases*, volume 1, Oxford University Press, Oxford, 1990.

3. F. R. W. McCourt, NMR-Basic Principles and Progress **13**, 55 (1975).

4. R. S. Wagner, R. L. Armstrong, C. Bissonnette, and F. R. W. McCourt, J. Chem. Phys. **92**, 5907 (1990).

5. C. Lemaire, R. L. Armstrong, and F. R. W. McCourt, J. Chem. Phys. **81**, 5275 (1984).

6. R. L. Armstrong, M. Bogdan, K. R. Jeffrey, C. Bissonnette, and F. R. W. McCourt, J. Chem. Phys. **99**, 5754 (1993).

7. W. E. Köhler and J. Schaefer, Physica **A120**, 185 (1983).

8. C. Bissonnette, C. E. Chuaqui, K. G. Crowell, R.J. Le Roy, R. J. Wheatley, and W. J. Meath, J. Chem. Phys. **105**, 2639 (1996).

9. R. R. Ernst, G. Bodenhausen, and A. Wokaun, *Principles of Nuclear Magnetic Resonance in One and Two Dimensions*, Clarendon, Oxford, England, 1987.

10. F. Bloch, Phys. Rev. **70**, 460 (1946).

11. M. L. Martin, G. J. Martin, and J. J. Delpuech, *Practical NMR Spectroscopy*, Heyden and Sons, London, 1980.

12. E. Fukushima, *Experimental pulse NMR : a nuts and bolts approach*, Addison, Toronto, 1981.

13. A. Abragam, *The Principles of Nuclear Magnetism*, Oxford University Press, Oxford, England, Reprint ed., 1986.

14. C. P. Slichter, *Principles of Magnetic Resonance*, Springer-Verlag, Berlin, 3rd ed., 1989.

15. B. Shizgal, J. Chem. Phys. **58**, 3424 (1973).

16. B. Shizgal, Chem. Phys. Lett. **20**, 265 (1973).

17. E. R. Hunt and H. Y. Carr, Phys. Rev. **130**, 2302 (1963).

18. H. C. Torrey, Phys. Rev. **130**, 2306 (1963).

19. C. J. Jameson, A. K. Jameson, and J.K. Hwang, J. Chem. Phys. **89**, 4074 (1988).

20. R. G. Gordon, J. Chem. Phys. **44**, 228 (1966).

21. P. W. Atkins, *Physical Chemistry*, Freeman, New York, 4th ed., 1990.

22. I. Oppenheim and M. Bloom, Can. J. Phys. **39**, 845 (1961).

23. R. F. Snider F. M. Chen, J. Chem. Phys. **48**, 3185 (1968).

24. W. N. Hardy, *Nuclear Spin Relaxation in Gaseous H_2, HD and D_2*, Ph.D. thesis, The University of British Columbia, 1964.

25. J. S. Blicharski and W. Nosel, Acta. Phys. Polon. **42**, 223 (1972).

26. P. Granger, K. Elbayed, J. Raya, P. Kempgen, and J. Rose, J. Magn. Reson. **A117**, 179 (1995).

27. R. F. Snider, J. Chem. Phys. **32**, 1051 (1960).

28. A. M. Arthurs and A. Dalgarno, Proc. R. Soc. Lond. **A256**, 540 (1960).

29. R. N. Zare, *Angular Momentum*, Academic, New York, 1988.

30. I.C. Percival and M. J. Seaton, Proc. Camb. Phil. Soc. **53**, 654 (1957).

31. M. E. Thachuk, *The Utility of Corrected Sudden Approximations for the Description of Atom-Linear Rotor Scattering*, Ph.D. thesis, University of Waterloo, 1991.

32. K. McLenithan, *Accurate Quantum Mechanical Decoupling Approximations for Molecular Scattering Theory*, Ph.D. thesis, University of Illinois at Urbana-Champaign, 1982.

33. F. A. Berezin and M. A. Shubin, *The Schrödinger Equation*, Kluwer, Netherland, 1991.

34. M. S. Child, *Molecular Collision Theory*, Academic, London, 1974.

35. D.E. Fitz, D. J. Kouri, D. Evans, and D. K. Hoffman, J. Chem. Phys. **74**, 5022 (1981).

36. W.-K. Liu, F. R. W. McCourt, and W. E. Köhler, J. Chem. Phys. **71**, 2566 (1979).

37. W.-K. Liu, F. R. W. McCourt, D.E. Fitz, and W. E. Köhler, J. Chem. Phys. **71**, 415 (1979).

38. W.-K. Liu, F. R. W. McCourt, D. E. Fitz, and D. J. Kouri, J. Chem. Phys. **76**, 5112 (1982).

39. P. O. Moreno, N.S. True, and C. B. LeMaster, J. Phys. Chem. **94**, 8780 (1990).

40. J. P. Chauvel, B. R. Friedman, H. Van, E. D. Winegar, and N. S. True, J. Chem. Phys. **82**, 3996 (1985).

41. C. J. Jameson, Chem. Rev. **91**, 1375 (1991), and the references therein.

42. Y. I. Neronov, A. E. Barzakh, and Kh. Mukhamadiev, Soviet Physics–JETP **42**, 950 (1976).

43. Y. I. Neronov and A. E. Barzakh, Soviet Physics–JETP **45**, 871 (1977).

44. H. Y. Carr, Physica **A156**, 212 (1989).

45. H. Y. Carr and E. M. Purcell, Phys. Rev. **88**, 415 (1952).

46. H. Y. Carr and E.R. Hunt, Phys. Rev. **121**, 20 (1961).

47. W. G. Pfann, *Zone Melting*, John Wiley and Sons, New York, 1966.

48. W. Gombler and H. Willner, Interl. Lab. **14**, 84 (1984).

49. W. Gombler, J. Magn. Reson. **53**, 69 (1983).

50. H. Vanni, W. L. Earl, and A. E. Merbach, J. Magn. Reson. **29**, 11 (1978).

51. W. L. Earl, H. Vanni, and A. E. Merbach, J. Magn. Reson. **30**, 571 (1978).

52. L. Ballard, C. Reiner, and J. Jonas, J. Magn. Reson. **A123**, 81 (1996), this is the most recent design reported for a high pressure gas phase probe.

53. R. A. Serway, *Physics for Science and Engineering with Modern Physics*, Saunders College Publishing, USA, 3rd ed., 1990.

54. C.L. Hutchinson and J. P. Kleinman, *The ARRL Handbook for Radio Amateurs*, American Radio Relay League Inc., USA, 69th ed., 1992.

55. M. Bogdan, K. R. Jeffrey, and R. L. Armstrong, J. Chem. Phys. **98**, 6154 (1993).

56. J.H. Dymond and E.B. Smith, *Virial Coefficients of Pure Gases and Mixtures*, Clarendon, Oxford, England, 2nd ed., 1980.

57. S. L. Apple, *Seal Design Catalogue*, Apple Rubber Products, Lancaster (New York), 1989, a perfect reference for calculation of all O-ring and groove designs.

58. R. S. Wagner, R. L. Armstrong, C. Lemaire, and F. R. W. McCourt, J. Chem. Phys. **84**, 1137 (1986).

59. J.M. Hollas and D. Phillips, *Jet Spectroscopy and Molecular Dynamics*, Blackie, New York, 1st ed., 1995.

60. W. Kalechstein and R. L. Armstrong, Can. J. Phys. **55**, 1083 (1977).

61. T. E. Raidy and F. R. W. McCourt, Chem. Phys. Lett. **48**, 299 (1977).

62. G. Govil, Appl. Spect. Rev. **7**, 47 (1973).

63. J. Brewer and G. W. Vaughn, J. Chem. Phys. **50**, 2960 (1969).

64. B. Schramm, E. Elias, and R. Pilger, Chem. Phys. Lett. **88**, 459 (1982).

65. D. A. McQuarrie, *Statistical Mechanics*, Harper and Row, New York, 1976.

66. T. L. Hill, *An Introduction to Statistical Thermodynamics*, Dover, USA, 1986.

67. I. F. Silvera, Rev. Mod. Phys. **52**, 393 (1980).

68. C. Lemaire, R. L. Armstrong, and F.R. W. McCourt, J. Chem. Phys. **87**, 6499 (1987).

69. A. G. Marshall and F. R. Verdun, *Fourier Transforms in NMR, Optical and Mass Spectroscopy*, Elsevier, Amsterdam, 1990.

70. J. R. Beckett and H. Y. Carr, Phys. Rev. **A24**, 144 (1981).

71. C. J. Jameson and A. C. de Dios, J. Chem. Phys. **98**, 2208 (1992).

72. C. Lemaire and R. L. Armstrong, Can. J. Phys. **63**, 179 (1985).

73. D. C. Ailion, Adv. Mag. Res. **5**, 177 (1971).

74. J. H. Noggle and R. E. Schirmer, *The Nuclear Overhauser Effect*, Academic Press, New York, 1971.

75. D. Neuhaus and M. Williamson, *The Nuclear Overhauser Effect in Structural and Conformational Analysis*, VCH Publications, New York, 1989.

76. H. W. Spiess, D. Schweitzer, U. Haeberlen, and K. H. Hausser, .

77. V. Mlynarik, Prog. Nuc. Mag. Res. Spect. **18**, 277 (1986).

78. J. Jeener and P. Broekaert, Phys. Rev. **157**, 232 (1967).

79. H. W. Spiess, J. Chem. Phys. **72**, 6755 (1980).

80. A. W. Overhauser, Phys. Rev. **92**, 411 (1953).

81. I. Solomon, Phys. Rev. **99**, 559 (1955).

82. K. E. Kover and G. Batta, J. Chem. Phys. **19**, 223 (1987).

83. S. Neugebauer, A. Taha, C. B. Lemaster, C. L. Lemaster, and N. S. True, Abstr. Amer. Chem. Soc. **211**, 253 (1996).

84. A. Nyborg, C. B. Lemaster, and N. S. True, Abstr. Amer. Chem. Soc. **211**, 411 (1996).

85. J. W. Nibler, P. Minarik, W Fitts, and R. Kohnert, Abstr. Amer. Chem. Soc. **211**, 42 (1996).

86. R. K. Harris, *Nuclear Magnetic Resonance Spectroscopy*, Longman, England, 1986.

87. A. Bain, 1996, Private Communication.

88. I. Solomon and N. Bloembergen, J. Chem. Phys. **25**, 261 (1956).

89. J. S. Blicharski and W. Nosel, Acta. Phys. Polon. **38**, 19 (1970).

90. N. Murali and B. D. N. Rao, J. Magn. Reson. **A118**, 202 (1996).

91. J. S. Blicharski, Acta. Phys. Polon. **36**, 211 (1969).

92. L. G. Werbelow, A. Allouch, and G. Pouzard, J. Chem. Soc., Faraday Trans. II, **83**, 871 (1987).

93. S. Grzesiek and A. Bax, J. Magn. Reson. **A116**, 10196 (1994).

94. S. Mohanty and H. J. Bernstein, J. Chem. Phys. **54**, 2254 (1971).

95. G. Tenti and F. R. W. McCourt, J. Chem. Phys. **65**, 623 (1976).

96. R. J. Le Roy, LEVEL 6.1 – *A Computer Program Solving the Radial Schrödinger Equation for Bound and Quasibound Levels, and Calculating Various Expectation Values and Matrix Elements*, University of Waterloo Chemical Physics Report CP-555R, October 1996.

97. R. J. Le Roy and C. Schwartz, *Eigenvalues and Matrix Elements for All Levels of All Isotopic Forms of Diatomic Hydrogen*, University of Waterloo Chemical Physics Report CP-301R, September 1987.

98. R. J. Le Roy, 1996, Private Communication.

99. H. B. Schlegel P. M. W. Gill B. G. Johnson M. A. Robb J. R. Cheeseman T. Keith G. A. Petersson J. A. Montgomery K. Raghavachari M. A. Al-Laham V. G. Zakrzewski J. V. Ortiz J. B. Foresman J. Cioslowski B. B. Stefanov A. Nanayakkara M. Challacombe C. Y. Peng P. Y. Ayala W. Chen M. W. Wong J. L. Andres E. S. Replogle R. Gomperts R. L. Martin D. J. Fox J. S. Binkley D. J. Defrees J. Baker

J. P. Stewart M. Head-Gordon C. Gonzalez M. J. Frisch, G. W. Trucks and J. A. Pople, GAUSSIAN94, *A Connected System of Programs for Performing a Variety of Semi-Empirical and Ab Initio Molecular Orbital (MO) Calculations*, 1994-1995, distributed by Gaussian Inc.

100. J. B. Foresman and Æ. Frisch, *Exploring Chemistry with Electronic Structure Methods*, Gaussian Inc., Pittsburgh, USA, 2nd ed., 1996.

101. J. R. Cheeseman, G. W. Trucs, T. A. Keith, and M. J. Frisch, J. Chem. Phys. **104**, 5497 (1996).

102. C. Schwartz and R. J. Le Roy, J. Mol. Spect. **121**, 420 (1987).

103. To obtain a copy of this file connect to the site *theochem.uwaterloo.ca* by *ftp*. Enter *anonymous* as your userid, and use *your email address* as your password. The data file is named *d2ar.nmr* and is located in the directory */pub/nmr_data/*. The file can be obtained by entering the command *get d2ar.nmr*.

104. J. M. Hutson and S. Green, MOLSCAT – *A Computer Program for Quantum Mechanical Close-Coupled Calculation of the Non-Reactive Scattering S-Matrix*, Version 14, September 1995, distributed by Collaborative Computational Project No. 6 of the Science and Engineering Research Council (UK).

105. S. Green, SBE – *A Computer Program Calculating Senftleben-Beenakker Cross Sections from the Scattering S-Matrix*, 1982, latest modification by S. Green 1994.

106. M. E. Thachuk, CRAVE – *A Computer Program Calculating the Thermally-Averaged Cross Sections from Energy-Dependent SBE Cross Sections*, University of Waterloo, 1990, latest modification by H. Sabzyan 1996.

107. R. J. Le Roy and R. B. Bernstein, J. Chem. Phys. **54**, 5114 (1971).

108. J. Reuss and S. Stolte, Physica **42**, 111 (1969).

109. P. W. Atkins, *Molecular Quantum Mechanics*, Oxford, London, 2nd ed., 1983.

110. M. Abramowitz and I. Stegun, *Handbook of Mathematical Functions*, Dover, New York, 1972.

111. To obtain a copy of this subroutine connect to the site *theochem.uwaterloo.ca* by *ftp*. Enter *anonymous* as your userid, and use *your email address* as your password. The subroutine is named *potenl.f* and is located in the directory */pub/leroy/*. The subroutine can be obtained by entering the command *get potenl.f*.

112. K. R. Foster and J. H. Rugheimer, J. Chem. Phys. **56**, 2632 (1972).

113. R. F. Code and N.F. Ramsey, Phys. Rev. **A4**, 1945 (1971).

114. H. Gilboa, B. Chapman, and P. W. Kuchel, J. Magn. Reson. **119**, 1 (1996).

115. J. Ganem and R. E. Norberg, Phys. Rev. **B43**, 1 (1990).

116. C. J. Jameson, A. K. Jameson, K. Smith, and N. C. Jackowski, J. Chem. Phys. **86**, 2717 (1987).

117. T. E. Raidy and F. R. W. McCourt, Chem. Phys. Lett. **38**, 300 (1976).

118. H. Kreek and R. J. Le Roy, J. Chem. Phys. **63**, 338 (1975).

119. G. B. Clark, 1995, Unpublished Work.

120. R. Wasylishen, Nmr relaxation and dynamics, in *NMR Spectroscopy Techniques*, edited by C. Dybowski and R. Lichter, pages 45–91, M. Dekker, New York, 1980.

121. J. Vojtik, I. Paidarova, V. Spirko, and M. Petras, Intrnl. J. Quant. Chem. **38**, 357 (1990).

122. J. Vojtik, I. Paidarova, V. Spirko, and J. Savrda, Chem. Phys. Lett. **157**, 337 (1989).

123. N.F. Ramsey, Phys. Rev. **58**, 226 (1940).

124. J. Lounila, K. Oikarinen, P. Ingman, and J. Jokisaari, J. Magn. Reson., Series A **118**, 50 (1996).

125. G. W. Flynn and J. D. Baldeschweiler, J. Chem. Phys. **37**, 2907 (1962).

126. A. S. Culf, H. Morimoto, P.G. Williams, W.J.S. Lockely, W.U. Primrose, and J. R. Jones, Journal of Labelled Compounds and Pharmaceuticals **38**, 373 (1996).

127. J. P. Bloxidge and J. A. Elvidge, Prog. Nuc. Mag. Res. Spect. **16**, 99 (1983).

128. A. L. Odell, in *NMR of Newly Accessible Nuclei*, edited by R. Tyko, volume 2, pages 27–48, Academic, New York, 1983.

129. The National Tritium Facility, Lawrence Berkely National Laboratory, Berkely, CA 94720, USA. This institute can be reached also via WWW at: *http://www.lbl.gov/LBL-Programs/NTLF*.